Mapping of Ice and Gas on 1000 AU Scales

Thesis

The Open University

Mapping of Ice and Gas on 1000 AU scales

A thesis submitted in partial fulfilment for the the degree of Doctor of Philosophy

Astronomy Discipline, Department of Physical Sciences

Aleksi Suutarinen, MSc, BSc

The Open University

DATE OF SUBMISSION : 13th March 2015

DATE OF AWARD : 21 JUNE 2015

ProQuest LLC.
789 East Eisenhower Parkway
P.O. Box 1346
Ann Arbor, MI 48106 – 1346

Abstract

Many of the molecules in interstellar space are in the solid state, in so-called interstellar ices. The research in this thesis is focused around two key astronomical questions; How is ice distributed in star forming regions? How is ice affected by – or affecting – star formation processes? I provide answers to these questions through the analysis of submillimeter and near-infrared observations,

The observations analysed in this thesis consist of (partially published) archival data acquired mainly with the AKARI and Herschel space telescopes, and the ground-based ESO/VLT. To facilitate the reduction and analysis of some of this data two major software packages (ARF2 and OMNIFIT) were created with the PYTHON programming language The operation of both packages is fully documented in the thesis appendix.

The study of methanol ice prevalence in star-forming regions found that methanol ice can be found towards many more lines of sight than previously reported, and that its abundance relative to water ice can vary between a few to $\sim$40%. I also confirm that methanol very likely exists mixed in a water-rich ice component, a result consistent with our current understanding of methanol ice formation.

Proof was found of high-temperature chemistry forming water in the warm post-shock gas of YSOs. In this same region it was found that up to 99% of the methanol is being destroyed as it is sputtered from the surfaces of dust grains into the gas phase.

A novel analysis technique of slitless AKARI near-infrared spectroscopy yields an unprecedented number of water ice column density estimates towards background star lines of sight covering 12 separate $10' \times 10'$ fields of view in as many molecular clouds. A moderate correlation is found between water ice column density and dust optical depth at 250 microns, with the correlation potentially varying from cloud to cloud.

Acknowledgements

It is the view of the author that no significant discoveries in modern science are thanks to any single person, and that this thesis is no exception.

My PhD supervisors, Dr. Helen Fraser and Dr. Stephen Serjeant have provided me with invaluable knowledge on not only the subject matter, but also on academia and academic life in general. I would especially like to thank Helen for her patience with me in my efforts to understand the chemical side of astrochemistry, and in her assistance with writing numerous telescope time proposals and applications for job opportunities following my PhD. Stephen deserves special thanks for the numerous fascinating discussions held mostly in the context of "Cosmology Coffee Club", and for invaluable comments provided for both telescope time proposals, and on various methodologies and algorithms I have consulted with him on, and for advice given towards the final stages of my thesis preparation. I would also like to give special thanks to Dr. Jorma Harju, who has served as an excellent mentor and example of what a scientist should be like, especially in the time leading up to and during the early stages of my PhD studies.

In addition to specific people, a great number (more than can be named here) of family members, friends and colleagues have provided me with invaluable emotional and practical support throughout the several ups and downs of my PhD studies. You know who you are, thank you.

Last but not least, a special group of friends and colleagues, I would like to thank all the members of the LASSIE research network. Thank you for all the great times spent in numerous conferences, training schools and workshops, getting lost together in foreign cities and trying to find restaurants able to fit all of us on our nights out. Best research network ever.

Hofstadter's Law: It always takes longer than you expect, even when you take into account Hofstadter's Law.

-Douglas R. Hofstadter

Contents

List of Figures

Chapter 1

Introduction

In the interstellar medium –the space between the stars– a significant fraction of molecules are formed in the solid-state, on and in interstellar ices. Given that these molecules are used as both the tracers and probes of the prevailing physical conditions in the interstellar medium, understanding the origin, distribution, and evolution of interstellar ices is a vital component in our understanding of the star and planet formation process.

This thesis addresses these key astronomical questions:

How is ice distributed in star forming regions?

How is ice affected by or affecting star formation processes?

1.1 The interstellar medium

The interstellar medium (ISM) is the matter that exists between the stars, both in the temporal and the spatial sense. As is illustrated in Figure 1.1, material in the Universe follows the constant cycle of interstellar material accreting together to form new stars. At the end of their lives, these stars eject much of their surface material into interstellar space, which then eventually repeats the cycle. Consequently the ISM has very similar relative abundances of elements as the stars from which it originates; by mass the gas in the ISM is composed of about 70% hydrogen (both atomic and molecular), 28% helium

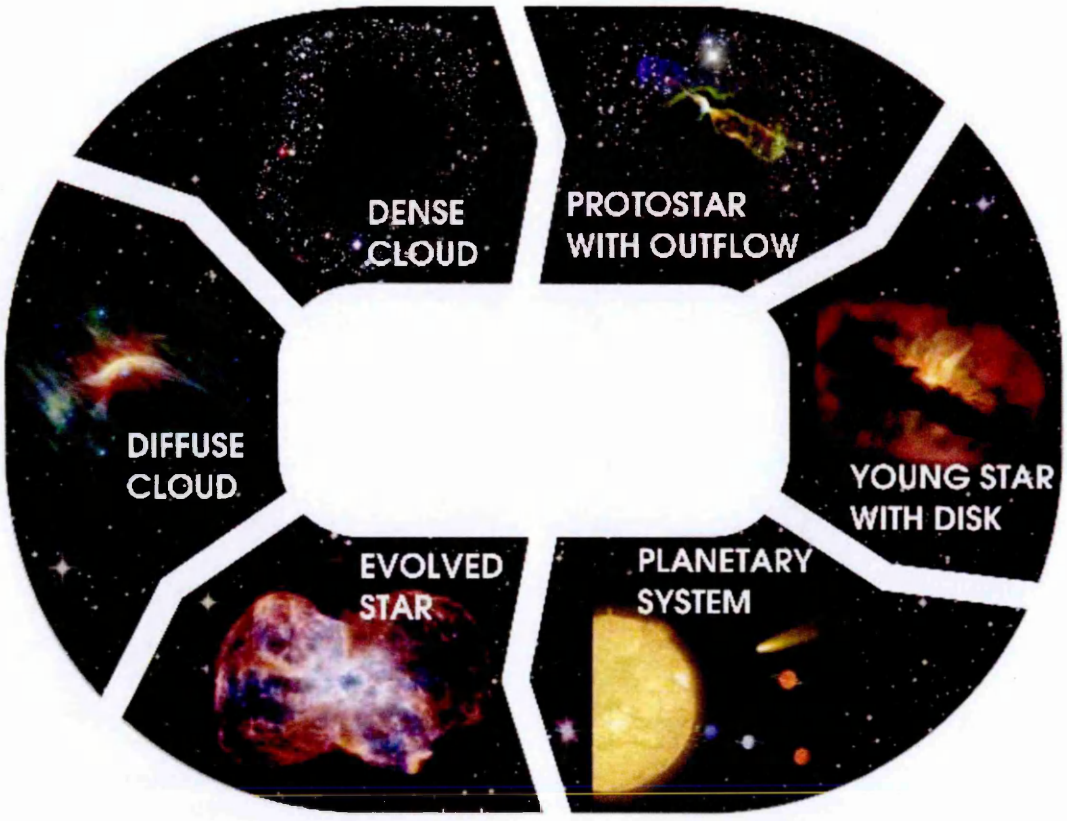

Figure 1.1: The stellar life cycle, where material is cycled between star systems and the interstellar medium. Figure reproduced from van Dishoeck (2014).

with the rest being heavier elements, which are often called "metals" in astronomers' nomenclature.

As is summarised in Table 1.1, the physical conditions in the ISM vary across a large range of densities and temperatures. The number density of the gas can range between 10^{-4} particles cm^{-3} and 10^{8} particles cm^{-3} and the temperature between 10 and 10^{6} K (e.g. van Dishoeck, 2014), with the low-density and high-temperature gas being classified as part of the diffuse ISM, while the high-density and low-temperature material is concentrated into interstellar clouds. The diffuse ISM consists mostly of atomic or ionised gas, while interstellar clouds are dominated by molecular material, both in the gas phase and even in the solid state, frozen on top of grains of dust.

Regardless of where it can be found, almost all the matter in the ISM will ultimately share the same fate: to be incorporated into the process of the creation of new stars. At some point, in a sufficiently dense and massive region of an interstellar cloud,

Table 1.1: A broad categorisation of the components of the ISM. This thesis predominantly concerns itself with molecular cloud regions. Reproduced from Ferrière (2001, and references therein)

Component	Typical temperature [K]	Typical density [particles/cm^3]
Molecular	$10-20$	10^2-10^6
Cold atomic	$50-100$	$20-50$
Warm atomic	$6000-10000$	$0.2-0.5$
Warm ionized	~ 8000	$0.2-0.5$
Hot ionized	$\sim 10^6$	~ 0.0065

the delicate balance between the forces that try to make the cloud break apart (such as gas pressure, turbulence and magnetic forces) and forces that try to make it collapse (gravity) will be tipped on the side of collapse by e.g. the shock wave coming from a nearby supernova or through random statistical fluctuations in local density. The details (e.g. Ward-Thompson and Whitworth, 2011) of how the collapse happens and what the physical conditions of the cloud are during the collapse define the type of star system produced at the end of it. Low-mass stars (stars with a mass lower than ~ 3 times the mass of the Sun, $M_\odot$), which are extensively discussed in this thesis, tend to result from a molecular cloud fragmenting –through statistical density fluctuations– into clumps whose mass and size are defined by the Jeans mass and Jeans length; measures of the smallest mass and and size of clump in the ISM which can condense into a star through self-gravity. High-mass stars (stars with a mass *higher* than $\sim 3M_\odot$) form in very dense and very massive dark molecular clouds, although the exact formation process is still not fully understood. The formation mechanism of star systems with multiple stars is similarly an open question, but is believed to be related to further fragmentation (through e.g. high turbulence) of the collapsing pre-stellar core. This thesis does not concern itself with high-mass stars or multiple systems, however, and thus they will not be discussed further.

Regardless of the type of star being formed, its birth is always marked by the beginning of nuclear fusion at the centre of the collapsing cloud core. Even after this the collapse of the surrounding material continues, but a significant fraction will not end up in the star itself but is either accreted into a protoplanetary disc around the star, or

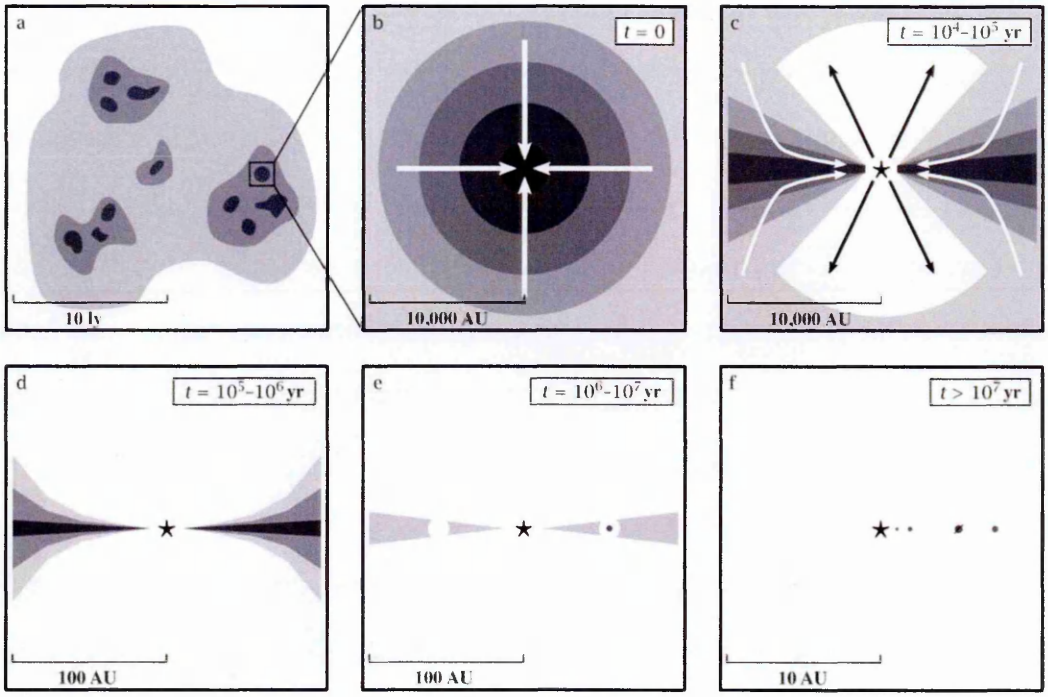

Figure 1.2: The process of star formation. (a) Molecular cores form within dense clumpy regions of the ISM, incorporating material originally in the diffuse ISM. (b) Core collapse is triggered by the density of the core becoming so high that gravity overcomes the forces preventing collapse. (c) A Young Stellar Object (YSO) forms in the center of the collapsing core while material is falling from the surrounding cloud into a circumstellar disc; bipolar outflows from the newly forming star sweep and compress material out of the inflated disk edges, compressing the disc in one dimension. (d) The star is fully formed, as is the circumstellar disc. The outflows have ceased. (e) Protoplanets start forming in the protoplanetary disc, cleaning their orbits of material. (f) After most of the material in the disc is incorporated into planets, a planetary system is established around the star. Figure reproduced from Visser (2009).

is launched back into the ISM through bipolar outflows along the rotation axis of the system. The protoplanetary disc is formed through the redistribution of the angular momentum of the material in the rotating protostellar core in such a way that a thick disc of matter is formed around the rotation axis of the system. The exact mechanism of how this redistribution happens is poorly understood, but the flow of material is believed to be guided through a combination of magnetic and gravitational torques combined with the viscosity of the accreting material. The exact mechanisms driving the outflows around protostars are similarly not well understood, but the outflowing material is believed to have originated from infalling material in the protoplanetary

disc being guided by the magnetic field lines of the star into its poles, from where it is launched at very high velocities (tens to hundreds of km/s) away from the system. This material often sweeps along with it material from the surrounding ISM, cleaning the immediate surroundings of the young stellar system of its disc of material, and forming distinctive outflow cones around the protostar. At later stages in the life of the young stellar object, the protoplanetary disc around it will fragment, and condense and aggregate to form planetesimals which will eventually clump together to form a planetary system around the young star. This physical process of star formation is summarised in Figure 1.2.

Of particular interest for this thesis are Figure 1.2 parts (c) and (d), which comprise the "young stellar object" (YSO) phases of the early life of the star. YSOs are classified as classes 0, 1, and 2 based on the shape of the spectral energy distribution (SED) of the object. Class 0 and 1 stages are best represented by Figure 1.2 (c), the key difference between the two stages being that class 0 YSOs are still heavily embedded and obscured within the core envelope, with almost no flattening of the disk; in class 1 objects the outflow cavity is significantly cleared, making the protostellar emission more prominent in the SED of the object. The transition to class 2 YSOs occurs in Figure 1.2 (d), once the circumstellar envelope has dissipated. The research and results presented in Chapters 3, 4, and 5 of this thesis span these evolutionary stages of YSOs, focused particularly in Chapter 4 on the interactions between the bipolar jets and the circumstellar envelope material. Chapters 3 and 5, whilst touching on YSO regions also reach back to earlier evolutionary stages, namely pre-stellar cores. These are illustrated in Figure 1.2 (a) and (b), and are sites of rich chemistry, primarily because of the high densities found there (see Table 1.1). It is during these stages in particular that the chemistry occurs which forms interstellar ices, and it is this broader chemistry that I outline in the next section.

Table 1.2: Molecules found in the ISM as of March 2015.[a],[b]

2 atoms	3 atoms	4 atoms	5 atoms	6-7 atoms	8+ atoms
H_2	C_3*	c – C_3H	C_5*	C_5H	CH_3C_3N
AlF	C_2H	l – C_3H	C_4H	l – H_2C_4	$HC(O)OCH_3$
AlCl	C_2O	C_3N	C_4Si	C_2H_4*	CH_3COOH
C_2**	C_2S	C_3O	l – C_3H_2	CH_3CN	C_7H
CH	CH_2	C_3S	c – C_3H_2	CH_3NC	C_6H_2
CH^+	HCN	C_2H_2*	H_2CCN	CH_3OH	CH_2OHCHO
CN	HCO	NH_3	CH_4*	CH_3SH	l – HC_6H*
CO	HCO^+	HCCN	HC_3N	HC_3NH^+	CH_2CHCHO?
CO^+	HCS^+	$HCNH^+$	HC_2NC	HC_2CHO	CH_2CCHCN
CP	HOC^+	HNCO	HCOOH	NH_2CHO	H_2NCH_2CN
SiC	H_2O	HNCS	H_2CNH	C_5N	CH_3CHNH
HCl	H_2S	$HOCO^+$	H_2C_2O	l – HC_4H*	CH_3C_4H
KCl	HNC	H_2CO	H_2NCN	l – HC_4N	CH_3CH_2CN
NH	HNO	H_2CN	HNC_3	c – H_2C_3O	$(CH_3)_2O$
NO	MgCN	H_2CS	SiH_4*	H_2CCNH?	CH_3CH_2OH
NS	MgNC	H_3O^+	H_2COH^+	C_5N^-	HC_7N
NaCl	N_2H^+	c – SiC_3	C_4H^-	HNCHCN	C_8H
OH	N_2O	CH_3*	HC(O)CN	C_6H	$CH_3C(O)NH_2$
PN	NaCN	C_3N^-	HNCNH	CH_2CHCN	C_8H^-
SO	OCS	PH_3	CH_3O	CH_3C_2H	C_3H_6
SO^+	SO_2	HCNO	NH_4^+	HC_5N	CH_3CH_2SH?
SiN	c – SiC_2	HOCN	H_2NCO^+?	CH_3CHO	CH_3C_5N
SiO	CO_2*	HSCN		CH_3NH_2	$(CH_3)_2CO$
SiS	NH_2	H_2O_2		c – C_2H_4O	$(CH_2OH)_2$
CS	H_3^+*	C_3H^+		H_2CCHOH	CH_3CH_2CHO
HF	SiCN	HMgNC		C_6H^-	HC_9N
HD	AlNC				CH_3C_6H
FeO?	SiNC				C_2H_5OCHO
O_2	HCP				$CH_3OC(O)CH_3$
CF^+	CCP				c – C_6H_6*
SiH?	AlOH				$C_2H_5OCH_3$?
PO	H_2O^+				n – C_3H_7CN
AlO	H_2Cl^+				i – C_3H_7CN
OH^+	KCN				$HC_{11}N$
CN^-	FeCN				C_{60}*
SH^+	HO_2				C_{70}*
SH	TiO_2				
HCl^+	C_2N				
TiO					
ArH^+					
NO^+?					

[a] List created based on `http://www.astro.uni-koeln.de/cdms/molecules`.

[b] All molecules have been detected (also) by rotational spectroscopy in the radio frequency to far-infrared regions unless indicated otherwise. * indicates molecules that have been detected only by their ro-vibrational spectrum, ** those detected by electronic spectroscopy only. Tentative and uncertain detections are indicated by "?".

1.2 Chemistry in the interstellar medium

While nuclear fusion processes in the hearts of stars and the addition of fission processes in supernovae are responsible for the creation of the elemental richness of the universe, it is in chemical processes largely inside of molecular clouds where the majority of the 180 or more molecules found in the ISM are formed (as of March 2015; see Table 1.2). The first one of these to be detected in the ISM was CH, which was originally observed towards ζ Ophiuchi by Adams (1941).

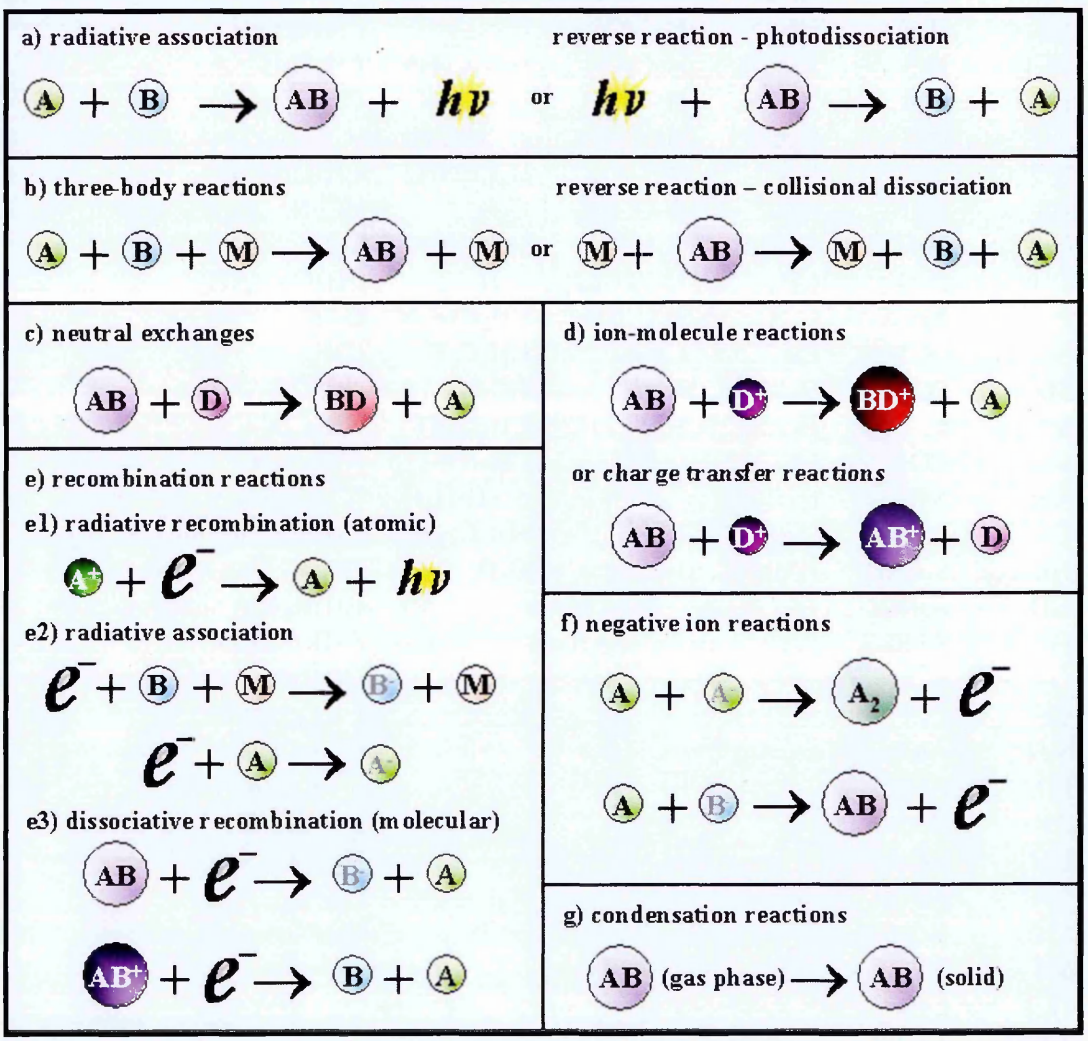

Figure 1.3: The chemical reactions dominating the gas-phase ISM. Figure adapted from Fraser, McCoustra, and Williams (2002).

The key reactions in the gas-phase ISM –leading to the formation of most of these 180+ molecules and ions– are summarised in Figure 1.3 Even in the relatively dense

environment of molecular clouds (in comparison with the diffuse ISM), number densities of the ISM gas are diminutive when compared with the number densities of e.g. Earth's atmosphere or even the best human-constructed vacuums. The chemistry in the gaseous ISM happens exclusively through two-body interactions, since the low densities make multi-body collisions –of the type shown in Figure 1.3b– vanishingly rare. Consequently, without a third body available to carry away excess energy from the reaction site, reactions are dominated by exothermic, barrierless processes, such as those shown in Figures 1.3d to 1.3f. Such reactions dominate in the cold ($T \lesssim 200\,\mathrm{K}$) ISM gas. The synergy between the gas and solid phase begins with the condensation (or freeze-out) processes summarised in Figure 1.3g.

The three of most abundant elements in the Universe, hydrogen (H) carbon (C) and oxygen (O), dominate the reactive chemistry of the ISM. Helium (He) is abundant, but as a noble gas, mostly unreactive. Of the thousands of reactions leading to the formation of hundreds of molecules in the ISM, of greatest interest to this thesis are the formation of water (H_2O), carbon monoxide (CO), and methanol (CH_3OH). The first two of these can be formed in the interstellar gas.

The formation of CO (carbon monoxide) –a molecule which is ubiquitous in dense ISM environments– occurs exclusively in the gas phase. One of the dominant reaction schemes (e.g. Langer, 1976) of producing CO relies on the presence of C^+, which is in molecular clouds produced mostly through cosmic ray ionization of C. The formation of CO from C^+ relies on repeated hydrogenation to form $CH_3{}^+$:

$$\mathrm{C} \xrightarrow{\mathrm{H_3^+}} \mathrm{CH^+} \xrightarrow{\mathrm{H_2}} \mathrm{CH_2^+} \xrightarrow{\mathrm{H_2}} \mathrm{CH_3^+}. \tag{1.1}$$

CH_3^+ can then follow a reaction chain starting with oxygen, followed by a dissociative recombination reaction:

$$\mathrm{CH_3^+} \xrightarrow{\mathrm{O}} \mathrm{HCO^+} \xrightarrow{\mathrm{e^-}} \mathrm{CO}. \tag{1.2}$$

H_3^+ is formed through cosmic ray ionization:

$$H_2 \xrightarrow{\text{c.r.}} H_2^+ \xrightarrow{H_2} H_3^+. \tag{1.3}$$

The H_3^+ generated by this process plays a vital role not just in the formation of CO but drives a significant number of chemical reactions in dense molecular cores, particular the ion-molecule and deuteration chemistries. Yet another reaction scheme for forming CO is for C^+ to react with O to produce CO^+. This can then react (e.g. Petuchowski et al., 1989) with a stray electron to either dissociate into C and O, or sometimes recombine into CO.

In warmer gas ($T \gtrsim 200\,K$) endothermic reactions such as the gas-phase formation of water (e.g. Bergin, Neufeld, and Melnick, 1999; Draine, Roberge, and Dalgarno, 1983; Glassgold, Meijerink, and Najita, 2009; Hollenbach and McKee, 1989; Tielens, 2005, also see Chapter 4) are made possible:

$$O \xrightarrow{H_2} OH \xrightarrow{H_2} H_2O. \tag{1.4}$$

However, water can also be found in cold dense ISM regions, where its origins are certainly not via reactions in hot gas, but surface chemistry on interstellar dust. The first solid-state detections of water actually pre-date its first gas-phase detections. Before Pilbratt et al. (2010) found gas-phase water with the Herschel Space Telescope, only upper limits for its abundances had been defined towards molecular cores with the Submillimeter Wave Astronomy Satellite (SWAS; Bergin and Snell, 2002) and the Odin satellite (Klotz et al., 2008). Over two decades prior to either of these studies, Gillett and Forrest (1973) had found frozen water in the dusty ISM.

1.3 Interstellar dust and ice

The ISM contains a small amount ($\sim$1% of total mass) of dust in addition to the gas. This dust consists of tiny chunks –from a few nanometres to a few microns (Williams

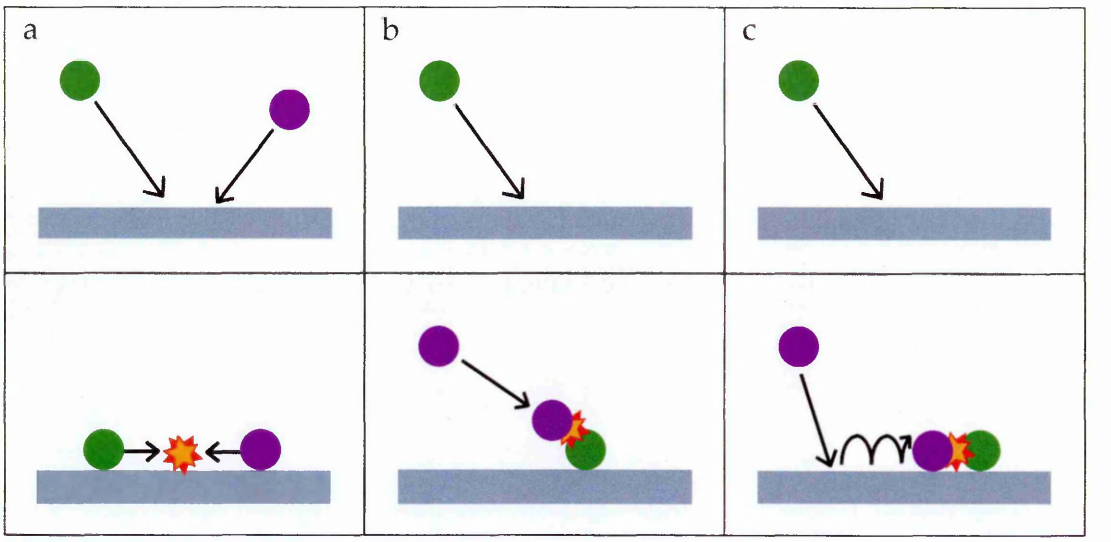

Figure 1.4: The three main mechanisms by which atoms can encounter each other on the surfaces of dust grains when grain-surface chemistry happens. In all cases the green atom adsorbs onto the grain first. (a) Langmuir-Hinshelwood. The second (purple) atom adsorbs in close proximity to the site occupied by the green atom. The two atoms diffuse on the surface until eventually meeting each other. (b) Eley-Rideal. The purple atom collides with the green atom. (c) Harris-Kasemo or "hot atom" effect. The purple atom lands on a site well-separated from the green atom with significant excess energy and is not accommodated to the surface. It then hops along the surface several times before encountering the green atom and forming a new molecule. Figure reproduced from Noble (2011).

and Herbst, 2002)– of mostly silicaceous and carbonaceous material often coated in a thin mantle of ice.

Despite its relatively low mass-fraction (in comparison to ISM gas), dust serves many important roles in both the physics and chemistry of the ISM. Most relevant to this thesis, it provides a surface upon which many molecules can freeze out, depleting gas-phase abundances of certain molecules when the freeze-out conditions are met. The most notable example of molecular depletion comes from CO, which freezes out onto grain surfaces at temperatures below $\sim$20 K (e.g. Duley, 1974) and/or H_2 densities above $\sim 10^4\,\mathrm{cm}^{-3}$ (Bergin and Langer, 1997). Of possibly even greater importance for this thesis, the dust provides a platform for atoms and molecules to be brought in close proximity of each other (a process unlikely to happen at ISM gas phase densities), and consequently the dust can facilitate chemical reactions that form molecules whose

presence in the ISM could otherwise not be explained. Three of the key chemical mechanisms by which surface reactions are facilitated are illustrated in Figure 1.4. Some of the most important molecules formed by this route are H_2, CH_3OH, and H_2O – with the latter two being the focus of this thesis. The formation of CH_3OH on grain surfaces happens via the repeated hydrogenation of CO (e.g. Tielens, 2005; Tielens and Hagen, 1982):

$$CO \xrightarrow{H} HCO \xrightarrow{H} CH_3O \xrightarrow{H} CH_3OH. \tag{1.5}$$

The grain-surface formation of H_2O is a more complicated matter (e.g. Ioppolo et al., 2008; Lamberts et al., 2013), but will generally involve the repeated hydrogenation of oxygen-bearing species such as O, OH, and O_2 (Tielens and Hagen, 1982).

When gas-phase atoms or molecules interact with the surface of a bare dust grain, they can adsorb in two different ways: via chemisorption and physisorption. When an atom or a molecule chemisorbs on a dust grain, it forms a strong chemical bond with the surface, usually a covalent or ionic bond. This strong bond can have energies in the order of a single electron volt or more, but requires that the adsorbing atom or molecule first overcomes a significant adsorption energy barrier with its kinetic or internal energy. The atoms or molecules in the cold ISM do not usually have enough kinetic energy to overcome this activation barrier on bare dust surfaces. Consequently, most atoms and molecules "frozen out" on cold ISM dust are physisorbed. A physisorbed atom or molecule has only a weak Van der Waals bond with the surface, with binding energies ranging from only 0.01 to 0.2 eV. This type of adsorption is either barrierless or has a very low energy barrier compared to chemisorption, and thus physisorption dominates in the dense ISM. Chemisorption has been postulated to occur in hotter regions of the ISM, for example diffuse ISM where H_2 formation is still known to be surface mediated, perhaps on the surfaces of carbonaceous dust, where chemisorption is a possibility (e.g. Balog et al., 2009; Cazaux and Tielens, 2004). These are not regions or mechanisms of most relevance to this thesis so henceforth I concern my discussion only with physisorption.

As atom-atom and atom-molecule reactions between physisorbed species lead to the formation of molecules at the grain surface, a so-called "interstellar ice" builds up. Comprised of adsorbed molecular material, these ice mantles are highly porous and amorphous, which leads to a rapidly increasing surface area, coupled with a highly non-uniform range of binding sites, such that adsorbates have a potentially wider range of physisorption biding sites to occupy (e.g. Gavilan, Lemaire, and Vidali, 2012; Hornekær et al., 2003; Kristensen et al., 2011). Some of these new sites can have much lower adsorption barriers than those of the bare dust grain, thereby increasing the chances of atomic or molecular adsorption from the ISM gas occurring and also the likelihood of retention of larger molecules (rather than their desorption) as they are formed.

Once formed, the ice layer can be further processed through chemical reactions (either barrierless or triggered by thermal heating, UV photons, or high-energy electrons) occurring between the ice constituents, forming new molecules. This cycle of ice formation and processing is illustrated in Figure 1.5. Many molecules (such as CH_3OH) which do not easily form in the gas phase can be formed through such reactions.

Regardless of where or how it forms, or whether it is in the gas phase or solid state, all molecular and atomic material in the ISM is detected in the same manner: through spectroscopic observations.

1.4 The origins of spectral features

Whether in the gas phase or frozen on top of grain surfaces, atoms and molecules in the ISM are detected via the tell-tale "signs" they leave in the energy distributions of electromagnetic radiation reaching our telescopes. In general, gaseous species are observed in emission –with an excess of flux against the background light–, and dust and ice predominantly observed in absorption; a lack of flux in the spectral energy distribution.

The purpose of this section is to summarise the basic principles of how absorption

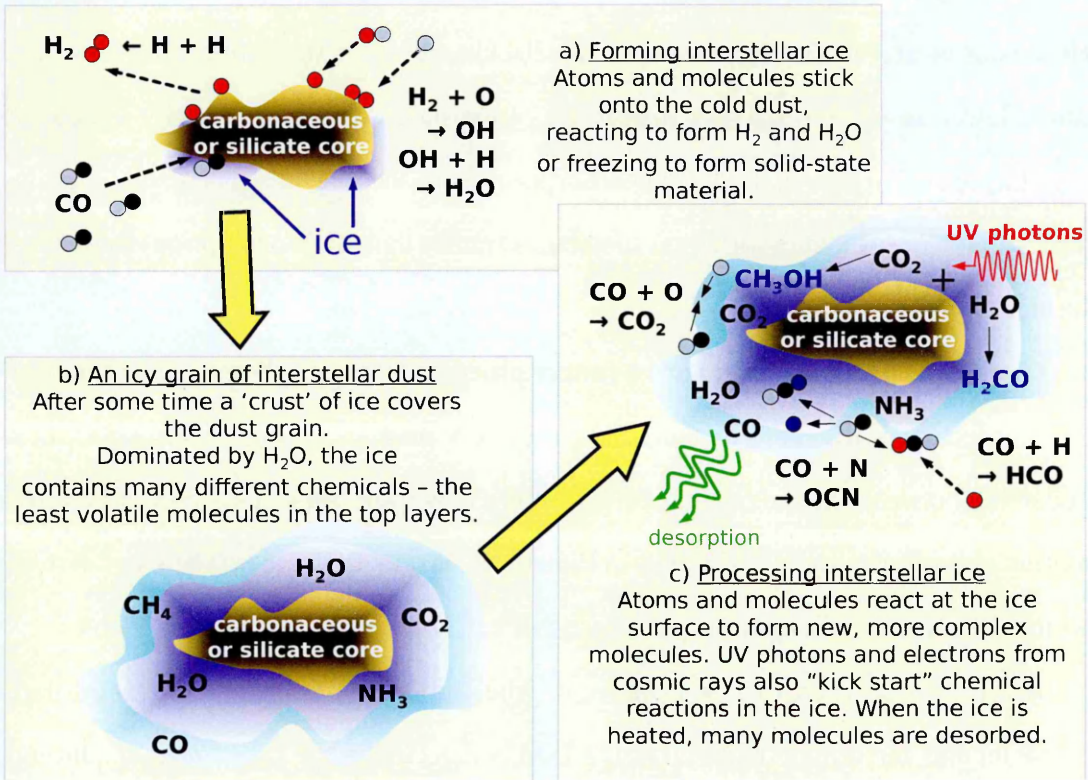

Figure 1.5: The formation and processing of ice upon dust grains.
(a) The initial formation of an ice layer, with simple gas-phase molecules and atoms adsorbing on the surface and sometimes reacting to form new molecules. Some of these molecules –such as H_2O– remain on the surface after their formation, while others –such as H_2– desorb almost immediately after forming. (b) A fully formed layer of ice is dominated by H_2O. (c) Additional processing of the ice produces molecules such as CH_3OH and H_2CO.

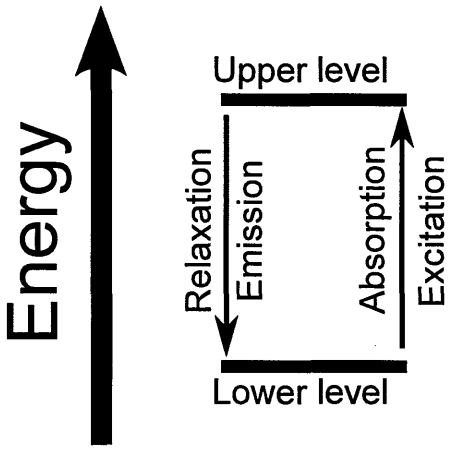

Figure 1.6: An illustration showing the basic principles behind energy level transitions. The upper and lower level represent two (of many) energy levels in an atom or molecule. The arrows represent a transition between the two levels, with excitation promoting the e.g. molecule to a higher energy level while relaxation returns the molecule to a lower energy level. The energy difference between the two levels determines the energy (and thus the frequency) of the absorbed/emitted photon, which is specific to the transition.

and emission lines emerge, followed by a slightly more detailed explanation pertaining to the gas-phase rotational spectroscopy of methanol (one of the molecules studied in this thesis), linking its complex spectral features to the basic physics principles and quantum mechanics explained below. I then compare and contrast the principles of gas-phase emission spectroscopy (required for Chapter 4 of this thesis) with those of solid-state adsorption spectroscopy, which is the basis of the interstellar ice studies in Chapters 3 and 5.

1.4.1 Basic principles

In describing the photoelectric effect Einstein (1905) showed that the energy of light can be quantized, namely that the energy of a photon E is proportional to its frequency ν via a constant of proportionality given by the Planck constant h:

$$E = h\nu \tag{1.6}$$

This equation is the basis from which astronomical spectra ranging from Fraunhofer lines (von Fraunhofer, 1814; Wollaston, 1802) in the optical wavelengths to CH masers (Rydbeck, Elldér, and Irvine, 1973) in radio frequencies can be understood.

Such lines are the result of the excitation (producing absorption lines) or relaxation/de-excitation (producing emission) of atomic and molecular material as it interacts with electromagnetic radiation. Basically, with the exclusion of their translation motion, all atoms and molecules are quantised entities, that is, they cannot possess just any energy, but exist in specific energetic state –in atoms the dominant energy levels are electronic states, associated with the arrangement of electrons around the nucleus– in molecules three key quantised energies come into play, electronic energy levels, associated with the arrangement of electrons in the bonds between the atoms of the molecule, rotational energy levels, associated with the rotation of the molecule about its key symmetry axes in the x y and z directions, and vibrational energy levels, associated with the perpetual oscillations of the bonds between atoms in the molecule (relative to each other) at temperatures above absolute zero.

Since my thesis is based in molecular spectroscopy I concern myself from here on with molecular transitions. These energy states are called quantised as they can only have certain specific energy values, and in molecules the Bohr-Oppenheimer approximation (Born and Oppenheimer, 1927) is valid – electronic transitions occur without changing the vibrational energy state of a molecule. However, rotational and vibrational energy states are strongly coupled. Given the complexity of all these aspects, and as a result of quantum mechanics, each energy state of the molecule is described by a set of quantum numbers, which are associated with the specific electronic, vibrational and rotational energy levels the molecule may occupy, and can be used to describe the detailed energy state of the molecule before and after a transition. When a molecule is excited ($\Delta E > 0$), it absorbs electromagnetic radiation and is promoted from a lower to higher energy state (producing absorption lines). When a molecule is de-excited/relaxed ($\Delta E < 0$), it emits radiation and falls back from a higher to a lower energy state. These basic processes are illustrated in Figure 1.6.

There are two key final points to mention in understanding spectroscopy and its association with the picture of quantised energy levels in a molecule. First, by the principles of Heisenberg's Uncertainty Principle (Heisenberg, 1927), the energy and lifetime of an excited state of a molecule can never both be known precisely at the same time. Consequently in any excitation/relaxation, the precise energy of the emitted photon can vary by a small factor, associated with the uncertainty in the energy of the upper and lower energy states (which itself is related to the precision with which the lifetime of these states is known). This results in spectral features not as single lines at a single frequency, but gives the characteristic natural line shape, described by a Lorentzian curve, with a peak at the expected frequency associated with the energy gap of the transition, and 'line wings' associated with those photons emitted at slightly different frequencies to the natural frequency. The second issue is that whilst molecules may posses a plethora of electronic, vibrational and rotational energy levels, a transition cannot occur for any one particular energy level to another one regardless.

The transitions are governed by a set of selection rules, which are deeply embedded into the quantum mechanics which also give rise to the quantum numbers. Typically selection rules are expressed in terms of the allowed changes to quantum number during a transition, and may be further constrained if rotational and vibrations energy of a molecule change concurrently.

All of this is difficult to illustrate abstractly, so in the next section a specific example is described.

1.4.2 The rotational spectroscopy of gas-phase CH_3OH

The spectroscopy of methanol is far from trivial, but since it is a molecule that appears in Chapters 3 and 4 of this thesis, it serves as an example to describe the origins of spectral features, with specific reference in this case to the gas-phase rotational spectroscopy of CH_3OH. Molecular spectroscopy is a specialised field, and those with an interested in obtaining a deeper understanding are directed towards general senior-

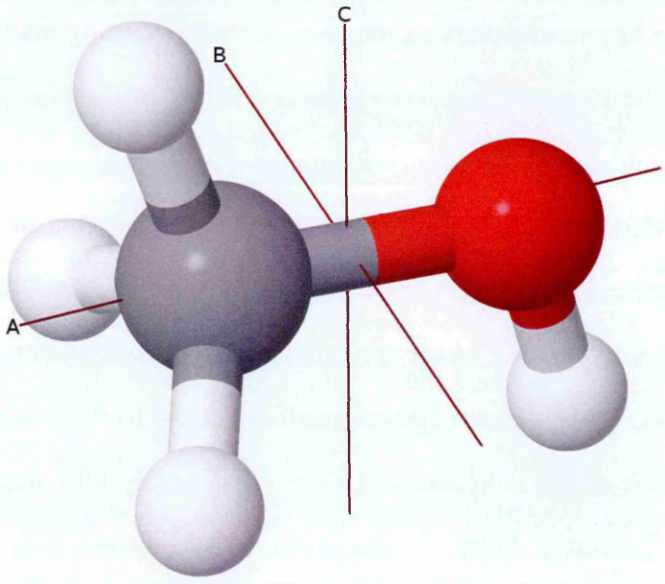

Figure 1.7: The 3-dimensional structure of the methanol molecule. The red sphere represent an oxygen atom, the gray one a carbon atom and the white spheres represent hydrogen atoms. Also shown are the symmetry axes of the molecule. This structure can be further split into the hydroxyl group (OH) and the methyl group (CH_3), with the main symmetry axis A being defined by the axis linking the carbon and oxygen atoms.

undergraduate level texts on the subject, such as Hollas (1992).

The CH_3OH spectral observations exploited for the research in Chapter 4 were measured in the sub-mm frequency range, a region of the electromagnetic spectrum associated with rotational energy changes in molecules. Rotational spectra depend on molecular shapes and the moments of inertia of the molecule when it rotates about 3 "imaginary" orthogonal axes which pass through the centre of mass of the molecule. Notation dictates that symmetrical tops are molecules with two rotational axes that have the same inertia (called b- and c- axes), and one unique rotational axis with a different inertia (called the a-axis). Symmetrical tops can be further divided into two categories. If the unique a-axis has a greater inertia than the degenerate b- and c-axes (i.e. $I_a > I_b = I_c$), the molecule is called an oblate symmetrical top and tends to resemble a Frisbee in shape. If the unique rotational axis has a lower inertia than the degenerate axes (i.e. $I_a < I_b = I_c$), the molecule is called a prolate symmetrical top, and somewhat resembles a rugby ball in shape. In reality most molecules are neither of these, but are in fact asymmetric rotors, which means the moments of inertia are not

equal along the three axes (i.e. $I_a \neq I_b \neq I_c$). The 3-dimensional shape of the CH_3OH molecule (illustrated in Figure 1.7) places it in the asymmetric rotor category.

Although CH_3OH is an asymmetric rotor, it is actually close to a prolate symmetric top molecule. The unique rotational axis (the a-axis) in CH_3OH is that of highest symmetry, which is defined by the axis linking the carbon and oxygen in the C-O of the molecule. This axis is known as a "three fold symmetry axis" or C_3, since each time the molecule is rotated through 120 degrees its methyl group (the CH_3 part of CH_3OH) re-produces a molecular orientation in space indistinguishable from the previous orientation 120 degree before. Had the hydroxyl group (the OH part of CH_3OH) of the molecule been linearly orientated with the C-O bond, methanol would be classifiable as a "proper" prolate symmetric top molecule. But, the OH (as Figure 1.7 illustrates) is angled with respect to the C-O bond, which causes the b and c axes to not have equal moments of inertia as required of a prolate symmetric top. However for the purposes of the simple spectroscopic picture here it is sufficient to understand that as the internal rotor (the hydroxyl group) is in perpetual motion, to a first approximation the b- and c-axes are degenerate in methanol. In reality there are actually 3 minima in the torsional potential energy surface, so many researchers in fact view the CH_3OH molecule from an alternate frame of reference, namely that the OH bond orientation is always fixed relative to the C-O bond, but that the methyl group (CH_3) provides the free rotor within the molecule.

As a consequence the rotational motion of CH_3OH is described by two quantum numbers, J and K, and any one rotational state is written with the notation J_K. The rotational quantum number J relates to the magnitude of the (quantized) angular momentum of the rotating molecule about the unique a-axis. This quantum number can take any non-negative integer value, as well as zero. As J increases, so does the rotational energy of the molecule, and energy levels associated with progressively higher J values become further separated from the previous levels. The selection rule $\Delta J = \pm 1$ –imposed by the conservation of angular momentum– applies for transitions between rotational states described by the rotational number J.

It is unlikely that the CH_3OH molecule will in reality be rotating about one axis in space, or that the axis it is rotating around will be aligned with the a-axis of the molecule. Rather the rotational motion will be some combination of rotations about each of the (defined) orthogonal molecular rotational axes. K is the quantum number representing the projections of the principle quantum number J onto the two other rotational axes b and c. When the moments of inertia around b and c are equal, typically there are $2J+1$ K levels for any value of J, with K having possible values in the range $J...0...+J$. The selection rule is $\Delta K = 0$. In asymmetric molecules there would be two K values, neither of which would be "proper" quantum numbers as they could not be conserved as the molecule rotates. However, for the low-lying rotational states of interest in this thesis (see Chapter 4) the "averaging" effect of the torsional motion of the methyl group (internal rotation) means that one K value is sufficient to describe the rotational motion of the molecule. Consequently the selection rules on K change a little, and $\Delta K = \pm 1$ are also allowed transitions.

The final vital component for describing the rotational energy levels of CH_3OH relates to the spin states of the hydrogen atoms in the methyl (CH_3) group in methanol. Hydrogen contains one electron and one proton both of which have intrinsic spins, which can be spin up or down, or have opposing spins. The spin of the proton is most relevant here. Consequently the three H-atoms in the CH_3 group might statistically exist with all three H proton spins aligned, or two of the protons with opposing spins to the third H proton. This gives rise to two states, the ground symmetrical state A-CH_3OH (as defined by the Pauli exclusion principle) and the doubly degenerate E-CH_3OH state. As a consequence of the coupling between the proton spins and the rotational energy the arrangement of the J and K states in each of these isomers are not identical, even in the ground state, and therefore give rise to distinct spectroscopic features. This is also illustrated in Figure 1.8 where it is clear to see the ground state rotation energy level in A-CH_3OH is $J = 0$ $K = 0$, whereas the ground state level in E-CH_3OH is $J = 1$ $K = -1$.

In reality, the true rotational spectra of methanol have been determined through

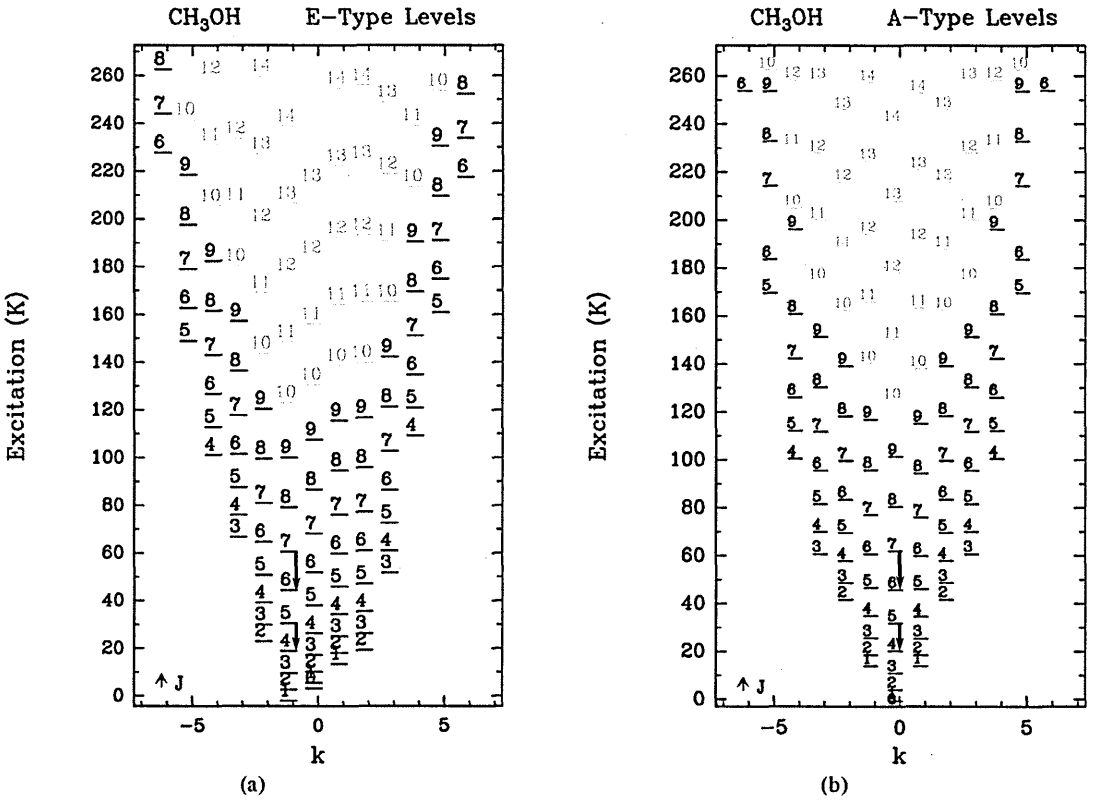

Figure 1.8: An energy level diagram for (a) E-CH_3OH and (b) A-CH_3OH. The number on top of each line is the J quantum number for the level, and the location of the line along the x axis describes its K quantum number. It is important to note that the energy levels are not arranged identically in the A and E states nor do they have the same rotational ground states. The arrows indicate the main CH_3OH transitions of interest to Chapter 4. Figure adapted from Leurini et al. (2004).

a complex set of experimental measurements and computational calculations which reproduce effects such as level crossings, perturbation by low lying vibrational states and torsional motion (which dominates over the K quantum number at $K \gtrsim 7$), all of which makes the CH_3OH gas-phase spectrum in the sub-mm exceptionally complex. Further details are discussed widely in the literature (e.g. Pei, Gou, and Zeng, 1988; Pottage, Flower, and Davis, 2001; Sutton and Herbst, 1988). Data for such energy levels for methanol and other complex molecules are available from data repositories such as the Cologne Database for Molecular Spectroscopy (`http://www.astro.uni-koeln.de/cdms/`; Müller et al., 2001; Müller et al., 2005).

In additional to understanding the origins of the rotational spectroscopy of a molecule when observing its transitions through observations, it is also important to under-

stand two other physical concepts in order to extract additional information about the ISM from the spectroscopy itself.

The strength of the line –pertaining to a specific energy transition– depends not only on the abundance of the material and the probability of the transition occurring between the two energy states in question, but is also subject to a multitude of physical processes which balance the excitation and relaxation/de-excitation between energy levels in interstellar matter, given that the ISM gas is not typically in local thermodynamic equilibrium (LTE) i.e. the energy levels are not simply populated according to Boltzmann's distribution. This is the domain of radiative transfer –which seeks to explain how specific physical conditions give rise to specific observed atomic or molecular line intensities and vice versa– and will be elaborated upon further in Chapter 4 where it is key to interpreting the results in the chapter.

Beyond the quantum mechanical effects described before, the shape of the line itself is also a tracer of physical conditions. In an astronomical context the line width and detected frequency of a spectral line traces primarily (but not only) the kinematics and temperature of the gas. Doppler effects can and will shift the line centre from its rest frequency (i.e. where the transition is measured in the laboratory or predicted by quantum mechanics) to a blue- or redshifted frequency determined by the velocity with which the object (cloud) being observed is moving relative to the Earth. Superimposed doppler effects are also be responsible for broadening of the spectral lines as a result of the emission arising from gas with molecules at a range of temperatures, velocity components and subject to turbulence. As a result of how closely the observed frequency and width of gas-phase spectral features is tied to the velocity of the emitting matter, published spectra of gas-phase lines (such as those shown in Chapter 4) are often plotted as intensity against a doppler-shifted velocity scale instead of intensity against e.g. observed frequency.

Interestingly, all this molecular rotational information is lost once (or whilst) the molecules are frozen out in the solid-state i.e. as ices on interstellar grains. In the solid state the rotational motion is hindered by the restrictive nature of the 2-dimensional

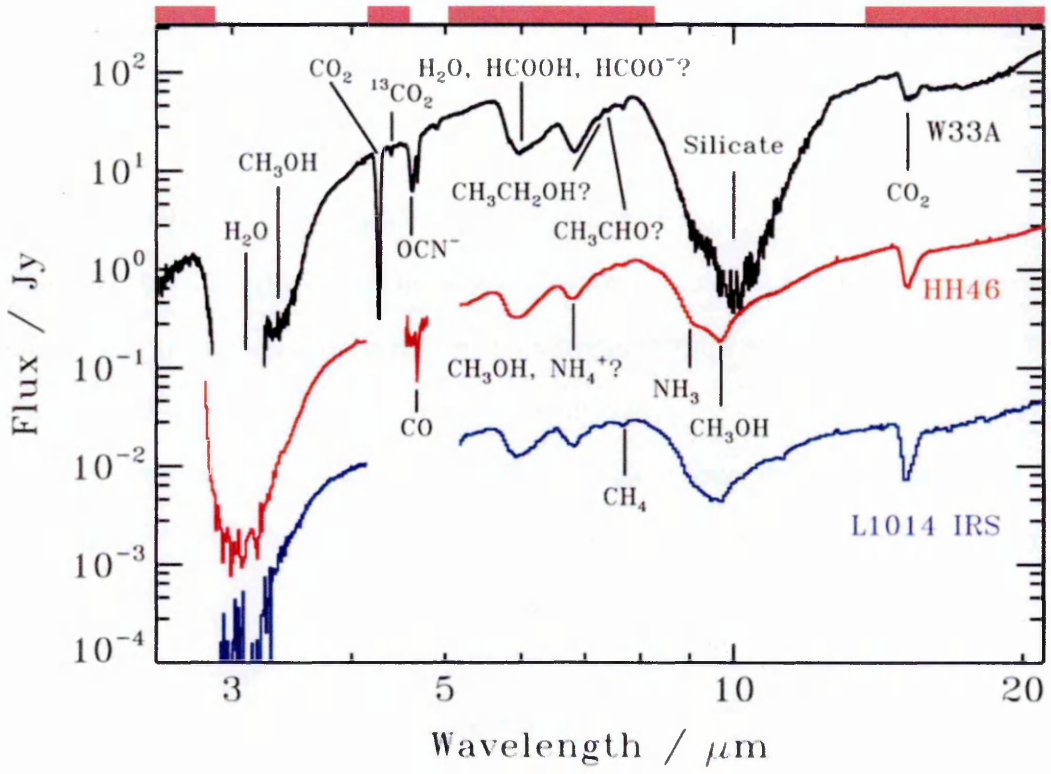

Figure 1.9: Near-to-mid infrared spectra of three protostars (W33A, HH46, L1014 IRS) showcasing the absorption signatures produced by various interstellar ices. The red bars at the top indicate the approximate wavelength ranges at which more than 50% of the incoming radiation is blocked by Earth's atmosphere, when performing ground-based observations. Figure adapted from Öberg et al. 2011a, and references therein.

nature of the surface. Given that molecules are bound to other molecules they are never free to rotate. Since solid-state molecular spectroscopy plays such a vital role in Chapters 3 and 5 of this thesis, I explore it further in the next section.

1.4.3 The spectroscopy of solid-state molecules

The features of interstellar ices (which always appear in absorption, requiring the presence of a bright infra-red (IR) background source for ice to be observed in any particular line of sight) are attributable to the vibrational modes of "functional groups" i.e. specific types of atoms, bonded together in specific ways within molecules in the ice (e.g. Hagen, Allamandola, and Greenberg, 1980; Nakanishi, 1962). The vibrations are observed in the IR region of the electromagnetic spectrum, and are characteristically

broad and featureless in comparison to the ro-vibrational transitions of warm gas-phase molecules whose transitions are observed in the same region (e.g. Pontoppidan et al., 2003a). For example all interstellar ices exhibit an O-H stretching mode absorption feature at a wavelength of approximately 3.1 μm, which is usually indicative of H_2O and possibly CH_3OH ice, but also could be associated with any molecule containing an O-H bond, i.e. the OH functional group. The O-H stretch feature arises from both the symmetric and asymmetric lengthening and shortening of the two O-H bond in the H_2O molecule, relative to each other. The exact frequency of the vibration ν is proportional to the square root of the force constant of the bond k, and inversely proportional to the square root of the reduced mass of the bond μ.

$$\nu \propto \sqrt{k/\mu}. \tag{1.7}$$

In other words, if the bond strength between the atoms in the functional group increases the OH stretching vibration appears at higher frequency and vice versa. Likewise if the reduced mass of the bond increases the frequency decreases, i.e replacing the H in the OH bond with i.e. deuterium (D) shifts the vibrational frequency from about 3 to about 3.5 microns. Tables 1.3 and 1.4 shows the frequencies at which typical functional groups oscillate in the solid state, for stretching and bending vibrations respectively. These tables –as do many other tables and plots related to ices in this thesis– make use of a frequency unit which is somewhat uncommon in astronomical (but not chemistry-focused) spectroscopy: reciprocal wave numbers. This unit is often used interchangeably with wavelength units, and the formula for converting between microns and cm^{-1} is

$$\lambda[\mu\mathrm{m}] = \frac{10^4}{\nu[\mathrm{cm}^{-1}]}. \tag{1.8}$$

Since rotational motion in the solid state is hindered, the wide-ranging rotational structure of any vibrational transition "collapses" making the wavelength span of a solid-state line narrower than the total span of the corresponding ro-vibrational gas-phase transitions, but much wider than any of the individual transitions. Of additional note is

Table 1.3: Typical infrared ice absorption features caused by stretching vibrations. Adapted from `http://bit.ly/1tSdL5R`

Functional Class	Range (cm^{-1})	Assignment
Alkanes	2850 – 3000	CH_3, CH_2 & CH
		2 or 3 bands
Alkenes	3020 – 3100	=C-H & $=CH_2$ (usually sharp)
	1630 – 1680	C=C (symmetry reduces intensity)
	1900 – 2000	C=C asymmetric stretch
Alkynes	3300	C-H (usually sharp)
	2100 – 2250	C≡C (symmetry reduces intensity)
Arenes	3030	C-H (may be several bands)
	1600&1500	C=C (in ring) (2 bands)
		(3 if conjugated)
Alcohols & Phenols	3580 – 3650	O-H (free), usually sharp
	3200 – 3550	O-H (H-bonded), usually broad
	970 – 1250	C-O
Amines	3400 – 3500	N-H (1°-amines), 2 bands
	3300 – 3400	N-H (2°-amines)
	1000 – 1250	C-N
Aldehydes & Ketones	2690 – 2840	C-H (aldehyde C-H)
	1720 – 1740	C=O (saturated aldehyde)
	1710 – 1720	C=O (saturated ketone)
	1690	aryl ketone
	1675	α, β-unsaturation
	1745	cyclopentanone
	1780	cyclobutanone
Carboxylic Acids	2500 – 3300	O-H (very broad)
& Derivatives	1705 – 1720	C=O (H-bonded)
	1210 – 1320	O-C (sometimes 2-peaks)
	1785 – 1815	C=O
	1750&1820	C=O (2-bands)
	1040 – 1100	O-C
	1735 – 1750	C=O
	1000 – 1300	O-C (2-bands)
	1630 – 1695	C=O (amide I band)
Nitriles	2240 – 2260	C≡N (sharp)
Isocyanates,Isothiocyanates,	2100 – 2270	-N=C=O, -N=C=S
Diimides, Azides & Ketenes		-N=C=N-, -N3, C=C=O

Table 1.4: Typical infrared ice absorption features caused by bending vibrations. Adapted from http://bit.ly/1tSdL5R

Functional Class	Range (cm^{-1})	Assignment
Alkanes	1350 – 1470	CH_2 & CH_3 deformation
	1370 – 1390	CH_3 deformation
	720 – 725	CH_2 rocking
Alkenes	880 – 995	=C-H & $=CH_2$
	780 – 850	(out-of-plane bending)
	675 – 730	cis-RCH=CHR
Alkynes	600 – 700	C-H deformation
Arenes	690 – 900	C-H bending & ring puckering
Alcohols & Phenols	1330 – 1430	O-H bending (in-plane)
	650 – 770	O-H bend (out-of-plane)
Amines	1550 – 1650	NH_2 scissoring (1°-amines)
	660 – 900	NH_2 & N-H wagging (shifts on H-bonding)
Aldehydes & Ketones	1350 – 1360	α-CH_3 bending
	1400 – 1450	α-CH_2 bending
	1100	C-C-C bending
Carboxylic Acids & Derivatives	1395 – 1440	C-O-H bending
Nitriles	1590 – 1650	N-H (1¡-amide) II band
Isocyanates,Isothiocyanates, Diimides, Azides & Ketenes	1500 – 1560	N-H (2¡-amide) II band

the effect of ice structure on the line width: crystalline ices where molecules are in a limited range of orientations and environments have much narrower solid state features than amorphous materials, where again the molecular environments are broad and also wide ranging. As a result, solid-state lines are much broader than gas-phase lines, and in some cases they are broader than even many dust absorption and emission features from e.g. silicates, SiC, PAH and fullerenes.

When combined with observations, the information in Tables 1.3 and 1.4 have allowed us to identify a number of solid state ice species unequivocally i.e. CO, CO_2 H_2O CH_3OH NH_3 CH_4, ^{13}CO, and $^{13}CO_2$. We have also been able to make reasonable (but still being debated) assumptions about others such as HCOOH, NH_4^+, and OCN^- on lines of sight towards high-mass, low-mass, and intermediate mass stars, as shown in Figure 1.9. What is obvious from this figure is that ice spectra appear remarkably

similar despite observations spanning over 4-5 orders of magnitude in flux. It is unlikely, perhaps with the exception of HDO, D_2O, and OCS (if such ices exist) that any other ice species will be unequivocally identified, simply because their concentrations in the solid state are so low as to preclude detection.

Determining the column density of ice from an observed spectrum also happens in a way that is very different from gas-phase. While gas-phase column density determinations rely heavily on radiative transfer computations and the (mostly) theoretical data required by it, the derivation of ice column densities from observations makes use of comparisons with largely experimental data. As ice column densities are fundamental to the research in Chapters 3 and 5, I will take some time here to discuss their derivation, and the nuances in the calculation between observational spectra and the extracted column density number.

The most common method of determining ice column densities starts by calculating the optical depth spectrum of an observation containing ice features by fitting a continuum to the detected flux around the feature itself, then taking the ratio of the two, using:

$$\tau = \ln\left(\frac{F_{\rm obs}}{F_{\rm cont}}\right), \tag{1.9}$$

where τ is the optical depth spectrum, $F_{\rm obs}$ is the observed flux spectrum, and $F_{\rm cont}$ is the continuum spectrum. When determining the optical depths of ices, a few different methods exist for the continuum baseline fits. The most commonly used method (e.g. Aikawa et al., 2012a; Gibb et al., 2004; Öberg et al., 2011a) fits a (usually) $2^{\rm nd}$ order polynomial around the ice feature of interest, sometimes (e.g. Pontoppidan et al., 2003b) making use of non-spectroscopic continuum data (i.e. an SED) in addition to the spectrum itself. More recent studies (e.g. Boogert et al., 2013; Noble et al., 2013) have made use of photometry towards the sources of interest to construct and redden a synthetic model SED for the background source, and use it as a local continuum. The optical depth fitting done in this thesis makes use of local polynomial fits around the features, since the supplementary data required for more sophisticated models was not

available towards most of the sources I am analysing.

Once the optical depth spectrum has been generated, there are a number of alternative methods to extract the ice column density. The first studies of ices (e.g. Whittet et al., 1988) did not report a column density for the ice at all, but instead simply reported the peak optical depth of the ice feature of interest at a wavelength where the absorption peak is predicted to be by a combination of laboratory experiments and computational models. The simplest method for calculating a column density from this makes use of the following equation (e.g. Murakawa, Tamura, and Nagata, 2000):

$$N(\text{ice}) = \tau_{\text{ice}} \frac{\Delta\nu}{A}, \tag{1.10}$$

where τ_{ice} is the peak optical depth of the ice absorption feature, $\Delta\nu$ is its FWHM (usually in cm^{-1}), and A is the band strength or "A-factor" (usually in cm/molecule) for the ice feature (e.g. Gerakines et al., 1995; Hudgins et al., 1993). The above equation is an approximation of the integrated form of calculating ice column density, expressed as:

$$N(\text{ice}) = \int \frac{\tau_{\text{ice}} d\nu}{A}. \tag{1.11}$$

While it would be possible to simply integrate over the optical depth feature of interest and divide the integral by the A-factor, this is not entirely physical for a number of reasons:

1. In some cases –such as the 3-micron O-H stretching feature– the peak of the absorption feature is saturated and not linearly representative of the true column of ice producing it.

2. The A-factors published in the literature are estimated from ices grown in laboratory conditions onto a slab-shaped surface. The ices grown in laboratory conditions are usually hundreds of microns thick, while on interstellar dust grains they usually consist of a few nanometers layer of ice on a grain rarely larger than about a micron in diameter. Since the grain sizes are smaller than the wave-

length of photons relating to ice features, the grain and electromagnetic field interact with each other in a manner which polarizes the grain, which in turn affects spectral line shapes and positions. It is thus vital to take these grain shape effects into account when determining the column density of ice constituents. Since these grain-shape effects modify the shape of the spectrum, its integrated area is modified as well and thus a new "effective" A-factor (usually labelled A') must be calculated for the column density estimates to be accurate. If these effects are not appropriately accounted for, applying an experimentally determined A-factor to Equation 1.11 will not result in a good ice column density estimate.

The first complication can be dealt with by first fitting a laboratory ice spectrum (which has first been modified to better approximate interstellar ices; see below) to the non-saturated part of the observed spectrum, and integrating over the fitted spectrum instead of observed spectrum. This method has been applied in e.g. Shimonishi et al. (2010). A step further (e.g. Boogert, Hogerheijde, and Blake, 2002; Noble et al., 2013; Pontoppidan et al., 2003b) is to simultaneously fit multiple laboratory spectra to the same feature, in an attempt to decompose the contribution of different ices to the observed absorption. This multi-component fitting methodology will be the focus of Chapter 3.

The second complications means that before the laboratory spectra can be properly fitted or before an accurate column density can be calculated from the result, the grain shape effects should be taken into account. A number of different methods are applicable in modelling the interaction between the EM field and the coated dust grain. Two such methods are called the "Mathis, Rumpl and Nordsieck" (MRN; Mathis, Rumpl, and Nordsieck, 1977) method and the "Continuous Distribution of Ellipsoids" (CDE; cf. Bohren and Huffman, 1983) method. The latter of these has been successfully applied to ice column density estimate calculations several times in the past (e.g. Ehrenfreund et al., 1997; Noble et al., 2013; Pontoppidan et al., 2003a; Tielens et al., 1991), and thus it is the method I will also make use of in Chapters 3 and 5. For this reason I will now elaborate on how CDE-correction works.

The first step leading to CDE-correction is to derive the complex optical constant

$\mathbf{m} = n + ik$ as a function of frequency for the laboratory ice which is being fitted to observations. This can be done by utilising the Kramers-Kronig analysis (e.g. Bohren and Huffman, 1983; Ehrenfreund et al., 1997; Hudgins et al., 1993) to the observed absorbance of the laboratory data. To calculate n and k as a function of frequency ν, the following equations can be utilised:

$$n(\nu) = 1 + \frac{1}{2\pi^2} \int_0^{\inf} \frac{\alpha(\nu')}{\nu'^2 - \nu} d\nu' \tag{1.12}$$

$$k(\nu) = \frac{\alpha c}{4\pi\nu}. \tag{1.13}$$

In these equations c is the speed of light, and α is the Lambert absorption coefficient. α can also be expressed (Ehrenfreund et al., 1997) in the form

$$\alpha = \frac{1}{h}\left[\tau(\nu) + \ln\left|\frac{\mathbf{t}_{01}\mathbf{t}_{12}/\mathbf{t}_{02}}{1 + \mathbf{r}_{01}\mathbf{r}_{12}\exp(4i\pi h\mathbf{m}/\lambda)}\right|^2\right], \tag{1.14}$$

where $\mathbf{r}_{pq}$ and $\mathbf{t}_{pq}$ are the complex reflection and transmission coefficients at the boundary pq (the boundary between the materials through which the radiation is passing), and h is the thickness of the ice measured in the laboratory while $\tau(\nu)$ is its optical depth as a function of frequency.

Application of Equation 1.12 in a real-world situation is problematic, because no spectra of an infinite frequency range exist to integrate over. However, in a near-infrared setting it is possible to approximate such an integration by expressing Equation 1.12 in the form

$$n(\nu) \approx n_0 + \frac{1}{2\pi^2} \int_{\mathrm{IR}} \frac{\alpha(\nu')}{(\nu'^2 - \nu^2)} d\nu', \tag{1.15}$$

where n_0 is the real part of the refractive index at high frequencies relative to the band being examined.

With Equations 1.12–1.15 it is possible to solve the complex refractive index of the ice starting from τ, but not in an analytical fashion; an iterative approach is required. An iterative solution to the Kramers-Kronig relation was presented in the form of a

FORTRAN77 program in Bohren and Huffman (1983). I adapted this program to my needs, and used it to calculate **m** for the laboratory ice used in Chapters 3 and 5 of this thesis.

With the optical constants at hand, it is now possible to perform the CDE correction itself by calculating a CDE-corrected version of the ice optical depth. In the infrared regime, the absorption cross section of the ice –$C_{\rm abs}$– on a hypothetical ellipsoidal dust grain normalised by the volume of the dust grain –V– can be expressed in the form (e.g. Bohren and Huffman, 1983; Ehrenfreund et al., 1997):

$$\frac{C_{\rm abs}}{V} = \frac{2\pi}{3\lambda} \sum_{i=1}^{3} \frac{2nk/L_i^2}{(1/L_i - 1 + n^2 + k^2)^2 + (2nk)^2}, \tag{1.16}$$

where λ is wavelength and L_i describes the geometry of the ellipsoid along all of its 3 axes, as constrained by $0 \leq L_i \leq 1$ and $\sum_{i=1}^{3} L_i = 1$. For example, for a sphere $L_i = 1/3$ for all axes, while an ellipsoid which is elongated along one axis would have $L_i > 1/3$ for that axis, while $L_i < 1/3$ for the other two axes, in such a way that $\sum_{i=1}^{3} L_i = 1$ still applies. With the CDE correction all ellipsoid geometries are made equally probable, and Equation 1.16 simplifies to

$$\frac{C_{\rm abs}}{V} \approx \frac{4\pi}{\lambda} \Im\left(\frac{\mathbf{m}^2}{\mathbf{m}^2 - 1} \ln \mathbf{m}\right). \tag{1.17}$$

$\frac{C_{\rm abs}}{V}$ is equivalent to τ (henceforth called $\tau_{\rm CDE}$) for spectrum fitting purposes, and thus the above equation can be used to describe a CDE-corrected laboratory spectrum ready for fitting to observations.

However, a CDE-corrected spectrum alone is not enough to help with calculating the ice column density; a CDE-corrected A-factor (A') is still needed. A' is defined with

$$A' = \frac{\int \tau_{\rm CDE}(\nu) d\nu}{N_{\rm noCDE}({\rm ice})}, \tag{1.18}$$

where the nominator contains the integrated area of the CDE-corrected ice feature, while the denominator contains the column density of the ice calculated with the non-

CDE-corrected A. With this equation A' can be calculated, and then the true N(ice) can finally be calculated.

Despite the challenges of observational ice spectroscopy, astronomical ices have been found to be critical in understanding the synergies between gas and dust in interstellar chemistry. This has motivated their study for several decades, often requiring close interaction between observers, experimentalists, and modellers.

1.5 The history of interstellar ice observations

Ever since frozen water was first detected (Gillett and Forrest, 1973) in the interstellar medium, interstellar ice has been a subject of keen study. Early near-to-mid-infrared observations (e.g. Capps, Gillett, and Knacke, 1978; Geballe, 1986; Grim et al., 1991; Leger et al., 1979; Merrill, Russell, and Soifer, 1976; Soifer et al., 1979) of ices in the ISM were combined with experimental and theoretical studies (e.g D'Hendecourt and Allamandola, 1986; Hagen, Allamandola, and Greenberg, 1979, 1980; Hagen, Tielens, and Greenberg, 1981; Kitta and Kraetschmer, 1983; Sandford et al., 1988) to show that water ice is highly abundant in the ISM, with the column density of water ice dominating over other detected ice species. The other major molecules observed easily in ISM ices are are CO and CO_2. Typical relative abundances of these and other common ices are in the ISM are summarised in Table 1.5.

As explained in the previous section, ice spectroscopy is limited to lines of sight with sources sufficiently bright at infrared wavelengths for ice absorption features to be observed against the IR black-body emission of the source. This limits the detection of ices into narrow "pencil beams" along the line of sight directly in-between the observer and the source. Furthermore, such spectroscopic observations historically were conducted one target at a time. As a result the total number of ice observations in the literature[1] is estimated at approximately two hundred individual lines of sight.

[1]e.g. Aikawa et al., 2012a; Boogert et al., 2008, 2011; Brooke, Sellgren, and Geballe, 1999; Chiar, Adamson, and Whittet, 1996; Gibb et al., 2004; Murakawa, Tamura, and Nagata, 2000; Noble et al., 2013; Öberg et al., 2011b,a; Oliveira et al., 2009; Pontoppidan, van Dishoeck, and Dartois, 2004;

Table 1.5: Typically detected abundances of some of the more common ices around low- and high-mass YSOs and molecular clouds, as reproduced from Öberg et al. (2011a). The reported number is the ice column density as a percentage relative to $N(H_2O)$. "XCN" refers to the ices detectable from the C = N stretching feature at $\sim 2165\,cm^{-1}$, most notably OCN^-.

Molecule	Molecular cloud	Low-mass YSO	High-mass YSO
H_2O	100	100	100
CO	31	29	13
CO_2	38	29	13
CH_3OH	4	3	4
NH_3	–	5	5
CH_4	–	5	2
XCN	–	0.3	0.6

Most of these lines of sight are from the large surveys by Murakawa, Tamura, and Nagata 2000(taken with several telescopes), Pontoppidan et al. 2003a (taken with the Very Large Telescope VLT) Gibb et al. 2004 (taken with the Infrared Space Observatory ISO), Öberg et al. 2011a, and references therein (Spitzer), and Noble et al. 2013 (AKARI). Furthermore almost all of these lines of sight are towards young stellar objects, which have strong spectra in the near-IR spectral range and are thus are among the easiest sources to use for estimating ice abundances. Few (e.g. Imanishi and Maloney, 2003; Oliveira et al., 2009; Shimonishi et al., 2008, 2010; Spoon et al., 2001, 2004; van Loon et al., 2005; Yamagishi et al., 2011, 2012, 2013) studies have been made of extragalactic ices, with even fewer of them have reached out further out than the Large Magellanic Cloud.

In examining the ice in our galaxy, several studies (Eiroa and Hodapp, 1989; Murakawa, Tamura, and Nagata, 2000; Noble et al., 2013; Whittet et al., 1988) have found a positive correlation between the column density of water ice $N(H_2O, \text{solid})$ and visual extinction A_V. This has lead to the idea of an "extinction threshold" below which no water ice seems to be detectable. Depending on study this threshold can take values between a somewhat wide range of 2 and 6. The concept of an extinction threshold will be further studied in Chapter 5.

Pontoppidan et al., 2003b,a, 2005, 2008; Shimonishi et al., 2008, 2010, 2013; van Loon et al., 2005; Whittet et al., 1988; Yamagishi et al., 2011, and even more cited in the upcoming text.

The Spitzer c2d ice legacy survey (Öberg et al., 2011a, and references therein) detailed the solid-state abundances of CO_2 (Pontoppidan et al., 2008), H_2O (Boogert et al., 2008), CH_4 (Öberg et al., 2008), and NH_3 (Bottinelli et al., 2010), towards approximately 50 low-mass YSOs and a small number of supplementary data towards background stars. From this large dataset it was concluded that there is generally little variation (with the exception of Taurus, which was found to have different ice distributions compared to other clouds) between the ice abundances of young stellar objects in different clouds. It was also concluded that there is little difference in the ice compositions of YSOs compared to background stars, with the exception of ice components associated with ice heating and segregation (such as pure CO_2) being more prevalent towards YSOs. On a similar note Noble et al. (2013) found that the 3-micron absorption feature primarily associated with water ice seems to vary in shape depending on the evolutionary stage of the material being probed.

The Infrared Space Observatory (ISO) legacy survey of interstellar ices (Gibb et al., 2004) has highlighted that while the presence of many solid-state molecules –such as H_2O, CO, CO_2, CH_3OH, and CH_4– can be well-characterised towards many lines of sight, a high degree of ambiguity and controversy still exists in fully understanding the origins of certain ice absorption features, such as the 3-micron "red wing" which will also be discussed in Chapter 3.

The sparse sampling caused by the pencil beam observations of ices means that almost all spatial mapping (a common practice with gas-phase molecules) efforts of ice to date (Murakawa, Tamura, and Nagata, 2000; Noble, 2011; Pontoppidan, 2006; Pontoppidan, van Dishoeck, and Dartois, 2004; Yamagishi et al., 2011, 2013, Noble et al. in prep.) rely heavily on interpolation between small numbers of individual lines of sight, and tend to cover very small (less than $1' \times 1'$) patches of the sky. Examples of two such maps are presented in Figures 1.10 and 1.11. Both of these studies have found the abundance of water ice to sometimes vary significantly at fairly short angular distances.

One notable exception is the ice map presented in Sonnentrucker et al. (2008),

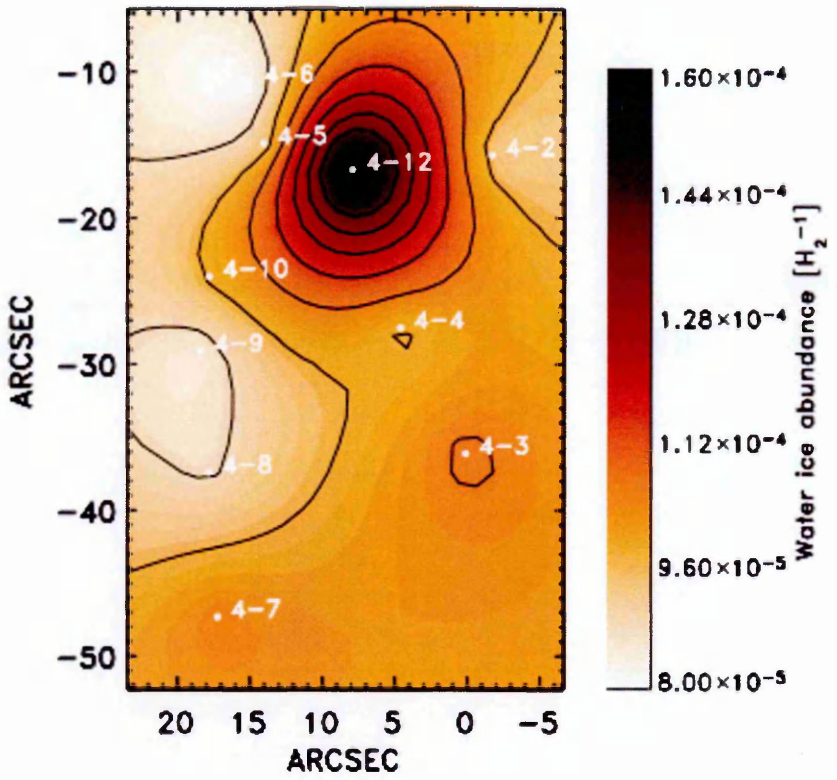

Figure 1.10: An interpolated map of water ice abundance (relative to H_2) towards SVS 4. The white markers and text indicate the lines of sight based on which the remainder of the map is constructed via interpolation, as described in Pontoppidan, van Dishoeck, and Dartois (2004), from which the figure is reproduced.

which serendipitously detected ice absorption against the broad IR emission of a HII region towards Cepheus A. They were then able to exploit the spectroscopic mapping capability of Spitzer to construct fully sampled maps of H_2O and CO_2 ice column density (calculated from peak optical depths at 6 and 15 microns) in a $50'' \times 50''$ patch of the sky. These ice maps are presented in Figure 1.12. The maps of Sonnentrucker report a correlation between $N(H_2O, \text{solid})$ and $N(H_{\text{tot}})$, and that the solid state features peak at approximately the same location as gas-phase (1,1) emission from NH_3 does.

It is findings such as the ones summarised above which stand as testament to the capability of ice absorption features in probing more than the abundances of solid-state molecules.

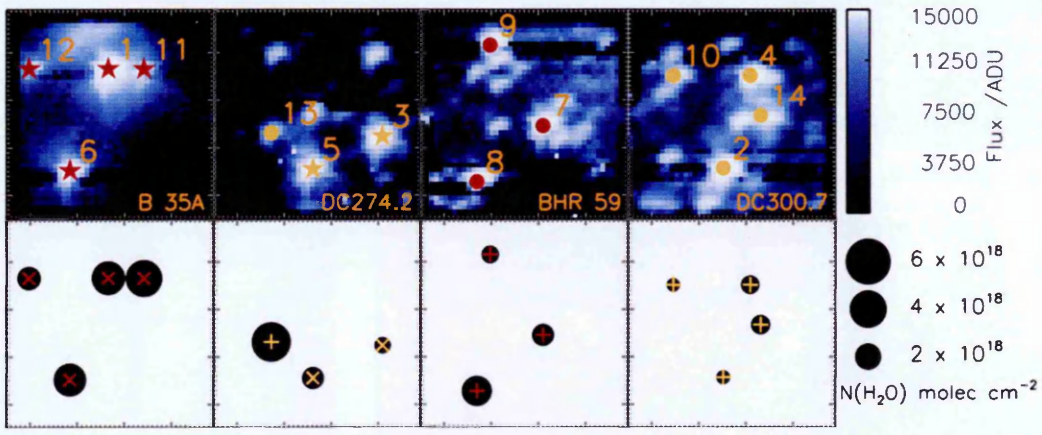

Figure 1.11: Water ice maps of molecular cores B 35A, DC 274.2-00.4, BHR 59, DC 300.7-01.0, as produced from data acquired by the AKARI space telescope. The size of each window is approximately $1' \times 1'$. Objects marked in orange yielded only upper limits on column densities. In the first row objects are marked with $\star$ for YSOs, or $\bullet$ for background stars, while on the second row these symbols are replaced by $\times$ and $+$, respectively. For the second row ice maps, the area of the black circle corresponds to the quantity being mapped, according to the scale on the right hand side. The first row is an imaging frame from AKARI, and the second row is the column density of H_2O ice. Adapted from Noble (2011) and Noble et al. (in prep.).

1.6 The structure and evolution of interstellar ices

The spectral signatures of interstellar ices reveal not only information about the abundances of ices towards the observed lines of sight, but also on their structure and composition.

One example of such effects can be illustrated with water ice, which in its crystalline form has a very differently shaped 3-micron feature compared to amorphous solid water (e.g. Mastrapa et al., 2009; Watanabe and Kouchi, 2008), with ice temperature also playing a role (e.g. Mastrapa et al., 2009) in the shape of the feature. These differences arise from a different distribution of available binding energies in the ice matrix, as was discussed in Section 1.4.3. Furthermore, mixed ices (where the ice matrix is constructed of multiple different molecules in close proximity to each other) both introduce new absorption features (e.g. Al-Halabi et al., 2004; Fraser et al., 2004) and/or modify existing features (e.g. Cuppen et al., 2011; Dartois et al., 2003, Dawes et al in prep.) in ways that are not explicable as a linear combination of the spectra of

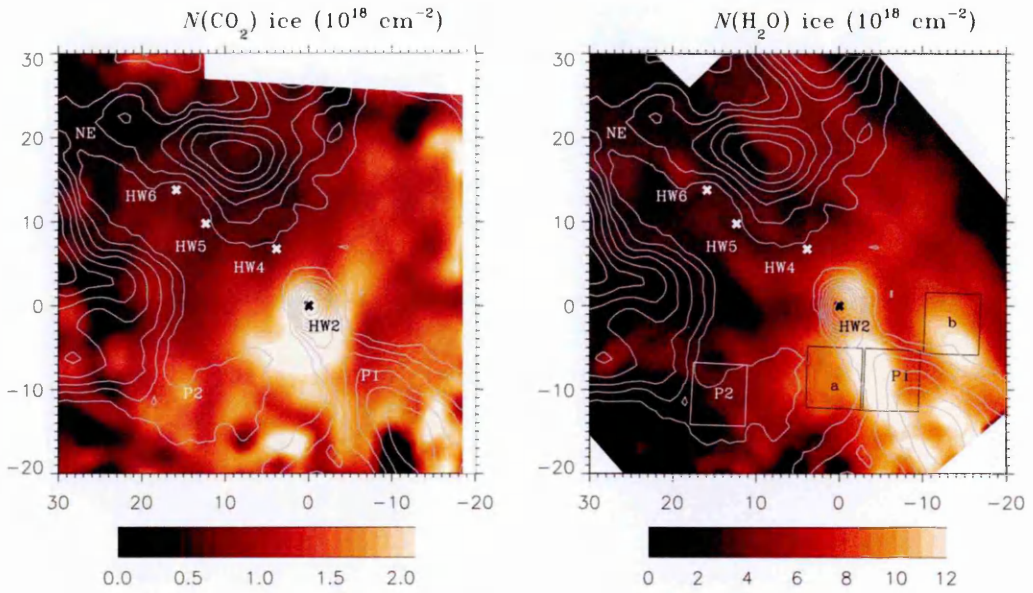

Figure 1.12: The column density of (left) CO_2 and (right) H_2O ice towards Cepheus A. The contours represent $NH_3(1,1)$ emission. Figure reproduced from Sonnentrucker et al. (2008).

pure ices. Finally, even the structure of the dust itself is known to affect the absorption features of the ices growing on it, as was discussed in the context of CDE correction in Section 1.4.3.

Based on studies of the spectral profiles of ices observed in the ISM, solid state materials are generally thought to have a two-layer structure consisting of a water-rich (also called polar, owing to the polar nature of water molecules) and a water-poor (also called apolar[2]) layer. This belief is largely based on studies of the shape of the absorption profile of frozen CO (e.g. Cuppen et al., 2011; Pontoppidan et al., 2003b; Tielens et al., 1991) and CO_2(e.g. Pontoppidan et al., 2008), both of which require at least two components (of a water-rich and water-poor mixture) in order to match observations. This two-layer scheme of interstellar ices is also supported by modelling results of ice formation (e.g. Cuppen and Herbst, 2007; Cuppen et al., 2009; Herbst and Cuppen, 2006). The water-rich layer contains ices such as H_2O, NH_3, CO_2, and CH_4. The water-poor layer contains mainly CO, which through hydrogenation can react to

[2]Referring to the water-poor layer as an apolar one may be a misleading, since in light of recent findings about spontaneous polarization by Plekan et al. (2011) it may actually also behave as a polar layer. Many works in the literature, however, still call the water-poor ice layer an apolar layer.

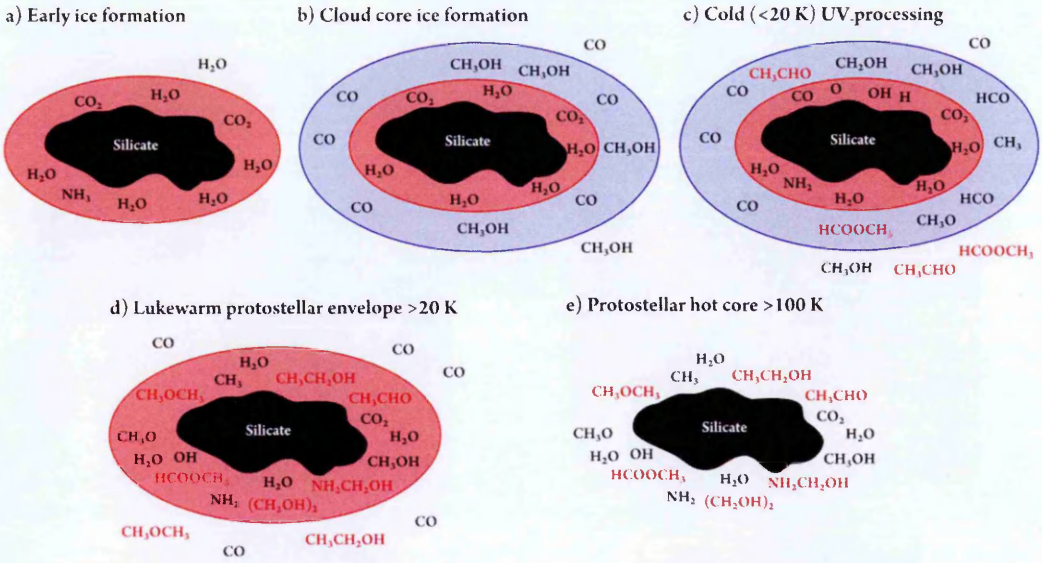

Figure 1.13: The proposed evolution of ices during star formation. Pink indicates water-rich ice and blue indicates water-poor ice. Small amounts of ice desorb through non-thermal mechanisms at all stages. Molecules marked with red text are produced through energetic processing. (a) At an early stage an H_2O rich ice forms through chemical reactions on the grain surface. (b) After the critical temperature and density is reached, the CO in the gas phase very rapidly freeze out onto the dust grains. (c) Far from the protostar but in areas exposed to its UV flux, photoprocessing of the water-poor ice layer produces complex organics such as $HCOOCH_3$. Additionally heating effects from IR photons which penetrate into the icy envelope lead to the mixing, migration, and occasionally separation of the ices. Consequently species such as CH_3OH and CO –which were initially part of the water-poor ice layer– may now be found "mixed" in the porous H_2O ices. (d) Closer to the protostar a majority (with some of it remaining trapped in the pores of the H_2O ice) of the CO ice layer has sublimated, enriching the gas phase with especially CO and CH_3OH. Photoprocessing produces e.g. NH_2CH_2OH in the polar ice envelope. (e) Very close to the protostar the dust temperature becomes so high that the ice mantle is fully sublimated into the gas phase, leaving the dust grains bare. Reproduced from Öberg et al. (2010a).

form to CH_3OH (e.g. Cuppen et al., 2009; Fuchs et al., 2009; Watanabe and Kouchi, 2002; Watanabe et al., 2004), and if subjected to energetic processing it can react even further to turn into molecules such as $HCOOCH_3$ and CH_3CHO, which belong to a family of molecules sometimes referred to as "complex organic molecules" or COMs (e.g. Belloche et al., 2014; Fedoseev et al., 2015).

As is illustrated in Figure 1.13, the formation of these two distinct ice layers are closely related to the anticipated formation mechanisms of interstellar ices and their evolution through star formation. In dense molecular cores the onset of ice formation

occurs when atoms accrete from the gas phase, leading predominantly through hydrogenation reactions to the formation of H_2O rich ice layers. The H_2O is porous and amorphous, and may contain additional "impurities" such as NH_3, CO_2, and possibly CH_4. As the densities increase CO critically freezes out, forming a hydrogen-bond poor upper layer to the H_2O-rich ice. This layer will also generate some CO_2 and significant amounts of CH_3OH as hydrogenation, oxidation, and OH radical reactions lead to the formation of larger molecules. These are the most likely scenarios to be observed in pre-stellar cores with lines of sight towards background stars. Even in these regions ice growth is not "catastrophic" – some CO remains in the gas phase and as recent observations show, cosmic ray and UV induced photodesorption replenish the gas phase with some of the ice molecules (e.g. Caselli et al., 2012). In protostellar regions ices are then further processed. This is a complex process which depends on the distance of the icy grain from the protostar, the degree to which the disk is turbulently mixed, and the temperature and density gradients within the disk (e.g. Visser et al., 2009). Nevertheless, as Figure 1.13 summarises, the evolution of ices can be basically split into two regimes here. far from the protostar where grain temperatures are still below 20 K, IR and UV photons penetrating the cold envelope have a significant effect. First the IR photons promote migration of molecules (without desorption) leading to mixing and segregation of the ice constituents in complex processes studies in the laboratory (e.g. Bisschop et al., 2006; Fayolle et al., 2011a). This can lead to small molecules such as CO and CH_3OH being trapped in the H_2O ice, so that they cannot desorb at the temperatures they would normally be expected to desorb at. Concurrently UV photons promote a complex photodissocation and photodesorption driven chemistry generating more complex species, especially in the CO ices. However, the CO desorption here can be promoted by cosmic rays (Bergin, Langer, and Goldsmith, 1995; Willacy and Williams, 1993), which happens faster than CO can adsorb onto dust grains at H_2 densities below a "critical density", which is $\sim 10^5 \mathrm{cm}^{-3}$ (Caselli et al., 1999). It is because of this that the earliest stages of ice mantle formation are dominated by the chemical reactions which produce H_2O on grain surfaces. The oxy-

gen required for this chemistry is depleted from the cloud before CO has a chance to adsorb and stay on the grain surface in any significant quantity. Closer to the protostar where grain temperature is greater than 20 K, the pure CO ice component partially sublimates, with the remaining of the CO, CH_3OH and other species in the water-poor ice layer migrate into the pores in the water-rich layer below, resulting in trapping. Eventually (at temperatures in excess of 100 - 110 K; Fraser et al., 2001) the water ice itself sublimates, leaving the dust grain bare of all but the heaviest molecules. Examples of molecules which may survive beyond this phase are NH_2OH (Ioppolo et al., 2014), and possibly even sugars and aldehydes (de Marcellus et al., 2015).

1.7 This thesis

This thesis looks at both the formation and destruction of ice mantles, using spectroscopic observations of both ice and gas to try and understand the initial formation of ice layers, and what can be found in the gas phase after both layers have desorbed in the violent outflow environment of YSOs. This is achieved through the use of archival data from primarily the AKARI and Herschel space telescopes supplemented with data from other astronomical databases.

This chapter has served as an overview to the wider field within which my research is applicable, and has given an overview of the historical literature, current understanding and key theoretical aspects associated with this work. In Chapter 2 I detail the telescopes, instruments, and observations which are the basis of scientific work in my thesis. In particular Chapter 2 is focused on AKARI and Herschel.

At the end of the thesis, in an appendix so as not to disrupt the scientific flow, I have documented the two major pieces of software that were written by me during this PhD: ARF2 and OMNIFIT. The appendix serves two purposes: first to detail some of the technical programming aspects of the data reduction and analysis undertaken to achieve the science in Chapters 3 and 5, and second as basic documentation for future users of the software. The intention is to make this code publicly accessible, in order to

make the methods presented in this thesis universally available to the wider astronomy community.

My three major results chapters follow the introduction and observations chapters. In Chapter 3 I analyse a wide array of near-infrared spectra towards both young stellar objects embedded in star-forming regions and background stars behind them. This analysis will provide answers to two questions:

> *How much methanol is in interstellar ices, and where is it, in the water- or CO-rich layers?*
>
> *What are the scientific merits of undertaking concurrent analysis of multiple ice absorption features on a single line of sight, as opposed to drawing conclusions one species at a time?*

In Chapter 4 I shift my gaze towards the gas-phase. By exploiting sub-millimetre observations of water and methanol towards the outflow environments of young stellar objects I seek to answer two questions related to the fate of water and methanol:

> *Is desorbed ice the only source of water in the post-shocked gas-phase in the outflows of YSOs or can water also be formed in high temperature gas phase reactions in the post-shock gas?*
>
> *What happens to the methanol as it desorbs from the grains into the gas phase?*

In Chapter 5 I return to the ice phase, first in a deeply technical discussion, leading to some scientific conclusions, where I detail the novel ice mapping technique I have applied on the slitless spectroscopic data from the near-infrared space telescope AKARI. It produces an unprecedented number of new water ice detections towards a total of 12 star-forming regions. In doing so, it will answer a single question:

> *Where is the water ice?*

Finally in Chapter 6 I reiterate the general conclusions of the results chapters, and pull the ideas back together, returning to the two key scientific questions of this thesis:

How is ice distributed in star forming regions?

How is ice affected by or affecting star formation processes?

In reaching these conclusions it is clear that there are other paths and ideas that could be pursued. The beginnings of some of these new ideas, together with potential future work is therefore briefly addressed at the end of Chapter 6.

Chapter 2

Observations

Archival observational data from a number of telescopes form the cornerstone of this thesis. The two telescopes which play the most prominent roles in this thesis –AKARI and Herschel– are both space observatories which reached the end of their operational lifespan. In this chapter the operations and instrumentation of both these telescopes are detailed in their own sections. Additional archival data was acquired and exploited from the retired ISAAC spectrometer of the Very Large Telescope (VLT; a ground-based telescope located in Chile), and from the the JxA and JxB (both also retired) instruments of the James Clerk Maxwell Telescope (JCMT; Hawaii). A number of other archival datasets appear sporadically in other results chapters, such as data from the Spitzer and the Wide Infrared Survey Explorer (WISE) space telescopes. The main purpose of this chapter is to give the reader a brief overview of the methods of data acquisition and additionally the rationale for the observations which provide the basis of my thesis work.

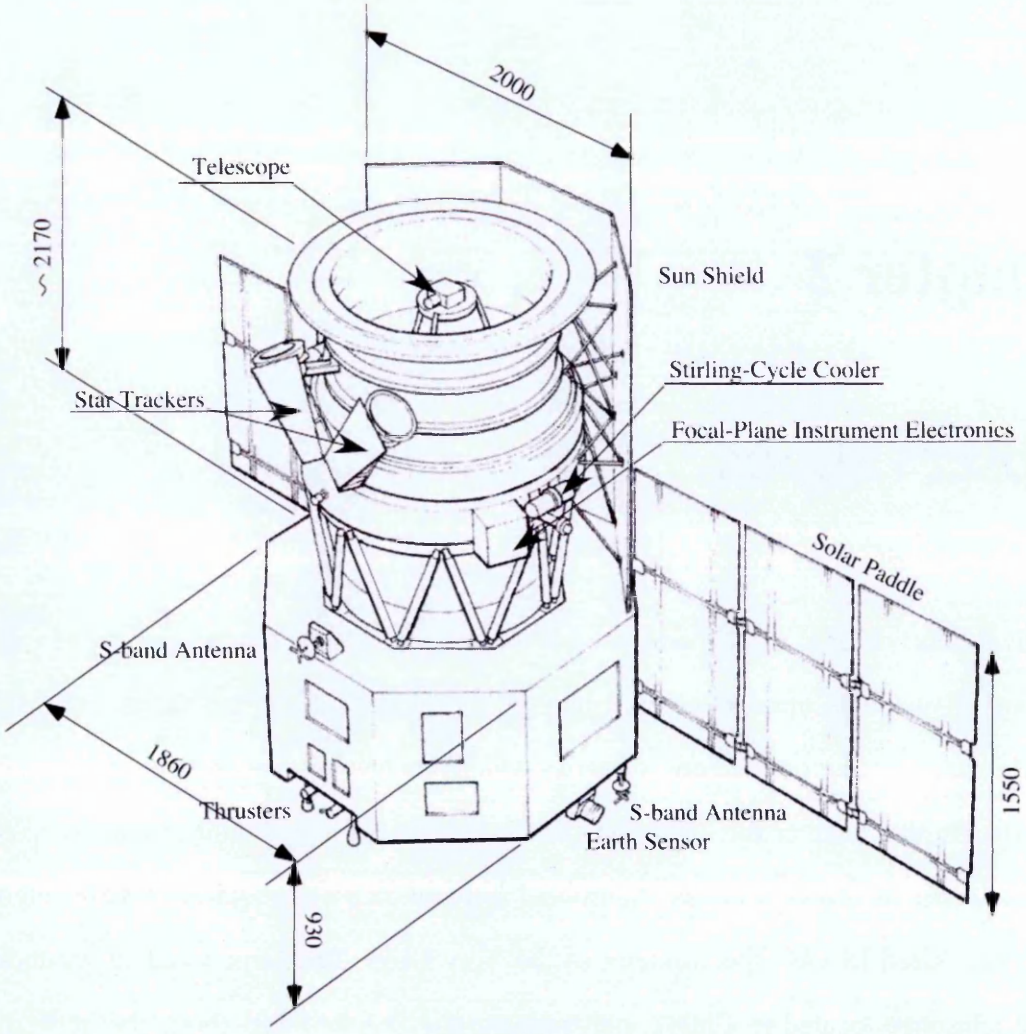

Figure 2.1: A schematic view of the AKARI space telescope. The numeric scales are in millimetres. This figure has been reproduced from ASTRO-F User Support Team (2005) Figure 2.2.1.

2.1 The AKARI space telescope

I exploit AKARI data in Chapters 3 and 5 of this thesis. Furthermore, I developed the pipeline ARF2 –documented in Appendix A at the end of the thesis– specifically to reduce AKARI spectroscopic data.

2.1.1 Mission summary

AKARI (previously known as ASTRO-F and before that as IRIS) was a space telescope operated by the Institute of Space and Astronautical Science of the Japanese

Aerospace Exploration Agency (ISAS/JAXA) in collaboration with European and Korean institutes with the primary goal of performing an all-sky survey in the mid- and far- infrared. The main equipment onboard AKARI consisted of a 68.5 cm primary mirror and two instruments: the Far-Infrared Surveyor (FIS) and the InfraRed Camera (IRC) (ASTRO-F User Support Team, 2005). Both instruments had both imaging and spectroscopic capabilities, although the available observing modes were primarily developed for imaging. The primary mirror and instruments of AKARI were cooled to cryogenic temperatures using onboard reserves of liquid helium.

AKARI was launched on the 21st Febrary 2006[1] into a polar orbit around Earth, at a height of $\sim$745 km. The lifetime operational stages of AKARI consisted of three phases preceded by a performance verification phase. Following the eponymous performance verification (PV) phase, phase 1 consisted of performing the all-sky survey, which was the primary mission of AKARI. The PV phase lasted for 2 months and phase 1 lasted for another 6 months, with phase 2 observations starting in November 2006. Phase 2 observations consisted of additional all-sky survey observations but also of other pointed observations carried out as part of AKARI's open-time programme. Phase 2 lasted until August 2007 when AKARI ran out of liquid coolant, marking the end of phase 2 and the beginning of phase 3. Phase 3 consisted of additional open-time pointed observations, but with only the near-infrared (NIR) capabilities of the IRC being used due to both FIS and the mid-infrared (MIR) components of IRC being rendered virtually useless by the increased temperature of AKARI. Phase 3 lasted until June 2011, following a power-supply malfunction which happened in May 2011. The transmitters aboard AKARI were turned off on November 24th 2011, marking the end of the AKARI mission[2].

[1] http://www.ir.isas.jaxa.jp/ASTRO-F/Observation/Newsletter/afnl_e_014.txt
[2] http://www.isas.jaxa.jp/e/topics/2011/1124_akari.shtml

2.1.2 Instrument overview

The AKARI spacecraft carried two instruments: the Far-Infrared Surveyor (FIS) and the InfraRed Camera (IRC).

2.1.2.1 the Far-Infrared Surveyor – FIS

The Far-Infrared Surveyor (Verdugo et al., 2007) was the instrument aboard AKARI which specialized in observing at a far-infrared wavelength range of 50 to 180 microns. The instrument was capable of performing photometric observations at four distinct bands, and could use a Martin-Puplett Fourier transform spectrometer to perform high-spectral-resolution spectroscopy in two separate bands.

The FIS holds no direct relevance to this thesis, and thus will not be discussed further. For more information on the instrument, see Verdugo et al. (2007).

2.1.2.2 The InfraRed Camera – IRC

The InfraRed Camera (Lorente et al., 2007; Ohyama et al., 2007) was the second instrument aboard AKARI, and it specialized in the observing in the near- and mid-infrared wavelength ranges, between 1.8 and 26.5 microns. As shown in the schematic view of the instrument in Figure 2.2, it consisted of three separate detectors: one for the near-infrared (NIR; $1.8 \ldots 5.3\,\mu$m) and two for the mid-infrared (MIR), split between "short" (MIR-S; $5.4 \ldots 13.1\,\mu$m) and "long" (MIR-L; $12.6 \ldots 26.5\,\mu$m) MIR. Each detector was capable of both imaging and multi-object spectroscopy observations in a field of view roughly $10' \times 10'$ in size, with the exact size of the field of view varying between detector and filter, as illustrated in Figure 2.3. For the sake of simplicity, all further references to the large ($\sim 10' \times 10'$) field of view in this thesis will be called the $10' \times 10'$ field of view, despite the precise size of the frame not being this in any detector/filter combination. In addition to the $10' \times 10'$ field of view, the AKARI detector also contained three slits, as also illustrated in Figure 2.3. From smallest to largest, these slits are often referred to as the short slit, long slit and square slit. The square slit

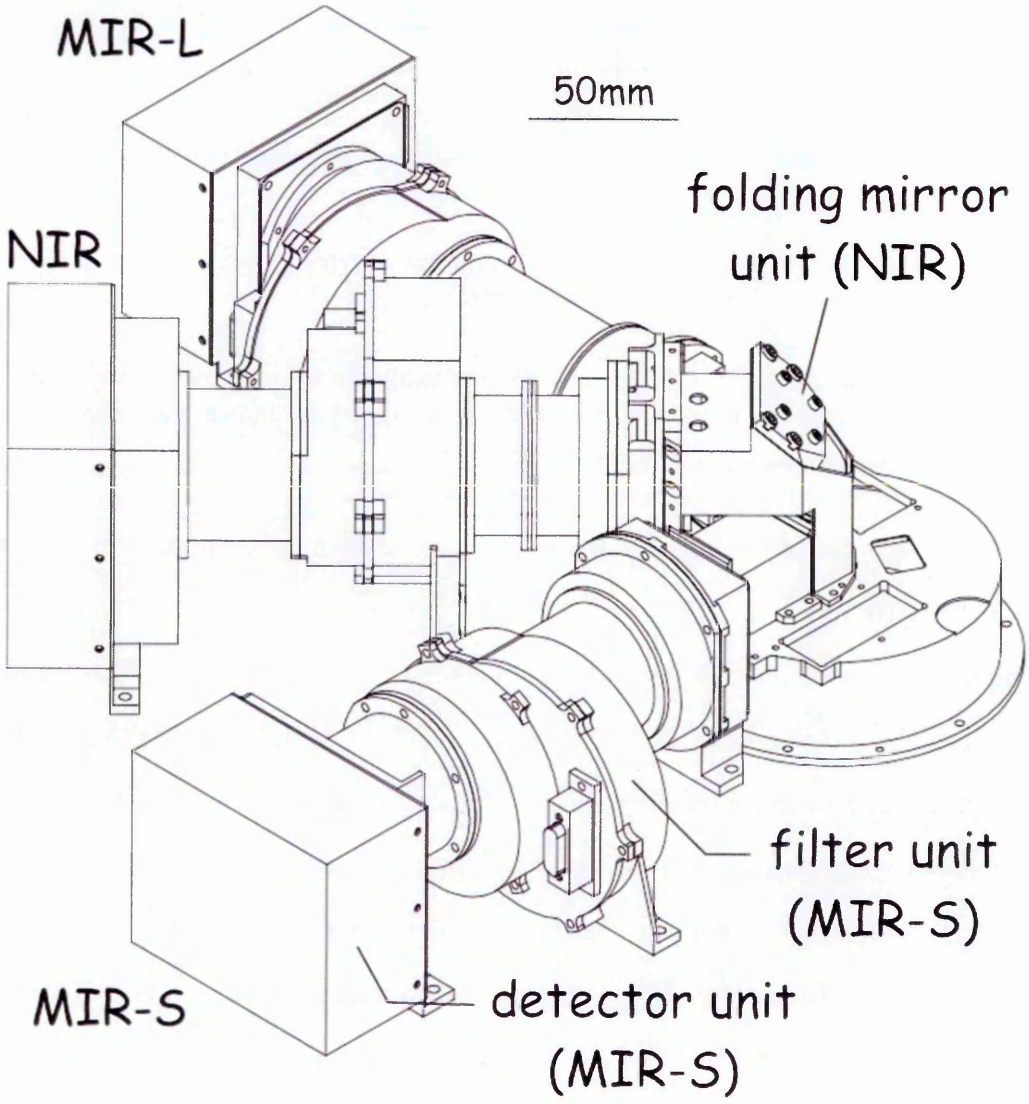

Figure 2.2: A schematic view of the AKARI IRC instrument. This figure has been reproduced from Lorente et al. (2007) Figure 2.0.1.

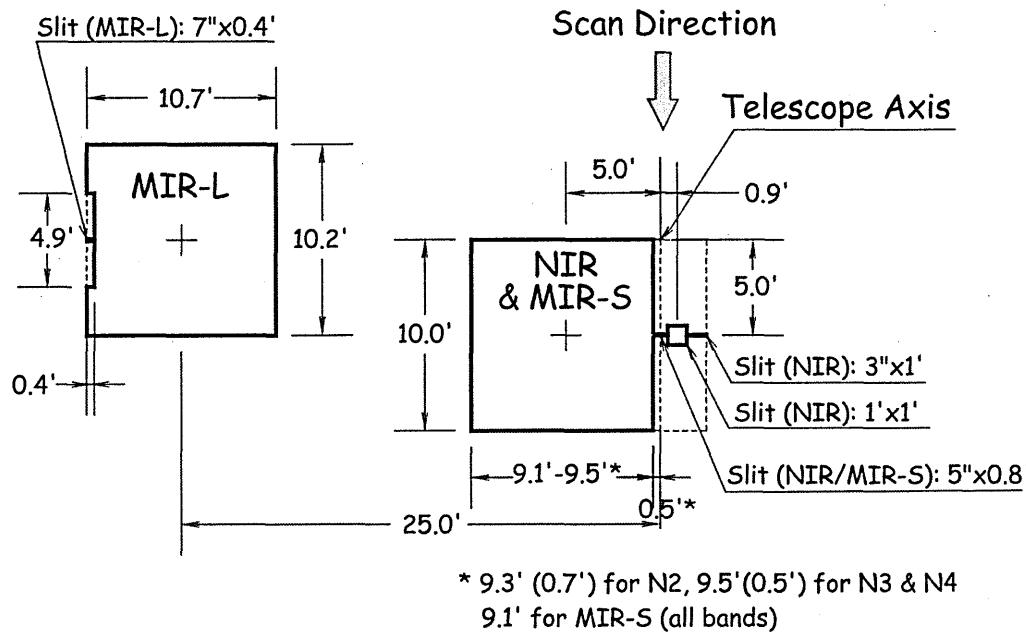

Figure 2.3: An illustration showing the sizes (in sexagecimal degrees) of the field of views observable with the three different IRC detectors. This figure has been reproduced from Lorente et al. (2007) Figure 2.0.2.

is also sometimes called the $1' \times 1'$ field of view, as it is essentially a miniature version of the $\sim 10' \times 10'$ FoV.

The imaging mode observations with each detector had a choice of 3 different filters, limiting the wavelength range to a narrower subset of the full detector range. The multi-object spectroscopic capability was capable of dispersing the light of all stars in these fields of view with the help of a grism or (in the NIR detector) a prism dispersion element. The main practical difference between the grism and prism dispersion was that the grism dispersion gave much higher resolution ($R \approx 120$ at $\lambda = 3.6\mu$m) compared to the prism ($R \approx 12$ at $\lambda = 3.5\mu$m), but suffers from much more severe "confusion" (the overlap of dispersion from nearby objects) in the $10' \times 10'$ field of view. The properties of the various imaging and spectroscopic modes available to the IRC are summarised in Table 2.1. The imaging filters and dispersion elements are mounted on independent filter wheel for each channel, and are selected during observations through rotation of the filter wheel.

NIR observations could be done simultaneously with MIR-S observations because of the way the IRC was constructed, and thus all observations taken in either channel

Table 2.1: A summary of the capabilities of the AKARI InfraRed Camera, in its various imaging and spectroscopic modes. Table adapted from Lorente et al. (2007) Table 2.0.1.

Detector channel	Filter name	Filter type	Wavelength range [μm]	Dispersion [μm/pix]
NIR	N2	imaging	1.9 – 2.8	N/A
	N3[a]	imaging	2.7 – 3.8	N/A
	N4	imaging	3.6 – 5.3	N/A
	NP[a]	prism	1.8 – 5.2	0.06@3.5 μm
	NG[b]	grism	2.5 – 5.0	0.0097
MIR-S	S7	imaging	5.9 – 8.4	N/A
	S9W	imaging	6.7 – 11.6	N/A
	S11	imaging	8.5 – 13.1	N/A
	SG1	grism	5.4 – 8.4	0.057
	SG2	grism	7.5 – 12.9	0.099
MIR-L	L15	imaging	12.6 – 19.4	N/A
	L18W	imaging	13.9 – 25.6	N/A
	L24	imaging	20.3 – 26.5	N/A
	LG2	grism	17.5 – 25.7	0.175

[a]Data involving these filters will be discussed in Chapter 5.
[b]Data involving this filter will be discussed in Chapter 3.

automatically contain data from the other channel as well.

The AKARI data exploited in this thesis was gathered with the near-IR capabilities of the IRC during phase 2. Although MIR-S data for each observation was also available, it was not analysed for this thesis because to do so would have required the construction of a separate new pipeline specialized for the analysis of AKARI MIR with its own complications (such as having to contend with the strong zodiacal background light observed in the MIR).

2.1.3 Observing with the IRC

Observations with the IRC were required to use exposure patterns ordered in a number of "astronomical observation templates" or AOTs. These AOTs cover a range of likely patterns to be useful in either imaging or spectroscopic observations, and operate as a mixture of exposure cycles, filter wheel rotations and micro-scan operations. Of these patterns, the one called AOT04 is the only spectroscopic exposure cycle, and was thus

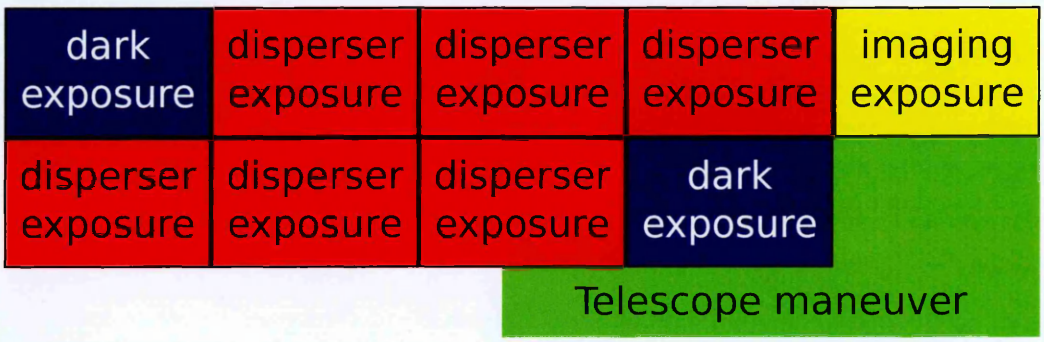

Figure 2.4: The progression of the AKARI spectroscopic observing cycle AOT4 from left to right, top row to bottom row. Each exposure takes approximately 63 seconds, with the entire observing cycle (including overheads) lasting about 10 minutes. The telescope is liable to maneuver during the last two exposure cycles, making the scientific usefulness of the data contained in the last disperser exposure suspect. This figure has been adapted from Lorente et al. (2007) Figure 2.2.6.

used for the observations exploited in this thesis. The progression of this exposure cycle is illustrated in Figure 2.4.

AOT04 produces a total of 8 frames of dispersed images and one frame taken with an imaging filter. Each AOT04 cycle also takes two dark exposures, both at the beginning and end of the cycle. Because of the way the observations are handled in conjunction with telescope attitude control, the end of AOT04 (and every other exposure cycle of AKARI) also had a chance of the telescope manoeuvring in the middle of exposure. When it happens, the last exposures become useless for scientific purposes, and should be ignored during data reduction. In AOT04 is the dispersed frames were taken either with the prism (NP) or grism (NG) dispersers, and the imaging frame taken in the middle of these observations was taken with the N3 filter. These observations are split into individual "pointings", each representing a single AOT observation and indicated by a 7-digit numerical code e.g. 4120021. Several pointings were repeated, and in such cases designated by an additional numeral preceded by a hyphen e.g. 4120021-001 and 4120021-002 for two repeated pointings. In this thesis I refer to such repeated pointings as "sub-pointings".

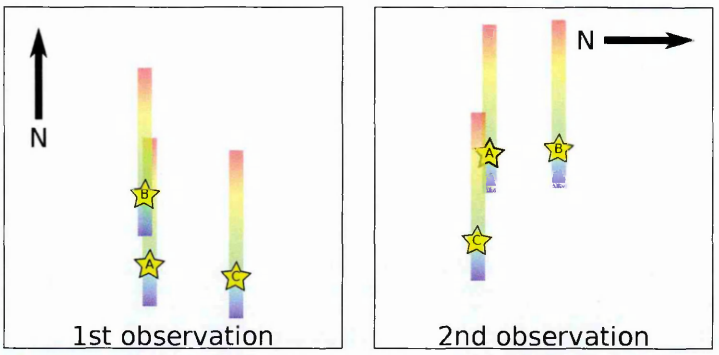

Figure 2.5: An illustration of how spectral confusion happens with AKARI observations, and how confused sources may be partially deconvolved from each other in an ideal situation. The first observation (shown in the left picture) is made with such a roll angle of the telescope that the top of the frame is aligned with north. In this case the red end of the spectrum from source A is confused with the blue end of the spectrum for source B, while the spectrum of C is not confused at all. The right picture shows the second observation of the same field of view but with such a roll angle of the telescope that north points towards the right instead. In this case the spectrum of B is no longer confused, while the blue end of the spectrum of A is confused with the red end of the spectrum of C. If both observations had been made, the full spectrum of C and B could be recovered from the first and second observations, respectively, and most of the spectrum of A could be recovered by taking its blue end from the first and its red end from the second observation.

2.1.4 Why AKARI?

The observations analysed in Chapters 3 and 5 of this thesis were partially or completely acquired as part of the AKARI IMAPE (PI: Helen Fraser) ice mapping programme, which sought to determine the abundance of H_2O, CO and CO_2 ice towards several molecular cores. The target listing for the IMAPE programme is presented in Table 2.2. These targets were selected on the basis of having been previously observed as part of the Spitzer legacy survey "cores to disks" (C2D; Evans et al., 2003) and would thus have much valuable supplementary data available to cross-correlate against the results of IMAPE.

AKARI was first and foremost designed to operate as an imaging telescope and its spectroscopic capabilities were pushed to their limits with the IMAPE programme. To avoid confusion between observed spectra, the spectroscopic mode of AKARI was intended to be used primarily through either one of the three slits of the AKARI frame

Table 2.2: The basic target information of the AKARI ice mapping programme IMAPE.

Pointing identifier	Core name	Disperser used	α_{J2000} [deg.]	δ_{J2000} [deg.]
4120002[a]	BHR59	NG	166.779	-62.097
4120004[b]	CB188	NP	290.067	+11.605
4120006[b]	DC274.2-00.4	NP	142.196	-51.612
4120007[a]	DC274.2-00.4	NG	142.196	-51.612
4120008[b]	DC275.9+01.9	NP	146.712	-51.107
4120009[a]	DC275.9+01.9	NG	146.712	-51.107
4120010[b]	DC291.0-03.5	NP	164.979	-63.738
4120011[b]	DC300.7-01.0	NP	187.871	-63.747
4120012[b]	DC346.0+07.8	NP	249.208	-35.618
4120018[a]	Mu8	NG	187.4024	-71.1775
4120021[b]	B35A	NP	086.1242	+09.1483
4120022[a]	B35A	NG	086.1242	+09.1483
4120023[a]	DC291.0-03.5	NG	164.979	-63.738
4120024[a]	DC300.7-01.0	NG	187.871	-63.747
4120034[b]	L1165	NP	331.7113	+59.0464
4120042[b]	DC269.4+03.0	NP	140.579	-45.815
4120043[a]	DC269.4+03.0	NG	140.579	-45.815
4121001[b]	BHR59	NP	166.779	-62.097
4121017[b]	Mu8	NP	187.4024	-71.1775
4121024[a]	DC300.7-01.0	NG	187.871	-63.747
4121035[a]	L1165	NG	331.7113	+59.0464
4121040[c]	BHR78	NP	189.079	-63.210
4121041[a]	BHR78	NG	189.079	-63.210
4121043[a]	DC269.4+03.0	NG	140.579	-45.815
4121044[b]	DC300.2-03.5	NP	186.054	-66.178
4121045[a]	DC300.2-03.5	NG	186.054	-66.178

[a] Analysed in Chapter 3.

[b] Analysed in Chapter 5.

[c] Analysed in Chapter 5, but no useful data could be extracted.

or with lone or well-separated sources observed in the "slitless" $10' \times 10'$ field of view. As will be shown in Chapter 5, however, the molecular clouds observed as part of the IMAPE programme had tens if not hundreds of bright sources occupying the $10' \times 10'$ field of view, making spectral confusion inevitable. The observing programme of IMAPE had predicted this and tried to plan around it by requesting that repeated pointings of the same cloud be made in such a way that a large amount of time would pass between two observations of the same cloud. If the observations were made in such a way, AKARI would have a different roll angle (which could not otherwise be manually adjusted by the observers) when observing the same cloud, and deconvolving confused spectra would be made significantly easier. The principle behind this idea is illustrated in Figure 2.5. The limitations of AKARI observing time allocation, however, caused these repeated pointings to be taken on subsequent orbits of the space telescope. This resulted in the telescope having practically the same roll angle on both observations and thus greatly hindered the effective deconvolution of most of the confused spectra.

Despite the difficulties first expected and then experienced in the data acquisition and reduction of its spectroscopic data, the AKARI space telescope is still the best instrument to have been available for the task of the type of ice mapping I am doing in this thesis. The reason for using AKARI for ice mapping is that it was the only telescope capable of concurrent observations of multiple lines of sight in the 2 to 5 micron wavelength range. As was illustrated in Figure 1.9 of the previous chapter, Earth's atmosphere either severely hinders (as is the case for the 3-micron water ice feature) or outright prevents (CO_2 at ~ 4.3 microns, although the IMAPE data relevant to this has already been analysed by Noble 2011 and Noble et al. 2013) the observation of several important ISM ice absorption features and thus makes ground-based observatories incapable of what the IMAPE programme sought to achieve. The only other telescopes which would have been capable of similar observations were the Infrared Space Observatory (ISO) and Spitzer, but ISO has been inoperational since 1998 and Spitzer is no longer capable of spectroscopy due to having run out coolant. Furthermore, no other observatory to date has been capable of simultaneous multi-object near-infrared

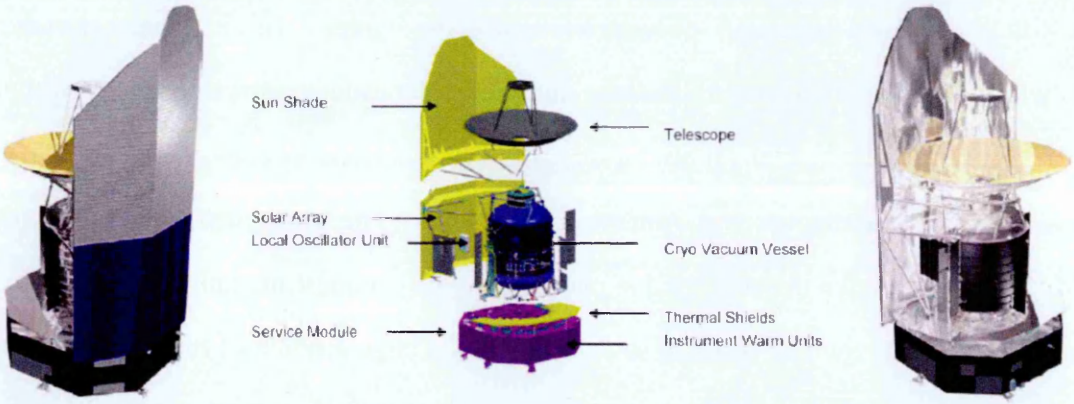

Figure 2.6: The Herschel space telescope. The left image shows the "warm" side of the telescope, and the right image shows the "cold" side. The middle image highlights the major components of the spacecraft. This figure has been reproduced from the Herschel observer's manual[4] Figure 2.1.

spectroscopy with a field of view as large as 10 by 10 arc minutes. In the future the James Webb Telescope (JWST) is set to be capable of similar feats and more relative to what AKARI was capable of, but it is not scheduled to become operational until sometime after 2018.

2.2 The Herschel space observatory

The data analysed in Chapter 4 has been partially acquired from Herschel, and public pre-reduced SPIRE data has been made use of in the analysis in Chapter 5.

2.2.1 Mission summary

The Herschel space observatory (formerly known as FIRST) was a mission operated by the European Space Agency (ESA) that performed imaging and photometry in the far-infrared and submillimeter parts of the spectrum. Its key science goals objectives included shedding light on the inter-relation between star and galaxy formation, the physics of the interstellar medium, astrochemistry, and planetary science studies. Herschel carried three science instruments: the two cameras/medium resolution spectrometers PACS and SPIRE, and a very high resolution heterodyne spectrometer HIFI.

[4] http://herschel.esac.esa.int/Docs/Herschel/pdf/observatory.pdf

These instruments received their light from a 3.5-metre main mirror (Pilbratt, 2008).

Herschel launched on 14th May 2009, entering the Sun-Earth L2 point and beginning commissioning operations. The performance verification and science demonstration phases started soon after the commissioning operations, and the first routine observations were executed on 18th October 2009. Herschel observations were generally split between priority 1 (OT1) and priority 2 (OT2) observations, with OT1 observations taking precedence over OT2. The operational lifetime of Herschel was limited by the supply of onboard liquid helium, which was used for cooling the telescope. After helium "boil off", the telescope would rapidly heat up to temperatures where observations in Herschel's sensitivity range were obscured by noise. This point was reached by the 29th April 2013, and Herschel was sent to its final resting orbit around the Sun on the 17th June 2013, marking the end of the mission.

2.2.2 Instrument overview

Herschel carried three instruments: the Photodetector Array Camera and Spectrometer (PACS), the Spectral and Photometric Imaging REceiver (SPIRE), and the Heterodyne Instrument for the Far Infrared (HIFI). Of these three, SPIRE and HIFI are relevant to this thesis.

2.2.3 SPIRE

The Spectral and Photometric Imaging REceiver (SPIRE) had both photometric and spectroscopic capabilities, but unlike PACS it operated at much longer wavelengths and could only (in spectrometer mode) produce sparsely sampled spectral maps within a 2′ field of view.

The photometer had an option of three different bands to observe. They were centred at 250, 350, and 500 microns, and were called PSW, PMW and PLW, respectively. The spectrometer had two choices of wavelength ranges: SSW which scanned between 194 and 313 microns, and SLW which scanned between 303 and 671 microns. The

Table 2.3: A summary of the capabilities of the SPIRE instrument of Herschel, in its various photometric and spectroscopic modes. Table adapted from the SPIRE handbook Table 2.1.

Sub-instrument	**Photometer**			**Spectrometer**	
Array	**PSW**[a]	**PMW**	**PLW**	**SSW**	**SLW**
Band [μm]	250	350	500	194-313	303-671
Resolution ($\lambda/\Delta\lambda$)	3.3	3.4	2.5	$\sim 40-1000$ @ 250 μm (variable)	
Unvignetted FoV	$4' \times 8'$			$2'$ (diameter)	
Beam FWHM [$''$]	17.6	23.9	35.2	17-21	29-42

[a] Archive data acquired with this mode will be used in Chapter 5.

spectrometer could produce spectra at three different spectral resolutions, compromising sensitivity for sharper spectra, although in practise the highest spectral resolution mode was almost always used. The different observing modes of SPIRE are summarized in Table 2.3.

Additional information about this instrument can be found from the SPIRE handbook[5].

2.2.3.1 HIFI

The Heterodyne Instrument for the Far Infrared (HIFI) was –unlike PACS and SPIRE– an instrument built for the sole purpose of producing high-resolution spectra. It could cover the frequency ranges of 480 to 1250 GHz ($625-240\,\mu$m) and 1410 to 1910 GHz (($625-240\,\mu$m) and was capable of observing in four different modes where could can trade spectral resolution for spectral coverage. At its highest resolution HIFI was capable of producing spectra at a resolution of 125 kHz, covering a frequency range of 230 MHz. The wide-band mode of HIFI covered a frequency range of 4 GHz, at a spectral resolution of 1 MHz. An example of a wide-band HIFI spectrum is presented in Figure 2.7.

The observable frequency range was split into several bands, and one of these must be selected when preparing the observation. Each band had a different effective beam

[5] http://herschel.esac.esa.int/Docs/SPIRE/spire_handbook.pdf
[7] http://herschel.esac.esa.int/Docs/HIFI/pdf/hifi_om.pdf

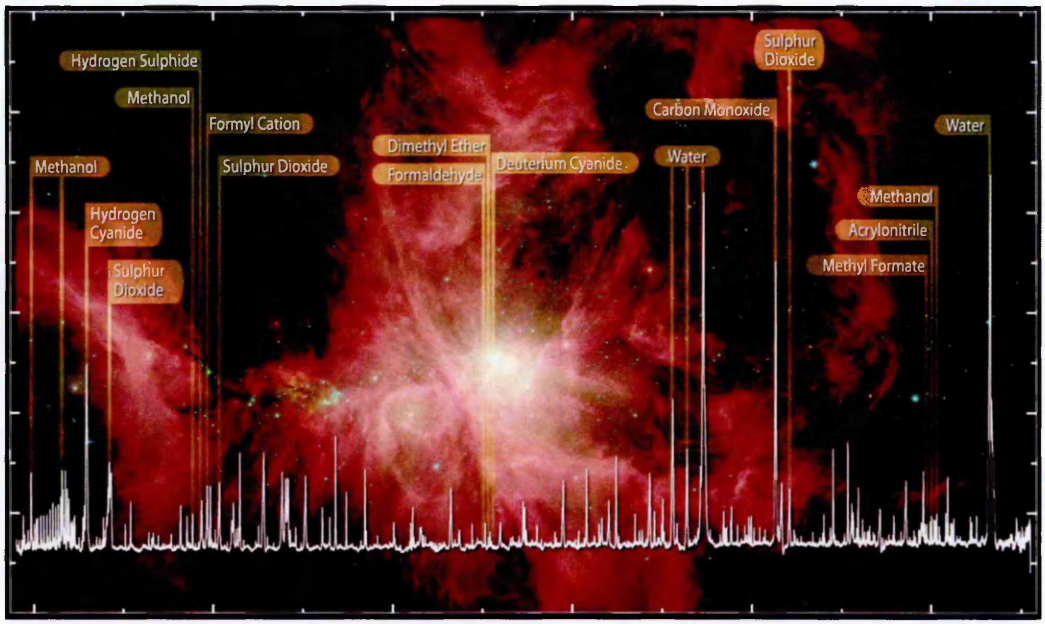

Figure 2.7: A famous spectrum acquired with HIFI during the early science demonstration phase of Herschel. The spectrum highlights several features of gas-phase water and organic molecules towards the Orion Nebula. ©ESA, HEXOS and the HIFI consortium. Image reproduced from the HIFI observer's manual[7].

size, and the highest-frequency bands had a maximum allowable frequency range of 2.4 GHz. Information about the different bands are summarized in Table 2.4.

2.2.4 Why Herschel?

Much like AKARI was the only telescope available at the time (or in the near future) to conduct the kind of science goals laid out by IMAPE, Herschel was the only telescope

[9] `http://herschel.esac.esa.int/Docs/HIFI/pdf/hifi_om.pdf`

Table 2.4: A summary of the frequency coverage and effective beam sizes and maximum bandwidths of the HIFI instrument of Herschel, in its available bands. Table adapted from the HIFI observer's manual[9] Table 3.1.

Band	**Frequency coverage** [GHz]	**Beam size (HPBW)**	**Max. bandwidth**
1	488.1 – 628.4	39″	4 GHz
2	642.1 – 793.9	30″	4 GHz
3	807.1 – 952.9	25″	4 GHz
4[(a)]	957.2 – 1113.8	21″	4 GHz
5[(a)]	1116.2 – 1271.8	19″	4 GHz
6+7	1430.2 – 1901.8	13″	2.4 GHz

[(a)] The HIFI data exploited in Chapter 4 was acquired with these bands.

capable of observing the gas-phase water sought in the Herschel key program WISH (Water In Star-forming regions with Herschel; van Dishoeck et al., 2011). Having observed a total of approximately 80 objects and having taken up 425 hours of Herschel's observing time, the many objectives of WISH revolved around understanding the formation and processing of gas-phase (and indirectly solid-state) water towards several star-forming regions. WISH achieved this by observing (among several other species; most notably CO and OH) H_2O emission and absorption in its various transitions ranging between $J = 1$ and $J = 9$. Many of these transitions have been completely unobservable by any other telescope before Herschel.

While not directly involved in the WISH project, the research presented in Chapter 4 makes extensive use of WISH data (for two H_2O and one CO gas-phase line) in its analysis. Thus it would not have been possible to make the discoveries of that chapter without the data available only from Herschel.

2.3 Other observatories

This thesis makes use of data acquired from a number of other observatories in addition to AKARI and Herschel. The other observatories do not provide data with a major role in this thesis. For this reason they do not have a lengthy description in their own sections, but all of them will be given a short introduction here, so they need not be reintroduced in later chapters and thus detract from the scientific narrative.

2.3.1 The James Clerk Maxwell Telescope (JCMT)

The James Clerk Maxwell Telescope (JCMT) is a ground-based single-dish telescope operating in the submillimetre wavelength regime. Having observed its first light in 1987, JCMT is located on top of Mauna Kea in Hawaii, and as of 2015 is operated by the East Asian Observatory.

The JCMT has been host to a number of instruments dedicated to both imaging and spectroscopy. Most notably regarding this thesis, some of the data analysed in

Chapter 4 was acquired from the JCMT using its RxA and RxB receivers. Of these two, RxB (comprising a part of the RxW receiver) is no longer operational. Both RxA and RxB are dual sideband heterodyne receivers. The frequency window of RxA is $211-276\,\mathrm{GHz}$ and its beam has HPBW of $20''$. RxB covered the frequency window $325-375\,\mathrm{GHz}$ and its beam had HPBW of $14''$.

2.3.2 The Very Large Telescope (VLT)

The Very Large Telescope (VLT) is an optical interferometer consisting of four 8.2 meter main telescopes and a four 1.8 meter auxiliary telescopes. In addition to its interferometric capabilities, the telescopes comprising VLT can be operated individually, and house a number of instruments suited for single-dish purposes. VLT is operated by the European Southern Observatory (ESO) and is situated at Cerro Paranal in Chile. The first of the VLT main telescopes received its first light in 1998.

Of the many instruments that are or have been used on the VLT, the now-decommissioned ISAAC (Infrared Spectrometer And Array Camera; Moorwood et al., 1998) spectrometer is the one of relevance to this thesis. Some of the spectroscopic data analysed in Chapter 3 was acquired using the $2.55-5.1$ micron detection capabilities of ISAAC. ISAAC was also capable of observing in the wavelength range $0.98-2.5$ microns. The instrument was mounted on the telescope UT3 (Melipal) and had both a low and medium resolution grating to be used in spectroscopy. Depending on selected slit size, the low resolution grating could produce spectra with a resolution ranging from $R = 180$ to $R = 1800$, and the medium resolution grating could produce spectra with $R = 1000$ to $R = 11500$.

2.3.3 The Spitzer Space Telescope

The Spitzer Space Telescope was an infrared space observatory which was operated by the National Aeronautics and Space Administration (NASA) and was launched in 2003. Before its supply of liquid helium was depleted in 2009, it was capable of both

imaging and spectroscopy in the near to far infrared ($\sim 3 - 180\,\mu$m) using its three onboard instruments IRAC (InraRed Array Camera), IRS (InfraRed Spectrograph), and MIPS (Multiband Imaging Photometer for Spitzer). In its current state (the Spitzer Warm Mission) only IRAC remains useful, and is capable of simultaneously observing at 3.6 and 4.5 microns. Chapter 5 of this thesis makes use of 8 micron maps obtained with IRAC when it was still capable of observing at that waveband. Furthermore, the C2D catalogue (Evans et al., 2003) which was made use of in the same chapter was compiled using all four bands of IRAC (3.6, 4.5, 5.8 and 8.0 μm).

2.4 Concluding remarks

What was presented above is merely the description of the telescopes. The data itself acquired from the telescopes will be discussed in their respective chapters. Some of this data –such as the previously published AKARI and VLT data discussed in Chapter 3– has already been reduced by others, and little extra work is needed to make it useful for the purposes of this thesis. Other data –like the JCMT CH_3OH data presented in Chapter 4– was non-reduced, but its reduction was a fairly straightforward process using well-established methods. The prism-dispersed slitless spectroscopy data from AKARI, however, is something which was both non-reduced and on which established methods could not be applied. For this reason a large part of Chapter 5 will be dedicated to describing the reduction process itself.

Obviously in exploiting archival data it is vital to undertake something new and different with the data being used. Prior to my research only the datasets from the AKARI $1' \times 1'$ NG ice spectra, and some of the data from the VLT/ISAAC observations had been discussed in previous publications (Noble et al., 2013; Pontoppidan et al., 2003a), although the same data had never been utilised for the purpose to which I exploit it in Chapter 3. The AKARI NP data which form the basis of Chapter 5 and JCMT and Herschel data which form the basis of Chapter 4 had also not been previously published or analysed, with the exception of the Herschel H_2O and CO spectra in

Chapter 4 which had previously been described in Kristensen et al. (2010a) and Yıldız et al. (2013), respectively. Nevertheless, all the research in Chapters 3-5 of this thesis is unique.

The information presented in this chapter is gathered mostly from various manuals, press releases, and newsletters presented on the official websites of their respective telescopes. For further information on the telescopes, the reader is directed to their websites and especially the manuals contained therein.

Chapter 3

Methanol Ice in Star-Forming Regions[1]

The study detailed in this Chapter seeks to disentangle some of the degeneracies in ice abundance measurements from near-infrared spectra while testing in a novel way a hypothesis presented in Cuppen et al. (2011), which postulated that CO in interstellar ices resides in a methanol-rich environment. The hypothesis is tested by making use of the fitting library for which documentation (not relevant to detailing the study presented in this chapter, but important for making use of the library itself) is provided in the appendix at the end of the thesis. Several different combinations of ice mixtures are fitted against both AKARI and VLT near-IR spectra, and the best combination is chosen by comparing it against previous similar studies found from the literature, and by discussing how much they make sense in light of our current understanding of ice growth and composition in the ISM. At the end, the hypothesis of Cuppen et al is verified, and a scenario of ice growth which best fits the modeling results is proposed.

[1]This chapter is based on a paper in an advanced stage of preparation, which is planned to be submitted to MNRAS in the near future with the author list: A. N. Suutarinen (me), A. Dawes, J. A. Noble, H. M. Cuppen, K. Isokoski, H. Linnartz, and H. J. Fraser

3.1 Introduction

Grain surfaces play a critical role in the broader picture of star formation, by acting as a formation platform and reservoir for several molecules, such as water (H_2O) and methanol (CH_3OH). As star formation progresses, molecules that have been formed or frozen-out in the solid-state are desorbed, either by thermal processes (as the grains are heated; Brown and Bolina, 2007; Collings et al., 2004; Viti et al., 2004) or non-thermal processes such as photo-desorption (Fayolle et al., 2011b, 2013; Öberg, van Dishoeck, and Linnartz, 2009; Öberg et al., 2009), sputtering (by energetic electrons or protons; e.g. Johnson, 1990, 1998) or as a by-product of further exothermic chemical reactions at the ice surface (Dulieu et al., 2013; Garrod, Wakelam, and Herbst, 2007).

The emission spectra detected from these desorbed molecules across a range of star-forming epochs, from pre-stellar to protoplanetary regions, are vital diagnostic tools to determine the prevailing physical conditions (such as temperature, density or ionisation fraction) in the local environment (e.g. Shematovich, 2012; van Dishoeck and Blake, 1998). When coupled with astrochemical models, the links between specific gas-phase species (and their solid-state precursors) may be ascertained, and chemical reactivity invoked as a clock by which to establish evolutionary star-formation sequences (e.g. Aikawa, 2013). For example, Caselli et al. (2012) proved that photo-desorption of H_2O ices could account for the (initially unexpected) Herschel HIFI detections of very cold, gas-phase H_2O towards the dense central core of L1544. Furthermore, Öberg, Lauck, and Graninger (2014) have recently shown that a number of complex organic molecules (COMs) have moderate gas-phase abundances (1 - 10 % of CH_3OH gas), even at the earliest stages of star-formation, on lines of sight towards Young Stellar Objects (YSOs) where CH_3OH ice was previously detected, corroborating earlier reports of a tentative correlation between ice and gas abundances due to non-thermal desorption processes in cold-envelope conditions (Öberg, Bottinelli, and van Dishoeck, 2009).

It is therefore increasingly important to constrain solid-state molecular abundances

in a variety of star-forming environments, particularly for those species which form direct bridges between gas-phase and solid-state chemistry. This both enables observational astronomers to continue utilising the gas-phase as an indirect tracer of ice, and acts as a basis for subsequent laboratory experiments to determine which reactions and non-thermal desorption processes should be included in our astrochemical models, linking gas-phase and solid-state chemistry to explain complex chemical evolution.

The abundances of the solid-state molecules can be readily estimated by observing infrared absorption features which arise from the functional groups of individual pairs of atoms on the icy surfaces of the interstellar dust grains being observed. For example, carbon monoxide is visible through the C-O stretching mode functional group at 4.7 μm ($\sim$ 2130 cm^{-1}), and both water and methanol contribute to the wide O-H and (in the case of methanol) C-H stretching mode features observable at around 3 μm ($\sim$ 3300 cm^{-1}; observable from the ground).

As will be elaborated upon in Section 3.2, methanol is an ideal "bridging" candidate, and constraining its solid-state abundance is the primary motivation behind this chapter. The greatest challenge in determining interstellar methanol ice abundances is unequivocally detecting the CH_3OH ice itself. The strong features in methanol ice always coincide with other interstellar solid-state spectral lines. The X-OH bending modes of H_2O and CH_3OH almost entirely overlap between $\sim$ 5 and $\sim$ 8μm, in a dense region of the interstellar solid-state spectrum which is notorious (e.g. Boogert et al., 2008) for how difficult it is to decompose these spectra into their contributory components. A second commonly looked at CH_3OH ice tracer, detectable in the past with SPITZER/ISO observations is the '9-micron' feature. This ν_4 C-O stretching mode of CH_3OH at $\sim$ 9.7μm lies on the wing of the interstellar silicate dust feature at 10 microns, as shown by Bottinelli et al. (2010).

The stretching vibrations of the O-H functional group contribute to a broad absorption feature common to both H_2O and CH_3OH. Close to this feature –as is illustrated in Figure 3.1– the C-H functional group stretching modes give rise to a number of additional features in the CH_3OH spectrum, with the "primary" feature being located at

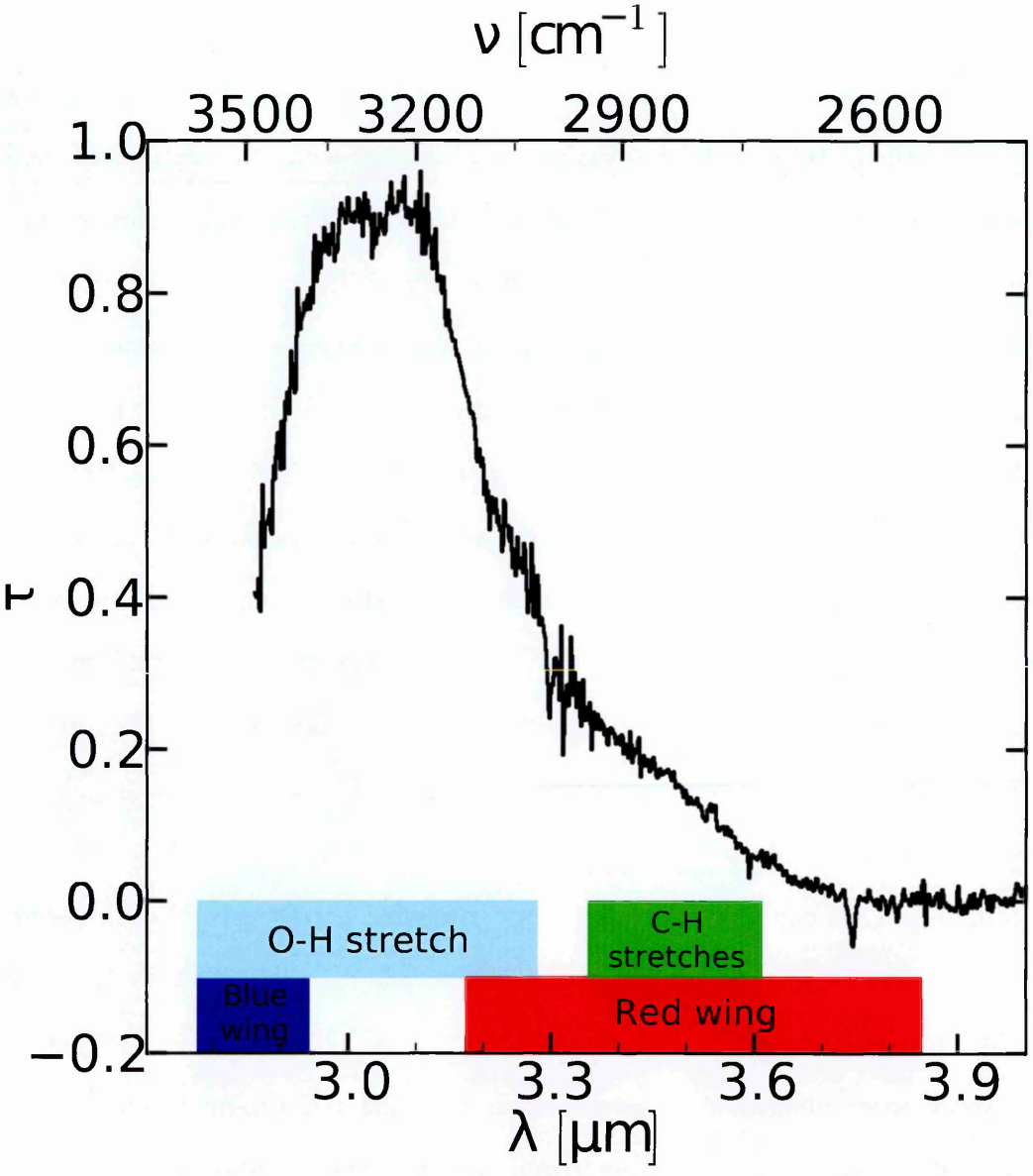

Figure 3.1: An illustration depicting the approximate wavelength ranges occupied by the various relevant (to this study) sub-features of the 3-micron ice absorption feature. The black line is one of the optical depth spectra from the VLT observations (see Section 3.3) analysed in this chapter. The rectangles show the wavelength ranges occupied by the features indicated in their respective annotations. In the context of this chapter, the O-H stretch is the feature associated with the presence of both H_2O and CH_3OH ices, while the C-H stretches are associated with only CH_3OH ice. The parts of the red wing not covered by any other feature are of a largely unknown origin (see Section 3.4.2.4), and introduce a degeneracy into the analysis of especially the C-H stretches. The blue wing has relevance in ice spectrum fitting, as will be discussed in Section 3.3.

3.47μm (e.g. Brooke, Sellgren, and Geballe, 1999; Pontoppidan, van Dishoeck, and Dartois, 2004). They are also often masked in observations by the strongly scattered 'red wing' or 'red shoulder' of H_2O (e.g. Tanaka et al., 1990), stretching from the O-H stretch peak at $\sim 3\mu$m as far as $\sim 3.9\mu$m. No physical model currently exists which is capable of fully explaining the nature of the red wing, although it has been suggested that it may be the result of scattering and/or ice thickness effects (e.g. Dartois et al., 2002; Smith, Sellgren, and Tokunaga, 1989; Thi et al., 2006). Features such as the 3.47-micron C-H stretch are sometimes detectable as a slight bump on top of the red wing, and can be at least partially decomposed from the red wing using e.g. the "Brooke method"(Brooke, Sellgren, and Geballe, 1999; Grim et al., 1991), in which a polynomial is fitted to the red wing and the optical depth of the residual is examined. This method has been used to detect CH_3OH ice towards high mass stars (Brooke, Sellgren, and Geballe, 1999), low mass stars, (Öberg et al., 2011a; Pontoppidan, van Dishoeck, and Dartois, 2004; Pontoppidan et al., 2003a, 2005) background stars (Chiar, Adamson, and Whittet, 1996; Grim et al., 1991) and even in extragalactic sources (Shimonishi et al., 2010, 2013; van Loon et al., 2005).

From all this we can see that, whichever wavelength region is employed, degeneracy in the relevant features interfere with determining methanol ice abundances in the ISM. Obviously it would be ideal -as Boogert et al. (2008) and Bottinelli et al. (2010) show- to simultaneously analyse both the 9.75 and 3.53 μm methanol features, but observational wavelength coverage, required ground-based observing time, and instrument sensitivity, have precluded this in all bar the 16 exceptional cases reported by Boogert et al. (2008) and Bottinelli et al. (2010). While the James Webb Space Telescope with its MIRI and NIRSPEC instruments is set to open up simultaneous observations of both the 3 and 9 micron bands, our only other option in advance of that is to try and cross-check and co-determine methanol ice abundances against multiple ice features fitting in a range narrow enough to be detectable in a reasonable time with a single telescope.

A fairly recent result presented in Cuppen et al. (2011) opens up this avenue for

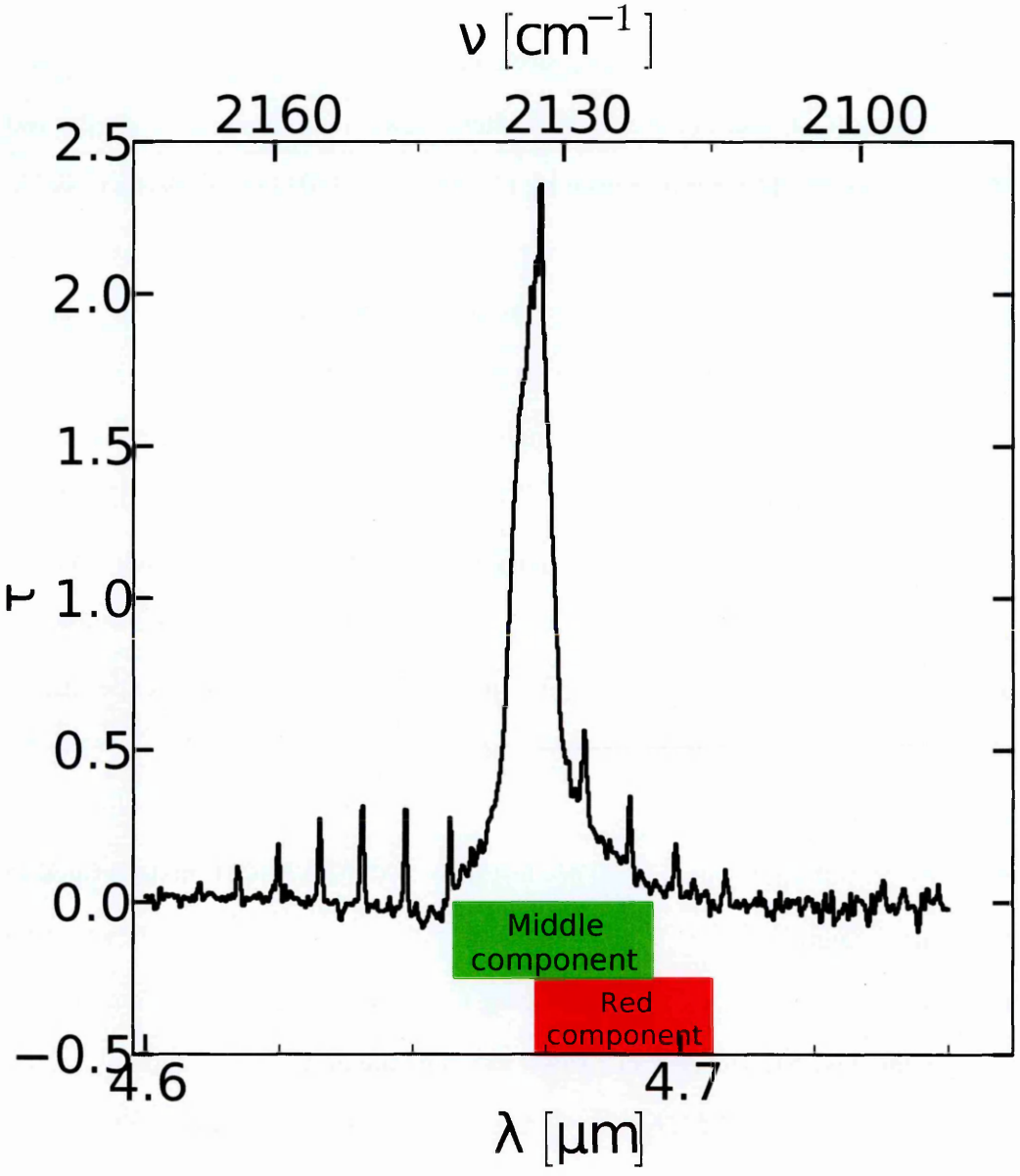

Figure 3.2: An illustration depicting the approximate wavelength ranges occupied by the two relevant (to this study) sub-features in the C-O stretch ice absorption feature. The black line is one of the optical depth spectra from the VLT observations (see Section 3.3) analysed in this chapter. The rectangles show the wavelength ranges occupied by the features indicated in their respective annotations. In the context of this chapter, the middle component is covered by pure CO ice. The red component (not to be confused with the red *wing* of the O-H stretch) is covered by a mixed CO ice such as the CO:CH_3OH mixture presented in Cuppen et al. (2011).

us, by showing that a CO:CH_3OH mixture can explain the "red component" (not to be confused with the 3-micron red wing) often found as part of the 4.67 micron C-O stretching feature. See Figure 3.2 for an illustration of the two C-O stretch components relevant to this chapter. Most of the C-O stretching mode absorption peak traces pure carbon monoxide (CO) ice, but the feature often shows a slight shoulder on the red side of the main peak. The mixture used by Cuppen et al. (2011) provided a possible explanation for a previous problem (e.g. Fraser et al., 2004) pertaining to reproducing the red component without producing an additional feature around $2152\,cm^{-1}$ never detected in astronomical spectra. The red component has historically been thought to be produced by a CO:H_2O ice mixture, which produces in addition to the red component the un-observed feature at $2152\,cm^{-1}$. The results of Cuppen suggest that CO in interstellar ices resides instead of a water-rich environment in a methanol-rich environment, where CH_3OH forms mainly as a result of grain surface reactions involving CO instead of e.g. from UV processing of H_2O. This is in line with laboratory experiments on CO hydrogenation (Fuchs et al., 2009; Hiraoka et al., 2002; Watanabe and Kouchi, 2002).

Furthermore -although Cuppen did not test this- any CO:CH_3OH mixture fitted to the the 4.7 μm region is also expected to show in the 3 micron region, now providing us with two "measuring sticks" in determining CH_3OH abundances. Making use of previously published AKARI and VLT observational data of both the 3 and 4.7 micron regions, *the first objective of this chapter is to study what the effects of the CO:CH_3OH mixtures of Cuppen et al. are on ice fits done to the 3 micron absorption features.*

In addition to producing features in the C-H stretches looked at by the Brooke method, methanol also contributes absorption to the 3-micron O-H stretching modes. This is often overlooked by studies making use of the Brooke method, despite the O-H stretch contribution of methanol necessarily replacing some of the absorption of water; the main contributor to the O-H stretch. An improvement to this would be to simultaneously consider the contribution of water to the 3-micron features while fitting them with the CO:CH_3OH mixture. Thus, *the second objective of this chapter*

is to attempt a simultaneous fit of multiple ice components to the 3-micron features, in order to reproduce as much of the observed absorption as possible.

This chapter is structured as follows. Section 3.2 presents further background information about the role of methanol as a bridge between the chemistry of the solid state and gas phase. In Section 3.3 I discuss the observational data set and spectrum fitting scheme used for the rest of the chapter. In Section 3.4 I present the results of the fit and in Section 3.5 I discuss these results, by examining the quality of the fits and comparing them to previous studies. Finally, I summarise the outcome of the study and present my conclusions and their astronomical relevance in Section 3.6.

3.2 Methanol as a bridge between the solid state and gas phase

Methanol is an ideal candidate molecule to link gas-grain processes. It has been detected in both the gas-phase and solid-state in star-forming regions, and (at least in low temperature cold-gas environments) there is no viable formation route in the gas-phase (Turner, 1998). Laboratory experiments (Fuchs et al., 2009; Watanabe and Kouchi, 2002), coupled with models (Cuppen et al., 2009; Fuchs et al., 2009) prove that CH_3OH formation is dominated by the hydrogenation of CO-ice through HCO and H_2CO intermediates to form CH_3OH. The laboratory yields from such experiments feasibly account for the abundances of CH_3OH ice reported from observations of cold-envelopes towards low-mass YSOs. Both models and laboratory studies therefore point towards scenarios where methanol will form ices which are either rich the methanol itself, or dominated by CO:CH_3OH ice mixtures on top of a water-dominated ice layer. Furthermore, temperature programmed desorption studies show that the methanol rich ice layer has a porous amorphous structure that can trap more volatile species (e.g. Fraser et al., 2004) much like water ice (e.g. Burke and Brown, 2010; Collings et al., 2003a, 2004; Viti et al., 2004), although once the methanol starts mixing directly with

water ice some volatiles are actually trapped less effectively and released sooner to the gas-phase (Burke and Brown, 2015). All this leads to the picture of ice evolution illustrated in the top row of Figure 3.3, depicting the evolution of these three constituents (CO, H_2O, and CH_3OH) of ISM ices during the pre-stellar and early YSO phases.

This cartoon is a simplification of the true ISM situation, but it serves as an excellent benchmark for both the methodology and the discussions in the remainder of this chapter. It is important to note that this figure illustrates the picture built up currently from astrochemical modelling and laboratory experimental viewpoints. Starting with ice formation on a bare grain:

(a) Initially H_2O ice formation dominates on the dust. At this stage, although we know that other reactions may occur, they are neglected since their products are not traced by the data considered in this study. The water ice formed here is both porous and amorphous. We assume, that CO hydrogenation will be competing with H_2O formation, and consequently any CO molecules that might accrete at this stage are most likely to react and form CO_2 (via HCO + OH) rather than CH_3OH, as suggested by laboratory experiments where the relative rates of water, CO_2 and methanol formation have been measured (e.g. Ioppolo et al., 2011; Noble et al., 2012). A very small fraction of methanol may form at this stage, embedded in the water ice at very low concentrations, this methanol is not expected to be detectable in observations.

(b) As the oxygen atoms become depleted (and therefore no longer available to react to form H_2O, OH, or CO_2), densities are also increasing while temperatures decreasing. As the densities approach the critical freezeout density of CO, increasing quantities of CO accrete to the H_2O ice surface. If these CO molecules are hydrogenated, we will start to form a thin layer of CH_3OH – this methanol can most likely be considered to be mixed with CO or possibly H_2O. As in the previous step, these small quantities of CH_3OH are most likely undetectable via observations.

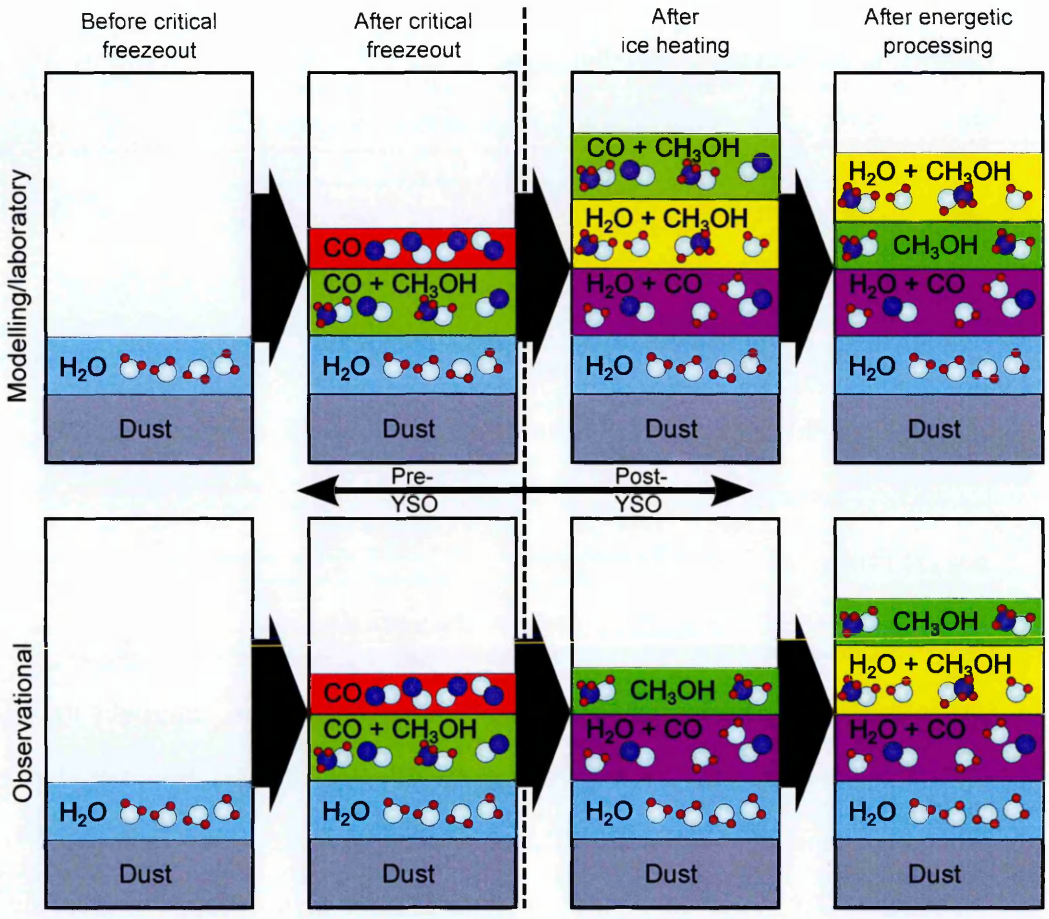

Figure 3.3: A cartoon diagram illustrating the evolution of the ice mantle on a dust grain at four key points during early star formation. The top row shows a scenario based on a combination of modelling and laboratory results in the literature, and the bottom row shows a scenario based on observations of methanol ice, as discussed in Section 3.2. The leftmost column shows the state of the ice before critical freeze-out of CO has happened, followed by the scenario immediately after freezeout in the second column. The third column shows the situation following dust and ice heating following the ignition of the YSO. The fourth column shows the situation following energetic processing by UV radiation from the protostar. Only ice components containing the ices of interest to this study (CO, CH_3OH, and H_2O) are shown, even in situations where other ices (most notably CO_2 and various COMs) are expected to be present. *The relative thicknesses of the ice layers illustrated here are not representative of the expected relative abundances of their respective ice components; the layers only indicate the potentially detectable presence of the ice.*

(c) As densities continue to increase, CO critically freezes out forming the "classical" ISM ice of a H_2O bottom layer with CO ice on top. Sandwiched between these layers is the very thin layer of CH_3OH:H_2O or CO:CH_3OH mixed ice (formed in the previous step), but at most likely undetectable concentrations.

(d) The thick CO ice layer formed as a result of critical freezeout in the previous step is hydrogenated throughout the process, producing mixed CO:CH_3OH ices which account for most of the CH_3OH observed in the ISM.

(e) The CO ice continues to accrete, but the surrounding gas-phase medium will run out of atomic hydrogen before it runs out of CO, and hydrogenation of the CO ice ends. This leads to a "pure" CO ice layer on top of a CO:CH_3OH ice layer, and the (unchanged) layers beneath it.

(f) As the cloud core continues collapsing, it heats up as the YSO in the center is ignited. This heating causes some CO to desorb, but some migrates into the porous water ice (and the CH_3OH layer) where it eventually becomes trapped (e.g. Burke and Brown, 2010, 2015; Collings et al., 2003b,a; Fraser and van Dishoeck, 2004). Consequently the pure CO ice layer disappears, leaving a CO:CH_3OH layer, and a CO:H_2O layer. These processes eventually lead to a complex morphology, but in simple terms it can be represented by four layered ice components: H_2O, H_2O:CO, H_2O:CH_3OH, and CH_3OH:CO.

(g) The ices are next energetically processed by mainly UV radiation and electrons, leading to additional CH_3OH formation from reactions between the trapped CO and the H_2O ice matrix (e.g. Palumbo, Castorina, and Strazzulla, 1999; Palumbo et al., 2008), as well as processing of the CH_3OH:CO layer to potentially produce radicals and COMs. These processes compete with thermal processing and thermal/non-thermal desorption mechanisms so that both the ice and gas phase end up having very rich chemistry.

(h) Eventually the various desorption mechanisms release all the remaining ice con-

stituents to the gas phase.

Of the steps outlined above, (a)-(e) apply to the pre-YSO stages shown in Figure 3.3, while steps (f) and (g) apply to the post-YSO stages in it.

Once formed, CH_3OH is purported to be the 'seed' molecule for COMs (Aikawa et al., 2012b; Garrod, 2013; Garrod and Herbst, 2006; Garrod, Weaver, and Herbst, 2008), either directly, via the desorption of products from energetic surface reactions, as illustrated by laboratory experiments (e.g. Hudson and Moore, 1999; Palumbo, Castorina, and Strazzulla, 1999), or via methanol desorption, followed by its gas-phase photo-dissociation and subsequent gas-phase reactions of the photo-products (e.g. Garrod, Weaver, and Herbst, 2008; Geppert and Larsson, 2008). Very recent experiments (Fedoseev et al., submitted) hint for COM formation also in atom addition schemes. Without methanol ice, current astrochemical models fail to generate most of the gas-phase COMs observed in star-forming regions. To generate sufficient COMs to match model and observational abundances, the same chemical reaction schemes then significantly overestimate both the gas- and solid-phase CH_3OH abundances (Garrod, Weaver, and Herbst, 2008). As recent models (Drozdovskaya et al., 2014) show, methanol chemistry (and abundance) is very sensitive to the local prevailing physical conditions. So, have we "missed" some of the CH_3OH ice in our abundance determinations, or not yet fully understood all the chemical mechanisms that link solid-state CH_3OH formation to the plethora of processes that eventually lead to the detection of gas-phase COMs in star-forming regions (e.g. Hocuk, Cazaux, and Spaans, 2014)?

Both options probably contain a grain of truth; it is known that CH_3OH can also be generated in the solid-state by energetic processing (by UV photons, ions, electrons or X-Rays) of ices containing (some combination of) H_2O, CH_4, CO and CO_2 (e.g. Hudson and Moore, 1999; Palumbo, Castorina, and Strazzulla, 1999; Pearce et al., 2012; Wada, Mochizuki, and Hiraoka, 2006), which in certain star-forming environments could enhance methanol ice abundances. However, the observed gas-phase and solid-state abundances of CH_3OH can vary by many orders of magnitude (>4-

6), depending on the spatial resolution of the observations (e.g. Aikawa et al., 2012b; Suutarinen et al., 2014; van Kempen et al., 2014). Without exception, gas-phase abundances are determined from emission spectra of CH_3OH tracing relatively small spatial scales and a much wider range of physical conditions than those that can be inferred from ice observations, where features are detected in absorption, across an entire star-forming envelope. The abundances of ice molecules can be reliably estimated from the observed infrared absorption features which arise from vibrations associated with the functional groups in molecules that comprise the icy surfaces of the interstellar dust grains. However, the process is complicated by the fact that the precise shape of the observed spectral lines depends on both the chemical (ice mixture, processing history and morphology) and physical (temperature, porosity, dust scattering and grain-shape effects) attributes of the observed granular medium. Without exception, gas-phase abundances are determined from emission spectra of CH_3OH tracing relatively small spatial scales and a much wider range of physical conditions (which are usually much better constrained) than those that can be inferred from ice observations, where features are detected across an entire star-forming envelope. It is difficult to compare these two different scales of spatial resolution, and perhaps this is where some of the conflicts between our picture of methanol ice environments built from the laboratory and astrochemical models, versus the picture from observational data arise.

Observational studies of methanol ice (e.g. Bottinelli et al., 2010; Dartois et al., 1999; Pontoppidan et al., 2003b; Shimonishi et al., 2010; Sonnentrucker et al., 2008) suggest a somewhat different morphology and environment for CH_3OH compared to the modelling/laboratory based picture painted above. It seems from observational data to date that most of the CH_3OH ice is in either a "pure" segregated ice layer or mixed with CO and CO_2 in the so-called apolar ice environment, with a relatively small fraction (if any) mixed with water ice. Furthermore, since all of these studies, when analysing the methanol ice environment, have excluded the Cuppen et al. (2011) result pertaining to the CO:CH_3OH-ice environment, they have therefore assumed the CO also exists in two key component environments – one water rich, another water

poor. There is already a disconnect between our analysis of ice environments from observational data of different ice components, as well as a disconnect between the modelling/laboratory and observational picture. The second row of cartoons of Figure 3.3 shows how the observational picture differs from the modelling/laboratory one. In this picture the pre-YSO phases of ice evolution (as far as CO, CH_3OH and H_2O are concerned) are functionally identical, but in the post-YSO phases the picture is different. With the heating of the dust grain, instead of forming an intermingled "goo" where everything is effectively mixed with everything, CH_3OH is considered to segregate into its own layer, while the CO mixes with the water layer, leaving us with a pure CH_3OH layer, a H_2O:CO layer, and a pure H_2O layer. The energetic processing phase of ice evolution would cause some of the H_2O:CO mixture to react with itself, forming CH_3OH and thus causing the formation of what is effectively a H_2O:CH_3OH layer. While the structure of the ice would be different, it would still contain the same layers as those predicted by modelling and laboratory experiments.

The aim of the remainder of this chapter is to use these two scenarios as the basis of an exploration of numerous different ice models which will be tested against observational data, and build a complete picture of CH_3OH formation and evolution prior to complex organic chemistry, i.e. up to before the energetic processing phase of ice evolution. The range of abundances, ice environments and distribution of methanol ice, together with other common ice species, such as CO and H_2O, can be inferred by combining observational and laboratory spectra, if the statistical sample of ice observations is large enough. Here I add 23 new methanol ice estimates (some of them upper limits) to the data already existing in the literature, on lines of sight towards both low-mass YSOs and background stars.

3.3 Methodology

3.3.1 Observations

The observational data used for this study consists of AKARI near-IR spectra, which have been previously published in Noble et al., 2013, and of VLT-ISAAC spectra partially published in Pontoppidan et al., 2003a. The total number of sources in these data sets is 52, with 23 of them being from AKARI and 29 from VLT. The lists of examined AKARI and VLT sources are presented in Tables 3.1 and 3.2, respectively. All the AKARI data used is pre-reduced in the study presented in Noble et al. (2013), including the continuum fits used in determining the optical depths. Some of the sources presented in Noble et al. were not analysed with the methodology used in this study because of missing or very poor quality data in either the C-O stretch or 3-micron features since, as will be elaborated on in the upcoming sections, data from both features is required. The VLT data I used is pre-reduced for the study presented in Pontoppidan et al. (2003a), but the continuum baseline to that data was reconstructed in this study, using polynomial fits with fitting ranges manually designated for each source in order to best avoid interference from gas phase emission lines and other artefacts left in the spectra. Only the VLT data which contained both the C-O stretch and 3-micron features were included in this study.

Table 3.1: The AKARI sources that are used in this study. Reproduced from Noble et al. (2013).

AKARI name	Simbad name	Type	α_{J2000} (degrees)	δ_{J2000} (degrees)	H (mJy)
AKARI-02	SSTc2d J054429.2+090856	YSO	86.122498	9.1490002	?
AKARI-03	2MASS J05443000+0908573	YSO	86.124964	9.1492458	0.442
AKARI-04	2MASS J05443085+0908260	YSO	86.128544	9.1406136	0.537
AKARI-05	2MASS J05443164+0908578	YSO	86.131846	9.1494267	1.320
AKARI-07	2MASS J09285020-5136373	YSO	142.20929	-51.610411	8.000
AKARI-08	2MASS J09285128-5136588	YSO	142.21379	-51.616373	9.080
AKARI-10	2MASS J10595211-6343000	Star	164.96722	-63.716741	15.700
AKARI-11	2MASS J10595548-6343210	Star	164.98119	-63.722508	2.320
AKARI-12	2MASS J11070622-6206057	Star	166.77597	-62.101584	4.190
AKARI-13	2MASS J11071041-6206013	Star	166.79341	-62.100358	5.380
AKARI-14	2MASS J11071034-6205345	Star	166.79304	-62.092943	1.140
AKARI-16	2MASS J12312792-6343221	Star	187.86635	-63.722816	5.090
AKARI-17	2MASS J12313060-6343376	Star	187.87753	-63.727139	16.400
AKARI-18	2MASS J12313217-6343306	Star	187.88413	-63.725144	4.370
AKARI-19	2MASS J12313247-6343105	Star	187.88539	-63.719644	24.800
AKARI-20	2MASS J12361240-6311509	Star	189.05177	-63.197538	3.030
AKARI-22	2MASS J15424185-3409435	Star	235.67439	-34.162102	3.406
AKARI-23	2MASS J16372876-3513588	Star	249.36990	-35.233002	121.759
AKARI-25	2MASS J16572088-1608241	Star	254.33701	-16.139999	2.004
AKARI-26	2MASS J16572151-1608423	YSO	254.33960	-16.145100	3.447
AKARI-27	2MASS J20573495+7737415	Star	314.39560	77.628197	4.737
AKARI-28	2MASS J22064175+5906156	YSO	331.67388	59.104326	0.452

Fitting a continuum baseline to the VLT data in the O-H stretch region also required extrapolation of the observed flux into wavelength ranges blocked by Earth's atmosphere and beyond the spectral coverage of the VLT-ISAAC detector. This is detailed in the following subsection.

3.3.2 Extrapolation of OH stretch blue wing in VLT

Features originating from atmospheric water prevent acquisition of useful spectroscopic data below $\sim 2.8\,\mu$m ($\gtrsim 3550$ cm^{-1}) in the VLT observations of the 3-micron features. The lack of data points beyond the blue wing of the O-H stretch absorption feature (see Figure 3.1) results in uncertainty of fitting an accurate continuum baseline to the observed spectra and thus affects the derived optical depths.

My method (illustrated as a flowchart in Figure 3.4) for estimating the baseline around and thus the optical depth of the OH stretch relies on making a reasoned estimate of the source flux at 2.7 μm, where I expect the optical depth (τ) to be zero in all cases. I tested the quality of this estimate by fitting a baseline in the form of a 3rd order polynomial to the observed spectrum between 3.70 and 3.95 μm, and by also forcing the fit to pass through the extrapolated point at 2.7 μm. Using the baseline fitted in this way I calculated the optical depth of the OH stretch feature, and attempted to fit a pure water ice laboratory spectrum (more details will be presented in Section 3.4.2.1) to a narrow part of the blue wing of the OH stretch, between 2.80 and 2.95 μm. I assumed that the best possible fit of the laboratory water spectrum to this stretch of the blue wing corresponds to the best possible baseline fit, and with this assumption in mind set the extrapolated flux at 2.7 μm to be the one which provides the best fit for pure H_2O at the blue wing.

The extrapolation method relies on several assumptions and it is thus prudent to examine the uncertainties associated with it. I compared two border cases of extrapolated 2.7 μm fluxes: one where the flux equals zero and one where it equals the flux of the same spectrum at 3.7 μm, where $\tau = 0$ on the red side of the 3-micron feature. An

Table 3.2: Information about the VLT sources which are used in this study. Reproduced mostly based on Pontoppidan et al. (2003a). These sources are all YSOs.

VLT name	Simbad name	α_{J2000} (degrees)	δ_{J2000} (degrees)	H (mJy)
CRBR 2422	CRBR 2422.8-3423	246.852554	-24.684281	?
EC 82	CK 3	277.487029	01.246222	49.694[a]
EC 90A	[B96] Serpens 7	277.490571	01.234914	205.826[a]
EC 90B	[B96] Serpens 7	277.490571	01.234914	205.826[a]
Elias 32	[B96] OphB2 5	246.868525	-24.455842	12.198[a]
GSS 30 IRS 1	BKLT J162621-242306	246.589250	-24.385110	47.676[b]
HH 100	V* V710 CrA	285.461158	-36.969336	36.199[a]
HH 46	HH 46	126.43271	-51.00908	?
IRAS 08375	[LLN92] IRS 13	129.8350	-41.33140	?
IRAS 08448	[LLN92] IRS 17	131.6408	-43.90920	?
IRAS 08470	[LLN92] IRS 19	132.2008	-43.54030	?
IRS 42	BKLT J162721-244142	246.839454	-24.695297	32.501[a]
IRS 43	BKLT J162726-244051	246.862233	-24.680783	4.006[a]
IRS 44	BBRCG 49	246.866779	-24.659308	3.460[a]
IRS 46	BBRCG 52	246.872646	-24.654497	9.026[a]
IRS 48	BKLT J162737-243035	246.904958	-24.509731	305.000[a]
IRS 51	BKLT J162739-244316	246.915950	-24.720853	14.371[a]
IRS 54	BKLT J162751-243145	246.965854	-24.529314	34.253[a]
IRS 63	GWAYL 4	247.89854	-24.02481	14.135[c]
L 1489	[BBM92] 8	061.179462	+26.315664	6.642[d]
R Cra IRS 5A	[B87] 7	285.450233	-36.956097	3.298[e]
R Cra IRS 5B	[B87] 7	285.450233	-36.956097	3.298[e]
Reipurth 50	HBC 494	085.114376	-07.458349	?
SVS 4-5	[EC89] SVS 4-5	277.48996	+01.21683	?
SVS 4-9	[EC89] SVS 4-9	277.491075	+01.214278	10.624[a]
TPSC 78	TPSC 78	083.807423	-05.394442	?
VSSG 1	ISO-Oph 24	246.578625	-24.472136	108.918[a]
VSSG 17	[B96] OphB2 6	246.875750	-24.462047	25.369[a]
WL 12	BBRCG 4	246.684146	-24.580097	3.208[a]

[a] Cutri (2003) [b] Barsony, Ressler, and Marsh (2005) [c] Beckford et al. (2008)
[d] Connelley, Reipurth, and Tokunaga (2008) [e] Haas et al. (2008)

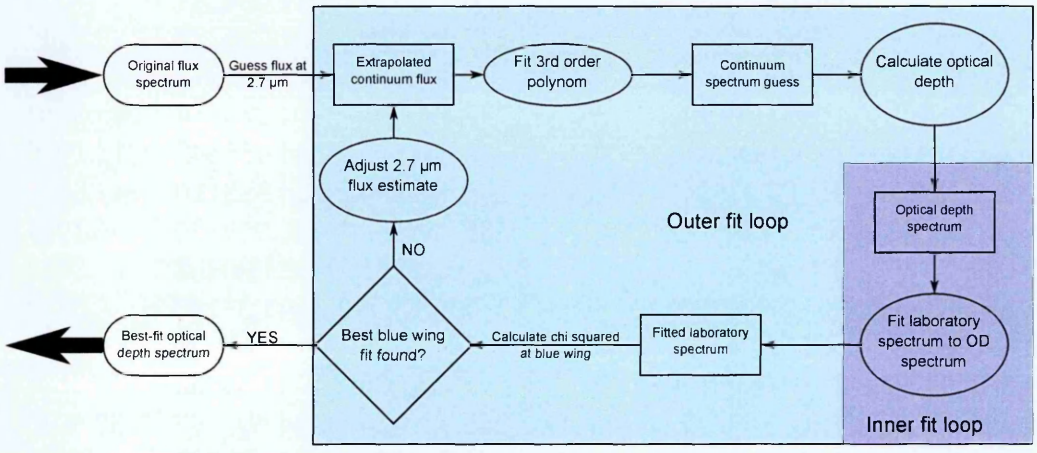

Figure 3.4: A flowchart describing the OH stretch optical depth estimation process for VLT data. The process is split into separate "inner" and "outer" fits. The outer fit loop attempts to find a best-fit solution to a single extrapolated point of flux at 2.7 μm, where I assume $\tau = 0$. It does this by starting with a reasoned estimate of the extrapolated flux, fitting a 3rd order polynomial to the observed flux while forcing the fit to pass through the extrapolated point, and then calculating an optical depth spectrum from the continuum fit. It then feeds the optical depth spectrum to the inner fit loop, which attempts fitting a pure H_2O laboratory spectrum to a narrow part of the blue wing of the 3-micron absorption feature. After finding the best fit, the best-fit parameters are returned to the outer fit loop. A χ^2 value is calculated from the best-fit parameters, and the process is iterated by varying the 2.7 μm flux until the lowest χ^2 is found. I assume this extrapolated flux to be the best estimate of the real flux at that point, and calculate the final optical depth from it. This optical depth is used in all further analysis.

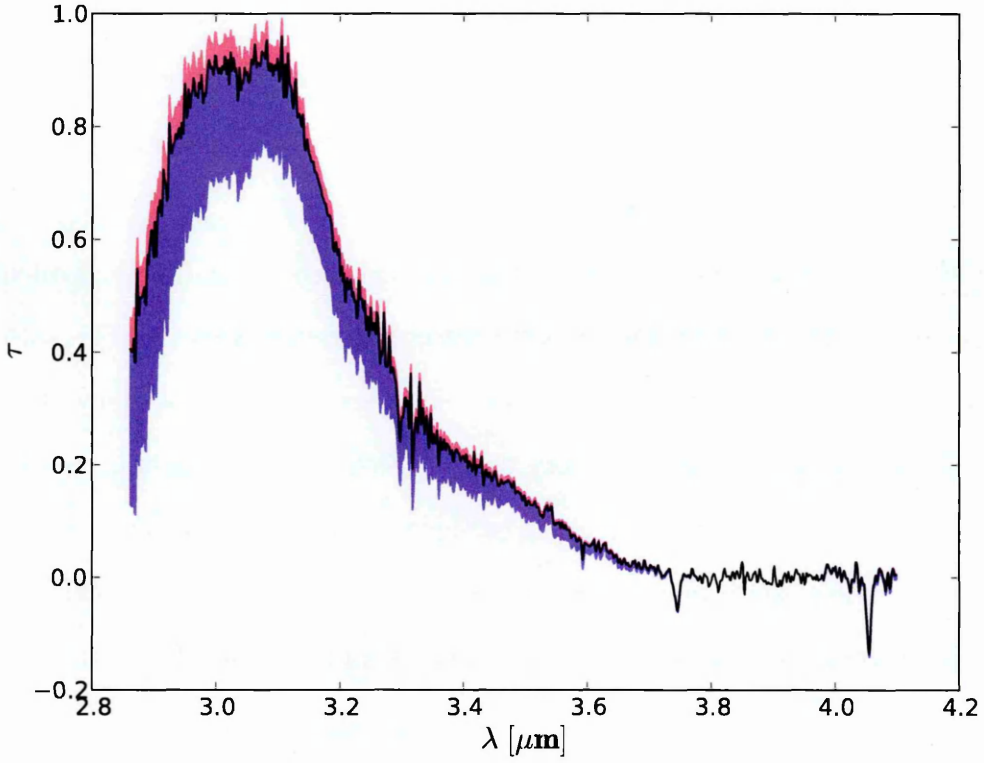

Figure 3.5: An example of the variation introduced to the optical depth of one of the VLT sources (EC 90A) when using either the maximum (red) or minimum (blue) constraint of the extrapolation method discussed in Section 3.3.2. The black line shows the best-fit extrapolated optical depth spectrum, which was used for the analysis conducted in all later sections of this study.

example of the potential range of variations in the derived optical depth in this range is show in Figure 3.5. The typical maximum possible systematic deviation in derived optical depths caused by this extrapolation method is approximately 50 %.

3.3.3 Fitting scheme

To answer the questions posed in the beginning of this chapter, and to gain a better understanding of the chemical evolution scenarios discussed in Section 3.2, the observational data discussed above is fitted with a combination of analytical and laboratory spectra. All fitting methods described in this chapter -with the exception of my implementation of the CH_3OH fitting method of Brooke, Sellgren, and Geballe (1999), which will be discussed separately- follow the same general scheme. The only changes between tested models are the specific components being fitted to the 3-micron region

of the observed spectra. Furthermore, each fitting method is applied in an identical "one size fits all" fashion to each object that is being examined, with the same (for each object) pre-fitting procedures being followed prior to minimization and the results of the minimization being analysed using identical methods.

In my fits I make use of my custom-built ice spectroscopy fitting library, written in PYTHON and utilizing the constrained least-squares fitting library LMFIT. This software is fully documented at the end of this thesis, in Chapter A. As most of my fitted spectra have been acquired from laboratory data, I follow laboratory astrochemistry standards in presenting the results and thus in most places use reciprocal wavenumbers (in units of cm^{-1}) instead of wavelengths when discussing the x axis. When performing a fit, the target spectrum under scrutiny is fed into the library and a fitting range is selected.

In many cases -such as the C-O stretching mode absorptions- the entire feature is included in the fitting range, but the O-H stretching mode that comprises a major part of the 3-micron feature is often saturated and thus including its peak in the fitting range would provide unrealistic fitting results. With this in mind I chose the range of the C-O stretching mode fits to be $2040-2250\,cm^{-1}$ ($4.45-4.90\,\mu m$), fully covering any features I wish to fit to the C-O stretch. For the O-H and C-H stretching mode fits I chose the fitting ranges to be $2820-2845\,cm^{-1}$ and $3400-3600\,cm^{-1}$, respectively. A C-H stretching mode between 2820 and $2845\,cm^{-1}$ was included in the fitting regions because this feature was noticed to be the constraining factor for fitting CH_3OH data into the red wing. Choosing the entirety of the red wing as a fitting range produced poor-quality fits because no published physical model is capable of reproducing the full range of observed absorption features in the red wing. The second range -between 3400 and $3600\,cm^{-1}$- is the blue wing of the O-H stretch illustrated in Figure 3.1. The frequency range between the two fitting ranges is considered to be a part of the saturated peak of the O-H stretch or a part of the unknown red wing, and is ignored in the fitting models.

Generally speaking, the models being fitted to observed spectra are a sum of one

or more analytical and laboratory spectra. The analytical and laboratory spectra are all interpolated and convolved to match the resolution and PSF (point spread function) of the observed spectrum. The fitting parameters are constrained to prevent the fitting of non-physical (i.e. with negative ice absorption) spectra to the observations. The spectra also have a CDE (continuously distributed ellipsoids; e.g. Tielens et al., 1991) grain-shape correction applied to them, in order to better approximate the properties of interstellar dust grains and their ice coating. The finer points of the methodology behind CDE correction were discussed in greater detail in Chapter 1 Section 1.4.3, and thus will not be reiterated here.

The C-O stretching mode fit in all cases consists of two individual components, the approximate locations of which on an observed ice spectrum are illustrated on Figure 3.2. The first component is a CDE-corrected Lorentzian, which describes the contribution of pure CO ice to the "middle component" (Pontoppidan et al., 2003a) of the C-O stretch. The function is presented in the form

$$\tau(\nu) = h \cdot \nu \cdot \Im\left[2\varepsilon(\nu) \cdot \frac{\log \varepsilon(\nu)}{\varepsilon(\nu) - 1}\right], \tag{3.1}$$

where h is the peak height of the function, ν is the frequency (in cm^{-1}), and $\Im$ indicates that only the imaginary component of the equation contained within the brackets is considered. Finally, $\varepsilon(\nu)$ is the complex dielectric function for a Lorentz oscillator, as a function of frequency:

$$\varepsilon(\nu) = \varepsilon_0 + \frac{\nu_p^2}{\nu_0^2 - \nu^2 - \gamma\nu \mathrm{i}}, \tag{3.2}$$

which is described in further detail in Pontoppidan et al., 2003a. In my fitting routines I only allow h to vary, and fix the other parameters as $\gamma = 1.5\ \mathrm{cm}^{-1}$, $\nu_p = 195\ \mathrm{cm}^{-1}$, $\varepsilon_0 = 1.67$, and $\nu_0 = 2138.5\ \mathrm{cm}^{-1}$, as also defined and described in Pontoppidan et al. (2003a). Finally, i is the imaginary unit.

The second component of the C-O stretch fit is the $CO:CH_3OH$ laboratory spectrum (presented in Cuppen et al., 2011) with a mixture ratio 1:1. While the ratio of the ice mixture producing the red component on interstellar ices is almost certainly not

always 1:1, there was no practical way to define the mixing ratio as a free parameter because different ratios cause the shapes of the absorption features to change subtly. Furthermore, I expect 1:1 to be a good enough simple approximation of the ice matrix producing the red component, because of the formation of methanol being closely connected to CO. The laboratory data is fitted to observations by means of a single free parameter in the form of a multiplier, k, which is fixed in the C-O stretch fit and carried over to be used in fitting additional components to the 3-micron region, where the CO:CH_3OH mixture also shows absorption features. If a different mixing ratio than 1:1 were to be used, the fitted data would have slightly different line shapes and (more importantly) the magnitude of effect the mixture has to the 3-micron region would change. If a mixture containing more CO than CH_3OH were to be used, the effect the fit (constrained by the C-O stretch) has on the 3-micron region would be decreased, while increasing the amount of CH_3OH relative to CO would cause the strength of the fitted features in the 3-micron region to become increasingly pronounced, until they no longer fit within the limits of observations.

The specific additional components used to fit the 3-micron O-H stretching mode and its associated red wing depend on the model being evaluated, but in each model they are all laboratory ice spectra. Four such models are examined. The first one (dubbed "Model 1") is the most basic of these models, and its primary purpose is to verify the hypothesis of Cuppen et al. (2011) by carrying over the CO:CH_3OH fit from the C-O stretch result to the 3-micron region, and fitting pure H_2O ice (Noble et al., 2013) to the residual left over when the contribution of the CO:CH_3OH fit is considered.

The second model (Model 2) adds a third component to the O-H stretch: a pure CH_3OH spectrum. This model serves as the simplest method of trying to fit as much of the red wing residual as possible, by allowing the C-H stretching features of the pure CH_3OH ice to fill in as much of the observed optical depth as possible. This model is also the one closest to the post-heating observational scenario presented in Figure 3.3 and discussed in Section 3.2, except with the H_2O:CO mixture replaced with a

Table 3.3: Summary of used fitting components in the O-H stretch band. All models used the same fitting components (pure CO and mixed CO:CH_3OH) in the C-O stretch band.

		Model			
		1	2	3	4
Component	CO:CH_3OH	✓	✓	✓	✓
	Pure H_2O	✓	✓		✓
	Pure CH_3OH		✓		
	CH_3OH:H_2O			✓	✓

CH_3OH:CO mixture.

Model 3 replaces the pure CH_3OH and H_2O components of Model 2 with a mixture of CH_3OH:H_2O (Dawes et al, in prep.). Four different mixing ratios (expressed in terms of N(CH_3OH)/N(H_2O): 17%, 23%, 31%, and 50%) were available for examination. Although unrealistic in terms of our understanding of ice formation (because it lacks a pure H_2O component), this model was considered as a test of having a minimal number of fitting parameters while still trying to fill as much of the 3-micron red wing as possible. Furthermore, it serves as a showcase example (which will be further illustrated in Section 3.4) of how a mixture of two ices (in this case H_2O and CH_3OH) produces a very different line shape than an equivalent linear combination of its respective pure ices. Model 4 is the more realistic variant of Model 3, and contains the pure H_2O component used Models 1 and 2 in addition to the components of Model 3.

The components used in all four models are summarised in Table 3.3.

3.3.4 Calculation of column densities

One of the objectives sought by my fitting methodology is to allow me to calculate N(CO, solid), N(H_2O, solid), and N(CH_3OH, solid) towards all the sources considered in this study. The method for calculating the column density is slightly different between different components.

Column densities are estimated from the fitted laboratory spectra by applying the formula

$$N(\mathrm{X}) = k \cdot \frac{\int \tau(\nu) d\nu}{A_{\mathrm{X}}}, \tag{3.3}$$

where $\int \tau(\nu)d\nu$ is the optical depth of the laboratory spectrum integrated over the relevant mode (e.g. the O-H stretch) for A_X, which is the band strength or "A-factor" of the relevant molecule and mode. Lastly, k is the multiplier of the spectrum acquired from the best-fit result. For the O-H stretch of the pure H_2O and the C-H stretches of the pure CH_3OH spectra the band strengths are $2.0 \cdot 10^{-16}$ cm^2 and 5.3×10^{-18} cm^2, respectively (Gerakines et al., 1995). For the mixed spectra (CO:CH_3OH and CH_3OH:H_2O) I used values for $\frac{\int \tau(\nu)d\nu}{A_X}$ (also known as the number of oscillators) instead of the band strengths. For the CH_3OH in the CH_3OH:H_2O data the oscillator numbers are 9.04×10^{17}, 8.95×10^{17}, 4.70×10^{17}, and 2.66×10^{17} cm^{-2} for the mixing ratios 17, 23, 31, and 50% respectively. For H_2O the oscillator numbers are 9.04×10^{17}, 8.95×10^{17}, 4.70×10^{17}, and 2.66×10^{17} cm^{-2}, respectively. For the CO:CH_3OH spectrum, the oscillator number for both CO and CH_3OH is 5.183×10^{17} cm^{-2}. Unlike with the A-factors, column densities calculated using the oscillator numbers are not dependent on integrating over a specific feature, but are calculated by simply multiplying the best-fit k with the relevant oscillator number.

For the CDE-corrected Lorentzian representing pure CO, N(CO) is calculated using (Pontoppidan et al., 2003a)

$$N(\mathrm{CO}) = 6.03 \text{ cm}^{-1} \times \tau_{\mathrm{peak}} \times A_{\mathrm{CO}}^{-1}, \tag{3.4}$$

where τ_{peak} is the peak optical depth of the fitted CDE-corrected lorentzian function, $A_{\mathrm{CO}} = 1.1 \times 10^{-17}$cm molec^{-1} is the A-factor for bulk CO (Gerakines et al., 1995), and the leading multiplication factor takes into account the CDE-correction, as described by Pontoppidan et al. (2003a).

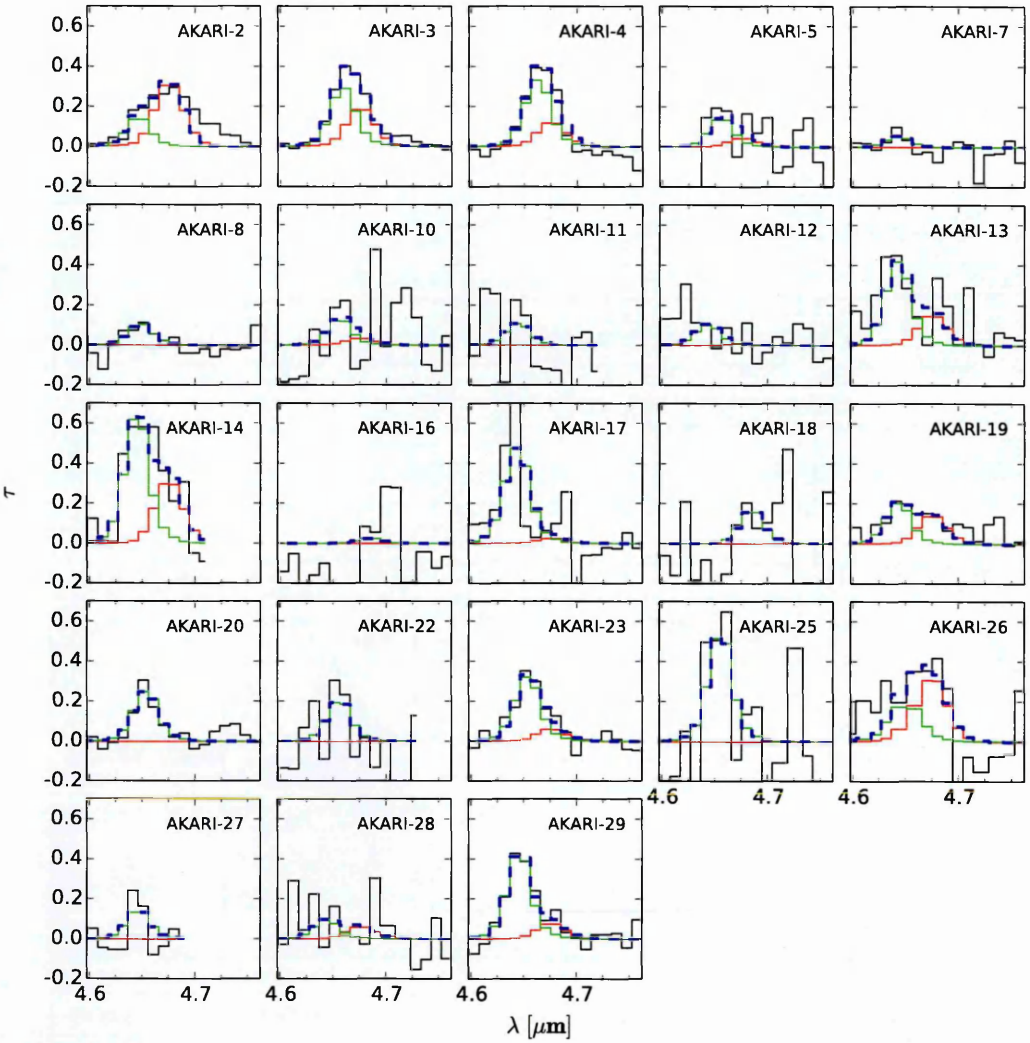

Figure 3.6: Fit results to the C-O stretch of the AKARI data, presented as thumbnails. Pure CO is represented by a green line, and the 1:1 CO:CH_3OH mixture is represented by a red line. The observations are represented by the black line and overall fit is represented by the dashed blue line.

3.4 Results

3.4.1 The C-O stretch

The fit results to the C-O stretch of each source are shown in Figures 3.6 and 3.7, for the AKARI and VLT data respectively. A closer look at the fit results to a single example source in both the AKARI and VLT data sets is presented in Figure 3.8. As is seen from the figure, the AKARI data has a much lower resolution than the VLT data, but identical fitting methods provide consistent results between them.

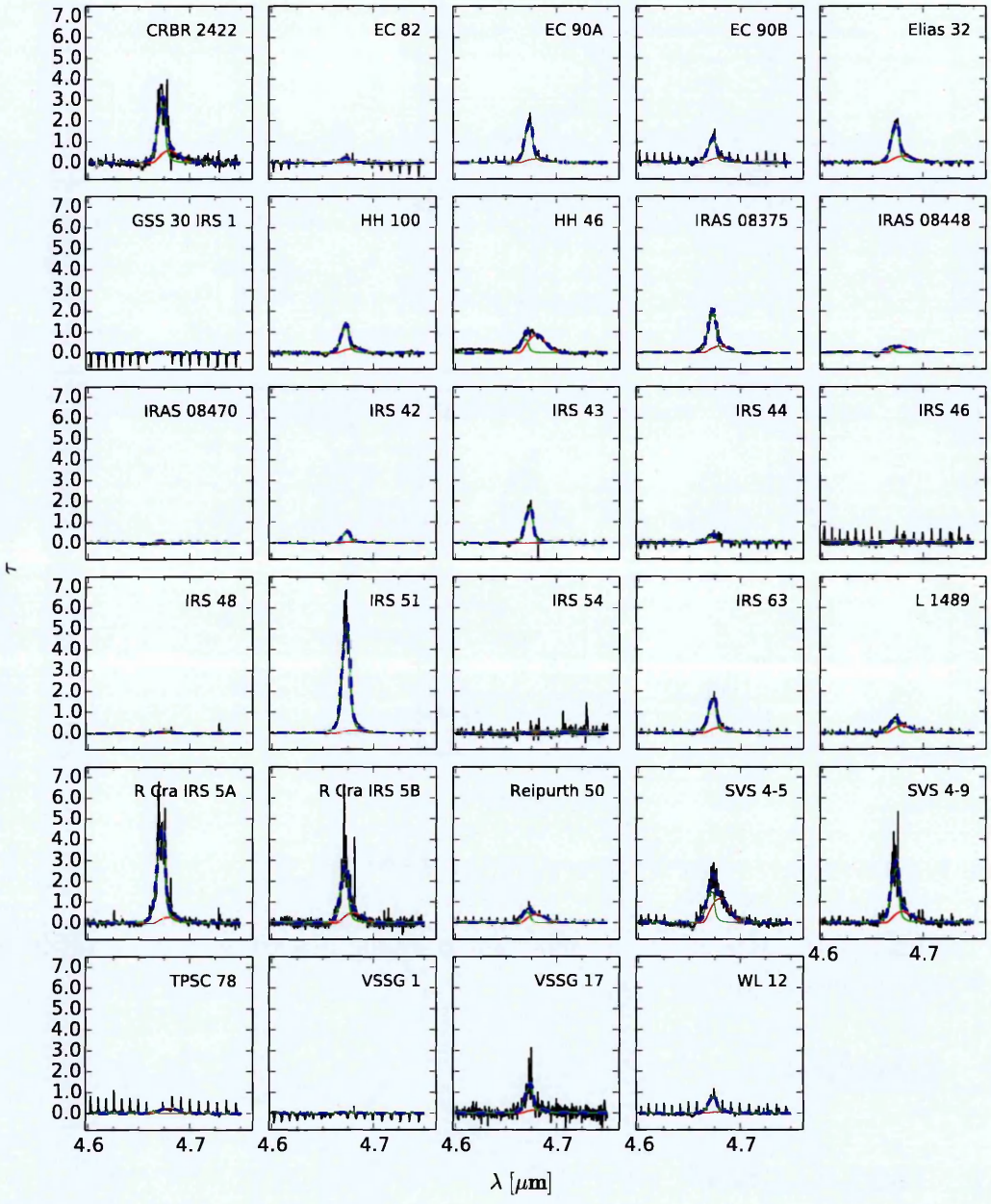

Figure 3.7: Fit results to the C-O stretch of the VLT data, presented as thumbnails. Pure CO is represented by a green line, and the 1:1 CO:CH_3OH mixture is represented by a red line. The observations are represented by the black line and overall fit is represented by the dashed blue line.

Table 3.4: The amount of CH_3OH in CO, as detected in the C-O stretch fit, in all the sources considered in this study.

Source	N(CH_3OH in CO) [10^{17} cm^{-2}]	Source	N(CH_3OH in CO) [10^{17} cm^{-2}]
AKARI-02	2.62 ± 0.26	CRBR 2422	2.93 ± 0.22
AKARI-03	1.59 ± 0.32	EC 82	≤ 1.03
AKARI-04	1.01 ± 0.58	EC 90A	0.91 ± 0.06
AKARI-05	≤ 1.79	EC 90B	1.11 ± 0.09
AKARI-07	≤ 0.73	Elias 32	1.50 ± 0.05
AKARI-08	≤ 0.66	GSS 30 IRS 1	≤ 0.28
AKARI-10	≤ 2.69	HH 100	1.00 ± 0.05
AKARI-11	≤ 2.41	HH 46	4.24 ± 0.07
AKARI-12	≤ 1.63	IRAS 08375	1.57 ± 0.12
AKARI-13	≤ 2.00	IRAS 08448	1.47 ± 0.07
AKARI-14	2.62 ± 0.49	IRAS 08470	≤ 0.74
AKARI-16	≤ 1.99	IRS 42	0.27 ± 0.02
AKARI-17	≤ 1.52	IRS 43	≤ 0.68
AKARI-18	≤ 2.48	IRS 44	≤ 0.64
AKARI-19	1.19 ± 0.40	IRS 46	≤ 1.07
AKARI-20	≤ 0.77	IRS 48	≤ 0.40
AKARI-22	≤ 2.31	IRS 51	0.63 ± 0.18
AKARI-23	≤ 0.84	IRS 54	≤ 1.86
AKARI-25	≤ 4.91	IRS 63	1.28 ± 0.05
AKARI-26	2.65 ± 0.78	L 1489	1.71 ± 0.05
AKARI-27	≤ 1.68	R Cra IRS 5A	≤ 1.55
AKARI-28	≤ 2.09	R Cra IRS 5B	2.40 ± 0.23
AKARI-29	≤ 0.94	Reipurth 50	2.07 ± 0.05
		SVS 4-5	5.77 ± 0.14
		SVS 4-9	2.71 ± 0.20
		TPSC 78	1.31 ± 0.10
		VSSG 1	≤ 0.41
		VSSG 17	≤ 2.80
		WL 12	≤ 0.50

Table 3.5: The amount of pure CO, as detected in the C-O stretch fit, in all the sources considered in this study.

Source	N(Pure CO) $[10^{17}$ cm$^{-2}]$	Source	N(Pure CO) $[10^{17}$ cm$^{-2}]$
AKARI-02	0.75 ± 0.11	CRBR 2422	18.05 ± 0.27
AKARI-03	1.59 ± 0.09	EC 82	1.51 ± 0.04
AKARI-04	1.82 ± 0.14	EC 90A	11.92 ± 0.06
AKARI-05	≤ 2.00	EC 90B	6.87 ± 0.07
AKARI-07	≤ 0.82	Elias 32	11.09 ± 0.05
AKARI-08	≤ 0.73	GSS 30 IRS 1	≤ 0.87
AKARI-10	≤ 3.00	HH 100	8.14 ± 0.04
AKARI-11	≤ 2.69	HH 46	4.29 ± 0.04
AKARI-12	≤ 1.82	IRAS 08375	12.27 ± 0.11
AKARI-13	2.30 ± 0.41	IRAS 08448	1.46 ± 0.03
AKARI-14	3.39 ± 0.21	IRAS 08470	≤ 0.99
AKARI-16	≤ 2.22	IRS 42	3.31 ± 0.01
AKARI-17	2.61 ± 0.78	IRS 43	11.11 ± 0.09
AKARI-18	≤ 2.77	IRS 44	2.37 ± 0.04
AKARI-19	1.12 ± 0.16	IRS 46	≤ 1.43
AKARI-20	1.36 ± 0.12	IRS 48	0.59 ± 0.01
AKARI-22	≤ 2.58	IRS 51	34.15 ± 0.23
AKARI-23	1.76 ± 0.11	IRS 54	≤ 2.48
AKARI-25	≤ 5.48	IRS 63	10.26 ± 0.05
AKARI-26	≤ 1.77	L 1489	3.56 ± 0.03
AKARI-27	≤ 1.87	R Cra IRS 5A	29.29 ± 0.32
AKARI-28	≤ 2.33	R Cra IRS 5B	16.40 ± 0.26
AKARI-29	2.24 ± 0.12	Reipurth 50	3.40 ± 0.03
		SVS 4-5	9.86 ± 0.12
		SVS 4-9	17.02 ± 0.21
		TPSC 78	0.77 ± 0.04
		VSSG 1	≤ 0.55
		VSSG 17	8.39 ± 0.17
		WL 12	5.06 ± 0.07

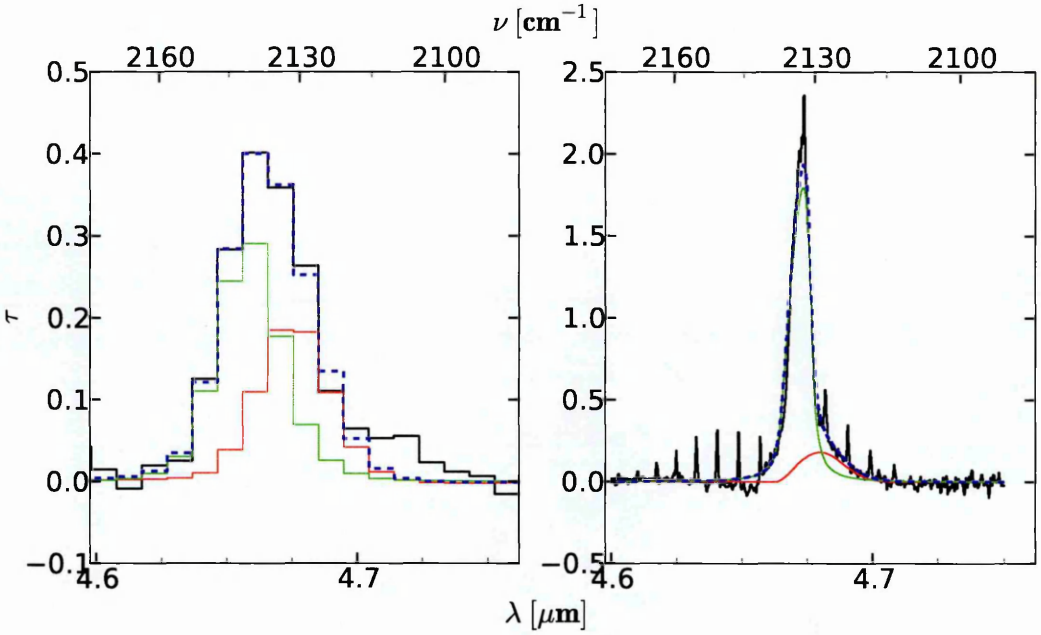

Figure 3.8: An example fit result of a pure CO (green line) and a 1:1 CO:CH_3OH mixture (red line) to the observed C-O stretch of a source from the AKARI (AKARI-03, left) and VLT (EC 90A, right) datasets. The observations are represented by the black line and overall fit is represented by the dashed blue line.

As is shown in Table 3.4, the fitting method produced greater than 3σ peaks in the fitted CO:CH_3OH component in a total of 6 cases of 23 in the AKARI observations and in 17 out of 29 cases in the VLT observations. Table 3.5 shows that most of the objects which do not produce a CO:CH_3OH detection often also lack detection in pure CO ice, although the reverse is not always true. These fits also immediately show that the red component from Cuppen et al. (2011) works as expected when tested against the AKARI and VLT datasets, corroborating their results in the C-O stretch.

3.4.2 The O-H stretch

Four each of the four models examined in this study, the total column densities of CO, CH_3OH, and H_2O ices could be calculated, and are presented for each source as a ternary plot in Figure 3.9. This plot shows the relative contributions (as percentages) of each of the three ices to the total ice column density towards each source.

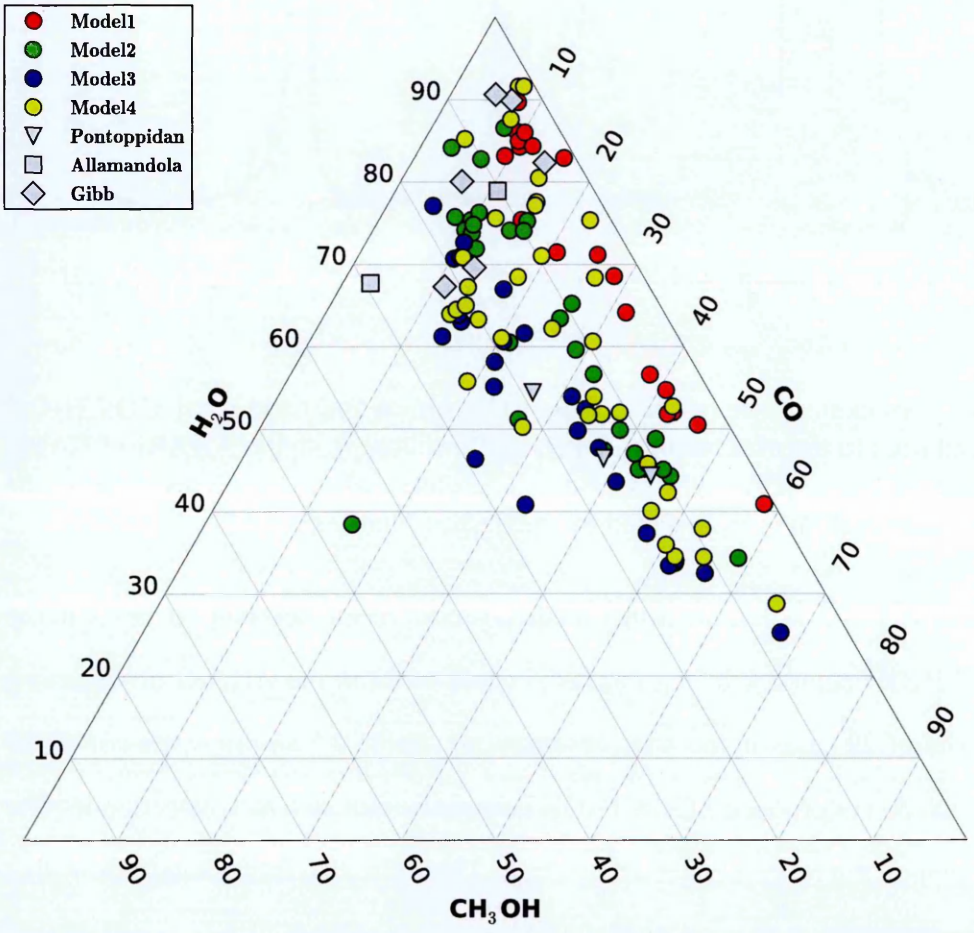

Figure 3.9: A ternary diagram showing the contribution of CO, CH_3OH, and H_2O to the total column density of ice, as defined by the sum of all three molecules, in all the sources and models examined in this chapter. Only cases where a non-upper limit value could be calculated for all three molecules were included. Models 3 and 4 have been calculated using the 23% CH_3OH:H_2O mixing ratio case. Also featured are values from Allamandola et al. (1992), Gibb et al. (2004), Pontoppidan, van Dishoeck, and Dartois (2004), and references therein, in cases where column densities for all three molecules were reported.

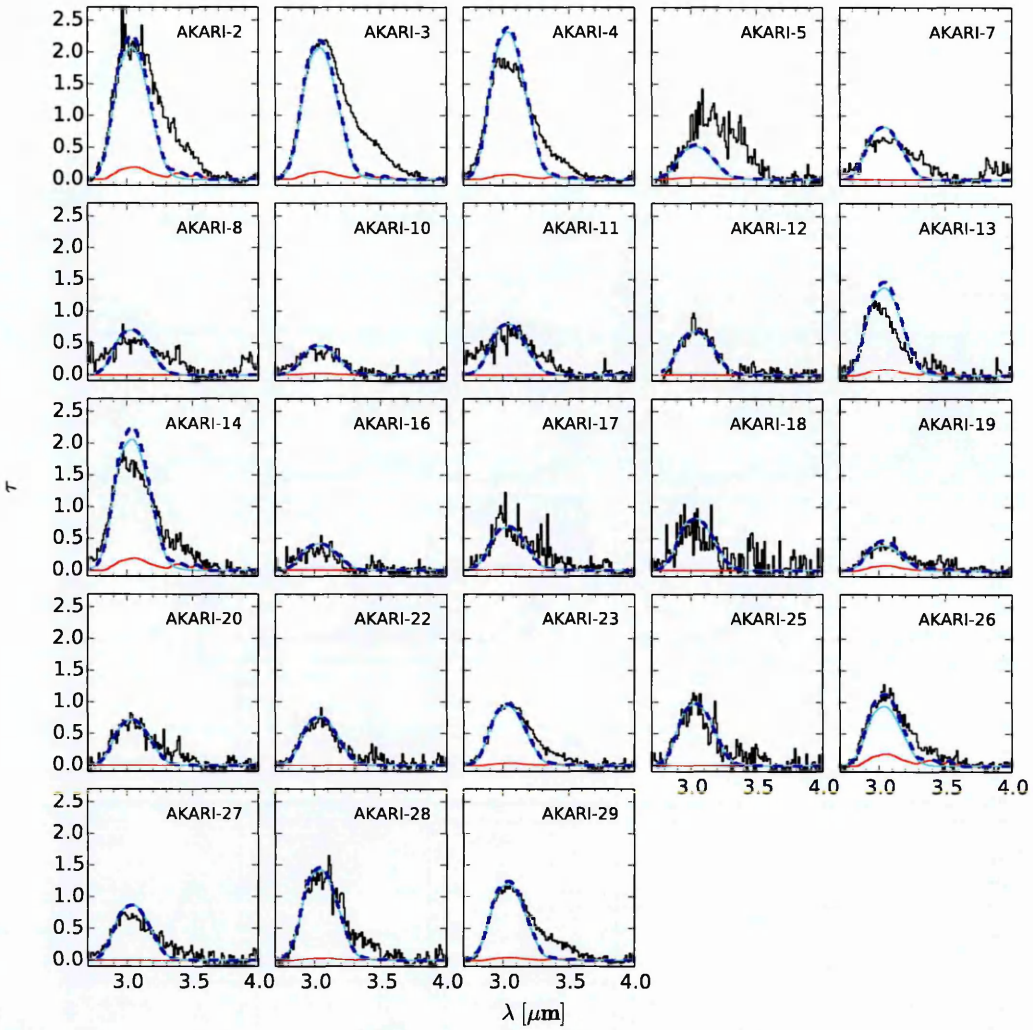

Figure 3.10: Fit results of Model 1 to the AKARI data, presented as thumbnails. The CO:CH_3OH and pure H_2O data are represented by red and cyan lines, respectively. The observed data and the overall fit are represented by a black and a dashed blue line.

3.4.2.1 Model 1

The fit results using Model 1 for each source are shown in Figures 3.10 and 3.11, for the AKARI and VLT data respectively. A closer look at the fit results to a single example source in both the AKARI and VLT data sets is presented in Figure 3.12.

This model is sufficient for fully explaining the observed 3-micron features of objects (such as AKARI-10) where no red wing is present. The CO:CH_3OH data does not overfit the red wing in any of the objects, showing that the red component fit from Cuppen et al. (2011) provides results consistent with the 3 micron features as well, but leaves a significant residual to the red wing. This is because the contribution of

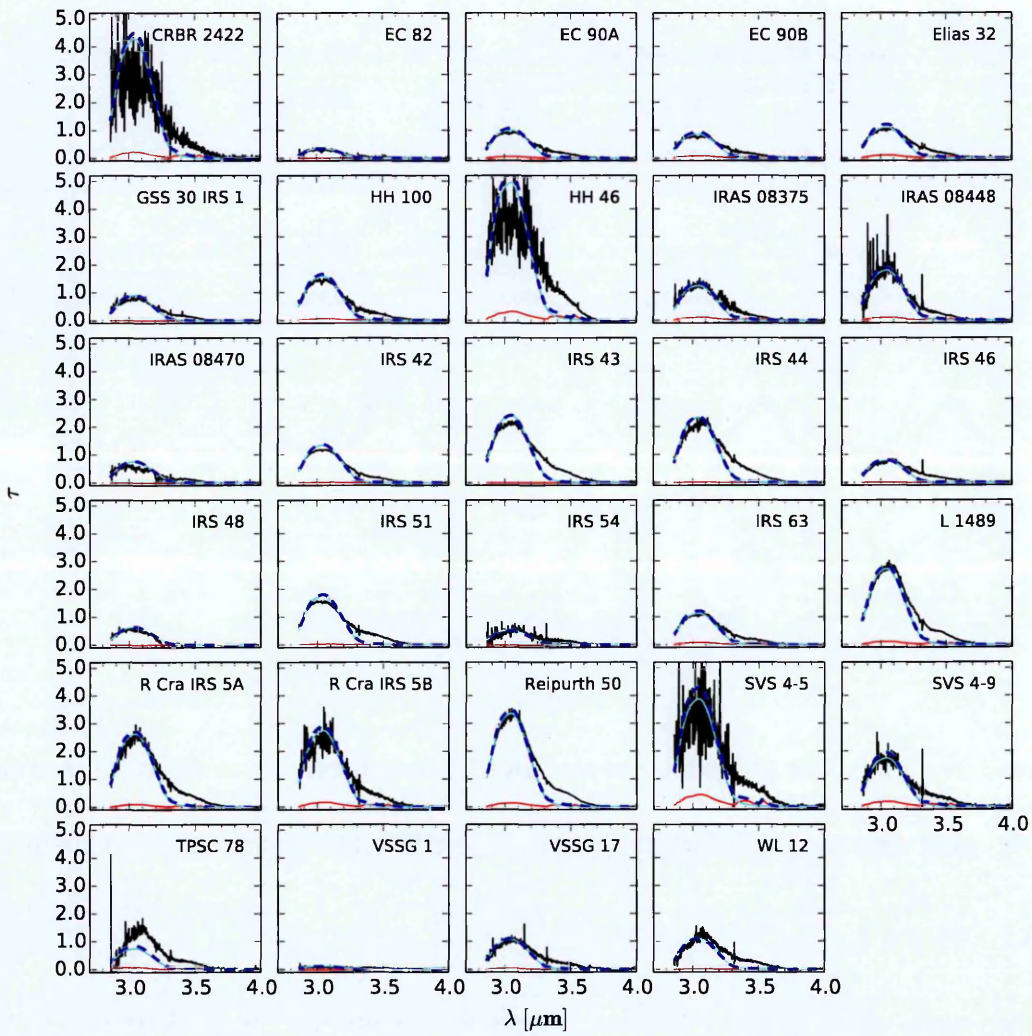

Figure 3.11: Fit results of Model 1 to the VLT data, presented as thumbnails. The CO:CH_3OH and pure H_2O data are represented by red and cyan lines, respectively. The observed data and the overall fit are represented by a black and a dashed blue line.

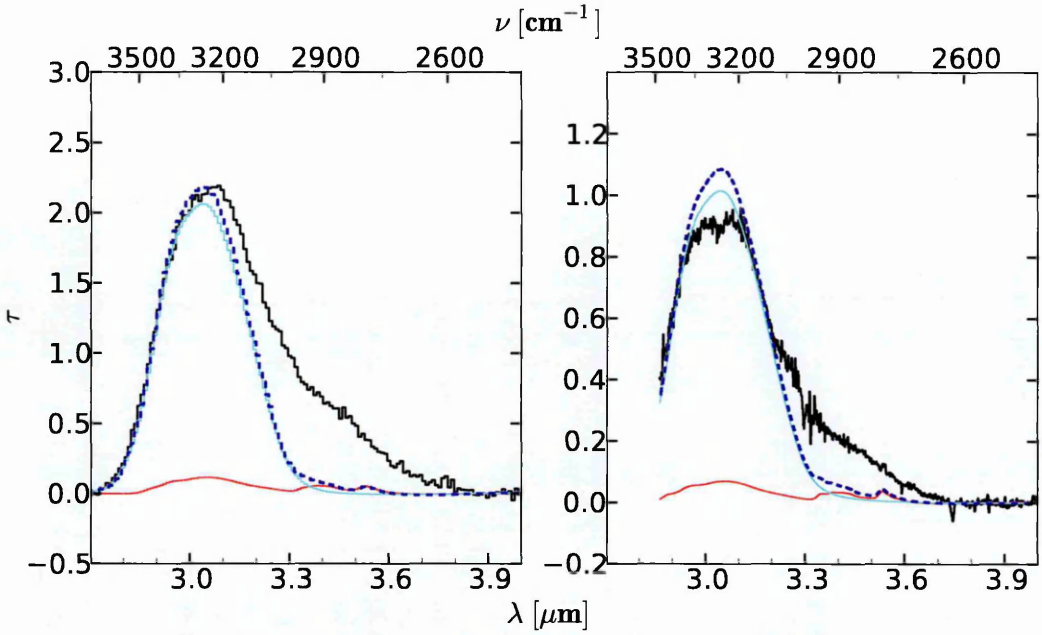

Figure 3.12: An example of the fitting results of Model 1 (Section 3.4.2.1) to a single source from the (left) AKARI and (right) VLT data examined in my study. These sources are the same as those shown in Figure 3.8. The CO:CH_3OH and pure H_2O data are represented by red and cyan lines, respectively. The observed data and the overall fit are represented by a black and a dashed blue line.

the C-H stretching features of the fitted CO:CH_3OH ice to the red wing absorption is negligible at the considered ice mixing ratio of 1:1. A significant residual is left in the red wing, and must be caused by absorption originating from something other than the ices considered in Model 1.

Table 3.6: Derived total column densities for all the sources, when using Model 1

Source	$N(H_2O)$ $[10^{17}\ cm^{-2}]$	$N(CO)$ $[10^{17}\ cm^{-2}]$	$N(CH_3OH)$ $[10^{17}\ cm^{-2}]$	Source	$N(H_2O)$ $[10^{17}\ cm^{-2}]$	$N(CO)$ $[10^{17}\ cm^{-2}]$	$N(CH_3OH)$ $[10^{17}\ cm^{-2}]$
AKARI-02	29.59 ± 1.26	3.37 ± 0.29	2.62 ± 0.26	CRBR 2422	58.99 ± 1.22	20.98 ± 0.35	2.93 ± 0.22
AKARI-03	29.57 ± 1.17	3.19 ± 0.34	1.59 ± 0.32	EC 82	4.76 ± 0.07	1.61 ± 0.10	≤ 1.03
AKARI-04	33.47 ± 1.12	2.84 ± 0.60	1.01 ± 0.58	EC 90A	14.01 ± 0.19	12.82 ± 0.08	0.91 ± 0.06
AKARI-05	7.81 ± 1.16	≤ 1.79	≤ 1.79	EC 90B	11.84 ± 0.17	7.97 ± 0.12	1.11 ± 0.09
AKARI-07	12.02 ± 0.73	≤ 0.73	≤ 0.73	Elias 32	15.28 ± 0.20	12.58 ± 0.07	1.50 ± 0.05
AKARI-08	10.24 ± 1.25	≤ 0.66	≤ 0.66	GSS 30 IRS 1	12.66 ± 0.19	0.43 ± 0.20	≤ 0.28
AKARI-10	6.56 ± 0.53	≤ 2.69	≤ 2.69	HH 100	22.09 ± 0.30	9.14 ± 0.07	1.00 ± 0.05
AKARI-11	11.58 ± 1.74	≤ 2.41	≤ 2.41	HH 46	68.52 ± 1.35	8.54 ± 0.08	4.24 ± 0.07
AKARI-12	10.19 ± 0.75	≤ 1.63	≤ 1.63	IRAS 08375	17.18 ± 0.25	13.84 ± 0.16	1.57 ± 0.12
AKARI-13	19.92 ± 0.60	3.56 ± 0.94	≤ 2.00	IRAS 08448	24.83 ± 0.53	2.93 ± 0.08	1.47 ± 0.07
AKARI-14	29.82 ± 1.19	6.01 ± 0.54	2.62 ± 0.49	IRAS 08470	10.65 ± 0.17	0.80 ± 0.15	≤ 0.74
AKARI-16	6.07 ± 0.93	≤ 1.99	≤ 1.99	IRS 42	18.70 ± 0.21	3.58 ± 0.03	0.27 ± 0.02
AKARI-17	9.78 ± 0.81	2.81 ± 1.67	≤ 1.52	IRS 43	33.47 ± 0.53	11.11 ± 0.18	≤ 0.68
AKARI-18	11.82 ± 1.76	≤ 2.48	≤ 2.48	IRS 44	32.44 ± 0.54	2.73 ± 0.08	≤ 0.64
AKARI-19	5.74 ± 0.52	2.30 ± 0.43	1.19 ± 0.40	IRS 46	11.18 ± 0.23	≤ 1.07	≤ 1.07
AKARI-20	10.42 ± 0.73	1.36 ± 0.35	≤ 0.77	IRS 48	8.86 ± 0.07	0.70 ± 0.04	≤ 0.40
AKARI-22	11.02 ± 0.51	≤ 2.31	≤ 2.31	IRS 51	24.45 ± 0.40	34.78 ± 0.29	0.63 ± 0.18
AKARI-23	13.44 ± 0.38	2.28 ± 0.33	≤ 0.84	IRS 54	7.23 ± 0.23	≤ 1.86	≤ 1.86
AKARI-25	14.16 ± 0.77	≤ 4.91	≤ 4.91	IRS 63	15.48 ± 0.20	11.54 ± 0.07	1.28 ± 0.05
AKARI-26	13.59 ± 0.61	3.61 ± 1.05	2.65 ± 0.78	L 1489	37.57 ± 0.52	5.27 ± 0.06	1.71 ± 0.05
AKARI-27	12.62 ± 0.52	≤ 1.68	≤ 1.68	R Cra IRS 5A	36.27 ± 0.55	30.77 ± 0.40	≤ 1.55
AKARI-28	20.58 ± 0.59	≤ 2.09	≤ 2.09	R Cra IRS 5B	37.91 ± 0.61	18.80 ± 0.35	2.40 ± 0.23
AKARI-29	17.19 ± 0.54	2.90 ± 0.43	≤ 0.94	Reipurth 50	46.27 ± 0.58	5.47 ± 0.06	2.07 ± 0.05
				SVS 4-5	53.59 ± 1.37	15.63 ± 0.19	5.77 ± 0.14
				SVS 4-9	24.13 ± 0.39	19.73 ± 0.28	2.71 ± 0.20
				TPSC 78	10.40 ± 0.74	2.08 ± 0.11	1.31 ± 0.10
				VSSG 1	1.63 ± 0.08	≤ 0.41	≤ 0.41
				VSSG 17	14.72 ± 0.28	9.21 ± 0.26	≤ 2.80
				WL 12	15.02 ± 0.39	5.42 ± 0.11	≤ 0.50

The total contributions of H_2O, CH_3OH and CO to the total ice abundance, are represented as red circles in the ternary diagram in Figure 3.9. In it I see that for Model 1 the total ice content is mostly dominated by H_2O originating from the pure H_2O ice component, though in several cases the total contribution of CO can reach up to 40 % and in one case even exceed 50 %. The contribution of CH_3OH to the total ice content varies mostly between 0 and $\sim$ 5 %, and in a few cases exceeding 10 %. The total column densities of the three ices in all objects, fitted using Model 1, are listed in Table 3.6. Table 3.7, which shows the ratio $N(CH_3OH)/N(H_2O)$ in all sources after application of Model 1, shows that the CO:CH_3OH ice causes a contribution of a few % to the reported ratio.

3.4.2.2 Model 2

The fit results using Model 2 for each source are shown in Figures 3.13 and 3.14, for the AKARI and VLT data respectively. A closer look at the fit results to a single example source in both the AKARI and VLT data sets is presented in Figure 3.15.

Table 3.7: $N(CH_3OH)/N(H_2O)$, as determined by Models 1 and 2, in all the sources considered in this study.

Source	$\frac{N(CH_3OH)}{N(H_2O)}$ Model 1, [%]	$\frac{N(CH_3OH)}{N(H_2O)}$ Model 2, [%]	Source	$\frac{N(CH_3OH)}{N(H_2O)}$ Model 1, [%]	$\frac{N(CH_3OH)}{N(H_2O)}$ Model 2, [%]
AKARI-02	0.89 ± 0.10	1.97 ± 0.36	CRBR 2422	0.50 ± 0.04	1.42 ± 0.12
AKARI-03	0.54 ± 0.11	2.17 ± 0.23	EC 82	–	–
AKARI-04	0.30 ± 0.17	0.66 ± 0.32	EC 90A	0.65 ± 0.04	2.10 ± 0.08
AKARI-05	–	–	EC 90B	0.94 ± 0.08	2.37 ± 0.12
AKARI-07	–	–	Elias 32	0.98 ± 0.04	2.56 ± 0.07
AKARI-08	–	–	GSS 30 IRS 1	–	1.49 ± 0.20
AKARI-10	–	–	HH 100	0.45 ± 0.02	1.95 ± 0.06
AKARI-11	–	–	HH 46	0.62 ± 0.02	2.11 ± 0.12
AKARI-12	–	–	IRAS 08375	0.91 ± 0.07	1.76 ± 0.11
AKARI-13	–	–	IRAS 08448	0.59 ± 0.03	1.78 ± 0.14
AKARI-14	0.88 ± 0.17	1.19 ± 0.37	IRAS 08470	–	1.22 ± 0.18
AKARI-16	–	–	IRS 42	0.15 ± 0.01	1.34 ± 0.05
AKARI-17	–	–	IRS 43	–	1.80 ± 0.08
AKARI-18	–	–	IRS 44	–	2.16 ± 0.07
AKARI-19	2.07 ± 0.73	–	IRS 46	–	2.91 ± 0.17
AKARI-20	–	–	IRS 48	–	–
AKARI-22	–	–	IRS 51	0.26 ± 0.07	2.06 ± 0.12
AKARI-23	–	–	IRS 54	–	3.46 ± 0.50
AKARI-25	–	–	IRS 63	0.83 ± 0.03	2.49 ± 0.06
AKARI-26	1.95 ± 0.58	–	L 1489	0.45 ± 0.02	2.23 ± 0.05
AKARI-27	–	–	R Cra IRS 5A	–	2.15 ± 0.10
AKARI-28	–	–	R Cra IRS 5B	0.63 ± 0.06	1.99 ± 0.11
AKARI-29	–	1.54 ± 0.32	Reipurth 50	0.45 ± 0.01	1.99 ± 0.05
			SVS 4-5	1.08 ± 0.04	3.01 ± 0.17
			SVS 4-9	1.12 ± 0.08	2.72 ± 0.13
			TPSC 78	1.26 ± 0.13	11.97 ± 1.83
			VSSG 1	–	6.58 ± 1.24
			VSSG 17	–	3.12 ± 0.19
			WL 12	–	4.30 ± 0.15

Inclusion of a freely varying spectrum which contributes to the C-H stretching modes in the red wing causes a much larger part of the red wing to be "filled" by the fitted model, as is to be expected. Furthermore, the strong O-H stretching mode of the pure CH_3OH spectrum ends up significantly contributing to the overall shape of the O-H stretch as well, and thus is also capable of producing (compared to Model 1) a slightly better fit to the observed blue wing.

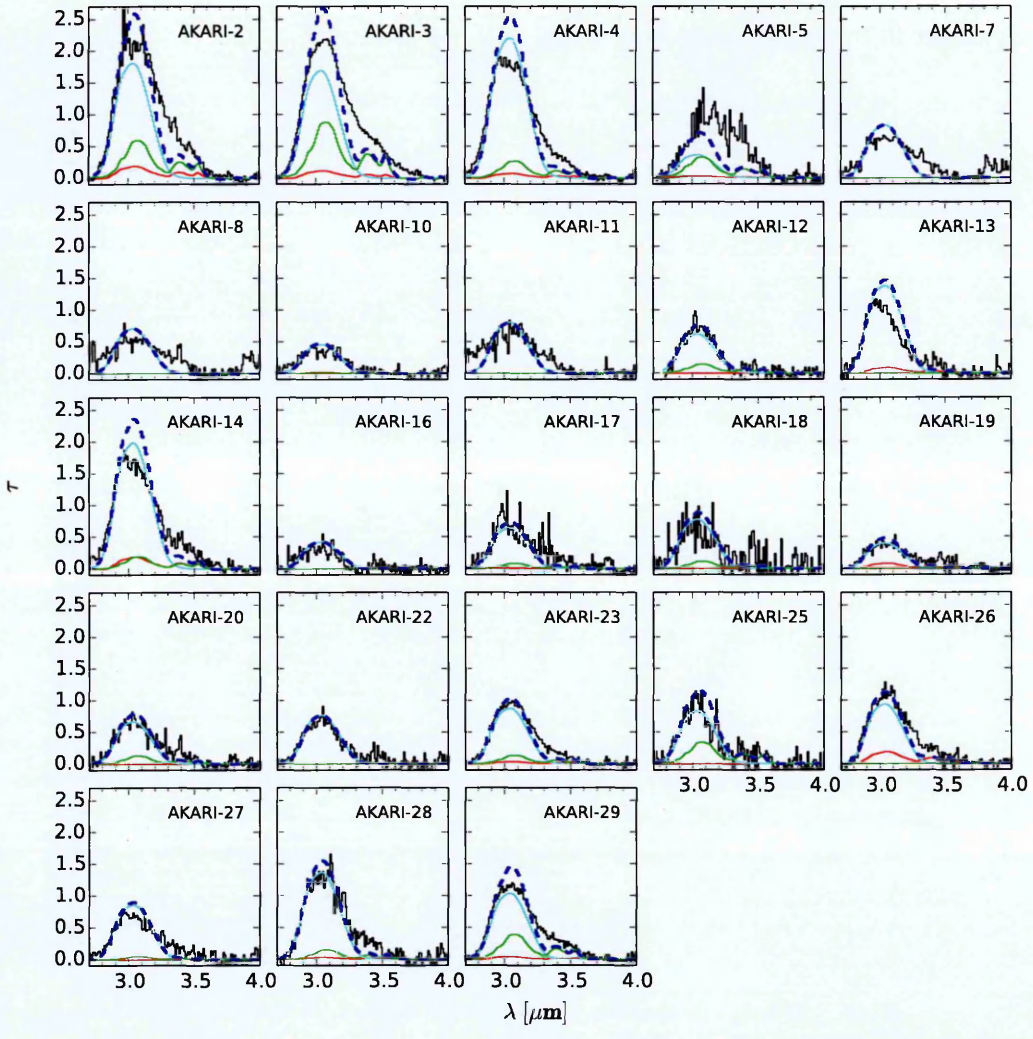

Figure 3.13: Fit results of Model 2 to the AKARI data, presented as thumbnails. The CO:CH_3OH, pure CH_3OH, and pure H_2O data are represented by red, green, and cyan lines, respectively. The observed data and the overall fit are represented by a black and a dashed blue line.

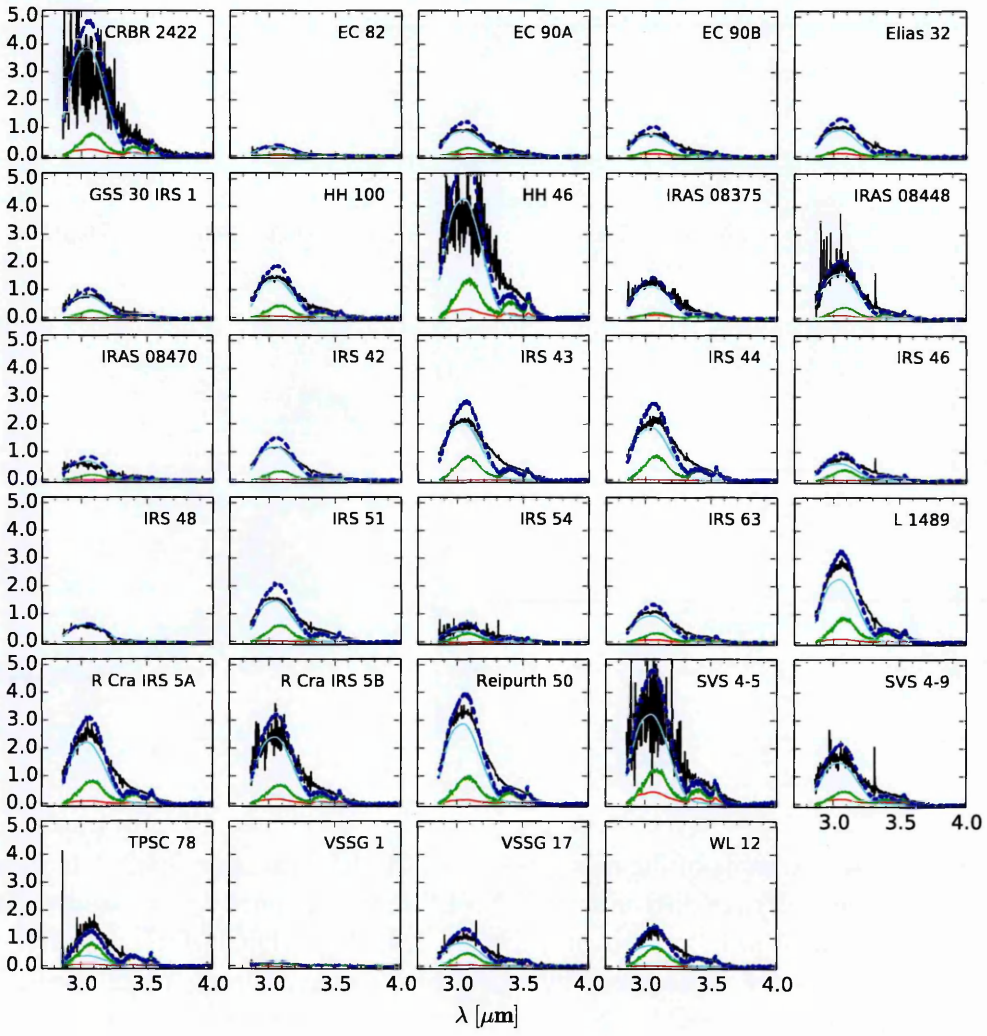

Figure 3.14: Fit results of Model 2 to the VLT data, presented as thumbnails. The CO:CH_3OH, pure CH_3OH, and pure H_2O data are represented by red, green, and cyan lines, respectively. The observed data and the overall fit are represented by a black and a dashed blue line.

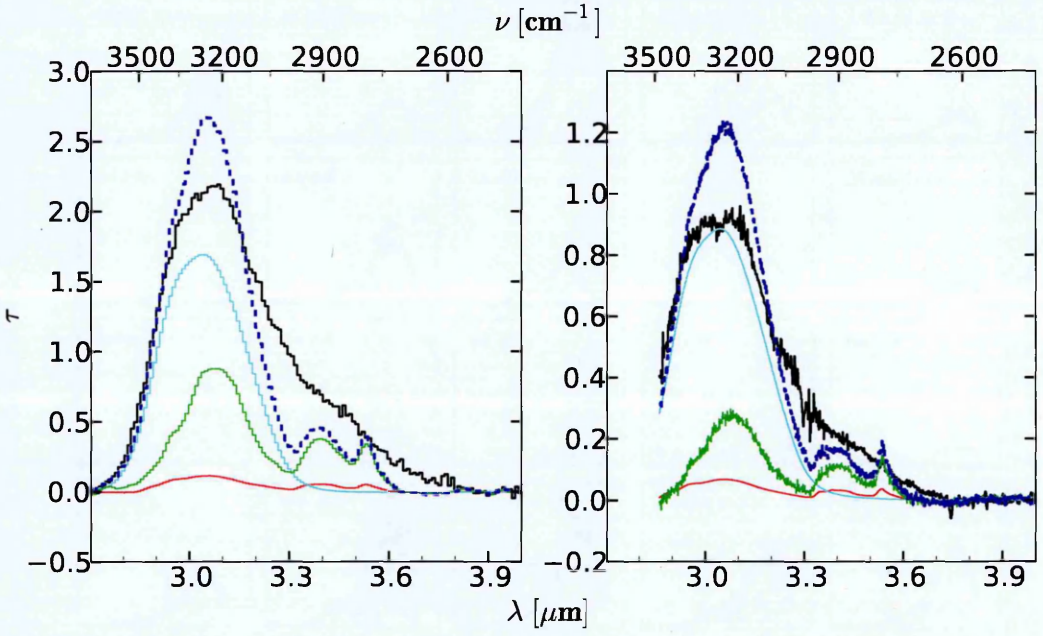

Figure 3.15: An example of the fitting results of Model 2 (Section 3.4.2.2) to a single source from the (left) AKARI and (right) VLT data examined in my study. These sources are identical to those shown in Figure 3.8. The CO:CH_3OH, pure CH_3OH, and pure H_2O data are represented by red, green, and cyan lines, respectively. The observed data and the overall fit are represented by a black and a dashed blue line.

Table 3.8: Derived total column densities for all the sources, when using Model 2

Source	$N(H_2O)$ $[10^{17}$ cm$^{-2}]$	$N(CO)$ $[10^{17}$ cm$^{-2}]$	$N(CH_3OH)$ $[10^{17}$ cm$^{-2}]$	Source	$N(H_2O)$ $[10^{17}$ cm$^{-2}]$	$N(CO)$ $[10^{17}$ cm$^{-2}]$	$N(CH_3OH)$ $[10^{17}$ cm$^{-2}]$
AKARI-02	25.98 ± 1.60	3.37 ± 0.29	5.11 ± 0.88	CRBR 2422	53.59 ± 1.33	20.98 ± 0.35	7.61 ± 0.63
AKARI-03	24.25 ± 0.78	3.19 ± 0.34	5.26 ± 0.52	EC 82	4.28 ± 0.07	1.61 ± 0.10	≤ 0.55
AKARI-04	31.85 ± 1.66	2.84 ± 0.60	2.11 ± 1.03	EC 90A	12.22 ± 0.14	12.82 ± 0.08	2.57 ± 0.09
AKARI-05	5.51 ± 1.84	≤ 2.00	≤ 2.73	EC 90B	10.38 ± 0.14	7.97 ± 0.12	2.46 ± 0.12
AKARI-07	12.02 ± 1.11	≤ 0.82	≤ 0.69	Elias 32	13.13 ± 0.13	12.58 ± 0.07	3.36 ± 0.08
AKARI-08	10.24 ± 1.94	≤ 0.73	≤ 1.15	GSS 30 IRS 1	10.81 ± 0.15	0.43 ± 0.20	1.61 ± 0.21
AKARI-10	6.56 ± 0.82	≤ 3.00	≤ 1.50	HH 100	18.97 ± 0.21	9.14 ± 0.07	3.70 ± 0.11
AKARI-11	11.58 ± 2.71	≤ 2.69	≤ 1.41	HH 46	59.19 ± 1.35	8.54 ± 0.08	12.49 ± 0.64
AKARI-12	9.19 ± 1.23	≤ 1.82	≤ 1.75	IRAS 08375	15.83 ± 0.27	13.84 ± 0.16	2.79 ± 0.17
AKARI-13	19.92 ± 0.91	3.56 ± 0.94	≤ 1.59	IRAS 08448	21.96 ± 0.58	2.93 ± 0.08	3.90 ± 0.29
AKARI-14	28.67 ± 1.80	6.01 ± 0.54	3.41 ± 1.05	IRAS 08470	9.31 ± 0.16	0.80 ± 0.15	1.14 ± 0.16
AKARI-16	6.07 ± 1.44	≤ 2.22	≤ 2.00	IRS 42	16.57 ± 0.15	3.58 ± 0.03	2.22 ± 0.08
AKARI-17	9.27 ± 1.23	2.81 ± 1.67	≤ 1.52	IRS 43	27.99 ± 0.34	11.11 ± 0.18	5.03 ± 0.22
AKARI-18	11.14 ± 2.67	≤ 2.77	≤ 4.36	IRS 44	26.16 ± 0.32	2.73 ± 0.08	5.65 ± 0.17
AKARI-19	5.73 ± 0.79	2.30 ± 0.43	≤ 1.27	IRS 46	8.53 ± 0.13	≤ 1.07	2.48 ± 0.14
AKARI-20	9.65 ± 1.08	1.36 ± 0.35	≤ 1.35	IRS 48	8.87 ± 0.08	0.70 ± 0.04	≤ 0.33
AKARI-22	11.02 ± 0.80	≤ 2.58	≤ 2.68	IRS 51	20.35 ± 0.29	34.78 ± 0.29	4.19 ± 0.23
AKARI-23	12.64 ± 0.48	2.28 ± 0.33	≤ 1.21	IRS 54	5.19 ± 0.20	≤ 1.86	1.80 ± 0.25
AKARI-25	12.07 ± 0.97	≤ 5.48	≤ 5.14	IRS 63	13.12 ± 0.12	11.54 ± 0.07	3.27 ± 0.08
AKARI-26	13.59 ± 0.94	3.61 ± 1.05	≤ 2.69	L 1489	31.46 ± 0.28	5.27 ± 0.06	7.03 ± 0.14
AKARI-27	12.34 ± 0.78	≤ 1.87	≤ 2.23	R Cra IRS 5A	30.60 ± 0.36	30.77 ± 0.40	6.57 ± 0.29
AKARI-28	19.70 ± 0.85	≤ 2.33	≤ 2.10	R Cra IRS 5B	33.15 ± 0.57	18.80 ± 0.35	6.58 ± 0.35
AKARI-29	14.80 ± 0.44	2.90 ± 0.43	2.28 ± 0.47	Reipurth 50	39.72 ± 0.34	5.47 ± 0.06	7.92 ± 0.17
				SVS 4-5	44.53 ± 1.37	15.63 ± 0.19	13.42 ± 0.63
				SVS 4-9	20.83 ± 0.34	19.73 ± 0.28	5.67 ± 0.26
				TPSC 78	5.13 ± 0.72	2.08 ± 0.11	6.14 ± 0.38
				VSSG 1	0.93 ± 0.08	≤ 0.41	0.61 ± 0.10
				VSSG 17	11.52 ± 0.18	9.21 ± 0.26	3.59 ± 0.22
				WL 12	10.33 ± 0.20	5.42 ± 0.11	4.44 ± 0.13

However, the sharp C-H stretching features of pure CH_3OH end up easily overfitting the red wing, and conspicuous "bumps" are left in the residual in parts where no contribution from C-H stretching is present. As is seen from the green circles of Figure 3.9, inclusion of pure CH_3OH to an ice model also causes an increase in the contribution of CH_3OH to the total ice column density in the trio of H_2O, CH_3OH and CO, in a few cases even causing it to become the dominant contributor. The ratio $N(CH_3OH)/N(H_2O)$ (Table 3.7) varies between a few and (in the few outlier cases) $\sim$20% according to this model.

3.4.2.3 Models 3 and 4

The fit results using Model 3 (using the 23% ratio CH_3OH:H_2O mixture) for each source are shown in Figures 3.16 and 3.17, for the AKARI and VLT data respectively. For Model 4 these are shown in Figures 3.18 and 3.19. A closer look at the fit results –and with multiple mixing ratios– to a single example source in both the AKARI and VLT data sets is presented in Figure 3.20.

Models 3 and 4 are highly degenerate with each other and in many cases end up returning identical results in the derived column densities, as the minimization will often completely eliminate the pure H_2O component in favour of the CH_3OH:H_2O component.

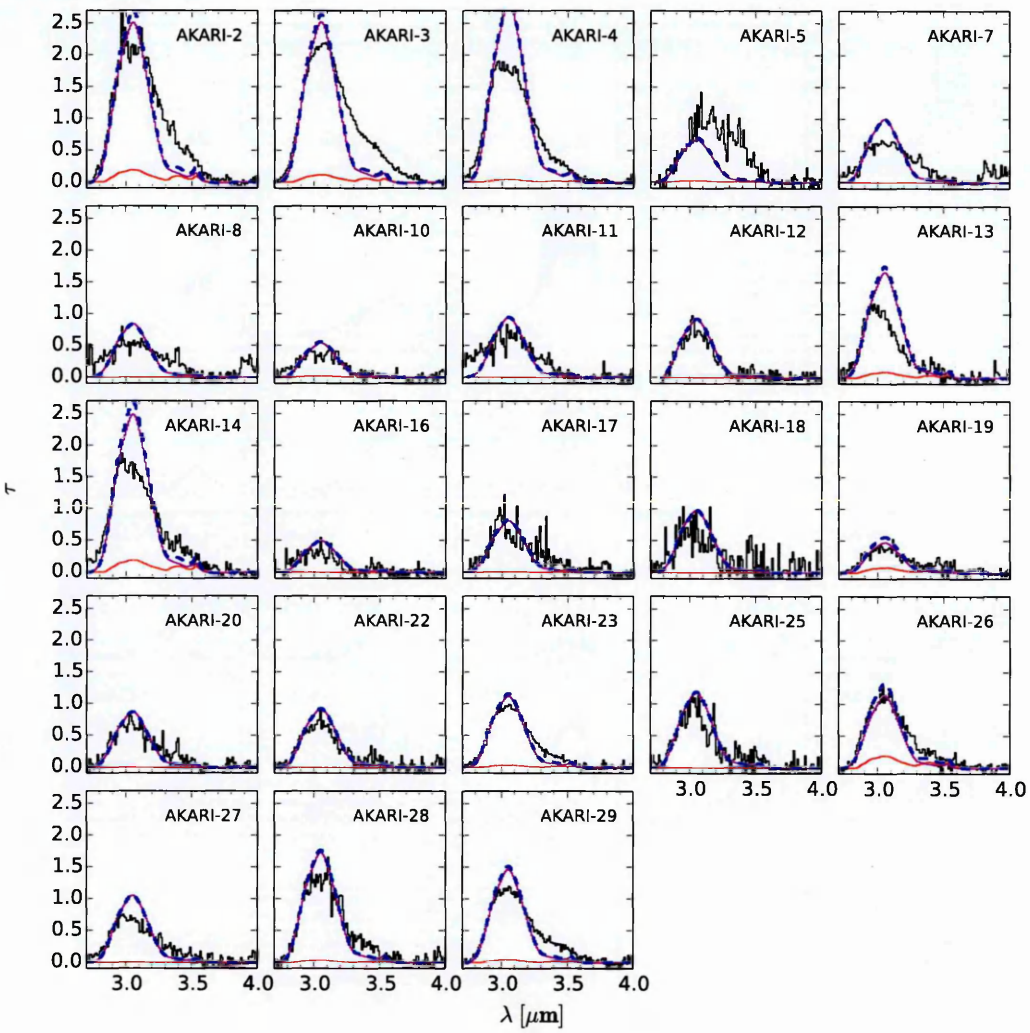

Figure 3.16: Fit results of Model 3 to the AKARI data, presented as thumbnails. The used mixing ratio for the CH_3OH:H_2O mixture is 23%. The CO:CH_3OH, CH_3OH:H_2O, and pure H_2O data are represented by red, magenta, and cyan lines, respectively. The observed data and the overall fit are represented by a black and a dashed blue line.

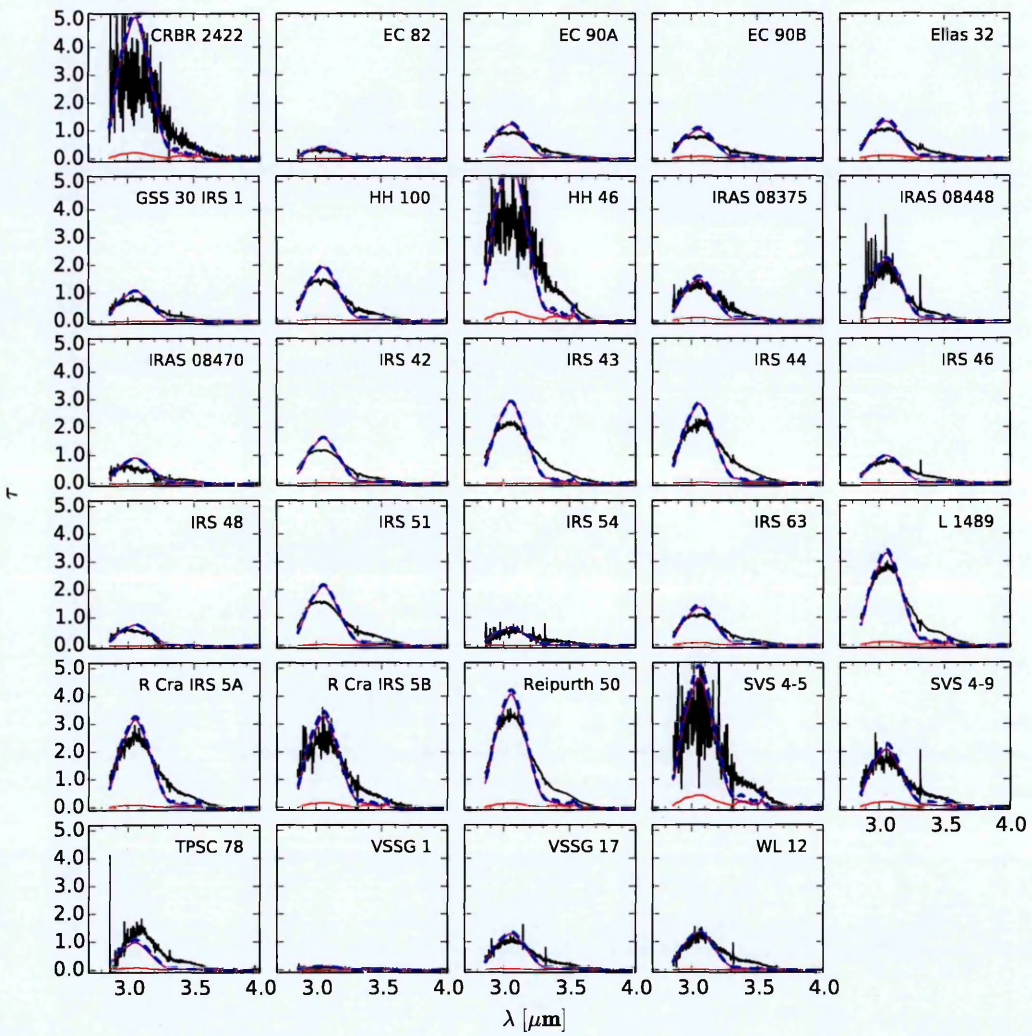

Figure 3.17: Fit results of Model 2 to the VLT data, presented as thumbnails. The used mixing ratio for the CH_3OH:H_2O mixture is 23%. The CO:CH_3OH, CH_3OH:H_2O, and pure H_2O data are represented by red, magenta, and cyan lines, respectively. The observed data and the overall fit are represented by a black and dashed blue line.

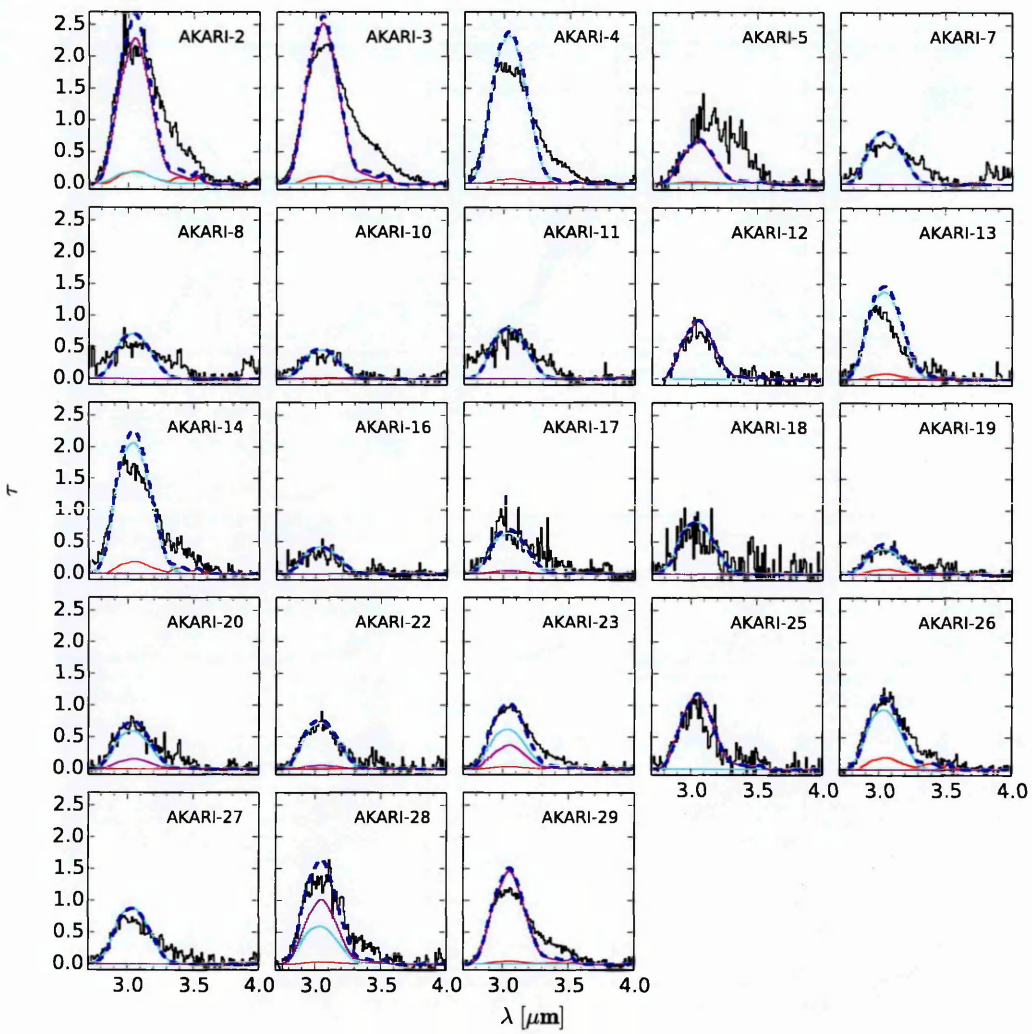

Figure 3.18: Fit results of Model 3 to the AKARI data, presented as thumbnails. The used mixing ratio for the CH_3OH:H_2O mixture is 23%. The CO:CH_3OH, CH_3OH:H_2O, and pure H_2O data are represented by red, magenta, and cyan lines, respectively. The observed data and the overall fit are represented by a black and a dashed blue line.

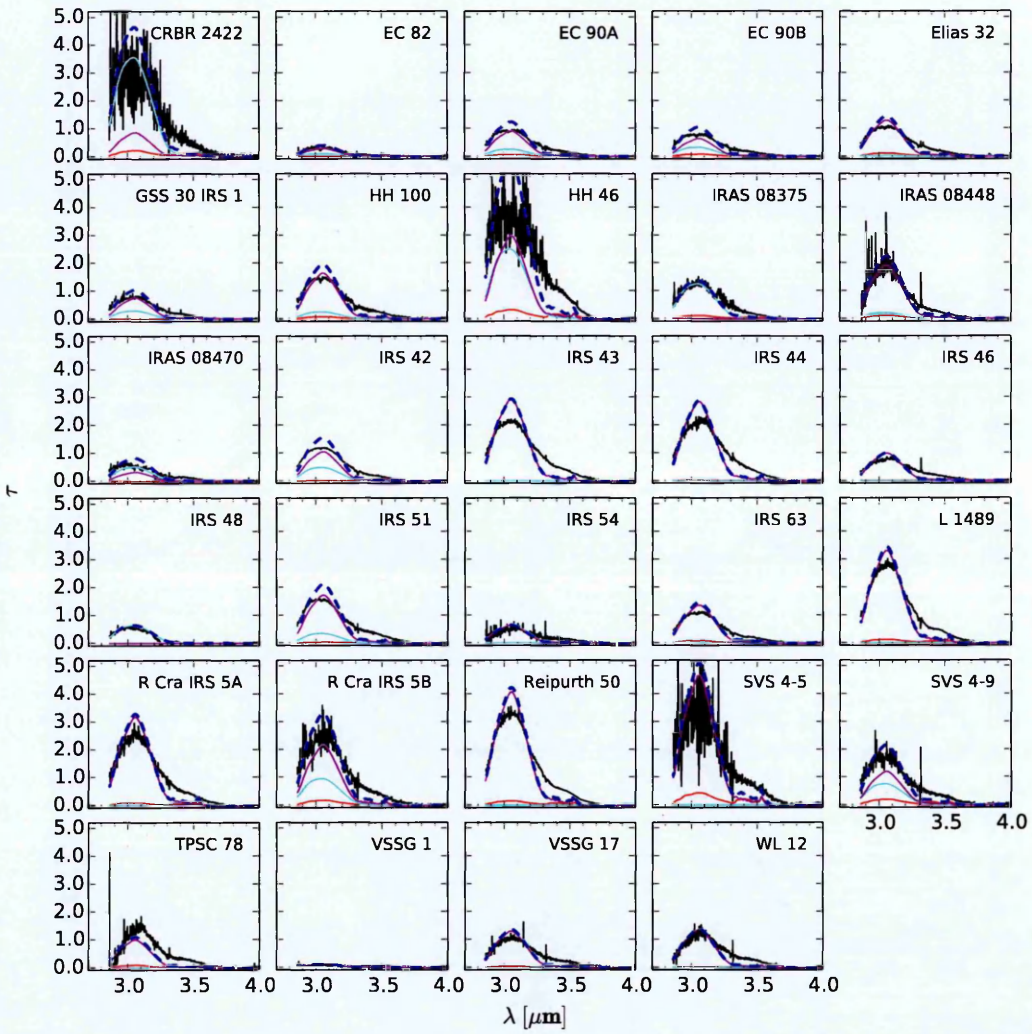

Figure 3.19: Fit results of Model 2 to the VLT data, presented as thumbnails. The used mixing ratio for the CH_3OH:H_2O mixture is 23%. The CO:CH_3OH, CH_3OH:H_2O, and pure H_2O data are represented by red, magenta, and cyan lines, respectively. The observed data and the overall fit are represented by a black and a dashed blue line.

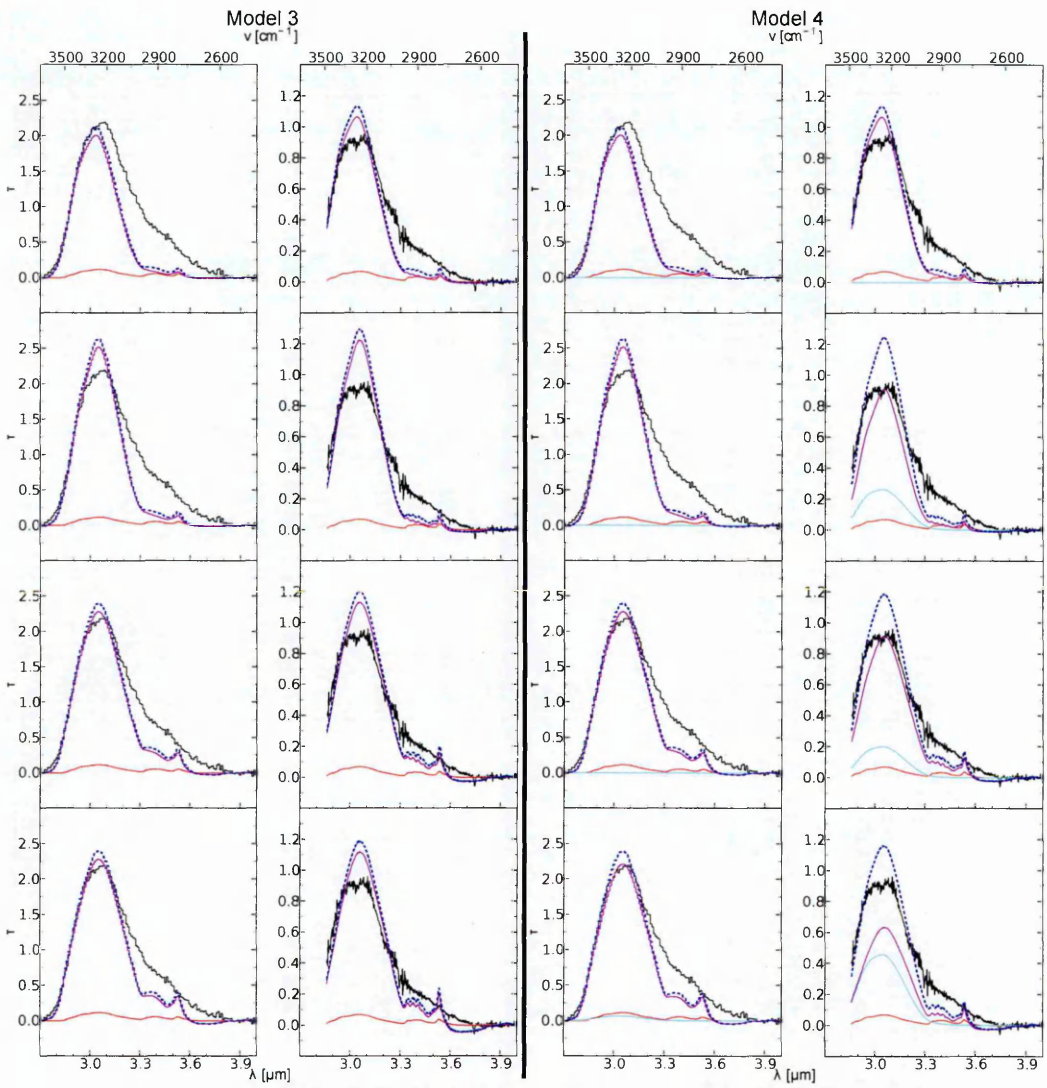

Figure 3.20: An example of the fitting results of Models 3 (left pair of columns) and 4 (right pair) to a single source from the (first and third column; AKARI-02) AKARI and (second and fourth column; EC 90A) VLT data examined in my study. These sources are the same as those shown in Figure 3.8. Each row represents a fit done using a different CH_3OH:H_2O mixing ratio. From top to bottom, the mixing ratios are 17%, 23%, 31%, and 50% respectively. The CO:CH_3OH, CH_3OH:H_2O, and pure H_2O data are represented by red, magenta, and cyan lines, respectively. The observed data and the overall fit are represented by a black and a dashed blue line.

Table 3.9: Derived total column densities for all the sources, when using Model 3. The mixing ratio used for the CH_3OH:H_2O mixture for the results presented here was 23%.

Source	N(H_2O) [10^{17} cm^{-2}]	N(CO) [10^{17} cm^{-2}]	N(CH_3OH) [10^{17} cm^{-2}]	Source	N(H_2O) [10^{17} cm^{-2}]	N(CO) [10^{17} cm^{-2}]	N(CH_3OH) [10^{17} cm^{-2}]
AKARI-02	15.01 ± 0.60	3.37 ± 0.29	6.13 ± 0.30	CRBR 2422	30.85 ± 0.66	20.98 ± 0.35	10.13 ± 0.27
AKARI-03	15.06 ± 0.46	3.19 ± 0.34	5.11 ± 0.34	EC 82	2.52 ± 0.04	1.61 ± 0.10	0.69 ± 0.09
AKARI-04	16.86 ± 0.63	2.46 ± 0.74	4.54 ± 0.74	EC 90A	7.44 ± 0.10	12.82 ± 0.08	2.64 ± 0.06
AKARI-05	4.03 ± 0.54	≤ 2.00	1.30 ± 1.44	EC 90B	6.27 ± 0.09	7.97 ± 0.12	2.57 ± 0.10
AKARI-07	5.97 ± 0.41	≤ 0.82	1.39 ± 0.41	Elias 32	8.12 ± 0.09	12.58 ± 0.07	3.39 ± 0.05
AKARI-08	5.03 ± 0.67	≤ 0.73	1.17 ± 0.74	GSS 30 IRS 1	6.72 ± 0.10	0.43 ± 0.20	1.57 ± 0.20
AKARI-10	3.24 ± 0.29	≤ 3.00	1.04 ± 1.30	HH 100	11.74 ± 0.15	9.14 ± 0.07	3.74 ± 0.06
AKARI-11	5.66 ± 0.92	≤ 2.69	1.32 ± 0.56	HH 46	36.24 ± 0.72	8.54 ± 0.08	12.71 ± 0.18
AKARI-12	5.62 ± 0.29	≤ 1.82	1.38 ± 0.58	IRAS 08375	9.02 ± 0.15	13.84 ± 0.16	3.68 ± 0.12
AKARI-13	9.93 ± 0.38	3.56 ± 0.94	3.58 ± 0.85	IRAS 08448	13.17 ± 0.27	2.93 ± 0.08	4.54 ± 0.10
AKARI-14	14.86 ± 0.68	6.01 ± 0.54	6.09 ± 0.52	IRAS 08470	5.61 ± 0.09	0.80 ± 0.15	1.31 ± 0.14
AKARI-16	2.99 ± 0.48	≤ 2.22	0.70 ± 4.73	IRS 42	9.91 ± 0.11	3.58 ± 0.03	2.59 ± 0.03
AKARI-17	4.87 ± 0.41	2.81 ± 1.67	1.35 ± 1.47	IRS 43	17.89 ± 0.26	11.11 ± 0.18	4.18 ± 0.16
AKARI-18	5.87 ± 0.90	≤ 2.77	1.37 ± 6.62	IRS 44	17.30 ± 0.26	2.73 ± 0.08	4.39 ± 0.09
AKARI-19	2.86 ± 0.27	2.30 ± 0.43	1.85 ± 0.41	IRS 46	6.01 ± 0.11	≤ 1.07	1.58 ± 0.13
AKARI-20	5.21 ± 0.37	1.36 ± 0.35	1.22 ± 0.35	IRS 48	4.59 ± 0.06	0.70 ± 0.04	1.18 ± 0.04
AKARI-22	5.54 ± 0.27	≤ 2.58	1.29 ± 0.86	IRS 51	12.99 ± 0.20	34.78 ± 0.29	3.67 ± 0.19
AKARI-23	6.72 ± 0.21	2.28 ± 0.33	2.08 ± 0.32	IRS 54	3.92 ± 0.11	≤ 1.86	0.92 ± 0.23
AKARI-25	7.14 ± 0.33	≤ 5.48	1.67 ± 2.19	IRS 63	8.26 ± 0.09	11.54 ± 0.07	3.21 ± 0.06
AKARI-26	6.78 ± 0.34	3.61 ± 1.05	4.24 ± 0.79	L 1489	20.14 ± 0.23	5.27 ± 0.06	6.41 ± 0.08
AKARI-27	6.31 ± 0.29	≤ 1.87	1.47 ± 0.60	R Cra IRS 5A	19.29 ± 0.26	30.77 ± 0.40	5.99 ± 0.24
AKARI-28	10.34 ± 0.29	≤ 2.33	2.93 ± 0.76	R Cra IRS 5B	19.97 ± 0.32	18.80 ± 0.35	7.06 ± 0.24
AKARI-29	8.77 ± 0.20	2.90 ± 0.43	2.70 ± 0.41	Reipurth 50	24.74 ± 0.27	5.47 ± 0.06	7.84 ± 0.08
				SVS 4-5	28.27 ± 0.69	15.63 ± 0.19	12.38 ± 0.22
				SVS 4-9	12.73 ± 0.20	19.73 ± 0.28	5.68 ± 0.20
				TPSC 78	6.07 ± 0.38	2.08 ± 0.11	2.73 ± 0.13
				VSSG 1	0.87 ± 0.04	≤ 0.41	0.20 ± 0.10
				VSSG 17	7.92 ± 0.13	9.21 ± 0.26	2.66 ± 0.20
				WL 12	8.22 ± 0.18	5.42 ± 0.11	2.28 ± 0.10

Table 3.10: Derived total column densities for all the sources, when using Model 4. The mixing ratio used for the CH_3OH:H_2O mixture for the results presented here was 23%.

Source	N(H_2O) [10^{17} cm^{-2}]	N(CO) [10^{17} cm^{-2}]	N(CH_3OH) [10^{17} cm^{-2}]	Source	N(H_2O) [10^{17} cm^{-2}]	N(CO) [10^{17} cm^{-2}]	N(CH_3OH) [10^{17} cm^{-2}]
AKARI-02	16.30 ± 17.46	3.37 ± 0.29	5.82 ± 1.96	CRBR 2422	54.32 ± 10.86	20.98 ± 0.35	4.16 ± 1.17
AKARI-03	15.06 ± 9.02	3.19 ± 0.34	5.11 ± 1.53	EC 82	3.24 ± 0.61	1.61 ± 0.10	0.50 ± 0.11
AKARI-04	33.60 ± 17.35	2.46 ± 0.74	0.64 ± 1.84	EC 90A	9.16 ± 1.63	12.82 ± 0.08	2.20 ± 0.19
AKARI-05	4.03 ± 14.66	≤ 2.00	1.30 ± 1.96	EC 90B	8.42 ± 1.49	7.97 ± 0.12	2.02 ± 0.19
AKARI-07	12.02 ± 10.38	≤ 0.82	≤ 0.10	Elias 32	8.37 ± 1.58	12.58 ± 0.07	3.33 ± 0.19
AKARI-08	10.24 ± 17.75	≤ 0.73	≤ 0.21	GSS 30 IRS 1	8.64 ± 1.66	0.43 ± 0.20	1.07 ± 0.27
AKARI-10	6.56 ± 7.67	≤ 3.00	0.28 ± 1.29	HH 100	13.37 ± 2.49	9.14 ± 0.07	3.32 ± 0.29
AKARI-11	11.58 ± 26.36	≤ 2.69	≤ 0.20	HH 46	52.68 ± 12.41	8.54 ± 0.08	8.46 ± 1.36
AKARI-12	5.62 ± 2.22	≤ 1.82	1.38 ± 0.78	IRAS 08375	17.18 ± 2.46	13.84 ± 0.16	1.57 ± 0.32
AKARI-13	19.92 ± 8.37	3.56 ± 0.94	1.26 ± 0.85	IRAS 08448	14.58 ± 4.65	2.93 ± 0.08	4.18 ± 0.54
AKARI-14	29.82 ± 19.33	6.01 ± 0.54	2.62 ± 2.30	IRAS 08470	8.92 ± 1.54	0.80 ± 0.15	0.46 ± 0.22
AKARI-16	6.07 ± 13.54	≤ 2.22	≤ 0.29	IRS 42	13.10 ± 1.81	3.58 ± 0.03	1.76 ± 0.20
AKARI-17	9.47 ± 13.25	2.81 ± 1.67	0.28 ± 1.98	IRS 43	17.89 ± 5.09	11.11 ± 0.18	4.18 ± 0.52
AKARI-18	11.82 ± 31.35	≤ 2.77	≤ 0.76	IRS 44	17.30 ± 5.04	2.73 ± 0.08	4.39 ± 0.50
AKARI-19	5.74 ± 7.28	2.30 ± 0.43	1.19 ± 0.43	IRS 46	6.01 ± 2.15	≤ 1.07	1.58 ± 0.24
AKARI-20	9.49 ± 11.25	1.36 ± 0.35	≤ 0.25	IRS 48	8.86 ± 0.66	0.70 ± 0.04	0.11 ± 0.09
AKARI-22	10.70 ± 7.95	≤ 2.58	≤ 0.39	IRS 51	15.27 ± 3.46	34.78 ± 0.29	3.08 ± 0.43
AKARI-23	11.21 ± 5.16	2.28 ± 0.33	1.04 ± 0.62	IRS 54	3.92 ± 2.33	≤ 1.86	0.92 ± 0.32
AKARI-25	7.14 ± 9.38	≤ 5.48	1.67 ± 2.42	IRS 63	8.26 ± 1.84	11.54 ± 0.07	3.21 ± 0.19
AKARI-26	13.59 ± 13.33	3.61 ± 1.05	2.65 ± 2.45	L 1489	20.14 ± 4.47	5.27 ± 0.06	6.41 ± 0.44
AKARI-27	12.62 ± 7.74	≤ 1.87	≤ 0.32	R Cra IRS 5A	19.29 ± 6.00	30.77 ± 0.40	5.99 ± 0.55
AKARI-28	14.57 ± 8.58	≤ 2.33	1.94 ± 1.18	R Cra IRS 5B	26.26 ± 5.32	18.80 ± 0.35	5.46 ± 0.63
AKARI-29	8.77 ± 5.80	2.90 ± 0.43	2.70 ± 0.76	Reipurth 50	24.74 ± 5.29	5.47 ± 0.06	7.84 ± 0.53
				SVS 4-5	28.27 ± 13.11	15.63 ± 0.19	12.38 ± 1.29
				SVS 4-9	17.69 ± 3.46	19.73 ± 0.28	4.41 ± 0.43
				TPSC 78	6.07 ± 3.25	2.08 ± 0.11	2.73 ± 0.74
				VSSG 1	0.87 ± 0.91	≤ 0.41	0.20 ± 0.13
				VSSG 17	7.92 ± 2.60	9.21 ± 0.26	2.66 ± 0.32
				WL 12	8.22 ± 3.58	5.42 ± 0.11	2.28 ± 0.36

The column densities of the ices derived in this way, represented by the (often overlapping) blue and yellow circles in Figure 3.9, produce abundance ratios where the contribution of CH_3OH to the total ice abundance is usually dominated by the used mixing ratio of the CH_3OH:H_2O. As can be seen in Table 3.12, Model 3 specifically causes a hard lower limit to be placed on the ratio $N(CH_3OH)/N(H_2O)$ at the used mixing ratio. Inclusion of a pure water spectrum in Model 4 allows column density ratios to once again drop below the mixing ratio.

Table 3.11: The amount of CH_3OH in H_2O, as determined using Models 3 and 4, in all the sources considered in this study. The mixing ratio used for the CH_3OH:H_2O mixture for the results presented here was 23%.

Source	N(CH_3OH in H_2O) Model 3, [10^{17} cm^{-2}]	N(CH_3OH in H_2O) Model 4, [10^{17} cm^{-2}]	Source	N(CH_3OH in H_2O) Model 3, [10^{17} cm^{-2}]	N(CH_3OH in H_2O) Model 4, [10^{17} cm^{-2}]
AKARI-02	3.50 ± 0.14	3.20 ± 1.94	CRBR 2422	7.20 ± 0.15	1.23 ± 1.15
AKARI-03	3.52 ± 0.11	3.52 ± 1.50	EC 82	0.59 ± 0.01	0.40 ± 0.07
AKARI-04	3.94 ± 0.15	≤ 0.13	EC 90A	1.74 ± 0.02	1.29 ± 0.18
AKARI-05	0.94 ± 0.13	0.94 ± 1.33	EC 90B	1.46 ± 0.02	0.91 ± 0.17
AKARI-07	1.39 ± 0.10	≤ 0.10	Elias 32	1.90 ± 0.02	1.83 ± 0.18
AKARI-08	1.17 ± 0.16	≤ 0.21	GSS 30 IRS 1	1.57 ± 0.02	1.07 ± 0.19
AKARI-10	0.76 ± 0.07	≤ 0.22	HH 100	2.74 ± 0.03	2.32 ± 0.28
AKARI-11	1.32 ± 0.22	≤ 0.20	HH 46	8.46 ± 0.17	4.22 ± 1.36
AKARI-12	1.31 ± 0.07	1.31 ± 0.52	IRAS 08375	2.11 ± 0.03	≤ 0.05
AKARI-13	2.32 ± 0.09	≤ 0.23	IRAS 08448	3.08 ± 0.06	2.71 ± 0.53
AKARI-14	3.47 ± 0.16	≤ 0.27	IRAS 08470	1.31 ± 0.02	0.46 ± 0.17
AKARI-16	0.70 ± 0.11	≤ 0.29	IRS 42	2.31 ± 0.02	1.49 ± 0.20
AKARI-17	1.14 ± 0.10	≤ 0.22	IRS 43	4.18 ± 0.06	4.18 ± 0.50
AKARI-18	1.37 ± 0.21	≤ 0.76	IRS 44	4.04 ± 0.06	4.04 ± 0.50
AKARI-19	0.67 ± 0.06	≤ 0.18	IRS 46	1.40 ± 0.03	1.40 ± 0.21
AKARI-20	1.22 ± 0.09	≤ 0.25	IRS 48	1.07 ± 0.01	≤ 0.04
AKARI-22	1.29 ± 0.06	≤ 0.39	IRS 51	3.03 ± 0.05	2.44 ± 0.39
AKARI-23	1.57 ± 0.05	0.53 ± 0.53	IRS 54	0.91 ± 0.03	0.91 ± 0.22
AKARI-25	1.67 ± 0.08	1.67 ± 1.04	IRS 63	1.93 ± 0.02	1.93 ± 0.18
AKARI-26	1.58 ± 0.08	≤ 0.39	L 1489	4.70 ± 0.05	4.70 ± 0.44
AKARI-27	1.47 ± 0.07	≤ 0.32	R Cra IRS 5A	4.51 ± 0.06	4.51 ± 0.49
AKARI-28	2.41 ± 0.07	1.42 ± 0.91	R Cra IRS 5B	4.66 ± 0.07	3.06 ± 0.59
AKARI-29	2.05 ± 0.05	2.05 ± 0.64	Reipurth 50	5.78 ± 0.06	5.78 ± 0.52
			SVS 4-5	6.60 ± 0.16	6.60 ± 1.28
			SVS 4-9	2.97 ± 0.05	1.70 ± 0.38
			TPSC 78	1.42 ± 0.09	1.42 ± 0.74
			VSSG 1	0.20 ± 0.01	0.20 ± 0.08
			VSSG 17	1.85 ± 0.03	1.85 ± 0.25
			WL 12	1.92 ± 0.04	1.92 ± 0.35

Table 3.12: $N(CH_3OH)/N(H_2O)$, as determined by Models 3 and 4, in all the sources considered in this study. The mixing ratio used for the CH_3OH:H_2O mixture for the results presented here was 23%.

Source	$\frac{N(CH_3OH)}{N(H_2O)}$ Model 3, [%]	$\frac{N(CH_3OH)}{N(H_2O)}$ Model 4, [%]	Source	$\frac{N(CH_3OH)}{N(H_2O)}$ Model 3, [%]	$\frac{N(CH_3OH)}{N(H_2O)}$ Model 4, [%]
AKARI-02	40.83 ± 2.57	35.68 ± 40.06	CRBR 2422	32.85 ± 1.13	7.66 ± 2.65
AKARI-03	33.93 ± 2.49	33.93 ± 22.74	EC 82	27.17 ± 3.51	15.39 ± 4.46
AKARI-04	26.91 ± 4.50	1.91 ± 5.56	EC 90A	35.53 ± 0.96	23.98 ± 4.75
AKARI-05	32.33 ± 36.11	32.33 ± 127.43	EC 90B	41.00 ± 1.63	23.96 ± 4.81
AKARI-07	23.35 ± 6.98	–	Elias 32	41.79 ± 0.83	39.80 ± 7.84
AKARI-08	23.35 ± 15.12	–	GSS 30 IRS 1	23.35 ± 3.00	12.41 ± 3.95
AKARI-10	32.12 ± 40.09	4.33 ± 20.36	HH 100	31.85 ± 0.67	24.79 ± 5.08
AKARI-11	23.35 ± 10.53	–	HH 46	35.06 ± 0.85	16.07 ± 4.58
AKARI-12	24.50 ± 10.45	24.50 ± 16.85	IRAS 08375	40.77 ± 1.51	9.14 ± 2.29
AKARI-13	36.09 ± 8.70	6.35 ± 5.04	IRAS 08448	34.48 ± 1.03	28.67 ± 9.85
AKARI-14	40.95 ± 3.96	8.77 ± 9.58	IRAS 08470	23.35 ± 2.61	5.16 ± 2.62
AKARI-16	23.35 ± 158.66	–	IRS 42	26.11 ± 0.44	13.46 ± 2.41
AKARI-17	27.61 ± 30.33	2.97 ± 21.33	IRS 43	23.35 ± 0.98	23.35 ± 7.26
AKARI-18	23.35 ± 112.81	–	IRS 44	25.39 ± 0.64	25.39 ± 7.95
AKARI-19	64.76 ± 15.47	20.65 ± 27.22	IRS 46	26.37 ± 2.14	26.37 ± 10.25
AKARI-20	23.35 ± 6.83	–	IRS 48	25.78 ± 0.88	1.26 ± 1.01
AKARI-22	23.35 ± 15.53	–	IRS 51	28.23 ± 1.50	20.15 ± 5.37
AKARI-23	31.00 ± 4.80	9.28 ± 6.98	IRS 54	23.36 ± 5.94	23.36 ± 16.08
AKARI-25	23.35 ± 30.72	23.35 ± 45.80	IRS 63	38.84 ± 0.80	38.84 ± 8.92
AKARI-26	62.47 ± 11.99	19.51 ± 26.28	L 1489	31.82 ± 0.52	31.82 ± 7.40
AKARI-27	23.35 ± 9.65	–	R Cra IRS 5A	31.03 ± 1.32	31.03 ± 10.06
AKARI-28	28.33 ± 7.36	13.29 ± 11.27	R Cra IRS 5B	35.35 ± 1.32	20.78 ± 4.84
AKARI-29	30.81 ± 4.78	30.81 ± 22.12	Reipurth 50	31.71 ± 0.48	31.71 ± 7.10
			SVS 4-5	43.77 ± 1.31	43.77 ± 20.80
			SVS 4-9	44.63 ± 1.75	24.94 ± 5.45
			TPSC 78	44.96 ± 3.57	44.95 ± 26.99
			VSSG 1	23.41 ± 10.95	23.41 ± 28.36
			VSSG 17	33.60 ± 2.60	33.60 ± 11.77
			WL 12	27.67 ± 1.36	27.67 ± 12.83

3.4.2.4 On the red wing

Throughout all tested models, the red wing of the OH stretch between $\sim$ 2600 and $\sim$ 3200 cm^{-1} leaves a prominent residual to the fitting results. This residual is suggested to possibly arise from light scattering effects by the ice layer (e.g. Noble et al., 2013). Another hint at a possible origin arises from energetic processing effects "smoothing out" the C-H stretching features in ice mixtures containing CH_3OH, which produces (M.E. Palumbo, private communication) a red wing feature reminiscent of what I observe in my spectra. Producing a physical explanation for the red wing is beyond the scope of this study, as such an endeavour would be worthy of its own study focused on the matter, but it is still of interest to discuss the non-physical methods which can be used to fit the red wing and how including such methods to the models described above would affect the results.

The fitting model presented in Brooke, Sellgren, and Geballe (1999) is one such method, and it was tested on the data set in this study. This method deals with the red wing of the O-H stretch by fitting to it a 3^{rd} order polynomial. The residual of the fit can then be examined for any residual features. This method also often considers the fitting of H_2O to the O-H stretching mode as a separate case from CH_3OH. This was tested by fitting the pure CH_3OH spectrum from Model 2 to the red wing residual left after performing a polynomial fit in the manner described in the "Brooke method".

Compared to the earlier methods, this method was highly sensitive to the choice of fitting range for the flux continuum baseline, with the residual most often being dominated by noise. In cases where the bump described in Brooke, Sellgren, and Geballe, 1999 rises above noise levels and a fit is achieved, considering the contribution of H_2O as a separately fitted case will easily cause the O-H stretching mode features to overfit, as CH_3OH also contributes to it. This effect is shown in Figure 3.21. The overfitting can be prevented by fitting H_2O data to the residual left over from subtracting the CH_3OH fit results from the O-H stretch.

When checking how the CO:CH_3OH data –after being fitted to the C-O stretch–

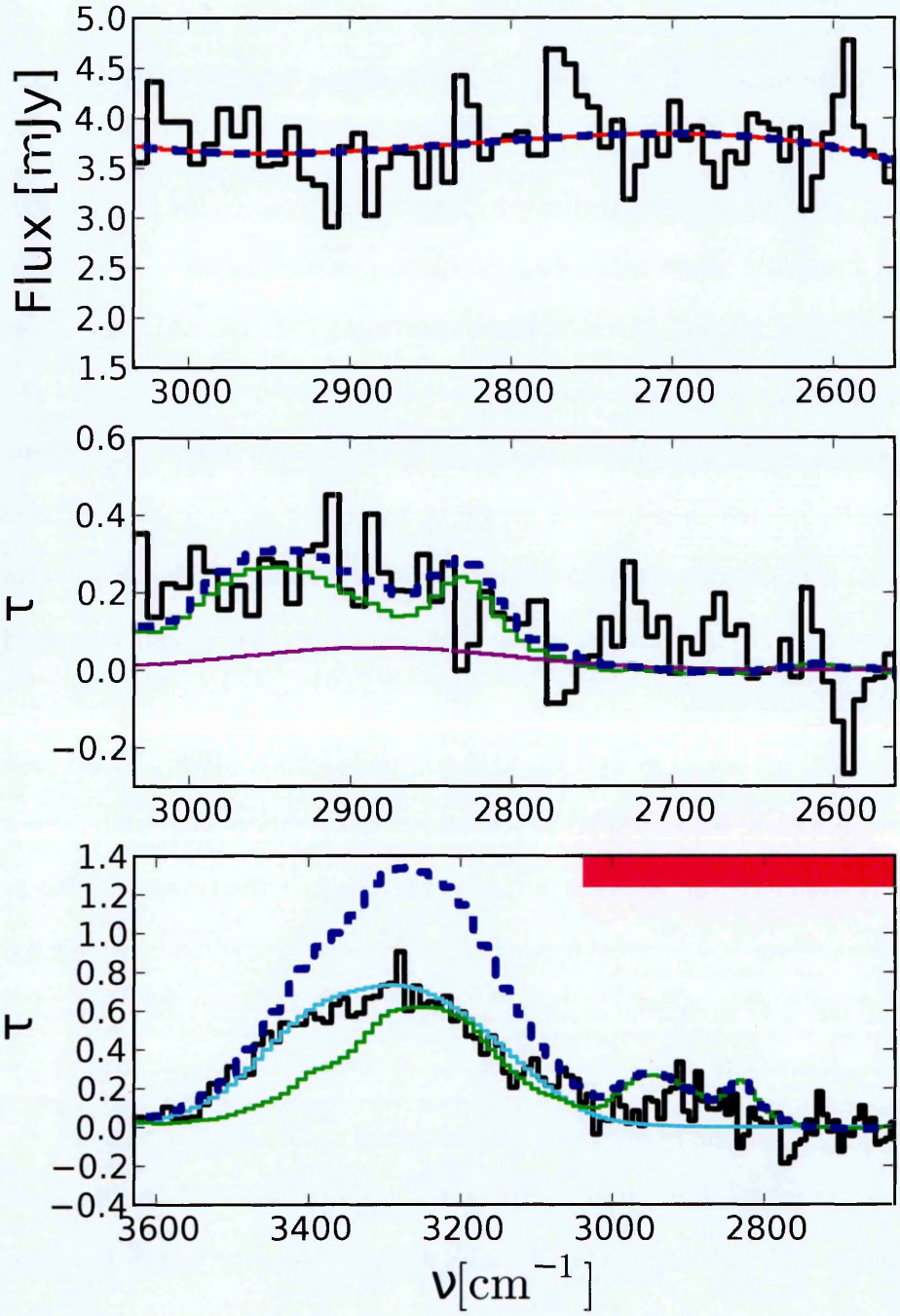

Figure 3.21: The result of attempting to apply the fitting method from Brooke, Sellgren, and Geballe (1999) to the AKARI data. The featured source is AKARI-21. The top plot shows a 3rd order polynomial fit (red-blue line) to the observed flux (black line) in the vicinity of the C-H stretches. The middle plot shows a fit of pure CH_3OH (green; from Method 2) and a gaussian (magenta) to the optical depth (black) derived from the continuum fit. The dashed blue line is the sum of the two. The bottom plot shows what the fitted CH_3OH looks like in the O-H stretching band, with a separately done pure H_2O (cyan; from Method 1) and the sum (dashed blue) of the separate H_2O and CH_3OH also shown. The red rectangle in the bottom plot shows the approximate frequency range plotted in the top and middle plots.

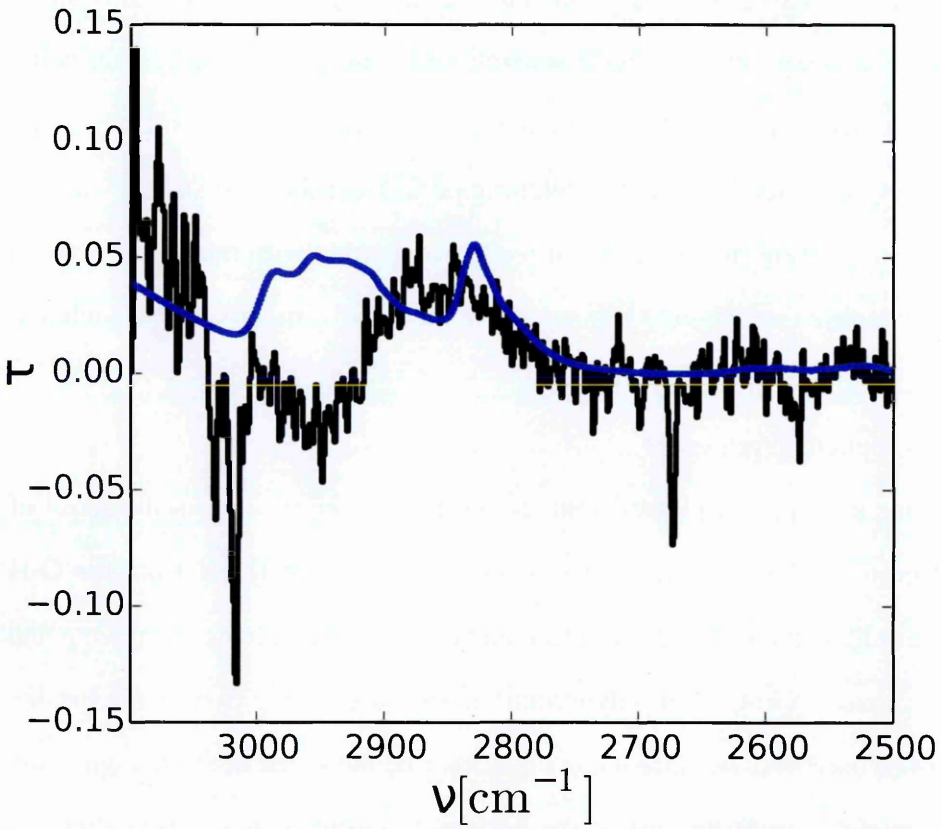

Figure 3.22: As the middle plot of Figure 3.21, but for the source IRS 63, and with only a CO:CH_3OH component overlaid on the spectrum, after having it separately fit to the C-O stretch of the same source. The strong dip in optical depth at $\sim 2900-3000\,\mathrm{cm}^{-1}$ is caused by gas-phase emission.

compares with the residual bumps of this method, I find that in several cases the peak optical depth of the C-H stretching features from CO:CH_3OH roughly match the peak optical depth of the residual. An example of this happening is shown in Figure 3.22. Using a different CO:CH_3OH mixing ratio would stop the serendipitously aligned features from happening.

The main issue in the applicability of the "Brooke method" is that it completely ignores the contribution from the O-H stretch to the red wing features, and thus fitting the O-H stretch (with e.g. water) after a separate red wing fit necessarily causes the O-H stretch to be overestimated. While the methods in this chapter consider both the red wing features (specifically the C-H stretching peaks) and the O-H stretch simultaneously, the Brooke fitting method is not directly compatible with the other methods of this chapter because the red wing subtraction in the Brooke method is conducted in frequency vs. flux space, while the other methods of this chapter operate exclusively in frequency vs. optical depth space.

However, one can apply a method mimicking the Brooke method in the sense of using a function to fit the red wing, but instead of doing it separately from the O-H stretch fits and in flux space, it is done simultaneously with the other components and in optical depth space. A low-order polynomial such as the one employed in the Brooke method cannot be used here because it can only describe the shape of the red wing and cannot in any useful way fit the rest of the 3-micron feature shapes. Truncating the polynomial to be non-zero only at e.g. the range between 2600 and 3100 cm^{-1} would not work either, as the discontinuity caused by this would produce strong artefacts in the total fit when the polynomial is summed together with the other fitted components.

Instead of truncating, one can try tapering the polynomial with the help of a window function which approaches zero towards the edges of where the polynomial is no longer expected to apply. Such a windowed function is used in the field of chromatography, where an "exponential-Gaussian hybrid function" (EGH; Lan and Jorgenson, 2001) has been used to describe the shape of asymmetric chromatographic peaks. As the name implies, this function has some properties of both an exponential and a Gaus-

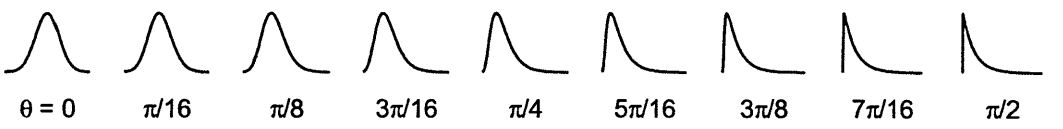

Figure 3.23: The effect of the asymmetry parameter θ to the shape of the exponential-Gaussian hybrid function. Figure reproduced from Lan and Jorgenson (2001).

sian function, and can transition in shape smoothly from one to the other with the application of control parameters. Though the application of the EGH in chromatography is irrelevant for the purposes of this chapter, the function itself can be adapted to fit most of the red wing features in this study remarkably well. Adapted to my purposes, the function can be expressed in optical depth as a function of reciprocal wave numbers (in cm^{-1}) with

$$\tau(\nu) = \begin{cases} H \times \exp\left(\frac{-(\nu_R-\nu)^2}{2\sigma^2\times\phi(\nu_R-\nu)}\right) & 2\sigma^2+\phi(\nu_R-\nu) > 0 \\ 0 & 2\sigma^2+\phi(\nu_R-\nu) \leq 0, \end{cases} \tag{3.5}$$

where H is the peak height of the function, σ describes the width of the Gaussian component, ϕ describes the steepness of the exponential component, and ν_R describes the frequency where the unmodified Gaussian peak would be placed. The function is constructed in such a way that its shape approaches a pure Gaussian form when $\phi \to 0$, or that it approaches the shape of a truncated exponential when $\sigma \to 0$. This asymmetry can be represented as a function of the ratio of the two, as described by

$$\theta = \arctan\left(\frac{|\phi|}{\sigma}\right). \tag{3.6}$$

Described in this way θ can take values between 0 and $\pi/2$, and will describe the level of asymmetry as illustrated by Figure 3.23.

Fits done with the EGH to the red wing reveal that it often takes on a Gaussian shape, which suggests that a simple Gaussian fit to the red wing may be just as effective as the EGH. Additionally the Gaussian would only have three fitting parameters (peak, centroid position and width) as opposed to the four of the EGH. Because of this a

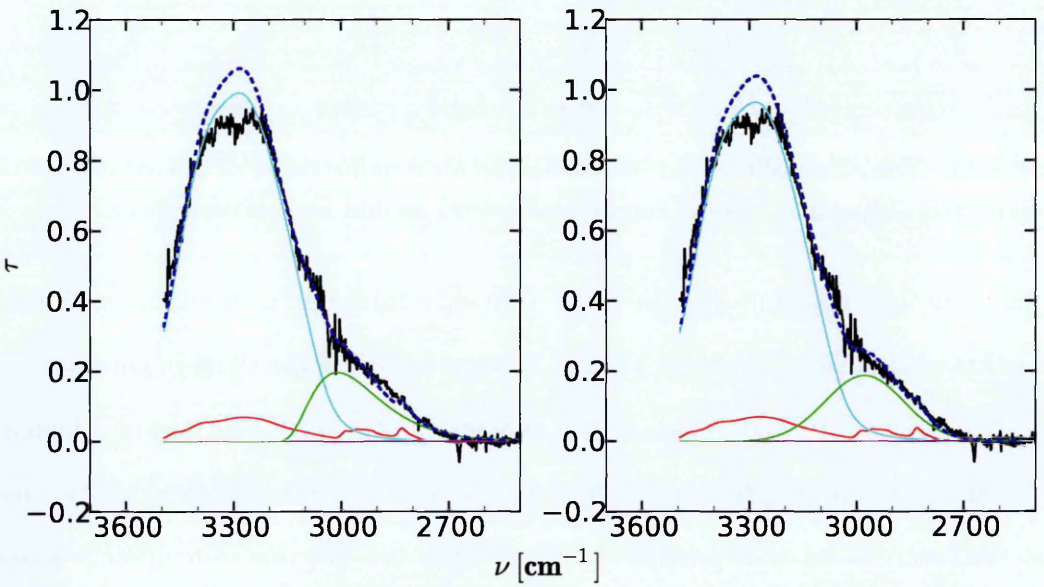

Figure 3.24: One of the VLT sources (EC 90A) fitted with a modified Model 4, with an added exponential-Gaussian hybrid (left) or gaussian (right) function to cover the red wing. The CO:CH_3OH, CH_3OH:H_2O, and pure H_2O data are represented by red, magenta, and cyan lines, respectively. The observed data and the total fit are represented by a black and dashed blue lines. The red wing function is represented by the green line.

Gaussian fit was also tested. An example result of both the EGH and Gaussian fits to a single VLT source is presented in Figure 3.24. In most cases the EGH takes on effectively a Gaussian shape, causing both fit methods to produce identical results.

Regardless of the red wing function used, its addition effectively suppresses any C-H stretch- containing components (such as any CH_3OH mixture) in the 3 micron band. For this reason in almost all cases utilizing a red wing model the only contributor of CH_3OH to the total ice column density is the CO:CH_3OH ice, which is fitted separately in the C-O stretch peak. The contribution of this to the C-H stretches in the red wing is negligible enough that the red wing model is largely unaffected by it.

3.5 Discussion

The results of my fitting methods can be discussed in the context of how well the models fit the observed data, and how they compare to the fitting methods used by previous studies. In addition to fit quality, the column densities derived from the models can

also be compared with previous studies, both through direct comparison of absolute column densities and column density ratios, and through discussion of the results in the context of existing knowledge of ice formation and processing.

3.5.1 Fit quality

The observations of the C-O stretch in cases with noticeable CO absorption benefit from the inclusion of CO:CH_3OH as the red component, corroborating the hypothesis of Cuppen et al. (2011). In the 3-micron region one can easily "hide" the extra absorption of the mixture under both the O-H stretch and its red wing with the C-H stretches, at the expense of replacing some of the H_2O absorption with that of the CH_3OH component of the CO:CH_3OH mixture.

Because no known physical model can be used to reproduce the red wing shape of the 3-micron features, any fits done by using it as a constraint are necessarily to be considered upper limits at best. The only reliable constraint to fits done in the 3-micron region is the blue wing of the O-H stretch, which is mostly unaffected by features in the red wing. The extent to which the blue wing is affected by the red wing arises from preventing the C-H stretches of the CH_3OH containing components from overshooting the observed red wing absorption. In the high-resolution VLT data this causes a noticeable effect in the calculated χ^2 of the blue wing fit in Model 3, because the constraint of the red wing prevents the blue wing slopes of the laboratory data and observations from aligning optimally, and because the blue wing shape of the CH_3OH:H_2O mixture data is slightly modified by the mixing ratio. This effect becomes more pronounced at higher mixing ratios of CH_3OH:H_2O, with the calculated χ^2 value increasing from $\sim$ 1800 with the lowest mixing ratio to $\sim$ 5300 with the highest mixing ratio. The effect does not persist in Model 4, because of the additional blue wing "compensation" provided by the pure H_2O spectrum.

In the context of ice composition in the ISM, these two observations about the blue wing suggest that if CH_3OH exists in a mixed ice environment with H_2O in the ISM,

its mixing ratio is likely small ($\lesssim 20\%$), or that there also exists a significant separate quantity of pure H_2O ice in addition to the CH_3OH:H_2O ice mixture.

3.5.2 Comparison with previous studies

The ratio $N(CH_3OH)/N(H_2O)$ in ices is often considered to range between a few % to $\sim$30% (e.g. Dartois et al., 1999; Gibb et al., 2004; Öberg et al., 2011a; Pontoppidan, van Dishoeck, and Dartois, 2004; Pontoppidan et al., 2003a). Considering CH_3OH to exist only in a CH_3OH:CO mixture (Model 1) or additionally in a pure form (Model 2) places the derived ratios in the lower end of the cited range, with the ratio rarely going above 20%. Allowing CH_3OH to also exist in a mixed environment with H_2O (Model 3) causes $N(CH_3OH)/N(H_2O)$ to never drop below the used mixing ratio and (e.g. in the case of using the mixing ratio of 23%) often go above 40%. If one also allows H_2O ice to exist in pure form in addition to its mixed form (Model 4), the ratios (in comparison to Model 3) fall to a range which varies between a few to $\sim$40%, rarely dropping below 10%. The variation in the ratio derived in this way is heavily dependant on the mixing ratio used for the fitted CH_3OH:H_2O mixture. Both Models 3 and 4 cause a detectable quantity of CH_3OH to be observable towards almost all lines of sight considered in this study.

The "Brooke method" (Brooke, Sellgren, and Geballe, 1999; Grim et al., 1991) of estimating CH_3OH ice abundances from the red wing of the 3-micron feature does not directly contradict with the models, if it is applied simultaneously with a fit of appropriate laboratory or analytical spectra to the O-H stretching mode absorption feature. Failure to do so in favour of e.g. considering the O-H stretch as a separate case will easily cause observed O-H stretching mode absorption to be over-fitted. The baseline fits done following the method of Brooke et al. often leaves a residual "bump" in the red wing. The peak optical depth of this bump serendipitously corresponds in many cases to the peak intensity of the C-H stretch components of a 1:1 mixing ratio CO:CH_3OH spectrum, after it is separately fitted as the red component in the C-O

stretching feature.

The derived values of the column density of CO ice attributable to the red component of the C-O stretch were compared to the values found in Noble et al. (2013) and Pontoppidan et al. (2003a) for the AKARI and VLT sources, respectively. The values derived here are systematically about a factor of 2-4 lower than the values derived in either study. This can be attributed to the different type of red component model being used in this study compared to that of Noble and Pontoppidan. The optical depth of the fitted red component feature itself is more or less the same for both the methods used here and the methods used in both Noble and Pontoppidan (compare Figure 3.8 in this chapter to Figures 8 and 3 of Noble et al. 2013 and Pontoppidan et al. 2003a, respectively). Of the other studies which simultaneously derived column densities of solid H_2O, CH_3OH, and CO only Pontoppidan, van Dishoeck, and Dartois 2004 (and references therein) had done so of two sources I also examined: SVS 4-5 and SVS 4-9. The column densities derived by Pontoppidan towards SVS 4-5 were 5.5×10^{18}, 2.7×10^{18}, and 1.9×10^{18} cm^{-2} for H_2O, CO, and CH_3OH respectively. For SVS 4-9 they were 2.5×10^{18}, 2.5×10^{18}, and 0.64×10^{18} cm^{-2}. Comparing these to my results of the same sources, I find that models 2, 3, and 4 produce reasonable matches regarding total N(H_2O), N(CO), and N(CH_3OH); model 1 heavily underestimates N(CH_3OH). Models 2, 3 and 4 all produce lower values of varying degrees (up to 50%) for both N(H_2O) and N(CH_3OH) than Pontoppidan.

The summed total column density of all considered molecules (H_2O, CH_3OH, and CO) is up to ~50% lower in my models than the results of Pontoppidan. I attribute the difference to the different methods used for calculating column densities. When using a ternary diagram (Figure 3.25) to compare the distribution between the three molecules, the closest match to the results of Pontoppidan towards SVS 4-5 is produced by model 3 and 4 (which are identical for this source), and model 2 (although model 4 is not far off) towards SVS 4-9.

The AKARI sources have been previously analysed by Noble et al. (2013), in which column densities for both H_2O and CO were derived, but the contribution of

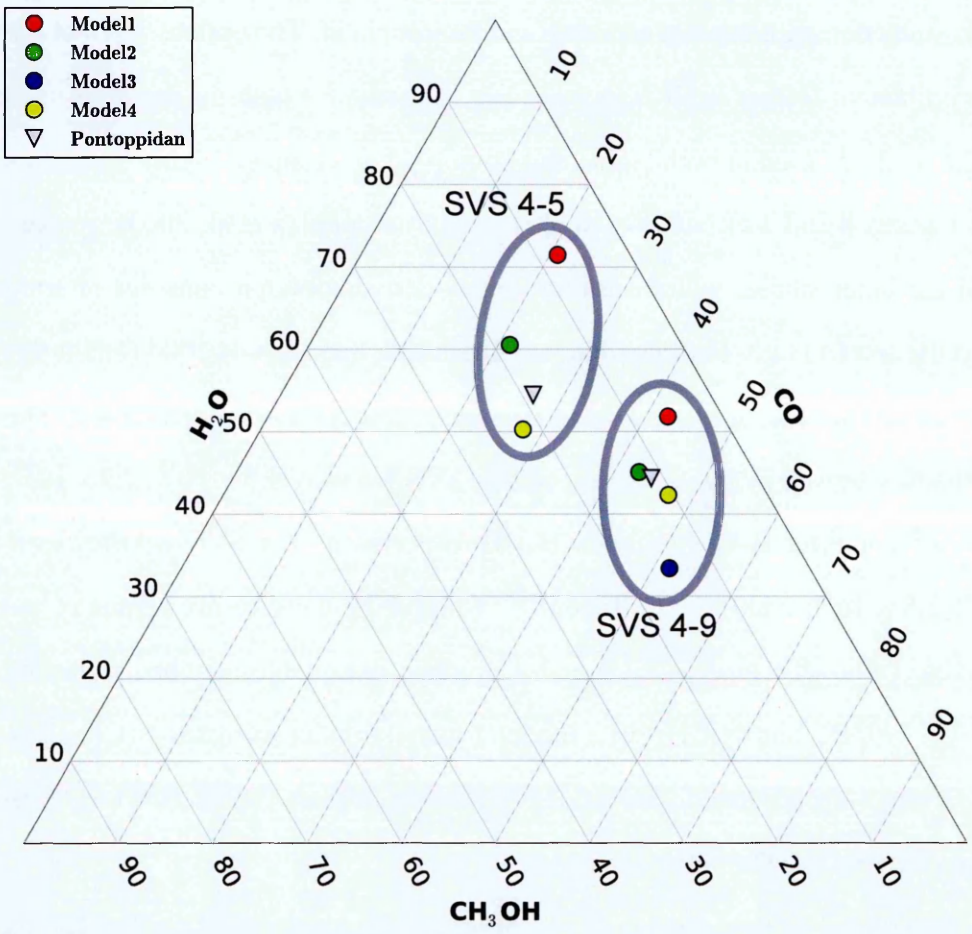

Figure 3.25: As Figure 3.9, except only SVS 4-5 and SVS 4-9 are included, for ease of comparison. The points enclosed by the ellipses refer exclusively to either SVS 4-5 or SVS 4-9, as annotated. The used mixing ratios for models 3 and 4 are 23%.

CH_3OH ice to the observed features was ignored. Because of this only Model 1 of this chapter is directly comparable with the results of Noble, since the contribution of CH_3OH ice to the fit results of Model 1 is minimal. A comparison between Model 1 and the results of Noble shows that the derived values of $N(H_2O)$ are within ~20% of each other, and in Model 1 the derived values of N(CO) are roughly 50% of the N(CO) values of Noble. The differences in $N(H_2O)$ can be attributed to the inclusion of additional absorption from CH_3OH in the $CO:CH_3OH$ data, and to the slightly different fitting area used between my study and the study of Noble. The differences in N(CO) I account to the completely different fitting methods used for the C-O stretch.

3.5.3 Comparison with ice evolution models

In Section 3.2 and in Figure 3.3 I presented a modelling/laboratory-based scenario and an observational (based on predominantly CH_3OH observations) scenario of ice evolution during the early stages of stellar evolution. How do these scenarios compare to what my fitting results imply?

The most obvious difference comes from the fact that I ignore the effect of $CO:H_2O$ ice, as this ice produces spectroscopic features which are not detectable in my or anyone else's observations of interstellar ices. Instead I follow the road laid out by Cuppen et al. (2011), and use a $CO:CH_3OH$ ice in the same context where a $CO:H_2O$ ice would have been used in the past. The simplest of my models using this approach –Model 1– immediately shows that the approach of Cuppen et al. works even when the fit of $CO:CH_3OH$ constrained by the C-O stretch is applied to the 3-micron O-H and C-H stretches.

In the 3-micron region the unknown nature of the "red wing" causes Models 2-4 to be highly degenerate with each other, although all of them agree with previous studies of H_2O, CH_3OH and CO ices to a reasonable degree. Model 3 can be disqualified on the grounds of water ice almost certainly being expected to be present in a pure form in the ISM, and thus the lack of a pure H_2O ice component in Model 3 makes it an

unrealistic one. The sharp red wing features of the C-H stretches in Model 2 make it behave somewhat erratically within the fitting constraints, while the smooth features of the mixed H_2O:CH_3OH ice used in Model 4 produces a much better overall fit to the red wing. While the degeneracies of the red wing fit mean that the presence of pure CH_3OH can not be ruled out, the rest of the discussion will focus on Model 4, which produces the best overall fit. In this model the ice components being probed are pure H_2O, pure CO, CO:CH_3OH, and H_2O:CH_3OH. This is of course only a representative fit, as the true ice matrix will most likely consist of a multitude of layers containing various mixing ratios, including layers with pure ice components for each molecule.

Of the small number of AKARI sources which probe background stars, a small number produce spectra which can be fitted with a combination of ice components consistent with the pre-YSO phases discussed in Section 3.2. Sources such as AKARI-10 and AKARI-12 show no detectable absorption at the 4.7 μm C-O stretch, and the 3-micron region consists of a pure O-H stretching feature without a red wing (see Figure 3.27). Some of these sources (such as AKARI-12) have very weak features at the frequencies where the red wing C-H stretches would be expected to appear, but the weakness of these features mean that they may simply be noise artefacts. Regardless, these two types of sources seem to be probing cloud conditions where the pure H_2O ice layer is still growing, with possibly trace amounts of CH_3OH mixing with the H_2O ice as small amounts of CO get trapped in the H_2O ice and get hydrogenated to sometimes produce CH_3OH.

Stages of ice evolution following critical freezeout seem to be traced by sources such as AKARI-23 and AKARI-14. Both of these sources have a clear pure CO ice feature at the C-O stretch, and AKARI-14 even has a red component in the C-O stretch, allowing for the fitting of the CO:CH_3OH mixture. As is evidenced in Figure 3.27, both of these sources also contain a detectable red wing feature in the O-H stretch. A small amount of a H_2O:CH_3OH mixture could be fitted to the red wing of AKARI-23, although the minimization of Model 4 did not converge to include the H_2O:CH_3OH component in AKARI-14. The red wing degeneracies would make it feasible to in-

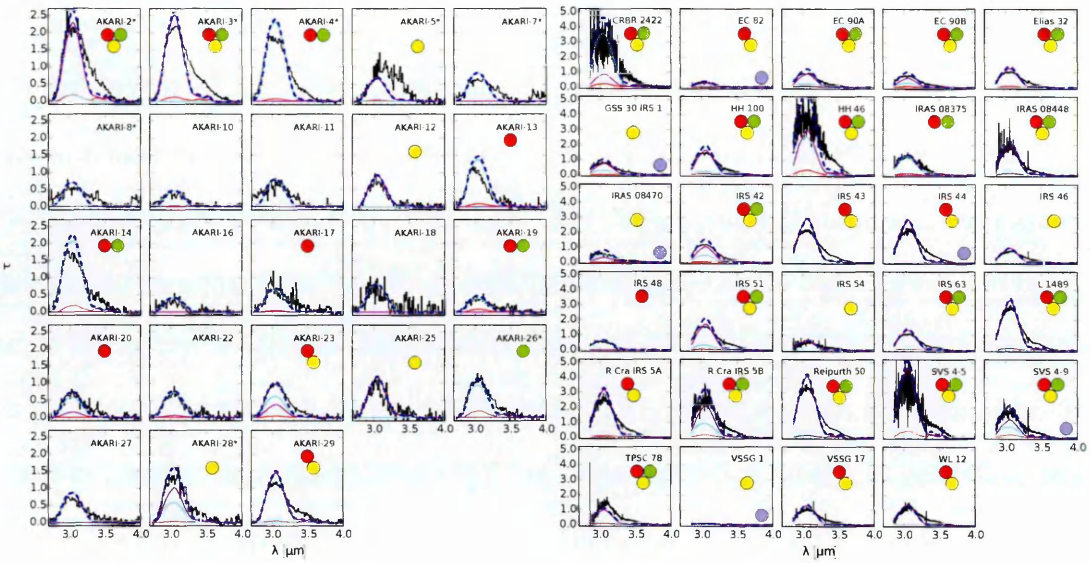

Figure 3.26: An overview of ice components detected with Model 4 towards both the AKARI and VLT sources. The fits plotted here are of the 3-micron region with the 23% CH_3OH:H_2O mixing ratio. The CO:CH_3OH, CH_3OH:H_2O, and pure H_2O data are represented by red, magenta, and cyan lines, respectively. The observed data and the total fit are represented by black and dashed blue lines. The red circles indicate a line of sight with a detection (from the C-O stretch fit) of pure CO, the green circles indicate one with a CO:CH_3OH detection, and the yellow circles indicate a H_2O:CH_3OH detection. Furthermore, the presence of strong gas-phase CO emission (as seen in the C-O stretch spectrum) is indicated by a blue circle in the VLT spectra, where the spectral resolution was high enough to visually detect gas-phase lines. The AKARI sources marked with an asterisk are YSOs.

clude a minor H_2O:CH_3OH component even in this source, though. It is interesting to note that of the background stars considered in this study, all sources which had a detectable C-O stretching component also included a red wing in the 3-micron region. This implies that the critical freezeout of CO is related to the "formation" of the 3-micron red wing. Forming small amounts of CH_3OH through contemporaneous hydrogenation of CO at the H_2O ice surface in the early stages of critical CO freezeout, followed by potential mixing happening in the early stages of ice warm up may feasibly produce what could be considered a H_2O:CH_3OH at this stage. The unfitted (by Model 4) parts of the 3-micron red wing mean that more than just CH_3OH is probably being produced in this stage as well.

Ice evolution stages related to the post-YSO (i.e. following the pre-stellar phase of stellar evolution) phases discussed in Section 3.2 are expected to be traced by the

sources classified as YSOs. As evidenced by the summary of ice detections in Figure 3.26, the fit results to the AKARI sources (despite their low spectral resolution) behave consistently with the fits to the VLT ones in this data set; a similar collection of ice component detections is found in the YSO set of the AKARI ice observations those found in the VLT observations (which are all YSOs). However, the high spectroscopic resolution of the VLT data provides us with an additional diagnostic tool in the form of the numerous gas-phase lines visible especially in the spectra of the C-O stretch (as was evidenced in Figure 3.7). While all the YSO spectra have prominent 3-micron red wings, some of them have no significant C-O stretch absorption feature. As is indicated in the VLT portion of Figure 3.26, the sources (such as GSS 30) which lack a C-O stretch absorption feature also tend to have strong gas-phase emission features around the C-O stretch feature, while the YSO sources (such as EC 90A) which still have a noticeable C-O stretch feature have their gas-phase lines in absorption. In other words, the sources without C-O stretch absorption most likely trace ice evolutionary stages following the heating up of the ice and CO ice desorption, as further evidenced by the emission of the warm gas along the same line of sight.

From this data combined with our previous understanding of ice evolution (discussed in Section 3.2) I propose a model for the evolution of ice in star-forming regions in the stages leading to YSO formation and up to the stages following ice heating around a new YSO. The pre-YSO phases of ice evolution (with example spectra for each proposed stage) are presented in cartoon form in Figure 3.27 and the post-YSO phases of evolution are presented in Figure 3.28.

As with all other ice models, the pre-YSO stages begin with the formation of a significant layer of H_2O ice. During its formation, however, my analysis of the AKARI and VLT data allow for the possiblity of the formation of a minor CH_3OH:H_2O ice component. This result is very tentative, however, and could easily be a spectral artefact caused by noise. After critical CO freezeout, a detectable (from the C-O stretch absorption feature) layer of CO ice has formed. Contemporaneous to this, the appearance of the "red wing" in the 3-micron absorption region allows for a CH_3OH:H_2O ice

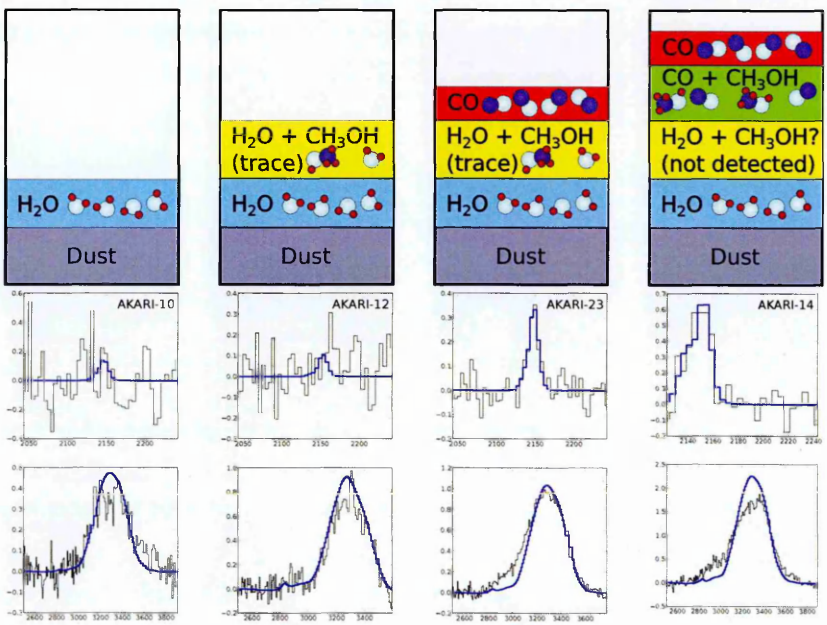

Figure 3.27: Cartoon diagram illustrating a proposed model of ice evolution (with the more advanced stages of evolution being to the right) in the pre-YSO phases of star formation. The cartoons at the top row indicate what ice components (of those containing CO, CH_3OH, and H_2O; all others are ignored by this study) are expected to be detectable at the proposed stages. The bottom row shows an example spectrum from the data set I examined, which I believe to be an example of ice at this evolutionary stage. The top spectrum shows the C-O stretch, and the bottom spectrum shows the 3-micron region. The black line indicates observations and the thick blue line indicates the fitting result. The first two stages I believe to be representative of ice evolution preceding critical CO freezeout, while the last two stages I believe to represent post-freezeout evolution before the ice starts heating up. *The relative thicknesses of the ice layers illustrated here are not representative of the expected relative abundances of their respective ice components; the layers only indicate the potentially detectable presence of the ice.*

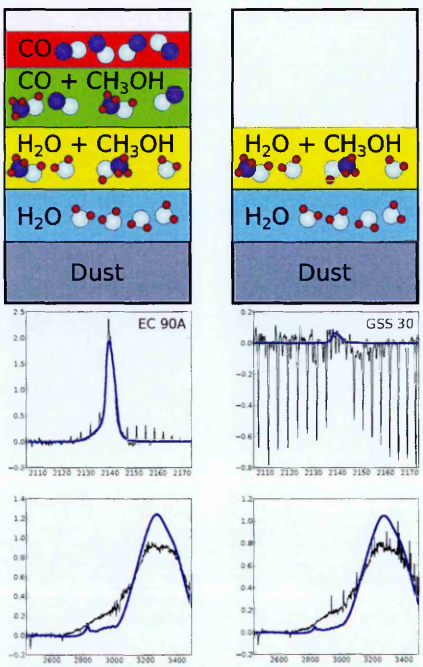

Figure 3.28: Cartoon diagram illustrating a proposed model of ice evolution in the post-YSO phases of star formation. The cartoons at the top row indicate what ice components (of those containing CO, CH_3OH, and H_2O; all others are ignored by this study) are expected to be detectable at the proposed stages. The bottom row shows an example spectrum from the data set I examined, which I believe to be an example of ice at this evolutionary stage. The top spectrum shows the C-O stretch, and the bottom spectrum shows the 3-micron region. The black line indicates observations and the thick blue line indicates the fitting result. The first stage I believe to be representative of the state of the ice immediately preceding ice warm up, while the second stage I believe to represent post-CO sublimation state of the ice. *The relative thicknesses of the ice layers illustrated here are not representative of the expected relative abundances of their respective ice components; the layers only indicate the potentially detectable presence of the ice.*

component to be fitted with a much higher degree of certainty, with the caveat that it may possibly be replaced by any similar component which would produce absorption in the 3-micron red wing. This is also the earliest stage at which the CO:CH_3OH ice component can be confidently detected, implying that hydrogenation of the growing CO layer creates one or more layers of ice which can be considered to be a CO:CH_3OH mixture.

The post-YSO stages consist of two discernible evolutionary steps: one preceding and another following the sublimation of the pure CO ice layer, most likely as a result of ice heating caused by YSO ignition. The pre-heating stage shows (when measured as different combinations of CO, CH_3OH, and H_2O ices) the greatest chemical complexity, with many sources containing detectable components of pure CO, pure H_2O, CO:CH_3OH, and CH_3OH:H_2O. The post-heating stage is characterised by the lack of a pure CO and CO:CH_3OH ice components, both of which have most likely sublimated from the grain surface and entered the gas phase as CO and CH_3OH.

3.5.4 Caveats

The two main caveats of my fitting method arise from both assumptions made about the temperature and structure of the ice being probed, and from assuming a single mixing ratio for both the CH_3OH:CO and CH_3OH:H_2O spectra throughout all lines of sight.

This study assumes that the observations are probing cold ice, and therefore laboratory spectra of ices measured at 10-20 K have been used. Furthermore, the water that is probed is assumed to be porous amorphous solid water. Both the temperature and structure of ice have effects on the shape of the absorption spectrum, and thus can influence especially the high-spectral-resolution VLT fits.

The caveat of CH_3OH:H_2O mixing ratio constancy has a dominating effect on the derived ratio of N(CH_3OH)/N(H_2O). It is not within the scope of this study to create a model which allows the mixing ratio to vary as a free parameter, as the study is

limited by the availability of discrete mixing ratios produced in a laboratory environment, and intermediate ratios can not be easily interpolated due to the complexities of changing absorption profile shapes between different ratios. A similar caveat applies to the CH_3OH:CO spectra used in this study, although the ratio in this case has been delibrately left at 1:1, in order to provide consistency with the study of Cuppen et al. (2011), which is being verified in this study.

In the event of e.g. an empirical model of CH_3OH:H_2O mixtures with a freely varying mixing ratio becoming available, the ratio could be constrained by observing the 9-micron silicate/methanol absorption band. This constraining could happen in a similar fashion to the constraints on the CO:CH_3OH spectrum in the 3-micron features with the help of its C-O peak features. Simultaneous observations of the 3-micron and 9-micron bands will be made possible by future instruments such as the James Webb Space Telescope (JWST).

An alternate route for constraining CH_3OH contribution in the 3 micron feature would come from producing a physical model capable of explaining the shape and origin of the "red wing", which is present as part of the 3-micron features towards many lines of sight. Because the red wing directly overlaps with the C-H stretching features, the contribution of CH_3OH to the C-H stretches will remain ambiguous until the unexplained parts of the red wing are explained.

3.6 Concluding remarks

This work started from the premise that the red component of CO-ice spectra is, as suggested by (Cuppen et al., 2011) entirely attributable to CO in a CH_3OH environment, rather than CO in a H_2O rich environment (e.g. Pontoppidan et al., 2003a; Tielens et al., 1991). The question then arose as to whether such a conclusion was consistent with other ice features, specifically whether the optical depth of the 3 μm OH- and CH-stretching region CH_3OH bands were consistent with the region where they overlap with the strong OH stretch of the H_2O ice band. To examine this effect, CO:CH_3OH

(mixing ratio of 1:1) laboratory spectra from Cuppen et al., 2011 were fitted to a total of 52 near-IR spectra observed using both the low-resolution AKARI/IRC and high-resolution VLT/ISAAC detectors. The examined near-IR regions were the 4.7 μm C-O stretching mode and the 3 μm O-H and C-H stretching mode absorption features. Other features originating from CO or H_2O in the fitted regions were considered with the use of additional analytical or laboratory spectra. Various different combinations of analytical and laboratory spectra were tested, as discussed in Sections 3.3.3, and 3.4.2.1-3.4.2.4.

From the fitting results the following conclusions can be drawn:

- The results clearly corroborate the hypothesis of Cuppen et al. (2011), confirming that the laboratory spectra of CO:CH_3OH (1:1) ices can effectively fit the red component of CO-ice spectra, eliminating the difficulties introduced by CO:H_2O ice mixtures, and the "missing" observational 2152 cm^{-1} band (Fraser et al., 2004).

- Considering the presence of a CO:CH_3OH ice component in the C-O stretch results in over half of the examined lines of sight having in them a detectable fitted quantity of CH_3OH mixed with CO.

- The red wing often found in the 3 micron absorption feature, while not fully reproducible by the models considered here or any other models known to this author, can easily conceal significant contributions from CH_3OH ice, either in mixed or pure form.

- A simultaneous fit of pure H_2O, pure CO, and mixed CH_3OH:H_2O ices in addition to mixed CH_3OH:CO constrained by the C-O peak, i.e. "Model 4", provides a good estimate of the CH_3OH ice content towards the lines of sight considered in this study, as determined from the 3-micron and C-O stretch near-IR features.

- Estimation of N(CH_3OH) from the 3-micron feature affects estimates of N(H_2O), and the ratio of the two. The ratio is estimated to vary from a few % to ~40%,

based on the measurements presented here. The average ratio is determined from the mixing ratio of the CH_3OH:H_2O mixture used in the fits.

Finally, a model of pre-YSO and early post-YSO ice evolution is proposed, as discussed in Section 3.5.3, and illustrated in Figures 3.27 and 3.28.

The fitting approach used here takes account of both grain shape effects and observational instrument point spread functions, such that a common fitting rationale can be applied across all the data, independent of its source or resolution, to extract CO, H_2O and CH_3OH ice abundances. It is a key achievement of this work that the AKARI ice abundance extraction methodology presented previously by Noble et al. (2013) is entirely transferable to the higher resolution VLT-ISAAC data, consolidating many years of careful error analysis on the former data, prior to making any claims of weak AKARI ice feature detections.

Chapter 4

Water and methanol in low-mass protostellar outflows[1]

The previous chapter showed that methanol ice is abundant in the ISM, and that its column density ratio against water ice can vary between a few and $\sim 40\%$ even towards lines of sight where it might previously have been observed. These ices will not remain in the solid state forever, though, and the grain surfaces around young stellar objects (YSOs) are subjected to thermal and non-thermal desorption processes which release molecules from the solid state into the gas phase.

In this chapter I have used gas-phase observations of CH_3OH and H_2O to determine what happens to them in shocked regions around low-mass young stellar objects (YSOs) where their stellar wind impacts with the inner outflow cavity walls of the surrounding cold envelope. By analysing the gas phase line emission ratios, I can show that evidence exists for significant high temperature gas-phase (re-)formation of water and for the destruction of most of the methanol during its sputtering from the solid state to the gas phase.

[1]This chapter has been published in a shorter format at MNRAS 2014 vol. 440 pp. 1844 (DOI: 10.1093/mnras/stu406) by the authors: A. N. Suutarinen (me), L. E. Kristensen, J. C. Mottram, H. J. Fraser, and E. F. van Dishoeck

4.1 Introduction

Water plays a unique role in probing the physical and chemical conditions of star-forming regions. In the cold regions of protostars, water is frozen out as ice covering the dust grains, with only trace amounts found in the gas phase ($\lesssim 10^{-7}$; Caselli et al., 2012; Herpin et al., 2012; Mottram et al., 2013; Schmalzl et al., 2014). The molecular outflows launched by the accreting protostar form an interesting laboratory for studying water in protostellar systems: the high water abundances observed in outflows ($> 10^{-6}$; Bjerkeli et al., 2012; Dionatos et al., 2013; Nisini et al., 2010; Santangelo et al., 2012; Van Loo et al., 2013; Vasta et al., 2012) arise from a combination of sputtering of ice mantles and direct gas-phase synthesis, however the relative water abundance contributions are unknown. Constraining the relative contributions of these two routes is important for using water as a diagnostic of the physical conditions in outflows, as well as constraining the chemistry in the various parts of the outflow.

Water formation on dust grains is a complicated process (e.g. Ioppolo et al., 2008; Lamberts et al., 2013), but generally involves the repeated hydrogenation of oxygen-bearing species such as O, OH and O_2 (Tielens and Hagen, 1982). The only efficient gas-phase formation route for H_2O is a high-temperature ($T \gtrsim 200$ K) neutral-neutral reaction chain (e.g. Bergin, Neufeld, and Melnick, 1999; Draine, Roberge, and Dalgarno, 1983; Glassgold, Meijerink, and Najita, 2009; Tielens, 2005):

$$\mathrm{O} \xrightarrow{\mathrm{H_2}} \mathrm{OH} \xrightarrow{\mathrm{H_2}} \mathrm{H_2O + H}. \tag{4.1}$$

Another common grain-surface material, methanol, can be formed on dust grains through repeated hydrogenation of CO (e.g. Tielens, 2005; Tielens and Hagen, 1982)

$$\mathrm{CO_{surface}} \xrightarrow{\mathrm{H}} \mathrm{HCO_{surface}} \xrightarrow{\mathrm{H}} \mathrm{CH_3O_{surface}} \xrightarrow{\mathrm{H}} \mathrm{CH_3OH_{surface}}. \tag{4.2}$$

Unlike water, gas-phase reactions that produce CH_3OH are very slow compared to grain surface chemistry for any of the physical conditions expected within protostellar

systems (Geppert et al., 2006).

Both water (e.g. Codella et al., 2010; van Dishoeck et al., 2011) and methanol (e.g. Bachiller et al., 1995; Kristensen et al., 2010a) have been detected in the gas phase of the outflows and shocks of young stellar objects (YSOs). In astrophysical environments the grain surface reaction chain leads to grain surface abundances of order $10^{-6} - 10^{-5}$ for CH_3OH with respect to gas-phase H_2 (e.g. Cuppen et al., 2009; van der Tak, van Dishoeck, and Caselli, 2000). This results in relative abundances of CH_3OH ice with respect to H_2O ice ranging from a few to $\sim$ 30 % (e.g. Boogert et al., 2008; Dartois et al., 1999; Gibb et al., 2004; Öberg et al., 2011a; Pontoppidan, van Dishoeck, and Dartois, 2004; Pontoppidan et al., 2003b) on lines of sight towards high- and low-mass YSOs. Models of cold dense clouds by Lee, Bettens, and Herbst (1996), which only include gas-phase production, result in gas-phase abundances of CH_3OH no higher than between 10^{-10} and 10^{-9} on timescales of up to 10^6 years (Garrod et al., 2006; Geppert et al., 2006).

In the context of YSOs and their outflows, I assume and expect all of the grain-surface formation of H_2O and CH_3OH to have already taken place during the preceding dark-cloud and prestellar core phases. Material is liberated from the grain surfaces either through thermal desorption, if the temperature of the dust grains rises above $\sim$100-110 K for water (Brown and Bolina, 2007; Fraser et al., 2001) and $\sim$85 K for methanol (Brown and Bolina, 2007) as they journey close to the protostar (Visser et al., 2009), or through sputtering in shocks. While photodesorption due to cosmic-ray induced UV radiation is expected to be important in the cold conditions found in protostellar envelopes (e.g. Caselli et al., 2012; Mottram et al., 2013; Schmalzl et al., 2014), it is unlikely to be dominant in the conditions found in outflows.

Therefore, any gas-phase CH_3OH observed in outflows will originate from desorbed ice mantle material, while gas-phase H_2O may originate either in warm shocked gas in outflows where the temperature exceeds $\sim$ 200 K (Bergin, Neufeld, and Melnick, 1999; Charnley, 1999) or from the grain mantles. *My first objective with this study is to test whether there is observational evidence in the emission spectrum of the*

outflow material for water formation in excess of what is expected to be seen from only ice mantle desorption, i.e. is the gas phase formation route activated?

My method for studying this is to examine the relative gas-phase column density variations of CH_3OH and H_2O derived in components of their emission spectra associated with the outflow and its shocked cavities, as seen towards the source positions of three prototypical YSOs. CH_3OH is a particularly good molecule for comparing against H_2O as it is a "pure" grain mantle species i.e. it is not formed in any significant quantity in the gas phase. Thus, any variations of $N(CH_3OH)/N(H_2O)$[2] are a result of independent variations in either $N(CH_3OH)$ or $N(H_2O)$.

Before using $N(CH_3OH)/N(H_2O)$ to study the variations of $N(H_2O)$, I had to first consider whether any CH_3OH is destroyed, either by dissociative desorption during sputtering or in the shock through reactions with H. This latter scenario would be somewhat similar to that involving another grain-surface product, NH_3, at positions offset from the YSO (Codella et al., 2010; Viti et al., 2011). *The second objective of this chapter is to provide observational limits on the extent of CH_3OH destruction in the outflows of low-mass YSOs.* This is accomplished by comparing the column densities to that of a CO line which traces the same gas as H_2O, such as CO J=10–9 (Nisini et al., 2013; Santangelo et al., 2013; Tafalla et al., 2013; Yıldız et al., 2013). The $N(CH_3OH)/N(CO)$ ratio can then be translated into the CH_3OH abundance $X(CH_3OH) = N(CH_3OH)/N(H_2)$ by assuming a constant CO abundance in the outflow, 10^{-4}.

This chapter is structured as follows. In Section 4.2 I describe the observations on which the science of this chapter is based, and then describe the immediate results in Section 4.3. In Section 4.4 I describe the decomposition of the acquired spectra into components, and explain which of these I assume to have the same physical origin. I will also discuss the likely physical conditions in the outflow, and use them to constrain the radiative transfer simulations which allow the observed line intensity ratios to be

[2]All the column densities discussed in this chapter in the form of e.g. $N(H_2O)$ refer to their gas-phase column densities, unless explicitly stated otherwise.

Table 4.1: Observed line parameters.

Line	Rest Freq.[a] (GHz)	θ_{mb} ($''$)	$E_{\rm up}/k_{\rm b}$ (K)	$n_{\rm cr}^{\rm (b)}$ (cm^{-3})
H_2O $2_{02}-1_{11}$	987.927	21[c]	100.8	8×10^7
CH_3OH 5_K-4_K	241 – 242	21	41 – 136	5×10^5
CH_3OH 7_K-6_K	338 – 339	14	65 – 256	1×10^6
CO 10 – 9	1151.985	18[c]	304.2	5×10^5

[a]Pickett et al., 1998

[b] Critical density at 200 K; for the CH_3OH transitions the values reported are for the highest S/N K=0 A transitions.

[c]Calculated using equation 3 from Roelfsema et al. (2011).

converted into column density ratios. In Section 4.5 I discuss the acquired column density ratios and place them in the context of the arguments and processes outlined above. Finally, in Section 4.6 I conclude that gas-phase water formation is indeed happening, and that methanol is being destroyed as it is sputtered from the solid state.

4.2 Observations

The data exploited in this chapter consist of spectroscopic observations of water (H_2O), methanol (CH_3OH), and carbon monoxide (CO) towards seven Class 0 and six Class I YSOs. The details of this sample are given in Table 4.2. Observations of the $2_{02}-1_{11}$ para-H_2O and CO J=10–9 transitions were obtained with the Heterodyne Instrument for the Far-Infrared (HIFI; de Graauw et al., 2010, also see Chapter 2) on the *Herschel* Space Observatory (Pilbratt et al., 2010) as part of the "Water in star-forming regions with *Herschel*" key programme (WISH; van Dishoeck et al., 2011). The J=5–4 and 7–6 K-ladders of CH_3OH were observed with the James Clerk Maxwell Telescope[3] (JCMT) with the RxA and RxB receivers, respectively. A summary of the frequencies, beam sizes and upper level energies ($E_{\rm up}$) can be found in Table 4.1.

[3]The James Clerk Maxwell Telescope was operated by the Joint Astronomy Centre on behalf of the National Research Council of Canada, (until January 2015) the Science and Technology Facilities Council of the United Kingdom, and (until 31 March 2013) the Netherlands Organisation for Scientific Research.

Table 4.2: Source properties

Source	D	Coordinates		$v_{\rm LSR}^{(a)}$	$L_{\rm bol}^{(b)}$	$T_{\rm bol}^{(b)}$	$M_{\rm env}^{(c)}$	Class
	(pc)	$\alpha_{\rm J2000}$	$\delta_{\rm J2000}$	(km/s)	$Lsol$	(K)	$(Msol)$	
NGC133 IRAS 2A	235	$03^{h}28^{m}55.^{s}60$	$+31^{d}14^{m}37.^{s}1$	+7.7	35.7	50	5.1	0
NGC133 IRAS 4A	235	$03^{h}29^{m}10.^{s}50$	$+31^{d}13^{m}30.^{s}9$	+7.2	9.1	33	5.2	0
NGC133 IRAS 4B	235	$03^{h}29^{m}12.^{s}00$	$+31^{d}13^{m}08.^{s}1$	+7.1	4.4	28	3.0	0
L483	200	$18^{h}17^{m}29.^{s}90$	$-04^{d}39^{m}39.^{s}5$	+5.2	10.2	49	4.4	0
L723	300	$19^{h}17^{m}53.^{s}70$	$+19^{d}12^{m}20.^{s}0$	+11.2	3.6	39	1.3	0
L1157	325	$20^{h}39^{m}06.^{s}30$	$+68^{d}02^{m}15.^{s}8$	+2.6	4.7	46	1.5	0
L1448-MM	235	$03^{h}25^{m}38.^{s}90$	$+30^{d}44^{m}05.^{s}4$	+5.2	9.0	46	3.9	0
Elias 29	125	$16^{h}27^{m}09.^{s}40$	$-24^{d}37^{m}19.^{s}6$	+4.3	14.1	299	0.3	I
GSS30-IRS1	125	$16^{h}26^{m}21.^{s}40$	$-24^{d}23^{m}04.^{s}0$	+3.5	13.9	142	0.6	I
L1489	140	$04^{h}04^{m}43.^{s}00$	$+26^{d}18^{m}57.^{s}0$	+7.2	3.8	200	0.2	I
L1551 IRS5	140	$04^{h}31^{m}34.^{s}10$	$+18^{d}08^{m}05.^{s}0$	+6.2	22.1	94	2.3	I
TMC 1	140	$04^{h}41^{m}12.^{s}40$	$+25^{d}46^{m}36.^{s}0$	+5.2	0.9	101	0.2	I
TMR 1	140	$04^{h}39^{m}13.^{s}70$	$+25^{d}53^{m}21.^{s}0$	+6.3	3.8	133	0.2	I

(a) Obtained from ground-based $C^{18}O$ or $C^{17}O$ observations (Yıldız et al., 2013)
with the exception of IRAS 4A for which the value from Kristensen et al. (2012) is more consistent with my data.
(b) Measured using *Herschel*-PACS data from the WISH and DIGIT key programmes (Karska et al., 2013).
(c) Mass within the 10 K radius, determined by Kristensen et al. (2012) from DUSTY modelling of the sources.

4.2.1 Data reduction

4.2.1.1 Basic reduction

The H_2O and CO data had already been reduced previously –as is discussed further in Kristensen et al. (2010a) and Yıldız et al. (2013) respectively–, and was used here without further processing. For the CH_3OH data, Maret et al. (2005) had previously performed a reduction and analysis for some of the sources. I chose to re-reduce the full CH_3OH dataset for all sources, as the raw JCMT data was still available on the Leiden Observatory file servers.

I wrote a PYTHON script to find and analyse line list files (created by LINEFINDER, programmed by U. A. Yıldız), and collect the locations of all files with potential data on relevant lines (the CH_3OH 5-4 and 7-6 lines) into a single master list. A separate GILDAS/CLASS[4] script was then used to extract the line data, apply a 1^{st} order baseline, and time-average the spectra for each source, before exporting the data in ASCII table format.

The manual aspect of the reduction involved selecting baseline windows for each source, and making sure that no obviously bad data was being included in the time-averaging. In cases (such as the NGC1333 sources) where mapping data with multiple offsets was available, only the offset closest to zero was included in creating the time-averaged spectra. Each spectrum was also divided by the main beam efficiency of the telescope at the appropriate frequency band.

4.2.1.2 Noise estimate and resampling

Across all the potential sources for this study, the amount of available useful data varied greatly, and as a result some sources had significantly higher noise than others. The total integration time per source is listed in Table 4.3.

The uncertainties reported in the rest of this chapter only relate to the intrinsic random noise in each spectrum, which is closely related to the integration time. For

[4]http://www.iram.fr/IRAMFR/GILDAS

Table 4.3: Integration time (only for non-erroneous data) per transition for all observed sources. A hyphen indicates lack of useful data.

Object name	Line integration time [min]				
	H_2O (2 – 1)	CH_3OH (5 – 4)	CH_3OH (7 – 6)	CO (3 – 2)	CO (10 – 9)
IRAS 2	18.3	180.3	192.0	4.0	17.8
IRAS 4A	18.3	40.0	160.0	1.0	17.8
IRAS 4B	18.3	175.0	111.0	4.0	8.9
L483	18.3	–	120.0	–	–
L723	18.3	–	120.0	–	–
L1157	18.3	10.0	190.0	–	–
L1448	18.3	–	120.0	–	–
Elias 29	18.3	110.0	–	–	–
GSS 30	18.3	155.0	–	–	–
L1489	18.3	–	120.0	–	–
L1551	18.3	285.0	–	–	–
TMC 1	18.3	10.0	–	–	–
TMR 1	18.3	–	120.0	–	–

the NGC1333 sources, typical σ_{RMS} levels (in channel sizes binned to 1 km s^{-1}; see next paragraph) for the H_2O, CO and both CH_3OH lines are 0.02, 0.17, 0.15 and 0.24 K respectively. The calibration uncertainty of the HIFI spectra is $\lesssim$ 10% (Roelfsema et al., 2011) and the calibration uncertainty of the JCMT spectra is $\sim$ 20%.

In the remainder of the chapter, when discussing the intensity ratios of the various lines included in this study, they have been resampled to fit a common velocity resolution of 1 km s^{-1} which was found to give a good balance between resolution and signal-to-noise ratio (S/N). Resampling also improves the S/N of the line wings, which are crucial for this study.

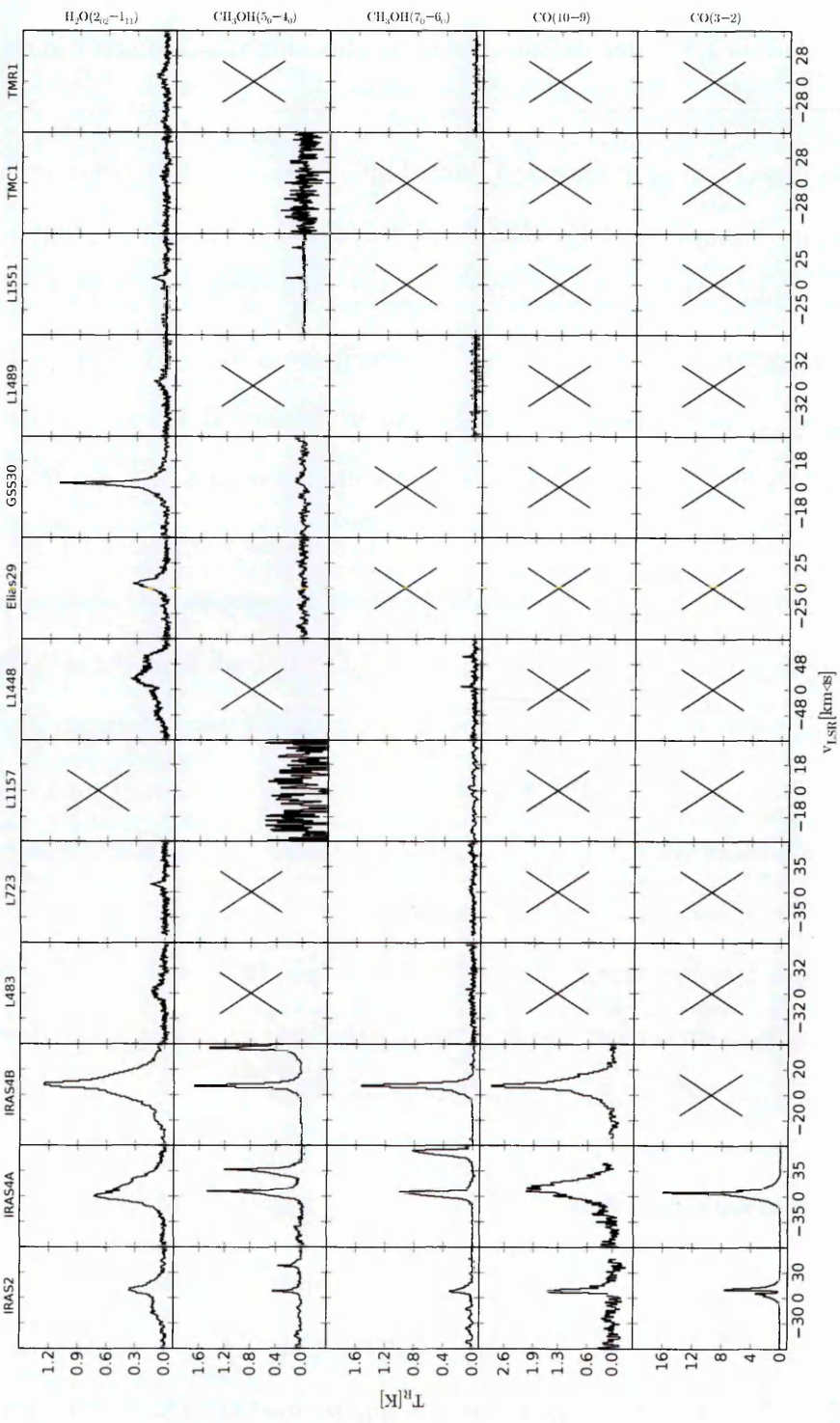

Figure 4.1: All the source/line combinations considered at the start of this study, with sources separated to their own columns and lines separated to rows. Missing data is indicated by a cross.

4.2.1.3 Source selection

The reduced spectra for all the sources are presented in Figure 4.1. As the main priority of this study was to examine the relative abundances of H_2O and CH_3OH, the quality of the data related to them was the deciding factor in choosing which sources to select for the rest of the study.

The obvious choices to drop are L1157 and TMC-1, because they not only have missing data but have very noisy CH_3OH 5-4 spectra (due to the low integration time, as evidenced in Table 4.3). Similarly L483, L723, L1489, L1551, and TMR-1 are disqualified from further study on account of extremely weak to no CH_3OH (and occasional p-H_2O) detections. L1448 has a very peculiarly shaped H_2O spectrum due to the high-velocity "bullets" of gas ejecta associated with this source (Kristensen et al., 2011). A weak CH_3OH 7-6 feature is visible, but comparing the shapes of the H_2O and CH_3OH spectra indicates that it would be necessary to understand the (non-trivial) process of disentangling the bullet features seen in the H_2O spectrum from the non-bullet emission, in order for a meaningful comparison to be possible with the little CH_3OH that is detected. Thus I disqualify L1448 from further study. Both Elias 29 and GSS 30 show strong detections of H_2O emission, but CH_3OH could not be detected, making it impossible to study the ratio between the species.

In the end I was left with three sources: IRAS 2A, and IRAS 4A and 4B. All of these have data and also show clear line detections in the H_2O and both CH_3OH bands, and thus form the basis for the remainder of this study.

4.2.1.4 Beam dilution correction

As seen in Table 4.1, the lines that are examined in this study have somewhat different beamsizes from each other, ranging from $14''$ with the CH_3OH $5_K - 4_K$ lines to $21''$ with the H_2O $2_{02} - 1_{11}$ line. These variations in beamsize lead to large variations from line to line in the beam dilution of the observed emission, which has to be compensated for if I am to make an accurate comparison between the different lines. To do this I

have applied the differential beam dilution correction method detailed in Appendix B of Tafalla et al. (2010) to the line ratios discussed in Sections 4.3.2 and 4.4.3.

The correction method is applied by assuming a simple gaussian beam, where the beam dilution factor is proportional to $\theta_{MB}^{-\alpha}$, where θ_{MB} is the FWHM of the beam being examined and α is a free parameter dependant on the source size and which can vary between 0 and 2. Tafalla notes that $\alpha = 2.0$ for a point-like source, 1.0 for a one-dimensional source, and 0.0 for a source infinitely extended in two dimensions. In my case, applying a beam dilution correction to an observed line intensity ratio between molecules 1 and 2, $T_{\mathrm{R},1}/T_{\mathrm{R},2}$, is given by using the equation:

$$(T_{\mathrm{R},1}/T_{\mathrm{R},2})_{\mathrm{corrected}} = (T_{\mathrm{R},1}/T_{\mathrm{R},2}) \times (\theta_{\mathrm{MB},2}/\theta_{\mathrm{MB},1})^{-\alpha}. \quad (4.3)$$

In order to apply this correction method to my data I had to first examine which value of α is most appropriate to my case. The effect of accounting for beam dilution, or lack thereof, in my case is best seen when comparing the line ratio of the two different CH_3OH lines against either the CO lines or the H_2O line studied in this chapter. To determine α I decided to use the CO (10-9) line because it is the one least affected by high optical depth. Assuming that emission from both of the CH_3OH lines' wings originate from the same physical region of the YSO I would expect that when beam dilution is taken into account correctly, the line ratios of both CH_3OH lines divided by the CO (10-9) would yield the same N(CH_3OH)/N(CO).

Based on this I decided to adopt $\alpha = 1.0$ as the beam-size correction exponent for all my cases. According to Tafalla et al. (2010) this implies that the emission I am probing is extended along one dimension when compared to my beam sizes, which makes sense for the edge of an outflow.

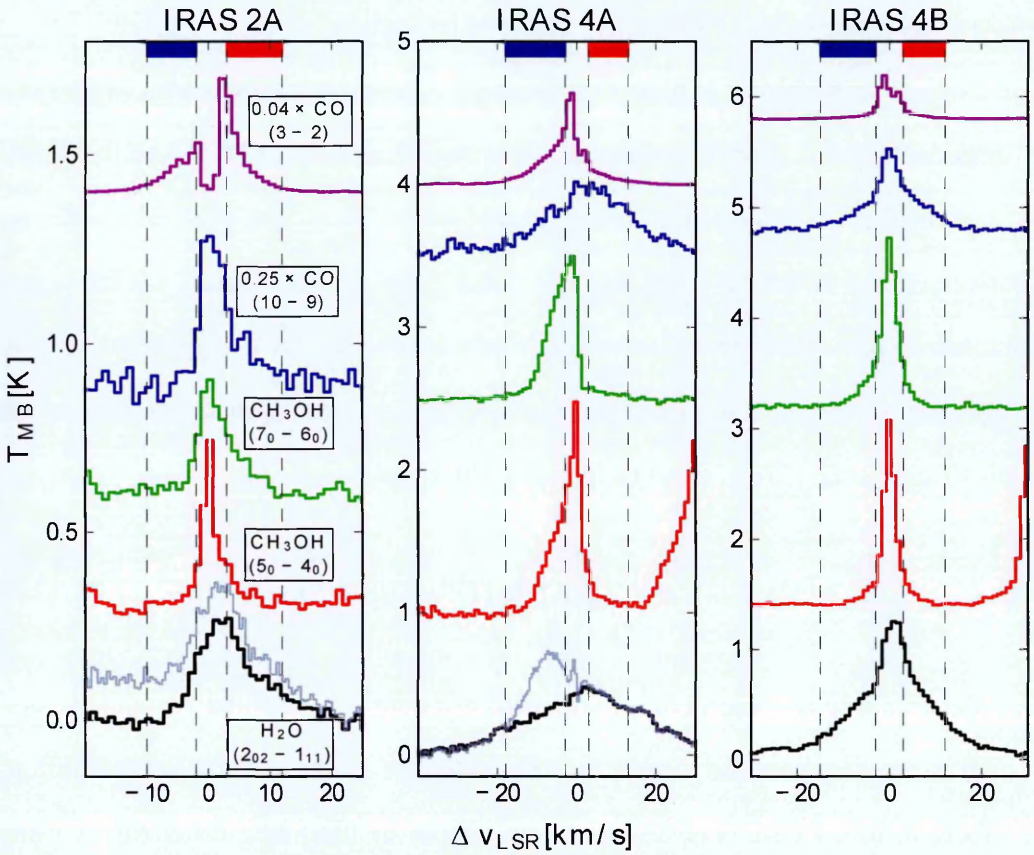

Figure 4.2: The emission of the $5_0 - 4_0$ (red) and $7_0 - 6_0$ (green) A-CH_3OH, the 10-9 (blue) and 3-2 (magenta) CO spectra plotted above the $2_{02} - 1_{11}$ p-H_2O spectrum (gray), which has been decomposed in the manner discussed in Section 4.5.4; decomposed spectra are shown in black. All spectra have been resampled to a common channel size of 1 km s^{-1}, and shifted in velocity so that their rest velocity is at $\Delta v = 0$ km s^{-1}. The CO 10-9 and 3-2 spectra have been scaled with multipliers of 0.25 and 0.04, respectively. The spectra are offset along the y-axis for clarity. The dashed vertical lines show the velocity ranges used for selecting the red and blue wings of the spectra, as colour-coded by the horizontal lines at the top.

Table 4.4: Velocity cuts for the line wings, relative to the local velocity of the source

Source	Red wing (km s^{-1})	Blue wing (km s^{-1})
IRAS 2A	$+3.0 \ldots +12.0$	$-10.0 \ldots -2.0$
IRAS 4A	$+3.0 \ldots +13.0$	$-18.0 \ldots -3.0$
IRAS 4B	$+3.0 \ldots +12.0$	$-15.0 \ldots -3.0$

4.3 Results

4.3.1 Line profiles

Figure 4.2 shows the H_2O spectra of IRAS 2A, IRAS 4A, and IRAS 4B, centered at their rest velocities, against both CH_3OH and CO spectra. For the wings of IRAS 2A all profiles are very similar, although the red wing of the H_2O spectrum extends to higher velocities than any of the other species by about 5 $km\,s^{-1}$. IRAS 4A is characterised by the highly asymmetric profile of the CH_3OH 7-6 spectrum compared to the H_2O and CO 10−9 spectra. The H_2O line wings towards both IRAS 4A and 4B extend to significantly higher velocities than the CH_3OH and CO 10−9 line wings by more than 10 $km\,s^{-1}$.

The CO 3−2 line shows a noticeable dip in intensity towards IRAS 2A at very low velocities. This is indicative of the low-velocity (i.e. mostly envelope) gas being very optically thick and self-absorbing. Previous studies (e.g. Takahashi et al., 2008) have shown that the CO 3−2 line can trace the hot outflow gases in star forming regions. However, according to Kristensen et al. (2013) low-J (i.e. J<10-9) CO emission does not trace the same cloud components as the H_2O $2_{02} - 1_{11}$ emission. Furthermore, Santangelo et al. (2012) have mapped both CO emission lines towards star-forming regions, and found that their distributions do not match. All of this suggests that CO 3-2 is not a useful transition to compare against the other lines considered in this study because of tracing different gas components, and I have omitted the CO 3-2 observations from now on.

Previous studies have found that the observed p-H_2O line profiles are generally complex and consist of multiple dynamic components (Kristensen et al. 2010b, 2011, 2012, 2013; Mottram et al. 2013, 2014). These components are typically associated with the envelope, outflowing and shocked gas and trace physical components not detected prior to Herschel. CH_3OH profiles, on the other hand, typically consist of just two components: one associated with the outflow and one with the envelope. In the this study I limit myself to studying the line wings only, and ignore the line centers

which are typically associated with envelope emission.

The velocity ranges used to define the red and blue wings of each object are indicated by the respectively coloured bars at the top of Fig. 4.2. The ranges were selected such that any envelope contribution is excluded (typically $\pm$ 3 km s^{-1} from the source velocity) and such that the line wings are completely included. Towards IRAS 4A and 4B, the red-shifted A-CH_3OH $5_0 - 4_0$ wing emission starts to overlap with E-CH_3OH $5_{-1} - 4_{-1}$ emission at velocities of + 5$-$10 km s^{-1} from the source velocity, which therefore sets the upper limit on the range to which I was able to compare the red-shifted velocity.

4.3.2 Observed line ratios

The line ratios of the two ground-state 5$-$4 and 7$-$6 A-CH_3OH transitions with respect to H_2O $2_{02} - 1_{11}$ and CO 10$-$9 are presented in Fig. 4.3. The line ratios are measured where $\Delta v \geq 3$ km s^{-1}(at lower velocities it is not possible to separate outflow emission from quiescent envelope emission), and where the S/N ratio is > 1 in both transitions. The CO 10$-$9 line profile towards IRAS 2A shows no blue-shifted emission in spite of the high quality of the data.

The CH_3OH / H_2O line ratios show a decreasing trend with increasing velocity over the range where CH_3OH is detected. This is particularly visible towards IRAS 4A in the blue wing, where the ratio decreases by more than a factor of 5. Most other line wings show a decrease of a factor of 2$-$3. In IRAS 2A the (noisy) line wings appear to exhibit constant line ratios, although the higher-S/N red $7_0 - 6_0$ CH_3OH line wing shows a noticeable decrease in the line ratio with respect to H_2O emission. The CH_3OH / CO 10$-$9 line ratios (Fig. 4.3) exhibit similar trends as the ratios with H_2O, consistent with the similarity of the H_2O and CO 10$-$9 profiles (Yıldız et al., 2013) tracing the same gas.

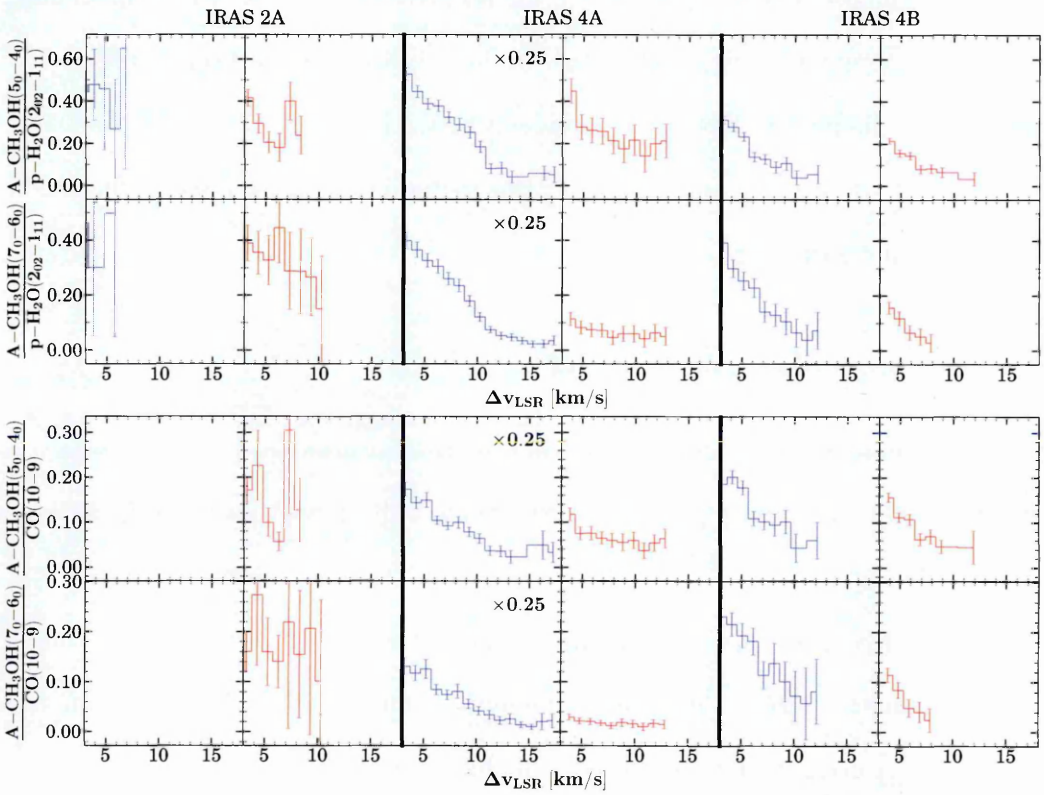

Figure 4.3: The ratio of the line intensities of two different A-CH_3OH lines ($5_0 - 4_0$ and $7_0 - 6_0$ over the line intensity of the $2_{02} - 1_{11}$ p-H_2O transition (*top*), CO 10–9 (*bottom*). The velocity along the x axis is absolute offset with respect to the source velocity for the blue and red wings, respectively. Only the velocity range covering the line wings tracing emission related to the outflows is included in the line ratios and all points where S/N < 1 for either line have been ignored. Some of the line ratios were scaled for visibility reasons (marked). The error bars only include measurement uncertainties and not relative calibration uncertainties.

4.4 Analysis

4.4.1 From emission to abundances: radiative transfer

While the intensity of line emission from a specific molecule can be intuitively considered to be directly related to the number of emitting molecules, and thus the line intensity ratios might be directly related to the relative abundances of two molecules, reality tends to be much more complicated. In the following subsections I will review the physics of radiative transfer –which explains how a line intensity can be translated into a molecular abundance– and then apply this method to my case through the use of specialized radiative transfer software.

4.4.1.1 The theory of radiative transfer

Consider an infinitesimally small cylinder (bottom surface area dA, length dr) which is subjected to radiation coming perpendicularly at the bottom with intensity I_ν directed at a solid angle $d\omega$.

This cylinder is suspended in a medium which causes the intensity of the incoming radiation to change by dI_ν as it passes the length of the cylinder, dr. In time dt this causes the energy contained in the cylinder to change by

$$dE = dI_\nu \, dA \, d\nu \, d\omega \, dt. \tag{4.4}$$

This change in energy is caused by both absorption and emission (I ignore scattering for my case), so that

$$dE = -dE_{\rm abs} + dE_{\rm em}. \tag{4.5}$$

The change in intensity due to absorption in the cylinder is directly proportional to intensity, and can be expressed as

$$dI_{\nu,{\rm abs}} = \kappa_\nu I_\nu \, dr, \tag{4.6}$$

where κ_ν is the absorption coefficient of the material, and represents how much incoming energy from the solid angle $d\omega$ gets absorbed by the material at frequency ν. If I replace dI_ν in Equation 4.4 with $dI_{\nu,\mathrm{abs}}$, I get the energy change due to absorption:

$$dE_{\mathrm{abs}} = \kappa_\nu I_\nu \, dr dA d\nu d\omega dt. \tag{4.7}$$

Complementary to κ_ν, I define the emission coefficient j_ν to represent how much energy the material emits into the solid angle $d\omega$ at frequency ν. Thus the energy change caused by emission is expressed by

$$dE_{\mathrm{em}} = j_\nu \, dr dA d\nu d\omega dt. \tag{4.8}$$

Placing equations 4.4, 4.7, and 4.8 into equation 4.5, I can derive

$$\frac{dI_\nu}{\kappa_\nu dr} = -I_{\mathrm{nu}} dr + \frac{j_\nu}{\kappa_\nu}. \tag{4.9}$$

The ratio $\frac{j_\nu}{\kappa_\nu}$ is also called the *source function*, and I will represent it with S_ν. Furthermore, $\kappa_\nu dr = d\tau_\nu$, where τ_ν is called *optical depth*. Placing these two into Equation 4.9, I arrive to *the basic equation for radiative transfer*:

$$\frac{dI_\nu}{d\tau_\nu} = -I_\nu + S_\nu. \tag{4.10}$$

Through integration, I can produce *the formal solution to the radiative transfer equation*:

$$I_\nu(\tau_\nu) = I_\nu(0) e^{-\tau_\nu} + \int_0^{\tau_\nu} e^{-(\tau_\nu - x)} S_\nu(x) dx. \tag{4.11}$$

At its most basic level, this equation is at the heart of all discussion about radiative transfer. In astronomical terms its first term describes how radiation from behind the cloud –represented by $I_\nu(0)$– is exponentially attenuated by the optical depth τ_ν of the cloud. The second term inside the integral describes emission –from e.g. excited molecular gas– happening in the cloud, also partially attenuated by optical depth.

4.4.1.2 Radiative transfer in practise: RADEX

Since the source function $S_\nu(x)$ in Equation 4.11 is not recoverable, solving Equation 4.11 requires simplifications, such as the rotational diagram (which applies only in Local Thermal Equilibrium or LTE, where the energy populations are assumed to have been thermalized to follow the Planck distribution) or iterative solutions such as those utilised by the non-LTE excitation software RADEX (van der Tak et al., 2007).

I can not rely the environment I am probing in this chapter to be in LTE, so I made use of RADEX to solve molecular abundances from the observed line emission. RADEX makes use of the escape probability approximation, which is a method for estimating the internal radiation field of a cloud in situations (like mine) where only global parameters such as the optical depth and total column density of the cloud are interesting. The escape probability approximation requires an assumption regarding the geometry of the emitting material, and RADEX provides three options. The plane-parallel "slab" geometry of de Jong, Dalgarno, and Chu (1975) is applicable to shocks, and thus I make use of it in my simulations.

The iteration process of RADEX starts from calculating the fractional level populations of the molecule being considered by making use of Statistical Equilibrium (SE):

$$\frac{dn_{\rm i}}{dt} = 0 = \sum_{j\neq i}^{\rm N} n_{\rm j} P_{\rm ji} - n_{\rm i} \sum_{j\neq i}^{\rm N} P_{\rm ij}. \tag{4.12}$$

In this $P_{\rm ji}$ represents interactions which excite molecules into level i while $P_{\rm ij}$ represents interactions which de-excite molecules. The populations of the levels which are being excited or de-excited are indicated by $n_{\rm i}$ and $n_{\rm j}$. In general form $P_{\rm ij}$ and $P_{\rm ji}$ are represented by the equation

$$P_{\rm ij} = \begin{cases} A_{\rm ij} + B_{\rm ij}\bar{J}_\nu + C_{\rm ij} & ({\rm i} > {\rm j}) \\ B_{\rm ij}\bar{J}_\nu + C_{\rm ij} & ({\rm i} < {\rm j}), \end{cases} \tag{4.13}$$

where $A_{\rm ij}$, $B_{\rm ij}$, and $C_{\rm ij}$ are the coefficients for spontaneous emission, stimulated emissi-

on/photo-absorption, and collisional (de-)excitation, respectively. $\bar{J}_\nu$ is the integral of the specific intensity J_ν over the full frequency range, where

$$J_\nu = \frac{1}{4\pi} \int I_\nu d\Omega. \tag{4.14}$$

In the above Ω is the solid angle over which the intensity I_ν is integrated to get specific intensity J_ν. From Equation 4.12 RADEX is capable of calculating the populations of the molecular energy levels, given information about A_{ij}, B_{ij}, and C_{ij} and the radiation field. In the first iteration it has little knowledge of the surrounding radiation field, though, and will calculate J_ν from only background radiation (usually the cosmic microwave background). After calculating the population levels, RADEX proceeds to calculate the optical depths for all lines using

$$\tau = \frac{c^3}{8\pi\nu_{ul}^3} \frac{A_{ul} N_{mol}}{1.064\Delta V} \left[x_l \frac{g_u}{g_l} - x_u \right], \tag{4.15}$$

where c is the speed of light, ν_{ul} is the frequency of the transition, A_{ul} is its Einstein A-coefficient, ΔV is the line full width at half-maximum (FWHM) in units of velocity, N_{mol} is the column density of the molecule being looked at, x_l and x_u are the fractional populations of the lower and upper energy levels, and g_u and g_l are their statistical weights. RADEX will also calculate the source function (as a function of transition frequency) using

$$S_{\nu_{ul}} = \frac{n_u A_{ul}}{n_l B_{lu} - n_u B_{ul}}, \tag{4.16}$$

where the nominator describes the emissive (j_ν) part of the source function, while the denominator describes its extinctive (κ_ν) part. In this equation A_{ul}, B_{lu}, and B_{ul} are the Einstein A- and B-coefficients for their respective transitions. n_u and n_l are the populations of the molecular energy levels in question. This version of the source function assumes "complete angular and frequency redistribution" of the emitted photons, i.e. that the emitted photon line profiles are identical to the absorption and stimulated emission line profiles.

The optical depth and source function can then be used to calculate the radiation field, which is fed into the population level calculations to calculate a new iteration of energy level populations, this time with an added internal radiation field adding to the background radiation. In my case, considering the contribution of the internal radiation field is where the escape probability approximation becomes relevant:

$$\bar{J}_{\nu_{\rm ul}} = S_{\nu_{\rm ul}}(1-\beta), \tag{4.17}$$

where $S_{\nu_{\rm ul}}$ is the freshly calculated source function, and β is calculated using the specific escape probability function, which for the slab model is

$$\beta_{\rm slab} = \frac{1-e^{-3\tau}}{3\tau}. \tag{4.18}$$

After recalculating the excitation levels, a new τ is calculated, and the iteration proceeds following the now established pattern, until τ reaches adequate convergence between subsequent iterations. Convergence is defined by τ changing less than a user-defined (small) amount between two iterations. The final value of τ is then output by the program.

Of course, in my case I am less interested in having τ calculated from $N_{\rm mol}$ than getting $N_{\rm mol}$ from observed I_ν. To be even more precise, I care about the ratio of two column densities derived from the ratio of two line intensity ratios. I do this instead of deriving column densities directly from line intensities because I am faced with a problem of severe parameter space degeneracy, and as the next section describes, I can use column density ratios to decrease the free parameter count by one.

4.4.2 RADEX and the degeneracy of the parameter space

RADEX, in addition to calculating optical depths from column densities, is capable of "running in reverse" with the help of PYTHON scripts provided in the software package. One of these scripts adds a second layer of iteration on top of RADEX's

normal functionality, by seeking a best-fitting column density which corresponds to a set of other freely adjustable simulation parameters which RADEX uses in its normal calculations.

The free parameters are the gas density ($n(H_2)$), temperature (T) and either the molecular column density (N) or the opacity (τ), given a line FWHM Δv. In all following simulations except those used for generating Figure 4.4 (where line width is used to control τ) I set the line width to 1 km s^{-1}, corresponding to the channel width in my data. I assume that the H_2O o/p ratio is 3.0 (Emprechtinger et al., 2013). All column densities involving H_2O presented for the rest of the chapter have made use of this ratio to convert N(p-H_2O) to $N(H_2O)$. The molecular line information RADEX uses is taken from LAMDA, (Schöier et al., 2005) with information for the individual molecules from Rabli and Flower (2010), Yang et al. (2010) and Daniel, Dubernet, and Grosjean (2011).

Constraints must be placed on the parameter space if I am to obtain a non-degenerate solution to my data analysis. Since I am only interested in the relative abundance variations of CH_3OH, CO and H_2O, the line intensity ratios must be converted to column density ratios. Here I discuss what constraints can be put on the gas density, temperature and opacity based on relevant envelope and outflow parameters, and what the effect of varying these parameters has on the final column density ratio.

4.4.2.1 Opacity and column density

Yıldız et al. (2013) have previously shown that the CO 10–9 line wings are optically thin in the objects of this study. For CH_3OH, observations towards exclusively outflow positions, such as L1157 B1 and B2 (Bachiller et al., 1995), result in inferred column densities in the line wings that suggest CH_3OH gas is also optically thin. For the rest of this study I assume that this is true towards the protostellar position as well.

Water emission is known to be optically thick towards the protostellar lines of sight (Kristensen et al., 2011) with opacities > 10 for the ground-state 557 GHz $1_{10} - 1_{01}$ transition. However, given the high critical density of water ($> 10^8$ cm^{-3} for the 987

GHz transition studied here) compared to the H_2 density, the effective critical density is given by $A_{ul}/(C_{ul}\tau)$ where A_{ul} is the Einstein A coefficient, C_{ul} is the collisional rate coefficient and τ is the opacity. Therefore, in the limit where the opacity is high but $n < n_{crit}$, the emission becomes effectively thin and a photon is lost for each radiative decay (Snell et al., 2000), i.e. while the emission may be optically thick it is effectively optically thin.

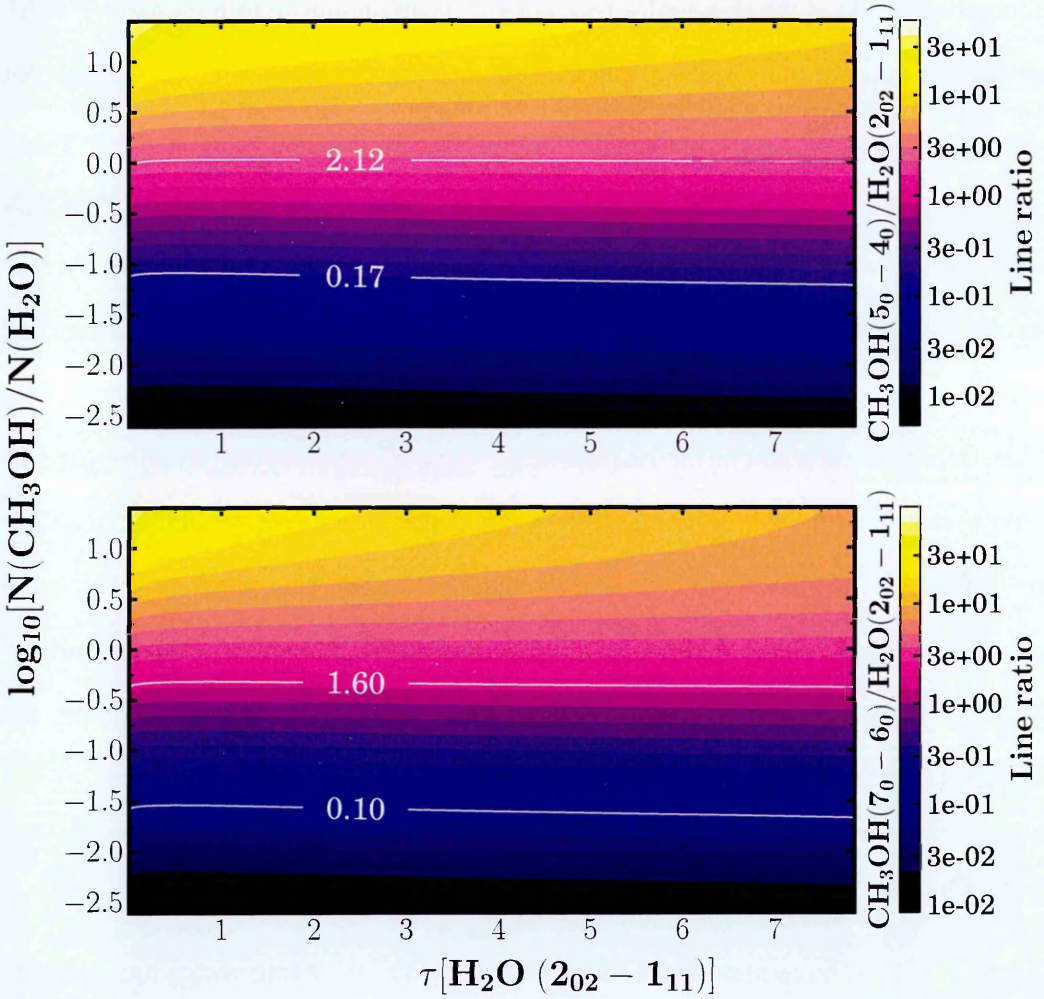

Figure 4.4: The simulated intensity ratio of CH_3OH $5_0 - 4_0$ (top) and $7_0 - 6_0$ (bottom) to p-H_2O $2_{02} - 1_{11}$ as contours of $\tau[H_2O\,(2_{02} - 1_{11})]$) (x axis) and $\log_{10}(N(CH_3OH)/N(H_2O))$ (y axis). The white contour lines show the maximum and minimum observed line intensity ratios for the blue wing of IRAS 4A, as shown in Fig. 4.3. The contour levels are logarithmically scaled. The kinetic temperature is fixed at 200 K and $n(H_2)$ is fixed at 10^6 cm^{-3}.

A grid of RADEX simulations was run to study how increasing opacity affects the conversion of the observed line intensity ratios into column density ratios (Fig. 4.4).

As can be seen, the effects of varying the opacity are limited, much less than a factor of two. The reason is that although the water emission is optically thick, it is effectively thin (see above). I therefore assume for the remainder of this study that the water emission is optically thin.

An additional constraint can be placed on the CH_3OH/H_2O column density ratio. If the relative gas phase abundances of CH_3OH and H_2O trace the relative ice phase abundance of the same molecules, values are expected to range from a few to 30% (e.g. Boogert et al., 2008; Dartois et al., 1999; Gibb et al., 2004; Öberg et al., 2011a; Pontoppidan, van Dishoeck, and Dartois, 2004; Pontoppidan et al., 2003b). Should gas-phase water formation be taking place, the gas-phase abundance ratio would be lower than the ice phase abundance ratio, and $[N(CH_3OH)/N(H_2O)]_{gas} < [N(CH_3OH)/N(H_2O)]_{ice}$. Using $T_{kin} = 200$ K and $n(H_2) = 10^6$ cm^{-3} ensures that the inferred $N(CH_3OH) < N(H_2O)$ is always true for my data, even with optical depth effects accounted for.

4.4.2.2 Temperature

Emission from several transitions in both A-CH_3OH and E-CH_3OH can be seen in the full spectra. Though most of the lines are very weak and/or overlapping with each other, the four strongest lines (The $5_0 - 4_0$ and $7_0 - 6_0$ transitions of $A - CH_3OH$, and the $5_{-1} - 4_{-1}$ and $7_{-1} - 6_{-1}$ transitions of $E - CH_3OH$) can be used to construct rotational diagrams, which make use of rotational transition lines to illustrate energy level populations, and from which it is possible to calculate the rotational temperature of the emitting gas.

To construct a rotational diagram one must assume local thermodynamic equilibrium (LTE), i.e. a state where the energy level populations are thermalized, and where the source function can be described by the Planck function:

$$S_\nu = B(T) = \frac{2h\nu^3}{c^2} \frac{1}{e^{h\nu/kT} - 1}, \tag{4.19}$$

where h is the Planck constant, c is the speed of light, ν is the frequency of the line

transition, k is the Boltzmann constant, and T is the (in this case rotational) temperature of the gas. Furthermore, if an isothermal medium is assumed, this form of S_ν is constant within said medium, and Equation 4.11 simplifies to the form

$$I_\nu(\tau_\nu) = S_\nu(1-e^{-\tau_\nu}) = B_\nu(T)(1-e^{-\tau_\nu}). \tag{4.20}$$

The third assumption is that the isothermal medium has very low optical depth, i.e. $\tau_\nu \ll 1.0$. This further simplifies the intensity to

$$I_\nu(\tau_\nu) \approx B_\nu(T)\tau_\nu. \tag{4.21}$$

The optical depth in this situation can be described by (Goldsmith and Langer, 1999)

$$\tau_\nu = \frac{h}{\Delta V} N_u B_{ul}(e^{h\nu/kT} - 1), \tag{4.22}$$

where N_u is the population of the upper level and B_{ul} is the Einstein B-coefficient of the transition corresponding to frequency ν, and ΔV is the full width half-maximum of the line (which is assumed to have a gaussian profile).

Further assuming that the source is uniform and perfectly contained in the beam of the detector, I can get the relationship between antenna temperature and intensity:

$$T_A = \frac{c^2}{2\nu^2 k} I_\nu. \tag{4.23}$$

Finally combining equations 4.21, 4.22, and 4.23 I get the upper level population as a function of integrated antenna temperature:

$$N_u = \frac{8\pi k \nu^2 \int T_A d\nu}{hc^3 A_{ul}}, \tag{4.24}$$

where A_{ul} is the Einstein A-coefficient, and $\int T_A d\nu$ is equal to $T_A \Delta V$ in the case outlined above.

One final step remains to extract the rotational temperatures, remembering that in

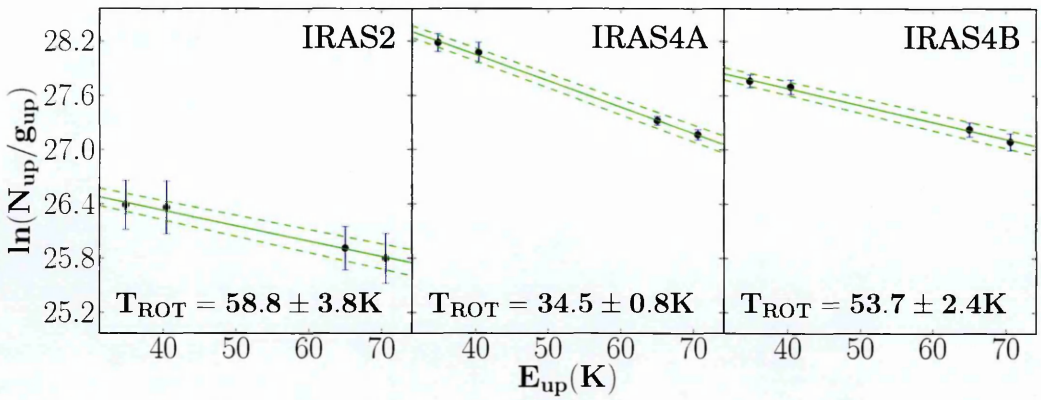

Figure 4.5: Rotational diagrams of CH_3OH for the integrated intensity of both wings in IRAS 2A (left), IRAS 4A (middle), and IRAS 4B (right). The solid green line is the linear fit to the shown points and the dashed green lines show the uncertainty range of the fit as determined by the 1-sigma uncertainties of the fit parameters.

LTE the level populations follow the Boltzmann distribution, in the form:

$$N_u = \frac{N}{Z} g_u e^{-E_u/kT}, \tag{4.25}$$

where N is the column density of the emitting molecules, Z is their partition function, g_u is the statistical weight of the upper energy level, and E_u is its excitation energy. This can be rearranged to the form:

$$\ln\left(\frac{N_u}{g_u}\right) = -\frac{1}{T} E_u[K] + \ln\left(\frac{N}{Z}\right), \tag{4.26}$$

which can be used as the basis of a linear fit $y = ax + b$ into the observed data. In this case $y \equiv \ln\left(\frac{N_u}{g_u}\right)$ (calculated from observations), $x \equiv E_u$ (available from databases), $a \equiv -\frac{1}{T}$, and $b \equiv \ln\left(\frac{N}{Z}\right)$. To get the rotational temperature, one therefore merely needs to fit a straight line to a plot of $\ln\left(\frac{N_u}{g_u}\right)$ against E_u and extract the rotational temperature from the gradient of the fit, given by $-\frac{1}{T}$.

The rotational diagrams constructed in this way are presented in Figure 4.5 for all three objects. I calculate $T_{rot} = 57.8 \pm 4.3K$ for IRAS 2A, $T_{rot} = 34.6 \pm 1.3K$ for IRAS 4A, and $T_{rot} = 53.7 \pm 2.0K$ for IRAS 4B. It is also possible to construct rotational diagrams separately for the red and blue wings of the three objects. In doing so one ends

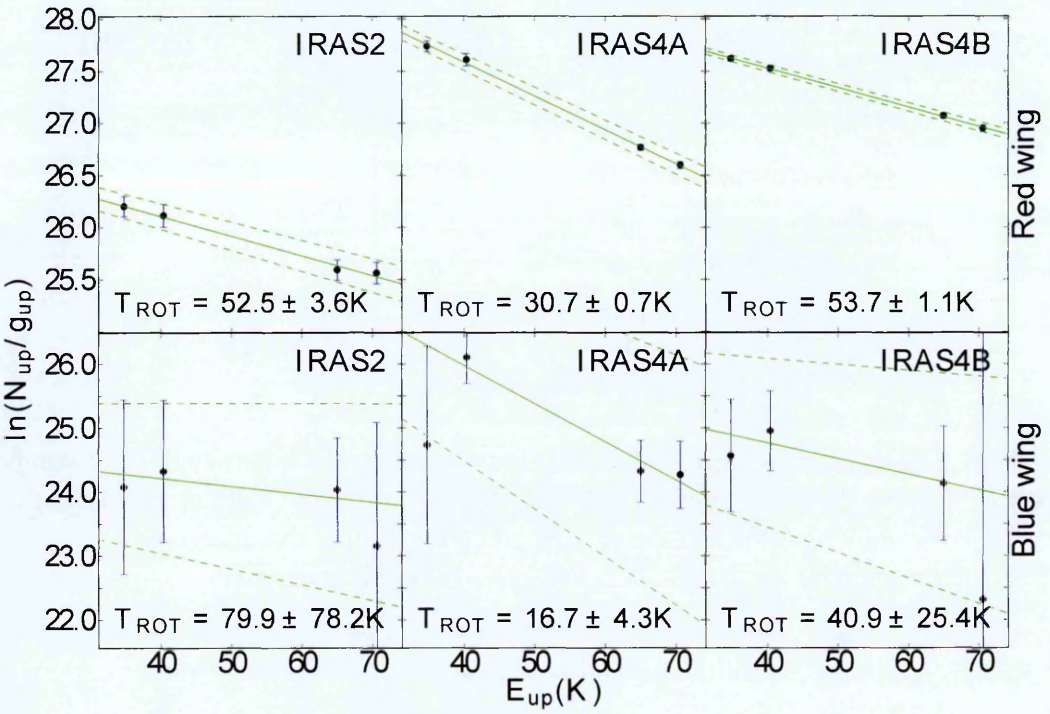

Figure 4.6: Rotational diagrams of CH_3OH for the integrated intensity of the (top row) red and (bottom row) blue wings in IRAS 2A (left), IRAS 4A (middle), and IRAS 4B (right). The solid green line is the linear fit to the shown points and the dashed green lines show the uncertainty range of the fit as determined by the 1-sigma uncertainties of the fit parameters.

up with $T_{rot,red} = 52.5 \pm 3.6K$ and $T_{rot,blue} = 79.9 \pm 78.2K$ for IRAS 2A, $T_{rot,red} = 30.7 \pm 0.7K$ and $T_{rot,blue} = 16.7 \pm 4.3K$ for IRAS 4A, and $T_{rot,red} = 53.7 \pm 1.1K$ and $T_{rot,blue} = 40.9 \pm 25.4K$ for IRAS 4B. The rotational diagrams used to calculate these values are shown in Figure 4.6. The difference in these rotational temperatures compared to those calculated with both wings implies that the excitation conditions may be different towards the red and blue wing of each object.

Regardless of whether they are calculated from the red wing, the blue wing, or both, the rotational diagrams towards the three sources place the CH_3OH gas excitation temperatures above "normal" cloud temperatures of 10-15 K but below outflow temperatures of 100−300 K. The latter range of temperatures is based on a typical warm temperature component seen in CO rotational diagrams of low-mass protostars (Green et al., 2013; Herczeg et al., 2012; Karska et al., 2013; Manoj et al., 2013). Since the rotational temperatures of CH_3OH are a fair amount below this temperature range,

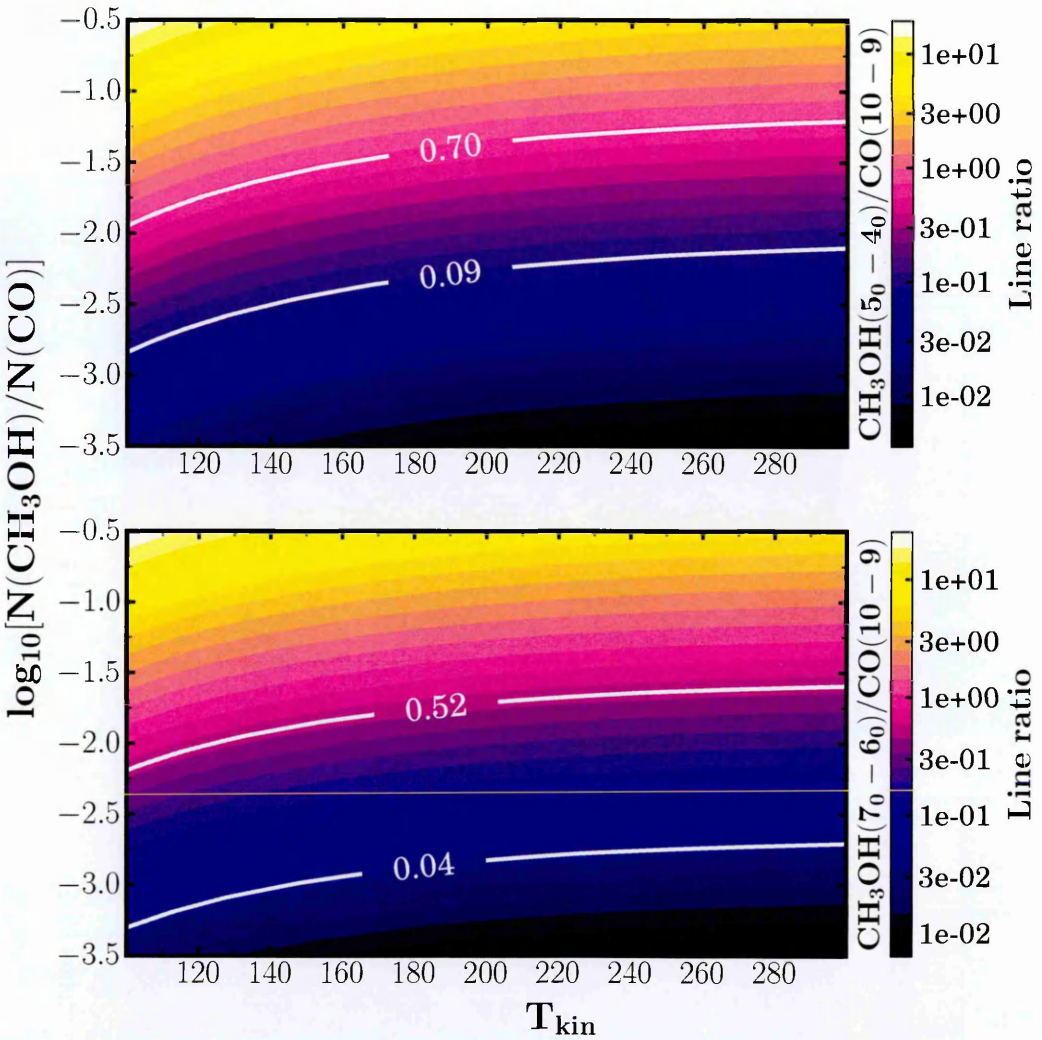

Figure 4.7: The simulated intensity ratio of CH_3OH $5_0 - 4_0$ (top) and $7_0 - 6_0$ (bottom) to CO $10-9$ as contours of T_{kin}) (x axis) and $\log_{10}(N(CH_3OH)/N(CO))$ (y axis). The white contour lines show the maximum and minimum observed line intensity ratios for the blue wing of IRAS 4A, as shown in Fig. 4.3. The contour levels are logarithmically scaled. $n(H_2)$ is fixed at 10^6 cm^{-3} and all lines are optically thin.

I conclude that CH_3OH must not be at LTE, where $T_{kin} = T_{rot}$ would apply. The kinetic temperature range used in the RADEX simulations is then set at the broad 100–300 K range.

Figure 4.7 shows that the inferred CH_3OH/CO column density ratio increases by a factor of ~ 3 from T_{kin} 100 to 300 K at constant density $n(H_2)$ of 10^6 cm^{-3}. The CH_3OH/H_2O column density ratio (Fig. 4.8) shows similar behaviour in the same kinetic temperature range.

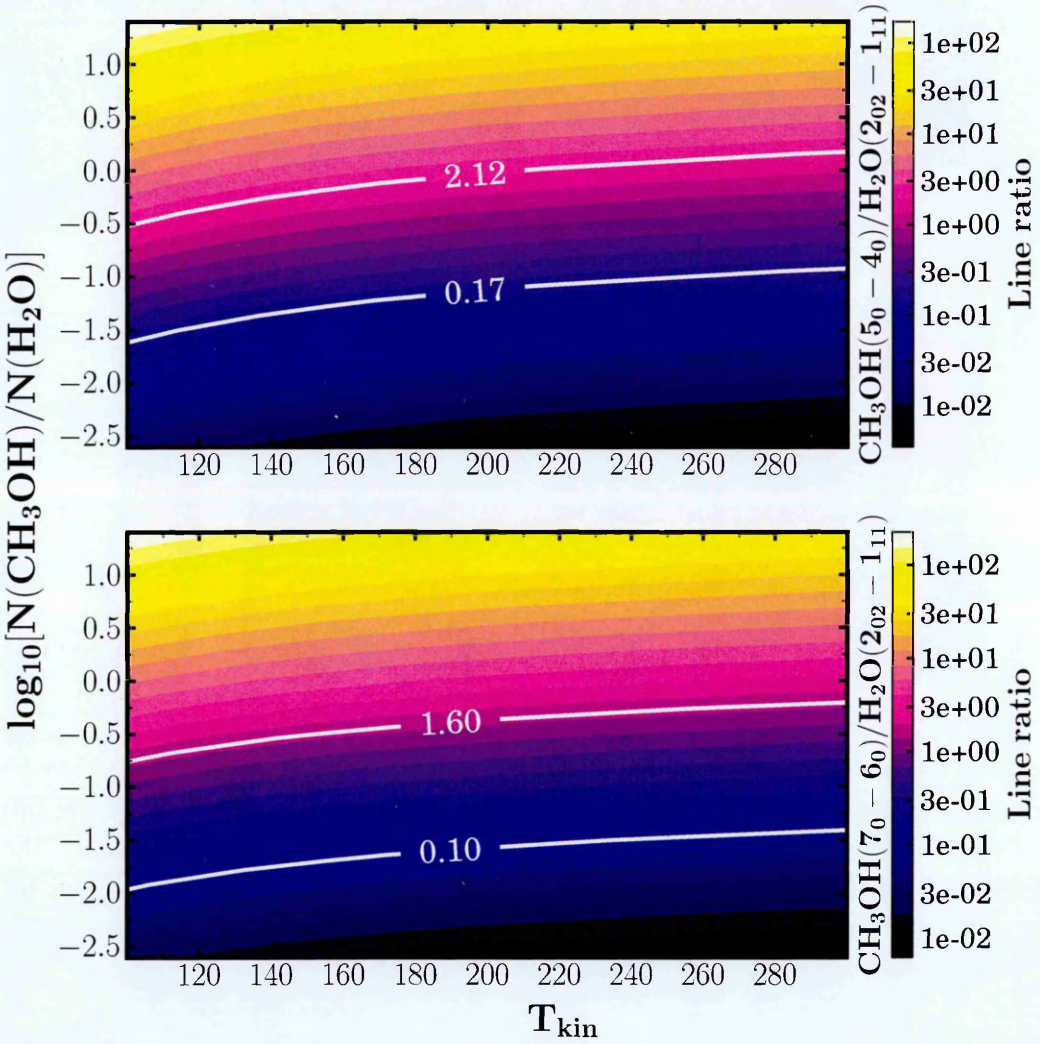

Figure 4.8: The simulated intensity ratio of CH_3OH $5_0 - 4_0$ (top) and $7_0 - 6_0$ (bottom) to p-H_2O $2_{02} - 1_{11}$ as contours of T_{kin}) (x axis) and $\log_{10}(N(CH_3OH)/N(H_2O))$ (y axis). The white contour lines show the maximum and minimum observed line intensity ratios for the blue wing of IRAS 4A, as shown in Fig. 4.3. The contour levels are logarithmically scaled. $n(H_2)$ is fixed at 10^6 cm^{-3} and all lines are optically thin.

4.4.2.3 Density

One way of obtaining estimates of $n(H_2)$ for the outflow material is to use the expected envelope density at a given distance from the protostar (e.g. Kristensen et al., 2012; Yıldız et al., 2013). Kristensen et al. (2012) estimated the envelope density as a function of distance for all sources in this sample based on fits to the continuum SED and sub-mm continuum maps, assuming a power-law density structure. Densities of $\sim 5 \times 10^6$ cm^{-3} were found at a distance of 1000 AU. Further away (2350 AU) the density is typically 10^6 cm^{-3}. Since the entrained gas in the outflow cavity walls can be either compressed by the shocks or expanding into the outflow cavity, I study $n(H_2)$ in the range of $10^5 - 10^7$ cm^{-3}.

The critical densities were listed in Table 4.1. The envelope densities exceed the CH_3OH and CO critical densities, whereas the H_2O critical density is never reached. Thus, the CH_3OH and CO level populations are expected to be thermally excited, whereas H_2O is sub-thermally excited. For CO and H_2O this conclusion has been verified by Herczeg et al. (2012) using excitation analysis of *Herschel* PACS observations. However, the rotational diagrams created for CH_3OH indicate that it has a rotational temperature ($\sim$ 50 K) a good deal below what the expected gas kinetic temperatures ($\gtrsim$ 100 K) are in the outflow. The critical density for CH_3OH is only barely below the density of the medium, though, and thus the likely scenario is that its rotational temperature does not quite match the kinetic temperature yet. This implies that the likely correct kinetic temperature and H_2 density are in the lower end of the temperature and density range I am exploring.

The effect the density range has on the line intensity ratio to column density ratio translation can be examined by running a grid of RADEX simulations in which τ and $T_{\rm kin}$ are kept constant (optically thin and 200 K, respectively) and $n(H_2)$ and the column density ratio are varied to produce line intensity ratios comparable to the observations. As both the CH_3OH and CO 10–9 line wings are optically thin (Yıldız et al., 2013, for CO), they form a good benchmark for exploring the effects of the physical environment

Table 4.5: Physical conditions in the RADEX simulations

Parameter	Value	Range	Effect(*)
$\tau(H_2O)$	Optically thin(a)	$0-20$	<0.1 dex
T_{kin}	200 K	$100-300$ K	0.5 dex
$n(H_2)$	10^6 cm^{-3}	10^5-10^7 cm^{-3}	1.0-1.5 dex(b)

(*) dex is shorthand for "order of magnitude"

(a) The H_2O emission is optically thick but effectively thin (see text and Snell et al., 2000).

(b) $n(H_2)$ has a greater effect on $N(CH_3OH)/N(H_2O)$ than on $N(CH_3OH)/N(CO)$

on the simulated line ratios whilst allowing me to ignore τ. The results of the RADEX simulation grid are shown as a contour plot in Figure 4.9, where they are compared with the observed ratios of CH_3OH/CO in the blue wing of IRAS 4A.

Figure 4.9 shows that variations of $n(H_2)$ across the assumed range can produce changes in the $N(CH_3OH)/N(CO)$ ratios up to a factor of 10, but that the increase depends only weakly on $n(H_2)$, as is expected when emission is thermalised and optically thin. The same exercise can be made for CH_3OH versus H_2O and the RADEX results are presented in Figure 4.10. Since H_2O excitation is sub-thermal, the effect of $n(H_2)$ on this ratio is greater than for CH_3OH versus CO. The resulting systematic variation in this case is ± 1 order of magnitude and varies almost linearly with density.

4.4.3 Molecular column density ratios

With the appropriate range of physical conditions established (summarised in table Table 4.5), it is now possible to address my original questions by exploring how the observed line intensity ratios translate into column density ratios. The excitation conditions are assumed to be constant as a function of velocity. In order to convert N(p-H_2O) into $N(H_2O)$ I have assumed a constant ortho-to-para ratio of 3:1 and thus multiplied all calculated p-H_2O column densities by 4. First I examine the CH_3OH/CO column density ratio in order to quantify how much CH_3OH from the grains reaches the gas phase intact. Second, I looked at the CH_3OH/H_2O ratio, to study how well the ratio of methanol to water matches their usual solid-state abundances. The resulting column

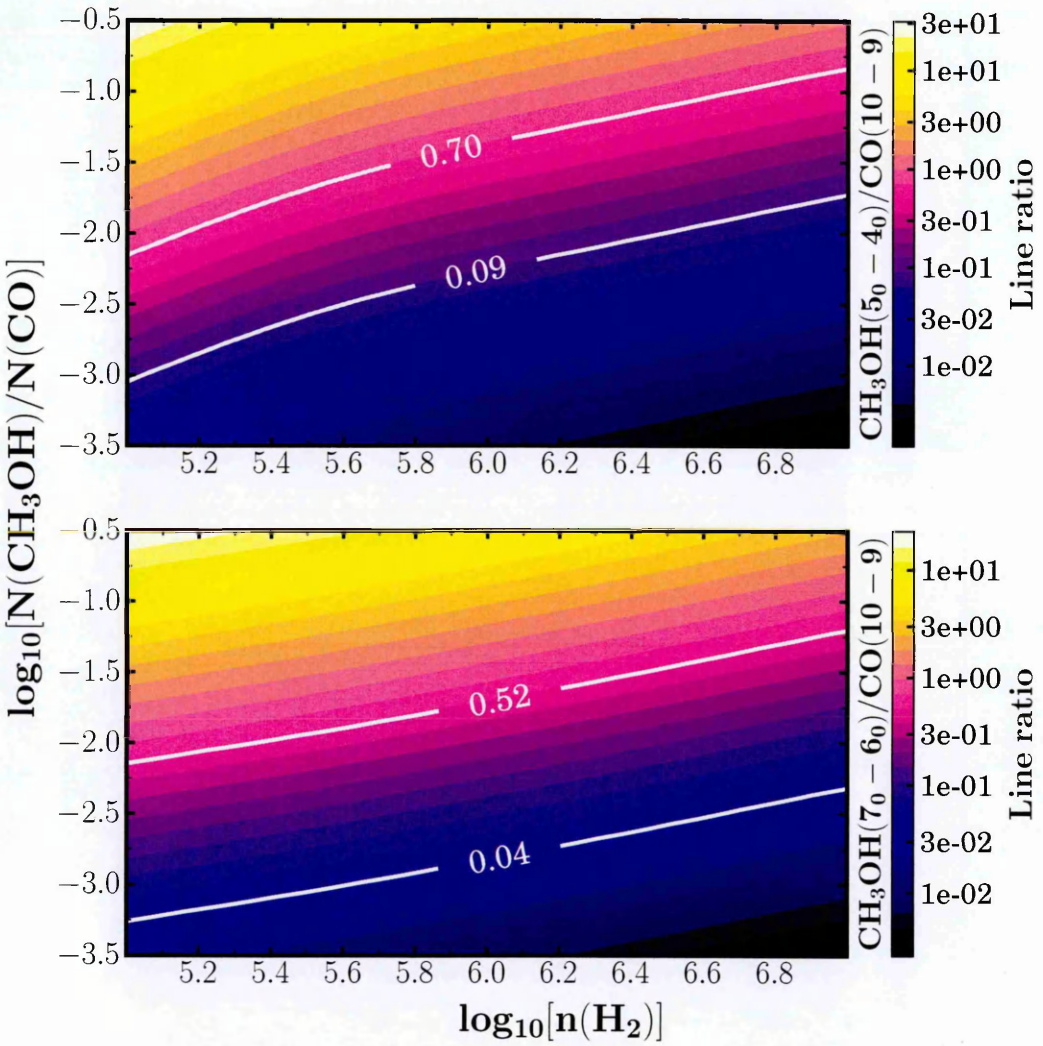

Figure 4.9: The simulated intensity ratio of CH_3OH $5_0 - 4_0$ (top) and $7_0 - 6_0$ (bottom) to CO $10 - 9$ as contours of $\log_{10}(n(H_2))$ (x axis) and $\log_{10}(N(CH_3OH)/N(CO))$ (y axis). The white contour lines show the maximum and minimum observed line intensity ratios for the blue wing of IRAS 4A, as shown in Fig. 4.3. The contour levels are logarithmically scaled. The kinetic temperature is fixed at 200 K and all lines are optically thin.

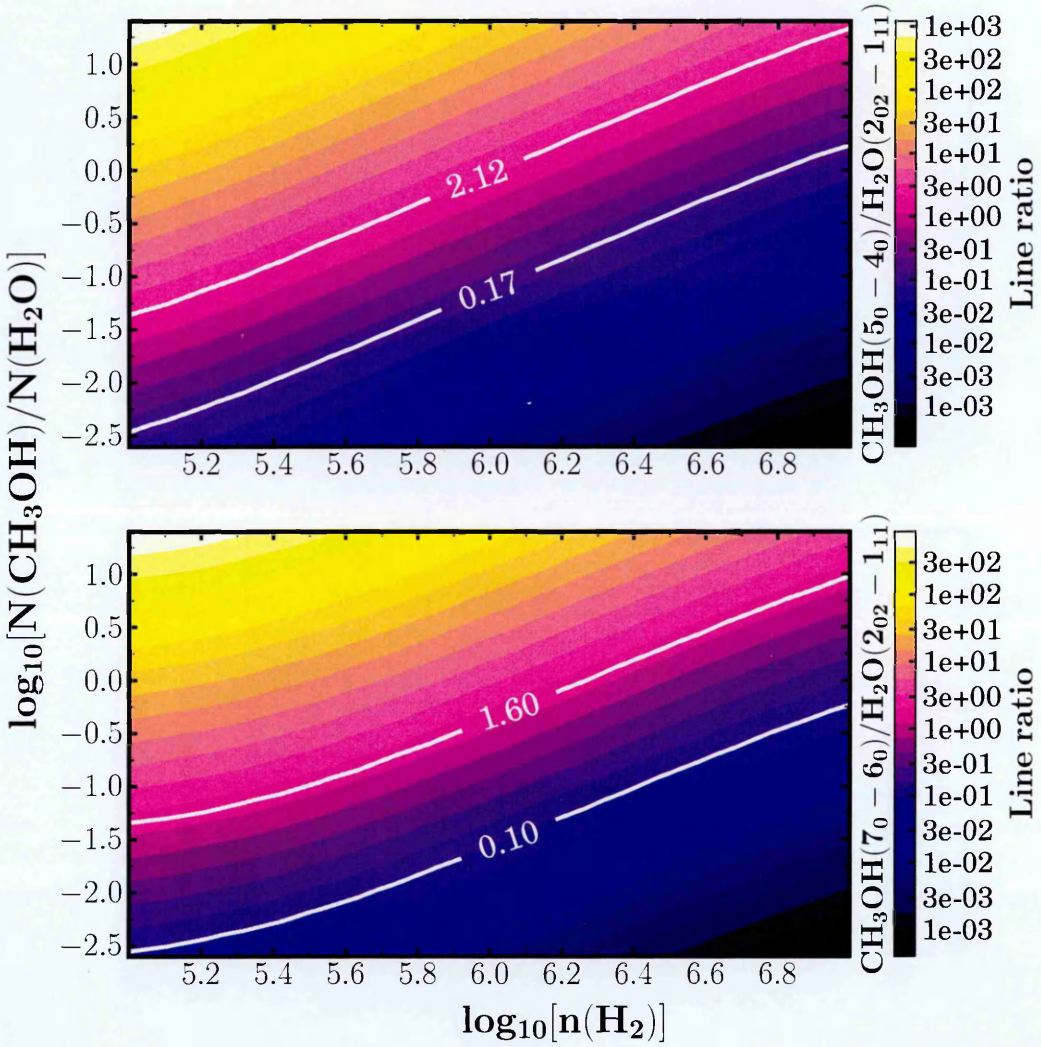

Figure 4.10: The simulated intensity ratio of CH_3OH $5_0 - 4_0$ (top) and $7_0 - 6_0$ (bottom) to p-H_2O $2_{02} - 1_{11}$ as contours of $\log_{10}(n(H_2))$ (x axis) and $\log_{10}(N(CH_3OH)/N(H_2O))$ (y axis). The white contour lines show the maximum and minimum observed line intensity ratios for the blue wing of IRAS 4A, as shown in Fig. 4.3. The contour levels are logarithmically scaled. The kinetic temperature is fixed at 200 K and all lines are optically thin.

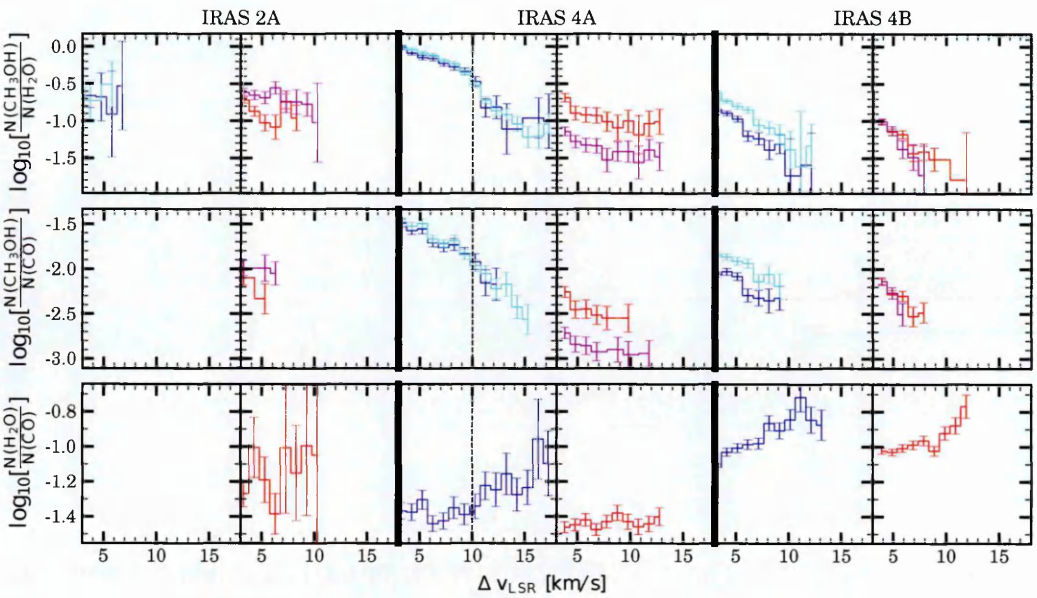

Figure 4.11: Line intensity ratios converted to their corresponding column density ratios using the physical parameters presented in Table 4.5. The ratios plotted in the two top rows were calculated using both the $5_0 - 4_0$ (red and blue) and $7_0 - 6_0$ (cyan and magenta) lines of CH_3OH. The dashed line at $\Delta v_{LSR} \approx 10$ km s^{-1} in the plots of the blue wing of IRAS 4A represents the approximate velocity where I see a gradient change (compared to lower velocities) in the behaviour of $N(CH_3OH)/N(H_2O)$ and $N(H_2O)/N(CO)$. The line intensity ratios from which the column density ratios of the bottom row are calculated were taken from Yıldız et al. (2013). Velocity is given as a magnitude with respect to the source velocity.

density ratios are summarised in Table 4.6.

The CH_3OH/CO column density ratios are shown in the middle row of Fig. 4.11. Since the line wing emission is assumed to be optically thin, the column density ratio is proportional to the line ratio. In all sources, the derived CH_3OH/CO column density ratio decreases with increasing velocity by up to a factor of five (in the case of the blue wing of IRAS 4A). The CH_3OH/CO column density ratio is on average $\sim 10^{-3}$. I follow the example of Yıldız et al., 2013 and assume a CO/H_2 abundance of 10^{-4}. This value may be too high by a factor of a few (Dionatos et al., 2013; Santangelo et al., 2013), or too low by a factor of a few (Lacy et al., 1994). When using this CO abundance the derived CH_3OH abundance is of the order of 10^{-7}, consistent with values reported towards other outflows (e.g. Bachiller et al., 1995; Tafalla et al., 2010).

The CH_3OH/H_2O column density ratio also decreases with increasing velocity offset, except towards IRAS 2A (Fig. 4.11 top row). The average column density ratio

Table 4.6: Column density ratio ranges from the lowest (3 km s^{-1}) to highest velocities (10−18 km s^{-1}, depending on source).

Source	$N(CH_3OH)/N(CO)$[a]		$N(CH_3OH)/N(H_2O)$[a]	
	3 km s^{-1}	max(v)	3 km s^{-1}	max(v)
IRAS 2A - blue	...	...	2(−1)	2(−1)
IRAS 2A - red	1(−2)	1(−2)	2(−1)	2(−1)
IRAS 4A - blue	3(−2)	3(−3)	1(0)	8(−2)
IRAS 4A - red	5(−3)	3(−3)	3(−1)	8(−2)
IRAS 4B - blue	1(−2)	4(−3)	2(−1)	3(−2)
IRAS 4B - red	8(−3)	3(−3)	1(−1)	2(−2)

[a] $a(b) = a \times 10^b$.

for all objects is $\sim 10^{-1}$. The $N(CH_3OH)/N(H_2O)$ ratios calculated from the two different rotational lines of CH_3OH are almost identical in the case of the blue wing of IRAS 4A, but noticeably different in the case of the red wing, by about a factor of 3, although the two transitions show the same trend. Up to 10 km s^{-1}the decrease in CH_3OH column density with respect to both CO and H_2O match each other closely and this is also reflected in the the H_2O abundance being almost constant when compared to CO 10−9, as is seen in the bottom row of Figure 4.11. Beyond 10 km s^{-1}this behaviour changes particularly in the blue wing of IRAS 4A and possibly in the red wing of IRAS 4B as well, with $N(CH_3OH)/N(H_2O)$ decreasing slightly more rapidly than $N(CH_3OH)/N(CO)$. The change is also seen in $N(H_2O)/N(CO)$ which begins increasing at velocities above 10 km s^{-1}.

4.5 Discussion

4.5.1 Magnetohydrodynamic shocks in young stellar objects

Magnetohydrodynamics (MHD) is a specialized area of fluid dynamics, which combines the equations of fluid motion with Maxwell's equations to create equations capable of describing the behaviour of charged fluids (which the ISM can be counted as, in this context) in the presence of both an ambient magnetic field and one created by the movement of the fluid itself. The full derivations of fluid motion relevant to de-

Figure 4.12: Clouds condensing behind the bow shock of an F/A-18 fighter jet as it accelerates to supersonic speeds. Image source/credit: NASA/Ensign John Gay, USS Constellation, U.S. Navy

scribing MHD shocks in YSOs are neither fully relevant nor practical to present within the scope of this thesis, but understanding how some of the derived physics works is useful in understanding the origin of the line emission I see in the observed spectra.

When speaking of shocks generated when outflows impact ISM envelopes in YSOs, an excellent analogy comes from the shock fronts forming in front of aircraft moving at supersonic speeds, such as the one shown in Figure 4.12. In this situation the density fluctuation in the air pushed along by the jet is trying to move faster than the maximum density propagation speed (the sound speed), which causes air to "pack" in a bow-like shape starting from the tip of the aircraft. The air packed in this way is both rapidly heated and compressed in places where the supersonic disturbance meets the non-supersonic air, and a bow shock is formed.

A similar event can happen in the ISM, when rapidly moving gas collides with slow-moving gas. In the ISM, however, the "Alfvén speed" of the material is more

than the sound speed, and more importantly there are two different Alfvén speeds which are relevant to ISM shock conditions: one for neutral material, and one for ions. The Alfvén speed for neutrals is given by

$$V_{\mathrm{A,n}} = \frac{B}{\sqrt{4\pi(\rho_{\mathrm{i}} + \rho_{\mathrm{e}} + \rho_{\mathrm{n}})}}, \tag{4.27}$$

and for ions it is:

$$V_{\mathrm{A,i}} = \frac{B}{\sqrt{4\pi(\rho_{\mathrm{i}} + \rho_{\mathrm{e}})}}, \tag{4.28}$$

where B is the strength of the magnetic field, and ρ_{i}, ρ_{e}, and ρ_{n} are the *mass* densities of ions, electrons and neutrals in the medium, respectively.

To aid the interpretation of these speeds, the Alfvénic Mach number for the neutrals is defined as:

$$M_{\mathrm{A,n}} = V_{\mathrm{S}}/V_{\mathrm{A,n}}, \tag{4.29}$$

and similarly for the ions as:

$$M_{\mathrm{A,i}} = V_{\mathrm{S}}/V_{\mathrm{A,i}}, \tag{4.30}$$

where V_{S} is the velocity of the fast-moving material relative to the material it is hitting, i.e. the velocity of the material in the shock frame.

In a medium consisting only of neutral material, creating a shock front analogous to that of the supersonic aircraft merely requires that $M_{\mathrm{A,n}} > 1$, which generates conditions where information about the oncoming shock wave propagates faster than the unshocked material can "prepare" for it. However, environments such as the outflow of a YSO contain a noticeable fraction of ions, and they can act as an intermediary for "warning" the unshocked material of the incoming shock. This causes the incoming shock front to smooth out considerably, and leads to significantly less heating of the shocked material as would happen if the Alfvén velocity for ions was lower than the shock velocity. The smoothed out shock is called a continuous shock or C-shock, and the unsmoothed shock is called the jump shock or J-shock. The density, velocity and temperature behaviour of these shocks is sketched in Figure 4.13.

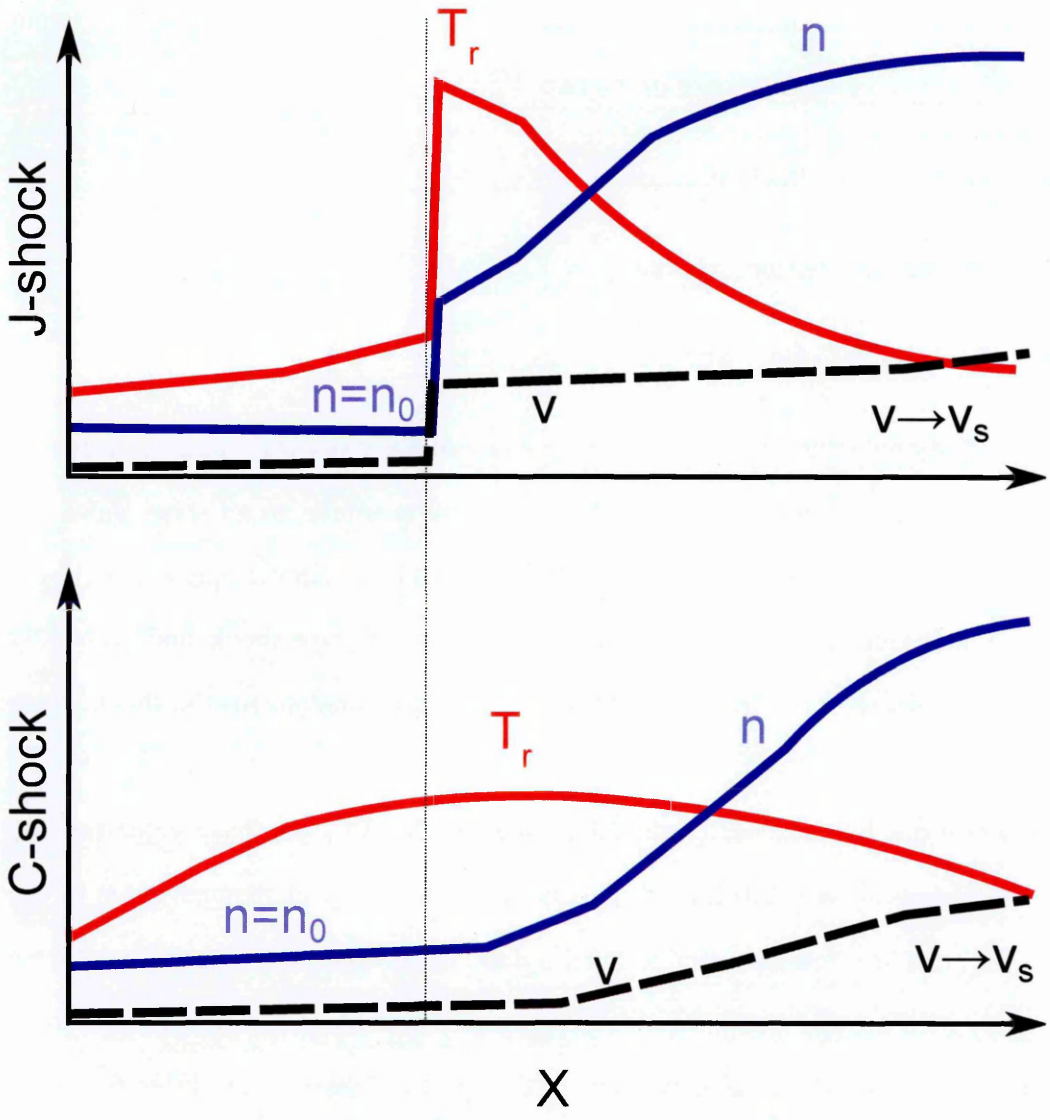

Figure 4.13: A cartoon representation of how the density (blue line), temperature (red line) and velocity (black dashed line) of the pre-shock material behaves before (left of black dotted line) and after (right of black dotted line) the shock front of a jump (J; top figure) or continuous (C; bottom figure) shock. The X axis represents a 1-dimensional cut-out of the distance, with the black dotted line representing the point where the neutral materials initially collide with each other. Reproduced based on Hollenbach and McKee (1989), Draine and McKee (1993), and Kristensen, L.E. (private communication).

Observations show that most of the mass in the YSO outflow consists of neutral material, and that therefore $\rho_n \gg \rho_i$. It follows from comparing Equations 4.27 and 4.28 that $V_{A,n} \ll V_{A,i}$ and thus it is found that the velocity of the high-velocity material will trace three types of interactions with the low-velocity material in YSOs depending on the relative velocity difference of the two, V_s:

- Non-shocked interaction, where $V_s < V_{A,n} < V_{A,i}$
- C-shocked interaction, where $V_{A,n} < V_s < V_{A,i}$
- J-shocked interaction, where $V_{A,n} < V_{A,i} < V_s$

One additional intermediate category of shock that can occur in YSOs is a steady-state CJ shock (e.g. Lesaffre et al., 2004), which starts similar to a C-type shock but then evolves into a J-type shock. This shock is caused by a specific magnetic field geometry which decelerates the ions in the shock front of a C-type shock, and eventually causes an adiabatic shock front to form which eventually transforms the shock into a J-type.

Observations by Crutcher et al. (2010) suggest that $V_{A,n}$ can have value ranging from ~ 0.2 kms^{-1} to ~ 2.0 kms^{-1}, depending on the level of magnetisation of the shock. $V_{A,i}$ can be a few thousand to ten thousand times this. If my observations were to directly measure the stellar wind which causes J-shocks, the emission from them would lie well beyond the velocity range of the spectra shown so far. THerefore I am not observing the gas entrained in the shock directly, but rather the gas that has met the shock and been deflected by it. To use another analogy, it is not the stream of water from the fire hose I am observing, rather I am observing the deflected streams of water rebounding from the proverbial wall that is the YSO envelope cavity wall.

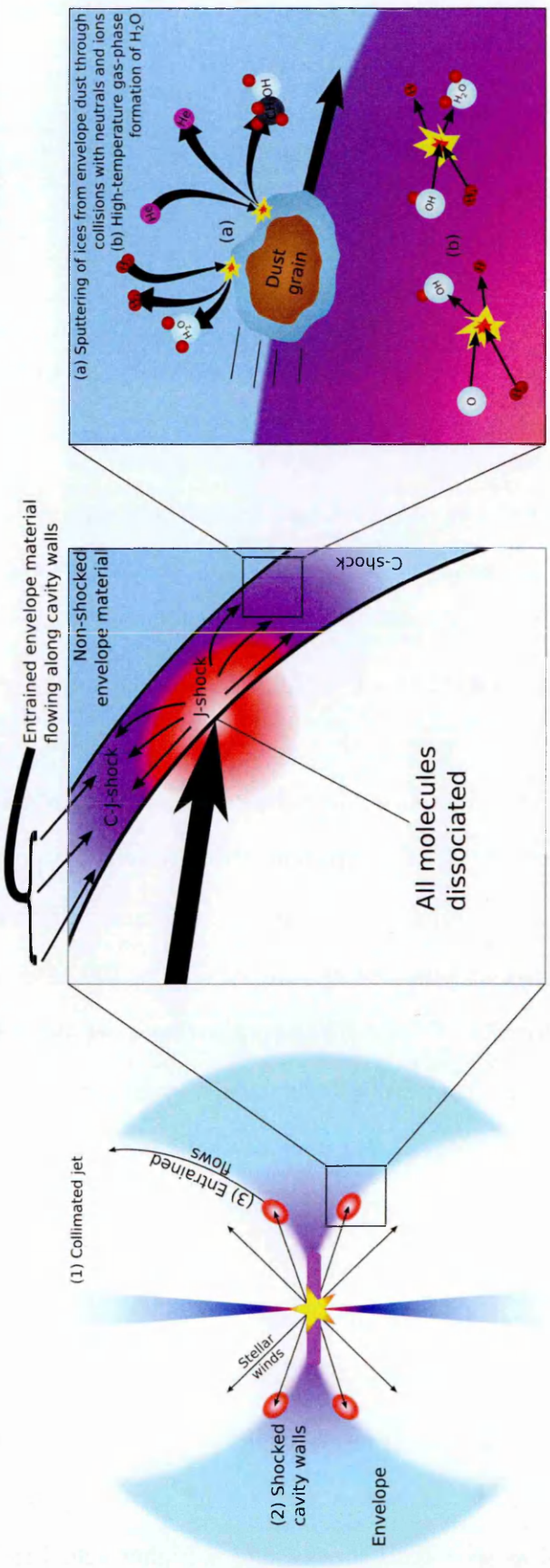

Figure 4.14: A cartoon (not to scale) illustrating the flow of material in the outflow regions of a young stellar object. The left part shows an overview of the region around the YSO, with the protostar and its protoplanetary disk in the middle of the envelope. A closer view of one of the shocked regions is illustrated in the middle part. The large arrow represents a maximum point of impact of the stellar wind on the envelope material, where the wind creates a very high-temperature (several 10^4 K) J-type shock which causes the dissociation of all affected molecules. Further away from the impact point a C-J-type shock (steady state shock) is created and even further away a stable C-type shock develops. In addition to the deflected material of the wind flowing along the cavity walls, material from the envelope is entrained and forced to flow along the direction of the deflected wind. The right figure shows the relevant chemical processes happening in the shocked material: (a) the sputtering of ices from grain surfaces by collisions with neutrals and ions, and (b) the high-temperature gas-phase formation of water.

4.5.2 Velocity structure and the origin of the line emission

As shown in Figure 4.14, the protostellar wind and jet interact with the envelope in several locations:

1. the stellar wind around the highly collimated bi-polar jet;
2. the shocked material where the stellar winds collide with the outflow cavity walls;
3. the entrained material of the envelope, swept up but not necessarily shocked by the deflected stellar wind material.

The last two of these are the environments most relevant to this study. In a scenario reminiscent of bow shocks (Smith, Khanzadyan, and Davis, 2003, also illustrated by the middle part of Figure 4.14), the point of impact between the stellar wind and outflow cavity walls will be dissociative and the shock will be J-type. The stellar wind colliding with the envelope material also becomes deflected by the cavity walls and sweeps up the surface layers in an entrained flow. The emission from the entrained flow is what is traced by the different velocity components of the observed spectra, and these components are what I refer to for the remainder of the chapter when discussing velocities. In the absence of other dissociating sources such as UV fields the J-shock typically takes place at velocities of $\sim 25{-}30\ \mathrm{km\,s^{-1}}$ (Flower et al., 2003; Lesaffre et al., 2013). Beyond this I see no line emission in any of the sources included in this study. Further removed from the impact point the post-shock gas has had time to cool down and molecules have had a chance to reform, while at the same time fresh molecular material from the envelope is being exposed to lower-velocity (secondary) shocks originating in the bow wings of the original shock. Depending on the local magnetic field geometry, these shocks may be C-type or non-dissociative J-type (C-J-type) shocks. In my observations this corresponds to line emission at velocities greater than a few $\mathrm{km\,s^{-1}}$: the line wings at the lowest velocities ($\sim 3{-}15\ \mathrm{km\,s^{-1}}$) probe the entrained envelope material as well as secondary shocks, and at higher velocities ($\gtrsim$

15 km s^{-1}) they probe the directly shocked material. The lowest-velocity material ($\lesssim$ 3 km s^{-1}) is only related to the quiescent envelope, and is ignored in my analysis.

The physical conditions prevailing in the shocked regions and entrained flows enables a number of chemical and physical processes to happen, two of which are especially relevant to my study and are illustrated in the right part of Figure 4.14. The sputtering effects (a) are relevant in entrained material where the gas and dust is not utterly destroyed in the process (C-J and C-shocks). Water and methanol ice that is sputtered from dust grains is expected to be present in the gas phase in both C-J- and C-shocked regions i.e. at velocities below $\sim$25 km s^{-1}. The gas-phase formation reaction of water (b) is expected to activate when sufficiently high temperatures ($T \gtrsim 200$ K) are reached in the shocked regions, and these regions are hypothesized to have an excess of water compared to CH_3OH and H_2O gas abundances derived from the solid-phase. This temperature threshold is met within the velocity range occupied by the C- and C-J-shocked regions and consequently will potentially have water formation happening, until the shock velocities exceed the physical conditions where H_2O will be dissociated.

This translation of velocity components in the spectra into different physical regions in the shock outflow cavity (summarised in Table 4.7) provides sufficient context for the rest of this discussion, in which I look at the results of the previous sections to answer the two questions I asked at the beginning of this chapter:

1. How much, if any, methanol is being destroyed in the outflows?

2. Is high-temperature water formation taking place in the outflows?

Table 4.7: Approximate observed velocity ranges for the different physical and chemical processes.

Approx. v range	Physical process	Chemical process
$\sim 3-10\ \mathrm{km\,s^{-1}}$	Secondary CJ and C shocks	CH_3OH and H_2O sputtered and partly destroyed during sputtering; CH_3OH destruction > H_2O destruction
$\sim 10-25\ \mathrm{km\,s^{-1}}$	Secondary CJ and C shocks	CH_3OH sputtered + partly destroyed during sputtering/through reactions with H; H_2O sputtered, partly destroyed by sputtering but also reformed
$\sim 3-10\ \mathrm{km\,s^{-1}}$	Secondary shocks entraining envelope material	Additional sputtering and associated destruction?
$\gtrsim 25\ \mathrm{km\,s^{-1}}$	Dissociative shocks	CH_3OH and H_2O destroyed completely; only H_2O reforms and is offset in velocity by the shock

4.5.3 Molecular destruction in outflows

In dissociative J-type shocks, reactions with H are the most efficient way to destroy CH_3OH and other grain products such as water and ammonia. The activation energy for methanol reacting with H ($\sim$ 2270–3070 K, Sander et al. 2011) is even lower than that of ammonia which has already been shown to be destroyed in post-shock gas (Viti et al., 2011). Destroying water in a similar manner is more inefficient because the activation energy is higher ($\sim 10^4$ K), but at shock velocities of 25–30 $\mathrm{km\,s^{-1}}$ the kinetic temperature is already $> 2\times10^4$ K (McKee and Hollenbach, 1980) and so H_2O will also collisionally dissociate. I can readily observe this difference in activation energies between CH_3OH and H_2O destruction by H (see Fig. 4.2). In all cases H_2O emission in the wings tapers off below the $1-\sigma$ noise level at significantly higher velocities ($\Delta v_{\mathrm{LSR}} > 25$ $\mathrm{km\,s^{-1}}$) than the CH_3OH emission, which drops below noise levels at approximately $\Delta v_{\mathrm{LSR}} = 10$ $\mathrm{km\,s^{-1}}$. The exception to this is IRAS 4A, which still shows trace methanol emission at up to 18 $\mathrm{km\,s^{-1}}$ and water emission at approximately 35 $\mathrm{km\,s^{-1}}$. In other words, methanol is undetectable beyond these velocity ranges most likely because it does not exist there.

The gas-phase CH_3OH abundances derived from the middle row of Figure 4.11 were compared to the expected solid phase CH_3OH abundances. Assuming that equal abundances of envelope CH_3OH gas originate from dust grains in both the low-velocity and high-velocity regimes, the data in Figure 4.11 shows that at high velocities, some fraction of CH_3OH originating from grain surfaces (90–99%) is "missing" in the gas phase. This CH_3OH is either not being sputtered from the grains, or (as is more likely) is being destroyed in the sputtering process or in the gas phase.

Sputtering occurs when a neutral species, typically H_2, H or He, collides with the ice mantle of a dust grain with enough kinetic energy to release the ice species into the gas phase. Sputtering at shock velocities down to 10 $\mathrm{km\,s^{-1}}$ predominantly takes place in C-type shocks (Flower and Pineau des Forêts, 2010), where the negatively charged dust grains stream past the neutral gas. At these velocities the kinetic energy

of each particle is of the order of 1 eV. Sputtering yields have been estimated theoretically, but not measured in the laboratory, although 1 eV is significantly higher than the desorption energy barrier of CH_3OH or H_2O (both below 0.5 eV, Burke and Brown 2010; Fraser et al. 2001). However, given the high kinetic energy, it is likely that at least some molecules could be destroyed, rather than simply being desorbed by the sputtering process. This is more likely for CH_3OH than H_2O, given that the gas-phase dissociation energy of CH_3OH to H+ CH_2OH is around 4 eV compared to just over 5 eV for H + OH (Blanksby and Ellison, 2003). Furthermore, strong evidence exists that dissociation barriers are lowered in the condensed phase (Woon, 2002). However, these sputtering processes are occurring in the same regions where I also expect methanol destruction by high-temperature gas phase reactions with hydrogen atoms. Consequently, although my observations cannot distinguish between the two processes, it is is clear that as the methanol abundance drops in the line wings, the sputtered methanol is being destroyed more readily than the water.

4.5.4 Water formation in outflows

At the highest outflow velocities, higher than those where I observe any methanol emission, water is readily observed. As discussed in Section 4.5.3, any water at even higher velocities will be destroyed by the J-shock and this is suggested by the lack of detectable H_2O emission beyond $\sim 25-30$ km s^{-1}. Though the water destroyed in the J-shock is expected to eventually re-combine via the high-temperature gas-phase reaction, the velocity of the re-formed water is observable only in the "offset" component directly tracing the shock itself. This component has been removed in the decomposition of the H_2O spectra used in this analysis, and was previously discussed in Kristensen et al., 2013. Below J-shock velocities, any water emission observed must have originated from H_2O formed through gas-phase synthesis directly in the warm shocked gas. In my data the column density ratio of H_2O/CO starts increasing at velocities higher than ~ 10 km s^{-1} with respect to the source velocity. I conclude that the

shift between water release from the grains and gas-phase water synthesis switches on at this velocity, since the water abundance remains constant with respect to CO (Yıldız et al., 2013) and CO is not destroyed unless the shocks have significantly higher velocities ($\sim$80 km s^{-1}; Neufeld and Dalgarno, 1989). This is especially apparent in the blue wing of IRAS 4A and the red wing of IRAS 4B; the water abundance increases by a factor of $\sim$2, due to gas phase formation. Below $\sim$10 km s^{-1}the data shows that the water abundance remains constant with respect to CO and I interpret this to indicate that gas-phase water (and methanol) at low velocities originated entirely from sputtered ice. There are two possibilities for this low-velocity component: (i) if we consider the outflows to be conical shells (e.g. Cabrit and Bertout, 1986, 1990) then a part of the cone, when projected onto the plane of the sky, will have a radial velocity component close to zero even if the 3D velocity in the cone is not zero anywhere; (ii) the post-shock or entrained material has decelerated and cooled down but has not had time to freeze out again yet (Bergin, Neufeld, and Melnick, 1998). A combination of both possibilities may naturally also be at play. Observations at higher angular resolution are required to break this degeneracy by pinpointing where the emission from the lower-velocity line wings originates spatially: inside the outflow cavity (option 1) or closer to the envelope (option 2).

4.6 Concluding remarks

In this chapter observations of H_2O, CH_3OH and CO line emission have been combined with RADEX simulations to constrain the gas-phase abundance variations of water and methanol towards three low-mass YSOs: IRAS 2A, IRAS 4A and IRAS 4B. It was found that:

1. The CH_3OH/CO column density ratio decreases by up to one order of magnitude with increasing velocity.

2. The abundance of CH_3OH in the shocked gas is more than 90% lower than that

reported for CH_3OH ice in the cold envelope. Given that the CO abundance is unaffected by shock chemistry across the velocity range investigated, this implies that CH_3OH is destroyed either during the ice sputtering process from dust grains or through gas-phase reactions with H in the outflow.

3. The H_2O/CO column density ratios increase by $\sim$ a factor of two, with the increase beginning at velocities above $\sim$10 km s^{-1}. This suggests that the gas-phase formation of water is active and significant at velocities higher than 10 km s^{-1}. No discontinuity is observed in the water column density as a function of velocity, implying that the transition is smooth and continuous between the observed water originating from ice sputtering and gas-phase routes.

4. The column density ratio of CH_3OH/H_2O also decreases with increasing velocity, closely matching the same trend in CH_3OH/CO column density ratio. Based on my prior conclusions, this implies that both H_2O and CH_3OH are sputtered from ices in these shocks, but that only CH_3OH is being destroyed, and no gas-phase H_2O formation is occurring, at least at velocities below 10 km s^{-1}.

5. In the blue wing of IRAS 4A, the CH_3OH/H_2O column density ratio decreases more steeply at velocities in excess of $\sim$10 km s^{-1} than the CH_3OH/CO column density ratio. This traces the high-temperature gas-phase formation of water in this higher velocity regime.

Consequently, gas-phase CH_3OH and H_2O abundances in shocked regions depend on the complex interplay between ice sputtering mechanisms, gas-phase destruction processes and high-temperature formation reactions. These conclusions hint towards future observational and experimental requirements to further constrain the physics and chemistry of H_2O and CH_3OH in outflows. In particular, trying to observe and quantify the efficiency of CH_3OH and H_2O ice sputtering by neutrals in a laboratory environment would contribute towards verifying and/or refuting the two main conclusions of this work; whether or not the two molecules are sputtered with equal efficiency, and if

CH_3OH can be destroyed in the sputtering processes. Observations resolving the outflow spatially close to the protostar, and mapping the variation of physical conditions, are also important to further constrain the origins of the line emission.

In the greater context of this thesis, an interesting note can be made by reminding ourselves of one of the results of Chapter 3: the CH_3OH ice is much more prevalent in the ISM than previously thought, with its abundance relative to H_2O possibly increasing as high as 40%. The study based on the chapter just concluded pre-dates the study presented in Chapter 3, and thus assumes a lower ($\sim$ 30%) upper limit of the column density ratio of methanol ice to water ice. This means that the actual destruction rate of CH_3OH during sputtering is possibly up to $\sim$ 30% higher than what was concluded above.

Chapter 5

Large-scale ice mapping with AKARI

What becomes clear from the work illustrated in Chapter 4 is that to fully understand the gas-dust synergy on spatially resolved scales –where chemistry is affecting star-formation processes– requires observations where both the gas emission and ice absorption are concurrently mapped. Moving from the "state of the art" in ice observing to the scenario described above is non-trivial, i.e. it is a huge leap between ice mapping on AU scales and the scenario of detecting interstellar ices on individual lines of sight and then statistically combining many such spectra to elucidate ice formation, evolution and destruction mechanisms (as illustrated in Chapter 3).

In this Chapter I present the first real attempts at multi-object ice detections, and the subsequent ice column density mapping on large (at least 1000 AU) scales. An unprecedented volume of ice spectra have been detected during the AKARI mission; here I focus on those spectra obtained in the near-infrared (NIR), slitless spectroscopic, prism observations in the AKARI open-time ice-mapping programme IMAPE. By the end of this Chapter I will show that my research has almost doubled the current count of lines of sight along which the column density of water ice is estimated, including lines of sight towards a total of 207 sources, of which 12 are low-mass YSOs and 145 are background stars. This set contains a total of 76 detections and 131 non-detections. Upper limits are defined for the non-detections. These data have been combined to produce 12 ice maps covering $10' \times 10'$ regions towards pre- and star-forming cores.

5.1 Introduction

As was discussed in Chapter 1, interstellar ices on the surfaces of dust grains play a critical role in the molecular chemistry of the interstellar medium. Material in molecular clouds cycles between the gas and solid phases via adsorption (sticking) and desorption processes, triggered thermally by temperature changes (as stars for example ignite – see e.g. Burke and Brown 2010; Viti et al. 2004) or through non-thermal processes such as sputtering by electrons, ions or high-energy neutrals (as seen in Chapter 4) or by photon stimulated desorption (e.g. Fayolle et al., 2011b, 2013; Öberg, van Dishoeck, and Linnartz, 2009; Öberg et al., 2009, 2010b). In-between these accretion and desorption cycles, species on and in the ices react with each other, forming molecules which would not otherwise efficiently form in the gas phase. Consequently, one question remaining to be answered is whether obtaining information on both the abundances and spatial distribution of solid molecular material in star-forming regions simply provides an insight into the global chemical networks in molecular clouds or whether it also probes the prevailing physical conditions in the local environment when the ices first formed. If the latter is true, it may even differentiate chemical diversity across a star-forming region, thereby illuminating the feedback between solid- and gas-phase chemistries. This is my motivation for attempting ice-mapping, as it comes back to one of the key questions posed at the beginning of this thesis: *Where is the ice?* Ice mapping also allows me to potentially understand how and why ice formation is triggered and comment on its spatial distribution. These are the overarching aims of this chapter, focused specifically on water ice.

5.1.1 Observing water ice

In the gas-phase, water (H_2O) can only form efficiently at relatively high temperatures, typically in post-shocked gas ($\gtrsim 200\,K$; e.g. Bergin, Neufeld, and Melnick, 1999; Charnley, 1999; Draine, Roberge, and Dalgarno, 1983; Glassgold, Meijerink, and Najita, 2009; Tielens, 2005), but a plethora of mechanisms have been shown (in the lab-

oratory at least) to lead to H_2O formation on cold interstellar grain surface analogues (e.g. Dulieu et al., 2010; Ioppolo et al., 2008; Lamberts et al., 2013). The first detections of water-ice were reported in the 1970's (Gillett and Forrest, 1973; Leger et al., 1979; Merrill, Russell, and Soifer, 1976), and to date water ice has been detected on $\gtrsim 300$ lines of sight towards high-mass YSOs (e.g. Gibb et al., 2004), low-mass YSOs (e.g. Öberg et al., 2011a), background sources probing molecular cloud material (e.g. Boogert et al., 2013; Noble et al., 2013), and even extra-galactic regions (e.g. Oliveira et al., 2009; Shimonishi et al., 2008, 2010, 2013; Spoon et al., 2002; Yamagishi et al., 2011, 2013), using both ground-based and space-borne infrared telescopes. This body of evidence has proven that H_2O is the most abundant molecular solid in the ISM, and typically has abundances in excess of most gas phase molecules (water ice abundances relative to H_2 tend to hover around 10^{-5}, while the abundances of most gas phase molecules are 2 or more orders of magnitude lower than this; see e.g. van Dishoeck and Blake 1998).

The abundances of molecular ices are derived from near- and mid-infrared (NIR and MIR) spectroscopic absorption features, attributable to the stretching and bending mode vibrations of the intra-molecular bonds in the molecular species that make up the ices. In fact, ice abundance calculations rely on a number of involved steps. First the observational spectral feature is fitted to a laboratory spectrum, which may or may not require additional processing to account for e.g. for grain shape effects. Second a column density of the ice species is derived from the fitting process, and finally –where the data is available– this column density is used to calculate an abundance relative to $N(H_2, \text{gas})$. In practise the process is more complicated. Often $N(H_2, \text{gas})$ is not known, so ice abundances are usually instead quoted relative to the column density of H_2O ice; the inherent uncertainties in calculating column densities from fits between laboratory data and observational spectra are known to be up to 30% (mostly limited by the laboratory data). Examples of this were discussed in Chapter 3. These are systematic errors and apply to all known ice data, but nonetheless show the complexities of observational ice spectroscopy. Perhaps most importantly, an uncertainty is introduced

even at the observational stage. In the MIR and NIR wavelength ranges chemists refer to the the vibrational mode features (detectable in the ISM through spectroscopy) as arising from "functional groups" of atoms.

As was discussed in greater detail Section 1.4.3 of Chapter 1, a functional group refers to a set of atoms –e.g. O-H with a specific bond between them within a molecule– whose characteristic vibrational frequency occurs at approximately the same wavelength regardless of the molecule in which the atoms are found. So for example the OH in water (H_2O) vibrates at around 3300 cm^{-1}, or 3.05 μm (e.g. Gibb et al., 2004, and references therein). As a result of ice features arising in this way, most molecules are traced by features at multiple different frequencies associated to the various bending and stretching modes its constituent atoms can exist in. For example water ice is also traced by its H-O-H bending mode vibration at $\sim 6.02\mu$m. Many of these ice features trace at the the same approximate frequency a multitude of different molecules we might expect in the ISM ice. An example of this is the 3-micron O-H stretching mode mentioned above, which also traces alcohols such as CH_3OH. The C-O triple-bonded stretching mode of CO is an exception to this rule, as it is unique to CO ice alone. The shared absorption features tracing multiple different molecules limit the number of IR spectral features in ice observations from which I can derive specific molecular abundances, and even how many species are unambiguously detectable in interstellar ices. Furthermore –since these absorption features are only detected in absorption– a background source strong in near-IR emission is required for observations. Common targets fitting this description are young stellar objects (which tend to be brighter than other stars in the NIR) embedded within molecular clouds, although any background star behind the molecular cloud of interest is also a suitable source, with the caveat that they are not necessarily very bright in the IR frequency range best suited for ice observing. Observing the 3-micron O-H stretch with ground-based near-IR telescopes is further complicated by the L-band cut-off by the water vapour in Earth's atmosphere. These spectral lines partially obstruct the interstellar ice absorption feature; the 6-micron bending mode feature likewise is completely unobservable with ground-based

telescopes. For this reason most observations water-ice have been made with space-based observatories such as the Inrared Space Observatory (ISO), Spitzer, and AKARI. Each one of these telescopes had limited lifespans at the low cryogenic temperatures necessary for NIR spectroscopy.

In this chapter my work focuses on the prominent water O-H stretching mode feature at $\sim$3 μm, from which the column density of water ice can be estimated. Whittet et al. (1983) first noticed a correlation between the water ice column density (or the optical depth $\tau_{3\mu m}$, which is presumed to correlate with $N(H_2O, \text{solid})$) and visual extinction A_V towards lines of sight where both have been reported. This correlation has been repeated by several studies (e.g. Eiroa and Hodapp, 1989; Murakawa, Tamura, and Nagata, 2000; Noble et al., 2013; Whittet et al., 1988) since, and a positive correlation has always been found. The study by Whittet et al. (1988) also found an "extinction threshold" at $A_V \approx 3.3$, below which no water ice was detected. From this it was hypothesised that water ice can not form on dust in regions characterised by these lower extinctions, possibly due to photo-dissociation and /or photodesorption of the water ice in the stronger interstellar radiation field, thus destroying the ice as fast as it can be formed. This threshold has been reaffirmed by other studies, although there are conflicting estimates on how low the critical A_V is when no more water ice is detected. Eiroa and Hodapp (1989) found water to be undetectable below $A_V \approx 5-6$ and suggests the difference arises either due to higher foreground extinction or a difference in the UV field in the vicinity of the molecular cloud (Serpens) in question. Murakawa, Tamura, and Nagata (2000) reported a scatter in the A_V threshold between 2 and 5 magnitudes depending on line of sight, and suggested that this is the result of A_V variations caused by a clumpy filamentary cloud structure. It is still unclear if the critical A_V is a real physical phenomenon tracing the onset of ice formation, or whether it is related to limitations in the detector capability, dependent on source brightness and realistic integration times in single-source line-of-sight observations. With this in mind, *the secondary objective of my research was to test with the large number of lines of sight available in the AKARI data, whether or not* $N(H_2O, \text{solid})$ *is subject to a real*

extinction threshold associated with ice formation or not.

5.1.2 Ice Mapping

When all of these factors are combined, it is perhaps not surprising –despite over 40 years since the first water ice detections– that the number of lines of sight on which ice observations are reported (and their spatial coverage) is very small in comparison to gas-phase maps of star forming regions. As was previously discussed in Chapter 2, it has only been with the advent of space-borne sub-mm telescopes –such as Herschel– that the prevalence of gaseous water has been established in interstellar regions. However –as was shown in Chapter 4– a significant fraction of the H_2O gas now detected through observing programmes such as WISH (van Dishoeck et al., 2011) originates from interstellar ices. For example, ice must be present in order to explain the detection of gas-phase water generated by non-thermal desorption of water ices deep in a pre-stellar core (Caselli et al., 2012). Such analysis is reliant on gas-grain models with many data inputs, which can be independently changed to influence the output gas abundances for comparison with observations. From a solid-state perspective, constraining the precise values of ice abundances, morphologies, compositions and components, and understanding how solid-state processes are affected by these parameters is fundamental to explaining the origins of the observed gases, and assisting the modelling process. This is another motivation for my attempt at ice mapping.

Of the previous ice mapping studies discussed in Chapter 1 Section 1.5, the AKARI ice mapping studies of Noble (2011) and Noble et al. (2013) are most relevant to this chapter. Noble et al. (submitted to MNRAS) extended their previous AKARI grism ice spectroscopy (Noble et al., 2013) to generate ice maps across the AKARI $1' \times 1'$ field of view towards 4 cores, comparing the resulting ice abundances of H_2O, CO and CO_2 to existing observational data on gas and dust temperatures and column densities in the same dense core regions. They conclude that the ice does not directly trace the gas or dust material, and is instead potentially strongly influenced by the kinematics of

star-forming regions i.e. by the local environment. The ice mapping method has even been extended to extra-galactic sources; Yamagishi et al. (2013) showed that H_2O ice is widely distribtuted in the nearby star-burst galaxy M82 whilst CO_2 ice is concentrated towards the galactic centre. While they do so on a very different astronomical spatial scale, they also attribute variations in CO_2:H_2O ice abundance ratios to changes in the "local" interstellar environments within the galaxy. Likewise, the same group showed that ice distributions of H_2O, CO_2 and OCN varied significantly across the edge-on galaxy NGC253, and differed significantly from that of the H_2 gas and PAH emission (Yamagishi et al., 2011). My work compliments these earlier ice mapping attempts, but also demonstrates unique qualities which will be vital for translating ice mapping observational techniques forwards to the JWST and E-ELT eras, where multi-object spectroscopy and IFU (integral field unit) observing are being promoted:

- I have attempted to construct maps from multi-object slitless spectroscopic detections, and therefore all my ice features are derived from data acquired simultaneously.
- My field of view is large –up to $10' \times 10'$– and focuses on galactic objects, thereby spanning diverse interstellar environments from extra-cloud regions to cloud edges and objects embedded within dense cores.
- I have this data towards multiple different molecular clouds.

Consequently my adopted method of mapping the ices themselves is very challenging from an observational, data reduction, and ice column density calculation viewpoints. An advantage of this approach is that the solid state material can be observed directly. The disadvantages (discussed in further detail in the upcoming sections) are the intrinsic limitations arising from how the data was observed and how it needs to be reduced. The step-change from one dimensional to two dimensional ice spectroscopy makes possible the testing of whether spatial ice abundance differences in a core are correlated with localised effects such as dust evolution, heating, density, turbulence,

Table 5.1: Target fields of view analysed in this chapter.

Core name	Pointing	Number of observations	α_{J2000} [deg.]	δ_{J2000} [deg.]
B35A	4120021	2	86.154	+09.170
BHR 59	4121001	1	166.803	-62.096
CB 188	4120004	2	290.065	+11.600
DC 269.4+03.0	4120042	1	140.594	-45.790
DC 274.2-00.4	4120006	2	142.208	-51.601
DC 275.9+01.9	4120008	2	146.691	-51.102
DC 291.0-03.5	4120010	2	164.966	-63.723
DC 300.2-03.5	4121044	2	186.090	-66.202
DC 300.7-01.0	4120011	2	187.886	-63.739
DC 346.0+07.8	4120012	1	249.225	-35.617
L 1165	4120034	2	331.668	+59.100
Mu 8	4121017	1	187.698	-71.041

and varying radiation fields. The spatial scales capable of being traced by the ice maps produced in this chapter allow me to focus on scales of a few thousand astronomical units.

The remainder of this chapter is structured as follows. First in Section 5.3 I briefly discuss the observations on which my work is based, and then proceed to discuss at length the detailed reduction and spectrum extraction process. After this –in Section 5.3.5– I utilise methods not dissimilar to those already previously employed in Chapter 3 to derive water ice column densities. I present ice maps created this way in Section 5.4, towards a total of 12 star-forming regions. In section 5.5 the data are discussed in the context of other ice observations, observable archival data towards the same molecular clouds, and finally in terms of the extinction threshold limit at which ices can be detected.

5.2 Observations

The main bulk of the data used in this study comes from the AKARI ice mapping programme IMAPE (PI: Helen Fraser) which consists of near- and mid-infrared spectroscopic observations towards a total of 13 molecular clouds. Both grism (NG) and prism (NP) observing modes were used for the observing, with 11 of the clouds ob-

served in the NG mode and all 13 clouds observed in the NP mode. An explanation of how these observing modes work was provided in Chapter 2, where a full list of target cores was also provided in Table 2.2. For the sake of convenience, the NP observations successfully (see below) analysed in this chapter (along with some relevant additional information) are also listed in Table 5.1. Analysing the NG observations in the $10' \times 10'$ window quickly proved to be fruitless, as the severe confusion between the NG spectra makes extraction of useful information very difficult to impossible. Worse still, the way NG observations were taken by AKARI required the target coordinates to be specified in the centre of the $1' \times 1'$ and as a result it was down to luck whether the telescope happened to be at an appropriate roll angle to align the $10' \times 10'$ window with the desired cloud. The $1' \times 1'$ window expectedly pointed at the desired patch of sky on every observation, but the roll angle of these observations ended up in all observations pointing the $10' \times 10'$ window directly away from the molecular cloud of interest. As a result even if the spectra on the $10' \times 10'$ NG observations were extractable, very few of them would be of the same sources as with their respective NP frames (preventing their use for improving the overall signal-to-noise of the observations) and are probing a patch of the sky where there are no molecular clouds and ice of any kind is almost certainly completely absent. For this reason the remainder of this chapter concerns itself only with the NP observations, which are expected to mostly trace H_2O ice at the 3-micron absorption feature. Both CO and CO_2 ice features would be theoretically observable at the NP wavelength range, but its very low resolution ($R \approx 12$) makes it unlikely for the narrow C-O stretching features of CO and CO_2 to be resolvable towards most lines of sight. Owing to how AKARI observed the near-infrared and mid-infrared channels simultaneously, mid-IR data would have also been available in addition to the near-IR data analysed in this chapter. This additional data was not analysed in this study, owing to the very significant complications (most notably the strong zodiacal light present in the mid-IR regime, and its effect on mid-IR spectroscopy) that the reduction of the mid-IR data would have introduced. One of the NP observations (towards BHR 78) had corrupt astrometry, which made source asso-

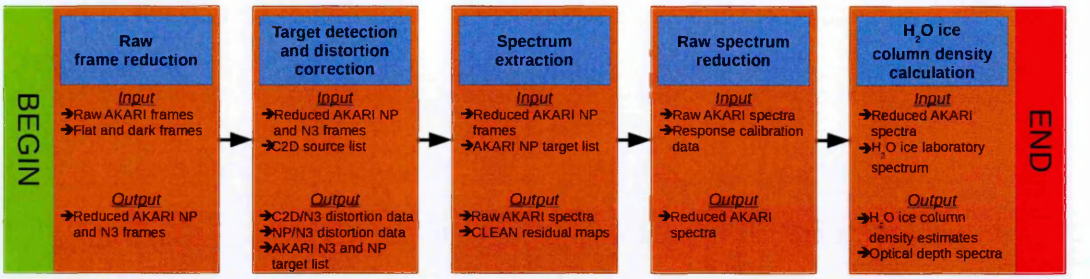

Figure 5.1: An outline of the full reduction process leading from raw AKARI data to water ice column densities, split into five main steps. Most of these steps are from the point of view of ARF2 split into several smaller steps, to be taken in succession in the order described in this chapter. Also listed are the main required inputs and outputs of each step.

ciation with c2d data (see Section 5.3.2) impossible for this core. Consequently BHR 78 was ignored in the analysis, bringing the final number of analysed cores to 12.

5.3 Methodology

Acquiring ice maps from the raw AKARI observations is a non trivial process, involving first some fairly standard processing of IR spectroscopic observational data, some reduction steps specific to AKARI, the extraction of ice spectra, and finally reduction and analysis of the spectral data to extract the column densities of water ice. The full journey from raw AKARI data to ice maps –the description of which will encompass most of this chapter and makes use of both of the software utilities detailed in Appendix A– is summarised on the flowchart in Figure 5.1. The first step on this path is the reduction and stacking of the raw AKARI data into a format from which spectrum extraction is possible.

5.3.1 Reduction of the raw AKARI data

Each NP mode observation made with AKARI produces a total of 12 FITS files relevant to my study:

- A single imaging frame, taken with the N3 filter (covering a wavelength range of 2.7 to 3.8 μm) in the middle of the observing cycle.

- Two dark frames, one taken right before the observing cycle and one at the end of it.

- Nine dispersed frames, where the final frame was often obtained during the telescope manoeuvre phase and therefore omitted.

Each of these frames consist of two sub-frames: one short (2.3 seconds) and one long (51 seconds) exposure version.

The imaging and dispersed frames in their raw form suffer from a number of effects (some of which are common to all CCD-equivalent observations, some of which are unique to AKARI) which must be accounted and corrected for, before the data is useful for scientific analysis. These effects and the order they are accounted for during the reduction are as follows:

1. The detector arrays have a number of bad pixels, which produce useless data. The locations of these pixels are recorded in a bad pixel mask, which is provided as part of the standard AKARI calibration dataset. The first operation to be undertaken with the raw AKARI data is flagging the pixels indicated by the bad pixel mask as bad data. Pixels masked in this way are ignored in subsequent reduction steps, and are written in the final reduced frame as a NaN (Not a Number) value.

2. At high (> 1000) number counts the response of the AKARI detector becomes non-linear, and must be corrected for in order to make the detected signal from especially bright sources correspond more realistically to their true brightness. This is corrected for by applying the formula

$$n_{\mathrm{corr}} = a_1 n_{\mathrm{rep}} + a_2 n_{\mathrm{rep}}^2 + a_3 n_{\mathrm{rep}}^3 + a_4 n_{\mathrm{rep}}^4 \tag{5.1}$$

to all pixels where the reported signal is higher than the threshold value of 1000. In this equation n_{rep} is the reported signal, n_{corr} is the corrected signal, $a_1 = 1.0288217$, $a_2 = -4.0339674 \times 10^{-5}$, $a_2 = 1.3556758 \times 10^{-8}$, $a_3 =$

$-1.5086542 \times 10^{-12}$, and $a_4 = 5.9679544 \times 10^{-17}$. This equation is adapted to ARF2 from the official AKARI data reduction pipeline[1].

3. At even higher number counts the reported signal suffers from a wrap-around effect, where a signal with a reported value that should be greater than 32768 instead flips back to negative numbers, counting up from -32768. This effect –more commonly referred to as arithmetic overflow– is symptomatic of the detected number counts being stored as 16-bit signed integers either before being written into FITS format, or by the software creating the original FITS files. As a result all arithmetic operations where the end result would be greater than $\frac{2^{16}}{2} = 32768$ –the highest positive number representable by signed 16-bit integers– flip around to -32768, the highest negative number representable by 16-bit integers. Although it would be possible to convert the wrap-around values useful numbers by adding 65536 to them, non-linearity effects already make data with this high number counts useless, and thus they are simply masked out instead. This was done by flagging all pixels where $n_{\mathrm{rep}} < -10000$ as bad data.

4. The frames need to have a flat-field correction performed on them, to account for variations in the detector sensitivity between different parts of the frame. A master flat-field frame is provided as part of the standard AKARI calibration package. This flat-field image was first divided by its own mean (to normalize its effects on detected flux), followed by dividing the frame being processed by the normalized flat-field.

5. As with all detectors, the AKARI detector array suffers from dark current, which needs to be corrected for with a dark frame. Each pointing used its own master dark frame, which was constructed from a median of the two dark frames taken during their respective observation cycle. Also, separate dark frames were used for the short and long exposure versions of the data. The dark correction was

[1]Available from `http://www.ir.isas.jaxa.jp/ASTRO-F/Observation/DataReduction/IRC/`

performed by subtracting the dark frame from the flat-fielded data.

An additional step is also taken in the reduction of the NP frames. These frames are stacked together, to create an image with a much improved signal-to-noise ratio compared to an individual frame. The stacking is done by averaging the images together, pixel by pixel. However, before this can be done the jittering of the individual frames has to be accounted for. Between each of the exposures of the NP frames the field of view of the telescope shifts noticeably, without the shift being reported in the astrometry of the FITS header. If this is not corrected for, the averaged NP frames would show several "ghost" images of the sources in the field of view close to but obviously not aligned with each other, making the averaged NP frame useless. To correct for this, the first NP frame is taken as a reference frame and a pixel shift is automatically determined to best align the other NP frames with the reference. The best shift is determined by subtracting the pixel values in a small area close to the center of the reference frame from the subsequent frames, as the frames are shifted along the x and y axes relative to the reference frame. The allowed range of motion which is explored is ± 10 pixels along both the x and y axes, and the shift which produces the smallest sum of the absolute residual values is declared as the shift which aligns the reference frame with the other frame. This is repeated for each of the 7 frames following the reference frame, and they are cropped in the appropriate way as determined by the shift values, so that they will align pixel-by-pixel with the reference frame. After the shifts have been determined and the images cropped (causing loss of tiny amounts of data at the edges of the frame) to align with the reference frame, they are averaged to produce the final NP frame.

As was described in Chapter 2, the full AKARI frame contains both the $1' \times 1'$ and $10' \times 10'$ windows in the same image, with a large blank space (reserved for dispersing the spectra into) surrounding both the $1' \times 1'$ window and the slit connecting the $1' \times 1'$ and $10' \times 10'$ windows. The noise in this blank area would interfere with the source extraction being done to the $10' \times 10'$ window, so the image was cropped to contain nothing but the $10' \times 10'$ window, which is the focus of this study. With this cropping

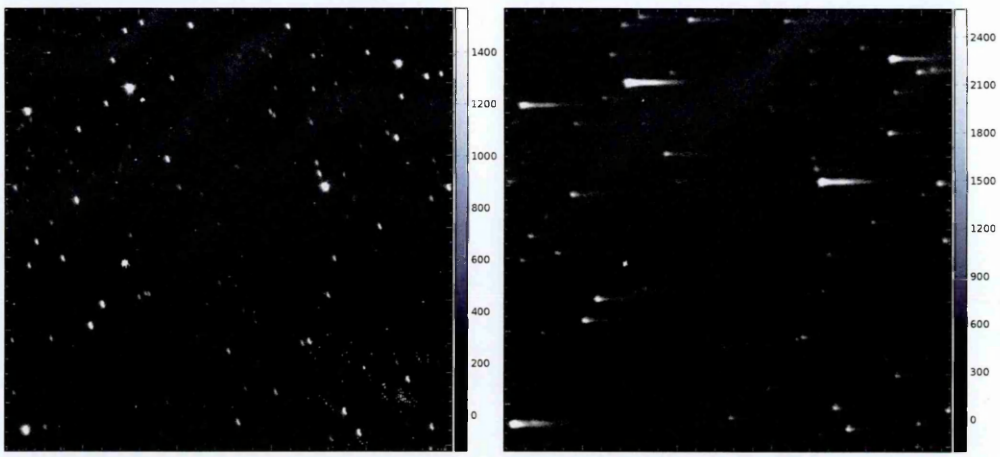

Figure 5.2: An example of a reduced N3 (left) and NP (right) short exposure frame towards DC300.7-01.0. The greyscale bar scales are in arbitrary digital units (ADUs).

done and the reduction steps above completed, the reduced images could be written to files and be ready for further processing. An example of a reduced N3 and NP frame are shown in Figure 5.2. Central to understanding the shapes of the features seen in the NP frame is the response calibration function of the AKARI prism disperser. This experimentally determined (by the AKARI mission scientists) function is used to convert the emission of an extracted AKARI spectrum into physical units. It also serves a second purpose of being highly useful in both pinpointing the location of a specific source on the NP frame, and also in providing information about the wavelength calibration of the spectrum. It does this through a very prominent peak in brightness (a result of 0th order diffraction) it exhibits at 2.4 μm. The response calibration function is shown in Figure 5.3.

In an ideal situation this further processing would be the spectrum extraction itself, but one final issue of the AKARI telescope has to be corrected for before extraction is possible: the field distortion.

5.3.2 Correcting for field distortion in the AKARI frames

One of the main challenges of spectrum extraction from the AKARI NP frames in the $10' \times 10'$ window comes from selecting the sources to extract. In a crowded field the

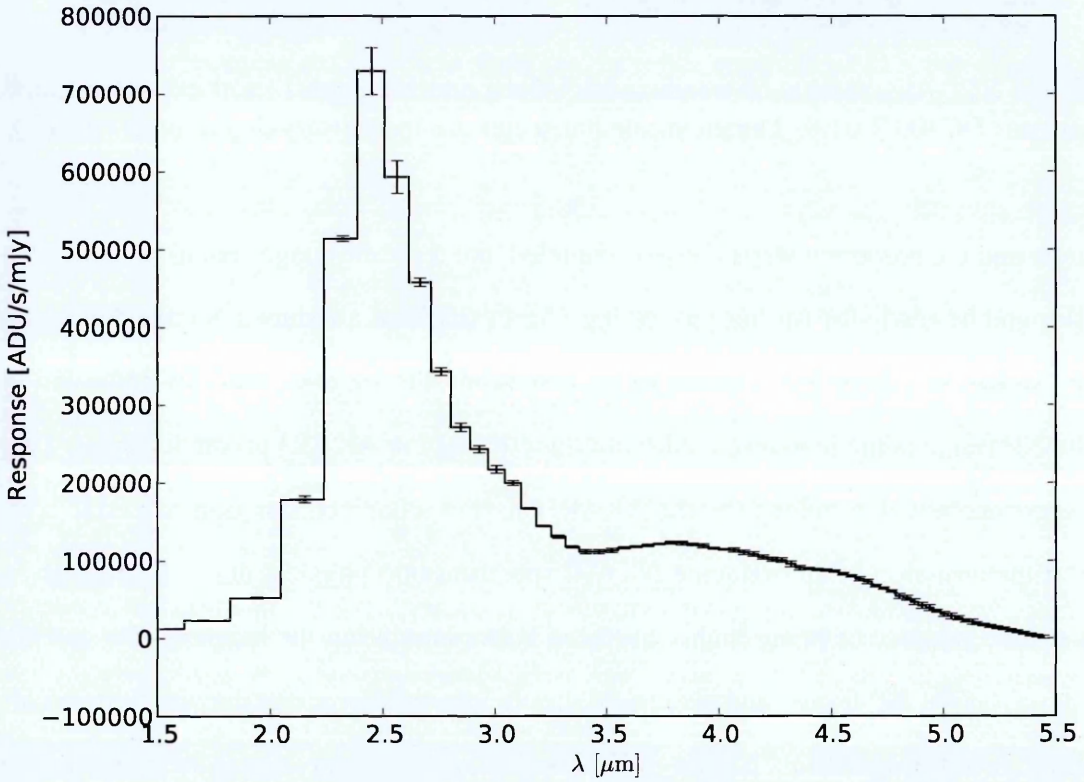

Figure 5.3: The AKARI NP response calibration function. On the x axis is the wavelength of the function in microns, and on the y axis is its response against time-normalized ADUs. Notice the very prominent peak in repsonse at $\sim$2.4 μm. This peak is used to both locate sources on the AKARI NP frame, and in the wavelength calibration of extracted spectra.

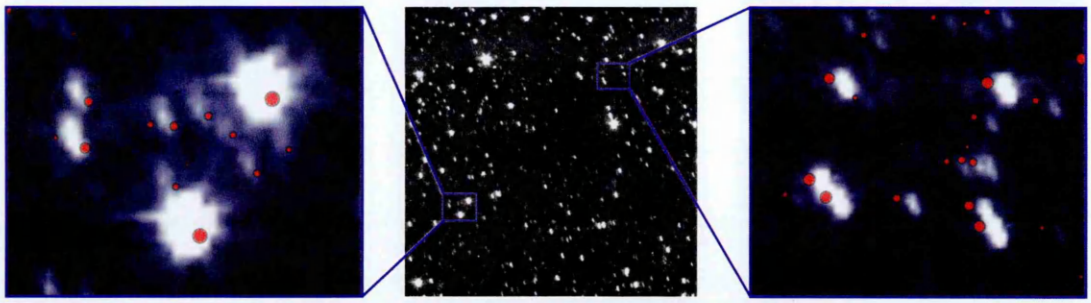

Figure 5.4: An example of the effects of distortion on the reduced AKARI N3 frame at different parts of the same field of view towards DC300.7-01.0. The middle image shows the entire $10' \times 10'$ field of view, while the left and right images show a zoomed in part at opposite sides of the full FoV, as indicated by the rectangles. The zoomed images have the locations of c2d sources indicated by red circles, with a larger circle meaning higher K-band flux according to c2d. Notice how the c2d sources are offset from their N3 locations down and to the right on the left image, while the c2d sources are offset up and to the left on the right image.

the large frame can easily contain hundreds of IR bright sources, which makes it impractical for them to manually selected, and thus requires the application of automatic methods. In the case of normal imaging frames such as the N3 frame, which contains mostly point-like sources, a utility such as SExtractor (Bertin and Arnouts, 1996) can be used to automatically find the source locations to a high degree of certainty. However, the dispersed light of the NP frame confuses these conventional methods and an alternate approach is required. An alternate automatic method is to rely on existing catalogues of sources towards the cores I am probing, and automatically select sources to extract based on the proximity of a local maximum towards a predicted catalogue source location. The c2d Spitzer Legacy catalogue (Evans et al., 2003) is perfectly suited for this job, because the target selection for IMAPE was originally made so that the AKARI observations were selected from c2d target regions.

With such a catalogue readily available one would expect that finding sources to extract from the NP frame is a matter of overlaying the catalogue sources on top of the NP frame and performing the source extraction based on these locations. The reality, however, is not this simple. The AKARI frames suffer from field distortion, the effects of which are illustrated in Figure 5.4. The field distortion causes source locations to change in a non-linear fashion towards different regions of the AKARI

CCD field, making simple corrections such as pixel offsets insufficient to translate the source locations of e.g. the c2d catalogue to align with AKARI sources. Furthermore, the effects of field distortion are different between the AKARI N3 and NP frames, because of prism optics introducing additional distortion to the path of the light.

The AKARI field distortion has been found (e.g. Helen Davidge private comm.; Lorente et al., 2007; Noble, 2011) to behave in a manner which can be modeled with a 2-dimensional polynomial warping function. A single un-warped point at coordinates (x,y) can be warped with an n^{th} order 2D polynomial to a point with coordinates (x',y') with the help of the equations

$$x' = \sum_{i=0}^{n}\sum_{j=0}^{n} P_{i,j}x^j y^i \tag{5.2}$$

$$y' = \sum_{i=0}^{n}\sum_{j=0}^{n} Q_{i,j}x^j y^i, \tag{5.3}$$

where $P_{i,j}$ and $Q_{i,j}$ are the two sets of 2-dimensional polynomial coefficients (with $n \times n$ elements each) required for calculating x' and y', respectively. The matrix-like nature of $P_{i,j}$ and $Q_{i,j}$ in the above equations hint at the relevancy of matrix algebra in the matter, and it is indeed possible to generalise the above to a pair of matrix transformations applied to an arbitrary point collection with k amount of (x,y) pairs to produce their n^{th} order polynomially warped equivalent x' coordinates with:

$$\begin{pmatrix} y_1^0 & y_1^1 & \cdots & y_1^N \\ y_2^0 & y_2^1 & \cdots & y_2^N \\ \vdots & \vdots & \ddots & \vdots \\ y_k^0 & y_k^1 & \cdots & y_k^N \end{pmatrix} \begin{pmatrix} P_{00} & P_{01} & \cdots & P_{0N} \\ P_{10} & P_{11} & \cdots & P_{1N} \\ \vdots & \vdots & \ddots & \vdots \\ P_{N0} & P_{N1} & \cdots & P_{NN} \end{pmatrix} \begin{pmatrix} x_1^0 & x_2^0 & \cdots & y_k^0 \\ x_1^1 & x_2^1 & \cdots & y_k^1 \\ \vdots & \vdots & \ddots & \vdots \\ x_1^N & x_2^N & \cdots & y_k^N \end{pmatrix} = \begin{pmatrix} x'_{11} & x'_{12} & \cdots & x'_{1k} \\ x'_{21} & x'_{22} & \cdots & x'_{2k} \\ \vdots & \vdots & \ddots & \vdots \\ x'_{k1} & x'_{k2} & \cdots & x'_{kk} \end{pmatrix}, \tag{5.4}$$

and y' coordinates with:

$$\begin{pmatrix} y_1^0 & y_1^1 & \cdots & y_1^N \\ y_2^0 & y_2^1 & \cdots & y_2^N \\ \vdots & \vdots & \ddots & \vdots \\ y_k^0 & y_k^1 & \cdots & y_k^N \end{pmatrix} \begin{pmatrix} Q_{00} & Q_{01} & \cdots & Q_{0N} \\ Q_{10} & Q_{11} & \cdots & Q_{1N} \\ \vdots & \vdots & \ddots & \vdots \\ Q_{N0} & Q_{N1} & \cdots & Q_{NN} \end{pmatrix} \begin{pmatrix} x_1^0 & x_2^0 & \cdots & y_k^0 \\ x_1^1 & x_2^1 & \cdots & y_k^1 \\ \vdots & \vdots & \ddots & \vdots \\ x_1^N & x_2^N & \cdots & y_k^N \end{pmatrix} = \begin{pmatrix} y'_{11} & y'_{12} & \cdots & y'_{1k} \\ y'_{21} & y'_{22} & \cdots & y'_{2k} \\ \vdots & \vdots & \ddots & \vdots \\ y'_{k1} & y'_{k2} & \cdots & y'_{kk} \end{pmatrix}. \tag{5.5}$$

In these equations the equivalent warped coordinate of the unwarped points are described by the x' and y' values on the diagonal of the matrices on the right hand side

of the equations, i.e. the warped equivalent of point (x_1,y_1) is (x'_{11},y'_{11}), for (x_2,y_2) it is (x'_{22},y'_{22}) and so on. The off-diagonal values in the matrices on the right hand side of the equations are of unknown relevance in the generalised case, but seem to have no utility at least in my situation.

My situation requires the construction of two sets of P and Q coefficient matrices: one for distorting between the c2d data and the N3 frames, and another for distorting between coordinates of the sources in the N3 frames to match with those found in the NP frames; in effect I am warping the real (c2d) data to align with the distorted AKARI coordinates. The conversion was chosen to be done this way around because the primary objective in the distortion correction is to automatically find sources to extract from the NP frame. The sources visible in the NP frames can all be found by applying SExtractor to the N3 frames, the coordinates of which can then be distorted to align with the NP frame. The association between N3 and NP sources happens by finding the local maximum (equivalent to the $\sim 2.4\,\mu$m sensitivity peak in the spectra; see Figure 5.3) inside a 3×3 pixel box on the NP frame, centered where the distortion from the N3 to NP predicts the SExtracted source to be. Most of the N3 sources can also be assigned with a c2d source identifier by distorting the pixel coordinate equivalents of their sky coordinates to align with the N3 frame souces, and then automatically associating the closest c2d/N3 source pairs together.

The distortion correction was performed as follows:

1. Correct for large-scale shifts between the c2d, N3 and NP coordinates by selecting a single source triplet (the same source found in c2d, N3 and NP) close to the center of each pointing. The (x,y) coordinate of this source is stored for each case, with the c2d (x,y) coordinate being represented using the world coordinate system of the N3 frame header. This triplet of coordinates is used to align this single source in each frame before further distortion corrections are performed, eliminating the large-scale shift and making it easier to characterize the small-scale distortion.

2. Manually associate a number of source pairs (c2d/N3 or N3/NP) in a single pointing with each other.

3. Evaluate the first iteration of the de-warping coefficient matrices for a 5^{th} order 2D polynomial by minimizing $\sum_{i=1}^{k}(x_i - x_i')^2$ and $\sum_{i=1}^{k}(y_i - y_i')^2$ (with x_i' and y_i' calculated with Equations 5.4 and 5.5) separately using a modified Powell's method (Powell, 1964).

4. Use the minimized P and Q to try and automatically guess the source pair associations in a new field of view, and correct them by hand in cases where a mis-association is noticed by visual inspection.

5. Minimizing the square-sum of the differences between the warped and un-warped coordinates again, using the increased number of coordinate pairs to improve the estimates for P and Q.

6. Repeat the last two steps until all fields of view have been evaluated twice.

7. Use the final P and Q estimates to warp the c2d source coordinates to N3 coordinates, and N3 source coordinates to NP coordinates and automatically associate the sources in the manner described in the previous paragraph.

The final number of the lines of sight (often having the same associated source multiple times between different sub-pointings) used in this iteration was 5496, although at $\sim$ 1000 sources it was found that manual correction of the automatically associated sources was no longer necessary, as the automatic association algorithm was associating sources between the three systems at an accuracy comparable or superior to a human being, with vastly improved speed. The final number of mis-associations is estimated to be less than 5%, based on how rarely any mistakes made by the algorithm had to be corrected. Vector field maps of the calculated distortions are presented in Figure 5.5.

These distortion maps could be used to automatically find the extraction targets in the NP frames, allowing me to move on to the spectrum extraction phase of the

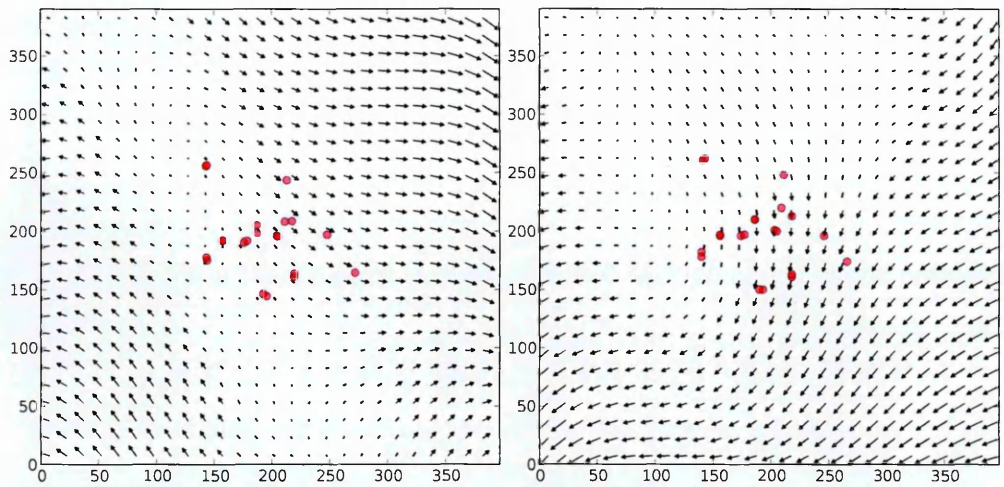

Figure 5.5: Vector fields representing the final distortion maps used in the automatic source association between the c2d catalogue and the N3 imaging frames (left image), and between the N3 frames and the NP dispersed frames (right image). The plotted sizes of the vectors have been normalized for clarity; the maximum x-axis and y-axis distortions on the left image are 6.34 and 7.78 pixels respectively. For the right image the maximum x and y distortions are 10.39 and 3.99 pixels, respectively. The red circles show the coordinates of the reference sources used for correcting for large-scale shifts between the three sets of data. The arrowheads of the very short vectors have been removed, for clarity.

reduction.

5.3.3 Spectrum extraction

The spectrum extraction is the most important part of the reduction process, and also the one most sensitive to errors. A successful extraction relies on keeping track of several factors:

- The correct detection of all strong spectrum-generating sources in the field of view
- Identifying the pixel coordinates of each part of the spectrum of each source.
- Decomposing the emission of multiple overlapping spectra where possible and masking out the confused parts of the spectra in places where decomposition is impossible.

- Taking properly into account non-linear gain and saturation in spectra where the source emission is very strong.
- Correct wavelength calibration of the extracted spectra
- Detecting and masking out bad data and artifacts from the extracted spectra

The sheer volume of data being analysed means that this all has to be done almost entirely automatically, as it is not practically feasible for a human to manually extract and reduce the spectra from the thousands of sources which are detected in the full AKARI IMAPE data set. This subsection describes the logic and methods which were used in going from the reduced AKARI frames and source detections to extraced spectra.

I first use the NP source locations detected by the N3/NP cross-associations to form the basis of the spectra to be extracted. Each source is designated an "extraction path" which describes the pixels associated with the spectrum of each source. The source location is the local emission maximum at low wavelengths, but this is not the beginning of the spectrum. The spectrum is seen to start 3 pixels before (in terms of offset along the dispersion axis) this, and it ends 58 pixels after the peak. This makes the full length of the extraction path longer than the one reported in Ohyama et al. (2007), because it was found that including the emission that has spilled over from the ends of the extraction path makes it easier to determine the precise pixel offset of especially the 2.4μm transmission peak, which is useful in calibration. From close inspection of the dispersion, it was determined that there is a tiny offset of 0.417 pixels in the end point of the extraction path along the axis perpendicular to the dispersion axis. If I define the dispersion axis as the x axis and the non-dispersed axis as the y axis, I can then define the extraction path of each source to start at deltaX=-5 px and end at deltaX=+58 px and deltaY=+0.417 px relative to the source coordinates. The extraction path itself is the line drawn between these two points, and the pixels which fall on this line.

With the extraction paths thus defined, I can look at the extraction itself. The default JAXA AKARI pipeline does the extraction by defining a box (usually 6 pixels wide along the y axis) around the (non-confused) source in question, and summing the pixels inside the box, along each point of the JAXA pipeline equivalent of the extraction path. This method will work adequately, as long as no other sources are inside the "extraction box" causing confusion. Noble (2011) improved upon this method in the case of the grism-dispersed (NG) spectra by –instead of defining a box– performing a PSF fit on each slice of the image containing dispersed emission from the soure(s) of interest. This PSF is fitted to a slice of the full image on the y axis, and takes the shape of a twin gaussian, as it was determined to be an adequate approximation of the grism PSF along the non-dispersed axis (Noble, 2011). This method proved to be very effective at extracting small numbers of grism-dispersed spectra out of the 1x1 arc minute AKARI field of view, and the results were later published in Noble et al. (2013).

The true problem in my case, however, arises in the form of the computational cost of applying this method in a situation where I can have dozens of extraction paths forming a chain of overlapping PSFs. The least-squares method –which is the standard approach for solving cases such as that of the partially overlapping PSFs– involves operating on matrices which have a number of elements in them that is the square of the number of parameters being fitted. This also means that a computation time needed to solve a least-squares problem increases as a square of the number of parameters being fitted. Thus, increasing the number of extractable sources by multiple orders of magnitude will quickly cause the total computation time to explode to a point where the extraction will no longer be feasible in reasonable timescales. An extraction of 3-5 sources takes approximately two minutes of computation time on the test computer. If I increase the source count from 5 sources to 500 sources (approximately the number of sources being extracted from a single frame in the "worst-case" scenario), the computation time multiplies by a factor of $(500/5)^2 = 10000$, causing a full extraction of some of the more crowded AKARI frames take about a week of uninterrupted calculations per frame. All of the 19 pointings which contain the spectra I am interested in

would thus take up to several months of computations to extract. As it will inevitably be necessary to repeat this extraction several times for debugging and extraction algorithm fine-tuning purposes, an iteration cycle of weeks (assuming only a single field of view is extracted during testing) to months (assuming full extraction) during such testing would be highly impractical.

The time bottleneck posed by the formidable computational requirements motivated the search for alternate solutions. First, let us consider the nature of the PSF degeneracy problem. The PSF degeneracy only poses a problem in cases where two extraction paths cross within a few full width half-maximums of each other. In most situations any single extraction path has only a few other paths interfering it. While these interfering paths may also have additional other paths interfering with them, these additional paths are unlikely to have a significant effect on the emission of the first path. I could thus try to look at "clusters" of about ten paths, with only a single path in the middle of these being the one which a spectrum is extracted from. This could then be repeated for each spectrum in the data set separately. However –while it would take significantly less time than the simultaneous fitting of all spectra– this method will still take about one minute per extracted spectrum on an average computer. When we consider that this process would have to be repeated for each of the thousands of extraction paths, the full extraction process would still easily end up taking several weeks of uninterrupted computations.

The nature of the spectrum extraction problem is essentially one of deconvolution, and thus the search for a time-efficient solution to it lead to looking at existing deconvolution algorithms. The CLEAN algorithm (Högbom, 1974) is a deconvolution method often used in e.g. the aperture synthesis of radio interferometry. CLEAN operates in roughly the following manner:

1. Input un-CLEANED image, list of expected source positions and a normalized PSF to the algorithm.

2. Find maximum point of emission in the image.

3. Find which source is closest to the emission maximum.

4. Align the peak of the PSF to match with that of the emission maximum.

5. Subtract from the image the PSF multiplied by a small fraction (e.g. 10%) of the emission maximum.

6. Add the subtracted intensity to a number representing the intensity of the source corresponding to the maximum.

7. Find the new maximum of the image.

8. Is the new maximum above a set threshold (e.g. a multiple of the image RMS)?

   (a) If YES, go to 3.

   (b) If NO, output list of source intensities as the CLEANed data.

With a few modifications, this method can also be applied to my case of spectrum extraction. Like with the Gaussian fit method, I stick to operating on a single 1-dimensional slices of the image, taken perpendicular to the dispersion axis. This slice will show features from any extraction path crossing through it, in the form of 1-dimensional PSF shapes of varying height. In each pointing, I find a single extraction path which is both strong and well separated from any other paths, and define the 1-dimensional PSF for the pointing from this path. The CLEAN algorithm is applied to the slice of the full image, with the PSF being the one defined above and the source positions being replaced by the points of the various extraction paths crossing the slice being CLEANed. The algorithm then gradually subtracts the 1-dimensional PSF from the slice while adding the subtracted intensities to the appropriate parts of the extraction paths. Because of the extraction paths sometimes pass very close to each other, it is sometimes not possible to deconvolve the emission from two sources with each other. It is during the assignment of the CLEANed flux when an attempt is made to combat this by checking the relative brightnesses of two potentially confused sources. In instances where there are multiple candidates for assignment of CLEANed flux, the

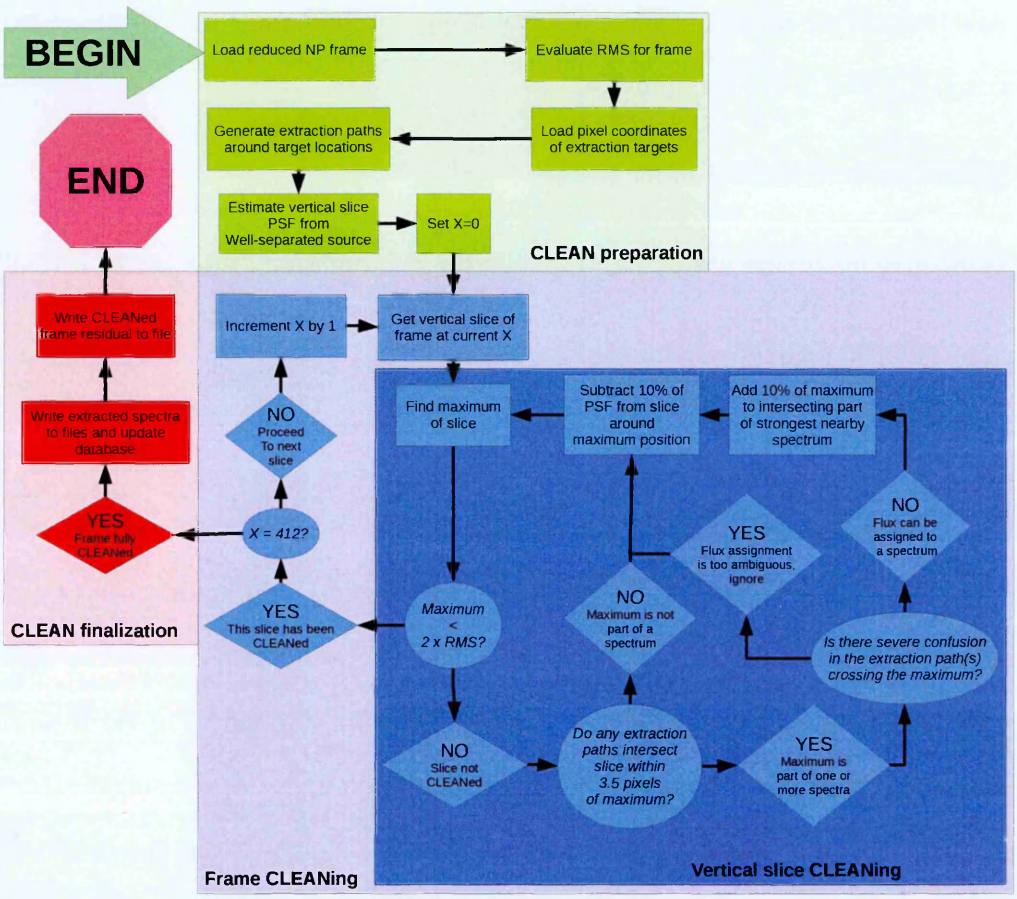

Figure 5.6: A flowchart describing the CLEAN process, as it is applied to my data. This process is repeated for each reduced NP frame, with short and long exposure versions treated as separate cases. The algorithm can be roughly separated into 4 general processes: CLEAN preparation, frame CLEANing, vertical slice CLEANing and CLEAN finalization. These are colour-coded with different backgrounds on the flowchart.

strongest of the candidates must be at least four times as bright (defined by the estimated flux of the source at its brightest point in the NP frame) as any other candidate. If such a source exists among the candidates, the CLEANed flux is assigned to its spectrum. If no such candidate exists, the CLEANed flux is not assigned to any spectrum. While this can sometimes cause potentially valid sources to be discarded as irrevocably confused (see Figure 5.9), it was found to most of the time adequately prevent confused sources from contaminating the data set with false spectral features. After a single slice has been CLEANed, I move on to the next slice of the image and repeat the process. This is repeated until each slice of the image has been CLEANed. At the end I have produced the spectrum for each source in the field of view. A flowchart of the CLEAN process –as applied to my case– is shown in Figure 5.6 and a screen capture of ARF2 in the middle of the CLEANing process is shown in Figure 5.7, and examples of the residuals left after CLEANing are shown in Figure 5.8.

The CLEAN algorithm proved to be an extremely time-efficient method of extracting spectra from the NP frames, with each frame taking approximately half an hour to fully extract. A number of caveats have to be kept in mind when looking at the spectra extracted in this way. The most significant factor is that I am completely ignoring the effect of the PSF blurring the emission in the direction along the dispersion axis. Instead I am assuming that all the emission applicable to a specific point along the extraction path of a specific source are spread out to pixels only perpendicular to the dispersion axis. This is not a valid assumption, because the various optics of the telescope and its instrumentation will inevitably cause blurring along both axes of the images captured.

The PSF along the axis perpendicular to the dispersion axis is something that can be characterised by looking at the shape of a well-separated spectrum along this axis, as was done with my CLEAN algorithm. The PSF of the emission along the dispersion axis, however, is a combination of a blurring effect likely similar to that seen along the perpendicular axis and an additional wavelength-dependent effect caused by the dispersion element itself. These two effects could not be separated from each other in

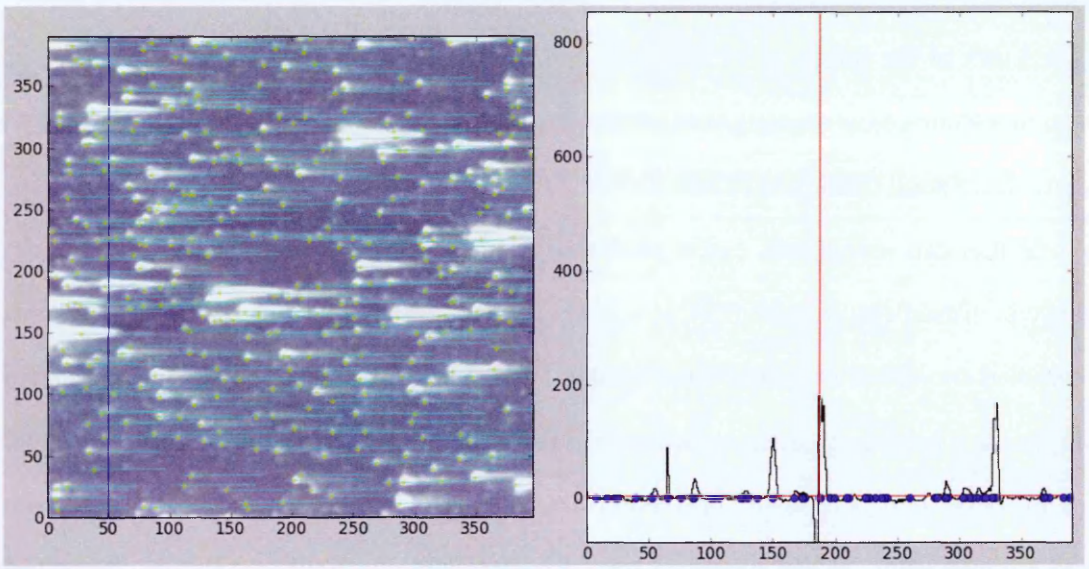

Figure 5.7: A screen capture of ARF2 in the middle of running the CLEAN algorithm on one of the NP frames. The left window shows the short-exposure NP frame with source extraction target locations and extraction paths overlaid with pale yellow dots and cyan lines. The vertical blue line indicates the current slice being CLEANed. The right window shows the slice of the short exposure NP frames being CLEANed. On this slice the blue circles indicate the locations of the extraction paths crossing the active slice, and the vertical red line indicates the last part of the slice which had a partial PSF subtracted from it. Close to the baseline is also a horizontal red line, which indicates the RMS level below which all points on the slice must drop for the algorithm to consider the slice properly CLEANed. Although this screen shot shows only the short frame being CLEANed, the CLEANing of the short and long exposures happens concurrently.

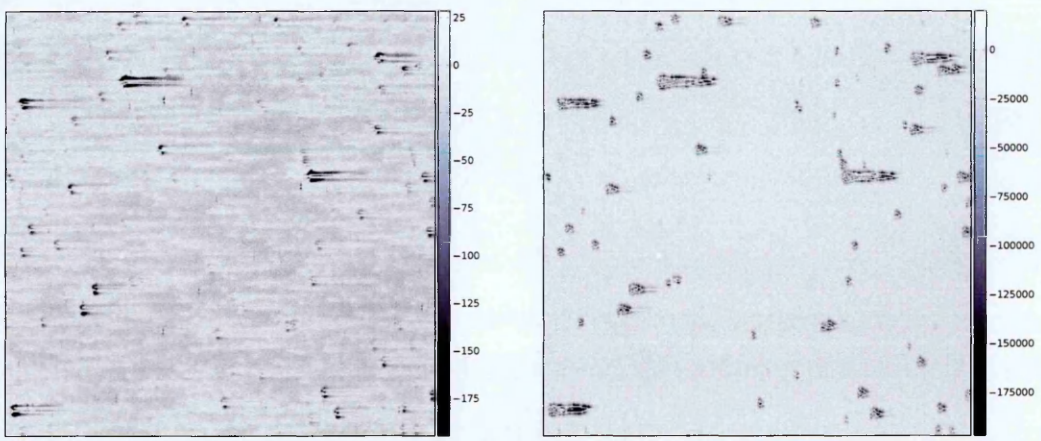

Figure 5.8: Examples of the residual images left after the CLEAN process, towards DC 300.7-01.0. The left image shows the residual of the short exposure image, while the right image shows the residual of the long exposure version. Notice the deep negative residuals around bright sources, especially in the long exposure frame.

a length of time which is feasible for this study, and thus the PSF along the dispersion axis is ignored in this study. What results from this is that each point in each extracted spectrum is likely to contain extra emission from its neighbouring pixels. In effect each spectrum is blurred to have a spectral resolution less than what is indicated by the AKARI NP specifications.

A second caveat with the spectrum extraction arises from the uncertainty of the 1-dimensional PSF which is used in the CLEANing. This PSF is constructed from a twin Gaussian fit based on a single source in the frame being CLEANed. The twin Gaussian is described by the function

$$y(x) = a_1 \exp\left[-\left(\frac{x-p_1}{w_1}\right)\right] + a_2 \exp\left[-\left(\frac{p_1+\Delta p_1}{w_2}\right)\right], \tag{5.6}$$

where a_1 and a_2 are the peak heights of the two Gaussian components, p_1 is the position of the first component while Δp_1 is the offset of the second component relative to the first. w_1 and w_2 are the full width half-maxima of the two components. Each of these parameters is allowed to vary within a constrained space. Most notably, p_1 is allowed to vary only ± 2 pixels from its initial guess (the source location) and Δp_1 is only allowed to vary between -1 and $+1$. Both w_1 and w_2 are allowed to vary between 0.5 and 5.0, and a_2 is never allowed to be higher than a_1.

This PSF –while reasonably accurate towards most sources in its field of view– is occasionally wider or narrower than the PSFs of other sources in the same FoV which are significantly brighter or dimmer than the source the prototype PSF was constructed from. The residual generated at the end of the CLEANing process with these other sources will often leave behind artifacts of negative emission, which is indicative that too much emission was subtracted from some sources. Much like the issue of the unknown dispersion axis PSF, this can not be improved upon much without a lengthy study focused solely on characterising the PSF of the AKARI NP observing mode. I can, however, characterise the uncertainty caused by the imperfect PSF by making use of the artifacts of negative emission. By calculating the RMS of the pixels surrounding

each part of each extraction path at the end of the CLEANing, I can estimate the uncertainty for each point of each extracted spectrum. Those parts of the spectra which have artifacts in the CLEAN image resulting from an imperfect PSF will this way result in a much higher reported uncertainty, allowing them to be considered with the appropriate-sized grain of salt.

As far as the author is aware, the CLEAN algorithm has never been applied to the extraction of spectra from a slitless multi-object spectroscopy field such as the AKARI NP fields. The novelty of the method combined with the caveats discussed above call for a healthy degree of skepticism on whether the method works as intended. To benchmark the method, it is compared with the results of the "Gaussian" extraction methodology, which has previously been proven to be effective in Noble et al. (2013). Although the Gaussian extraction is extremely time-inefficient in most fields of view considered in this chapter, it could be performed in a reasonable amount of time for the pointings towards B35A. Extracting sources from B35A with the Gaussian extraction method is time-efficient because it contains very few sources compared to the other studied cores and thus the Gaussian extractor does not become overwhelmed in its minimizations. The first of such benchmarks can be performed right after the spectrum extraction, by comparing the raw extracted spectra from both methods. Both extractors produced spectra from several same sources, and examples of such spectra are shown in Figure 5.9. Comparing spectra between the two methods, most differences between CLEANing and Gaussian extraction falls to those seen in spectrum 5.9a. The spectra extracted through CLEANing tend to exhibit a slightly (by $\sim 20-30\%$) higher baseline flux, and the x axes of the spectra from the two methods are offset by a few pixels. The stronger CLEANed spectra can be explained by the CLEAN method picking up more of the background emission from the frame and assigning it to spectra, and –as will be seen when discussing the same comparisons between fully reduced spectra– wavelength calibration eliminates the x axis offset between the extracted spectra from the two methods.

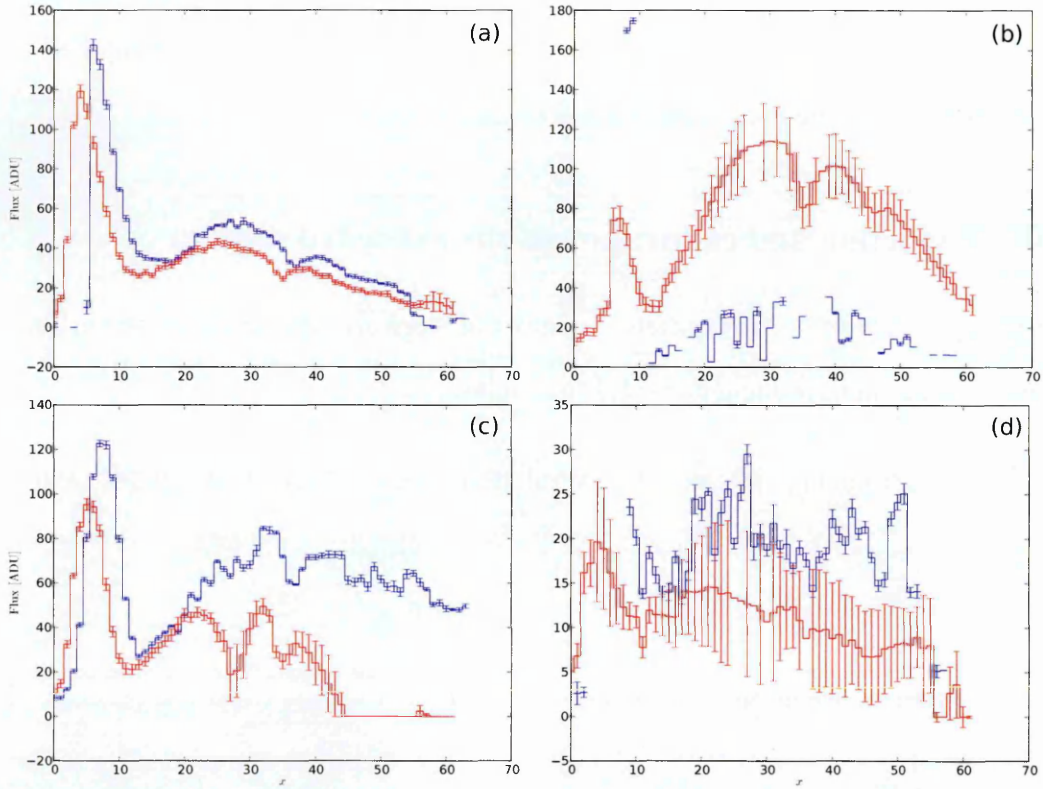

Figure 5.9: A collection of spectra towards B35A showing some spectra extracted from the NP frame using the (blue spectra) CLEAN and the (red spectra) Gaussian extraction method. These spectra illustrate both typical extracted spectra of varying quality, and the differences caused by the two different extraction methods. Spectrum (a) is a typical fairly high-quality spectrum procduced with both methods, showing a strong water absorption feature at $x \approx 12$ and a CO_2 ice feature at $x \approx 36$. Spectrum (b) shows another strong water absorption feature in the gaussian-extracted spectrum but noise in the CLEANed spectrum. This is a result of the confusion filtering happening during the operation of the CLEAN method, causing it to (sometimes overzealously, such as in this case) ignore the majority of the emission from this spectrum because it runs too close to another strong spectrum. The gaussian extraction has no such filtering implemented, and will thus extract the spectrum even with potential confusion causing issues. Spectrum (c) shows another strong water absorption feature, with the Gaussian-extracted and CLEAN-extracted spectra strongly disagreeing with each other at $x > 20$. Such an effect is most likely the result of the CLEAN extraction picking up background emission (which is fairly strong in B35A, and could not be fully removed) and assigning it to a spectrum. The Gaussian method will tend to better ignore such emission, as it does not conform well to an expected Gaussian-shaped PSF. Spectrum (d) shows a case where the extraction has apparently failed (most likely due to a weak or misplaced source) with both methods, resulting in what is effectively noise as the extracted spectrum.

At this stage the differences between the CLEAN and Gaussian extraction methods seem acceptable, and I can proceed to the reduction and analysis of the CLEAN-extracted spectra. The benchmarking is not yet over, though, and more comparisons will be performed at the end of the spectral reduction phase.

5.3.4 Reduction and calibration of the extracted spectra

After the spectra have been extracted, a number of steps are still necessary to perform on them in order to have them be useful for analysis:

1. A number of data points exist in several of the extracted spectra which are clearly artifacts caused by bad data in the NP frames or glitches in the extraction process. These outliers must be filtered out of the spectra.

2. Most spectra are duplicated in both the short and the long exposure versions of the NP frames. Each long and short exposure spectrum corresponding to the same source has to be merged together, while paying special attention to filter out or correct data points where saturation and non-linear effects in the long exposure produce data inconsistent with the short exposure.

3. Many of the targets were observed twice in a row, in two "sub-pointings". This means that several sources can have their S/N increased by merging their respective spectra from these two observations.

4. The spectra at this point are expressed with a pixel offset from the source location on the x axis, and the pixel value (in arbitrary digital units or ADUs) at this offset on the y axis. The x axis values need to be converted to physical units, through the application of wavelength calibration.

5. After wavelength calibration, the y axis data can then be converted to physical units (flux) as well, through the application of response calibration.

6. At the end of the reduction and calibration, a final pass is made on the spectra

in order to crop out bad data. The data is also convolved in order to improve the S/N ratio at the expense of some spectral resolution.

The reduction process begins with the outlier-filtering. In this phase all the data which returned error codes (because of e.g. missing data) during the extraction process is filtered out. Also all data points where the S/N < 1.0 are filtered out. Finally each data point is compared to the median of a set number consisting of itself and its adjacent points. If the data point under scrutiny is greater than three times this median, it is considered an outlier (most likely caused by a cosmic ray that was missed during the image reduction process) and is filtered out. All data points filtered out in this way have both their x and y values removed, and the data filtered in this way is written into files, ready for the next step: merging the short and long exposures.

The second step is the merging together of the short and long exposure spectra for each source. The exposure times for the short and long exposures are listed as 2.3 seconds and 51.0 seconds, respectively. To merge the short and long exposures together, the data in both cases is first divided by the exposure time, after which a weighted average of the two is taken. The weight is calculated by the formula

$$w = \frac{t_{\mathrm{exp}}}{(\Delta y / t_{\mathrm{exp}})^2}, \tag{5.7}$$

where t_{exp} is the exposure time, and Δy is the uncertainty of the data. As mentioned previously the long exposure time data becomes unreliable at very high intensities, due to a combination of saturation and unaccounted-for detector non-linearity. It was empirically found that the time-normalized long exposure data ceases to align correctly with the short exposure data at points where the short exposure exceeds $\sim$ 150 ADUs. All long exposure data points where this condition is fulfilled were masked out, effectively causing these parts of the spectra to contain signal only from the short exposure data. An additional consideration with the exposure time merger is that, on visual inspection, the time-normalized short and long exposures do not align with each other even at the points where non-linearity effects or saturation is expected to happen.

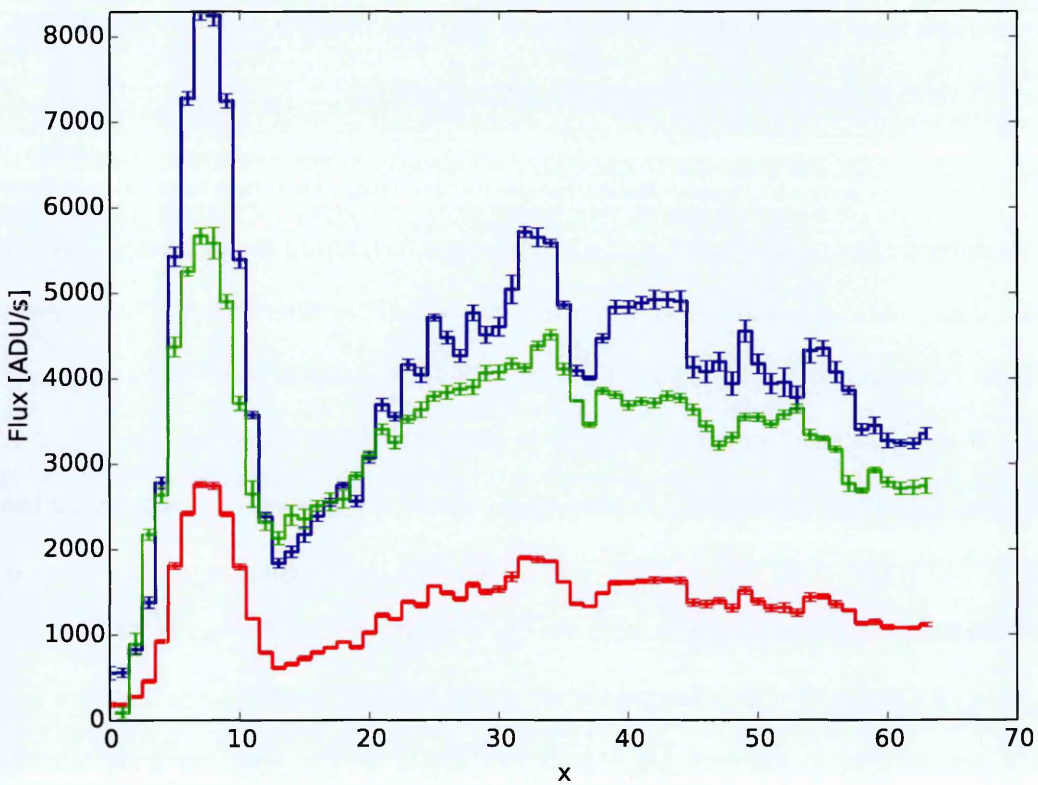

Figure 5.10: Time-normalized short and long exposure spectra of SSTc2d J054430.9+090826. The time-normalized short exposure version is plotted with a red line, and the long exposure version is plotted with a green line. The blue line is the time-normalized short exposure spectrum after it has been multiplied by a factor of 3 in an attempt to compensate for the unknown mismatch between the short and long exposures.

Through testing it was discovered that the time-normalized short exposure is too dim (or the long exposure too bright) by approximately a factor of 3. The precise cause of this discrepancy is unknown, but it can be corrected for by multiplying the signal in the time-normalized exposure data by 3 before performing the weighted averaging of the short and long exposures. After this correction –an example of the results of which is shown in Figure 5.10– the signal from the time-normalized short and long exposure spectra agree to a reasonable degree with each other in all places where they are expected to agree i.e. in parts of the spectrum not belonging to the 0th order diffraction regime.

The third step was that of merging spectra of the same source taken in two different sub-pointings together. In this step the c2d source association was made use of. Spectra

in two different sub-pointings which had been associated with the same c2d object were declared to be two observations of the same source, and a weighted average (with the weight set as the inverse of the uncertainty) of the spectra was taken and passed on for further processing. Several spectra merged in this way were visually inspected, and found to have indeed have shapes similar enough to plausibly originate from the same source. No contradictory spectra were found among those merged; another testament to the effectiveness of the automatic source association algorithm.

The fourth step is where the wavelength calibration is performed. This step is closely related to the sixth step –the response calibration– as the response curve was made use of in the wavelength calibration step, and an accurate response calibration requires an accurate wavelength calibration. The transformation of delta-pixel values along the spectrum extraction path can be handled through the application of a 3rd order polynomial, such as the one presented in Tsumura et al. (2013). With this polynomial the relation between the delta-x values and wavelength can be expressed in the form

$$\Delta x = a\Delta\lambda_{\rm ref}^2 + b\Delta\lambda_{\rm ref} + c - a\Delta\lambda_{\rm peak}^2 - b\Delta\lambda_{\rm peak} - c \quad (5.8)$$

$$= a(\Delta\lambda_{\rm ref}^2 - \Delta\lambda_{\rm peak}^2) + b(\Delta\lambda_{\rm ref} - \Delta\lambda_{\rm peak}) \quad (5.9)$$

where $\Delta\lambda_{\rm peak} = \lambda_{\rm peak} - \lambda_{\rm ref}$ is the difference between the selected thoroughput maximum and the reference wavelengths. $\Delta\lambda_{\rm ref} = \lambda - \lambda_{\rm ref}$ is the difference between the calibrated wavelength equivalent of Δx and the reference wavelength. The reference wavelength is set to be 3.5 μm, which is the wavelength at which dispersion of the prism in the NP filter is well defined. The peak wavelength is nominally supposed to be at approximately 2.4 μm. This peak is also found in the response calibration curve (further described in the sixth step), and its immediately adjacent data points have the same general shape as the peaks found in the uncalibrated spectra. Both the response calibration curve and many of the extracted spectra show a second, weaker but clearly detectable, local maximum at approximately 3.8μm. The local peaks of the response

curve at 2.4 and 3.8 μm were compared by hand with the peaks found at fully extracted but otherwise featureless spectra to find values for the parameters of the wavelength calibration polynomial in order to cause the peaks of the extracted (and wavelength calibrated) spectra to line up with the peaks in the response calibration spectrum. The set of parameters which achieve this are $\lambda_{\text{peak}} = 2.57\,\mu\text{m}$, $a = 4.63\,\frac{\text{px}}{(\mu\text{m})^2}$, and $b = 17.84\,\frac{\text{px}}{\mu\text{m}}$. The parameter c, while set during the calibration, does not affect the calibration results.

The fifth step –as previously mentioned– was the response calibration step. Once the wavelength calibration has been performed, the data is compatible for converting its ADU flux units to millijanskys. This is made possible by a wavelength calibration function, adapted from Tsumura et al. (2013). The data from the fifth step was divided by the response function provided as part of the standard AKARI calibration package, producing the response calibrated spectra which are ready for finalization.

The sixth and final step is where the spectra are finalized for analysis. At the end of the last step it was noticed that the reduced data is generally of very poor quality at wavelengths lower than 2.5 μm and higher than 4.6 μm. Additionally, it was decided that the noise in the data at this point was still significantly high, and could be improved upon at the expense of spectral resolution. For this reason the spectra were convolved with a gaussian kernel with a standard deviation of 3 units along the x axis. This phase also performs a final check on the spectrum, to determine whether it may be of appropriate quality for further analysis. If no part of the spectrum increases above 5 mJy flux, the spectrum is considered to be below the sensitivity limit of AKARI and is considered pure noise. After the cropping and convolution, the finalized spectra were written to files. These files form the basis of the remainder of the analysis, in which the ice maps are created.

These reduction steps were performed not only on the CLEAN-extracted spectra but also the spectra extracted from B35A using the Gaussian extraction method. An example of how the spectrum of a single source (SSTc2d J054430.9+090826, also featured in its raw form in Figure 5.9c) behaves throughout the reduction process in

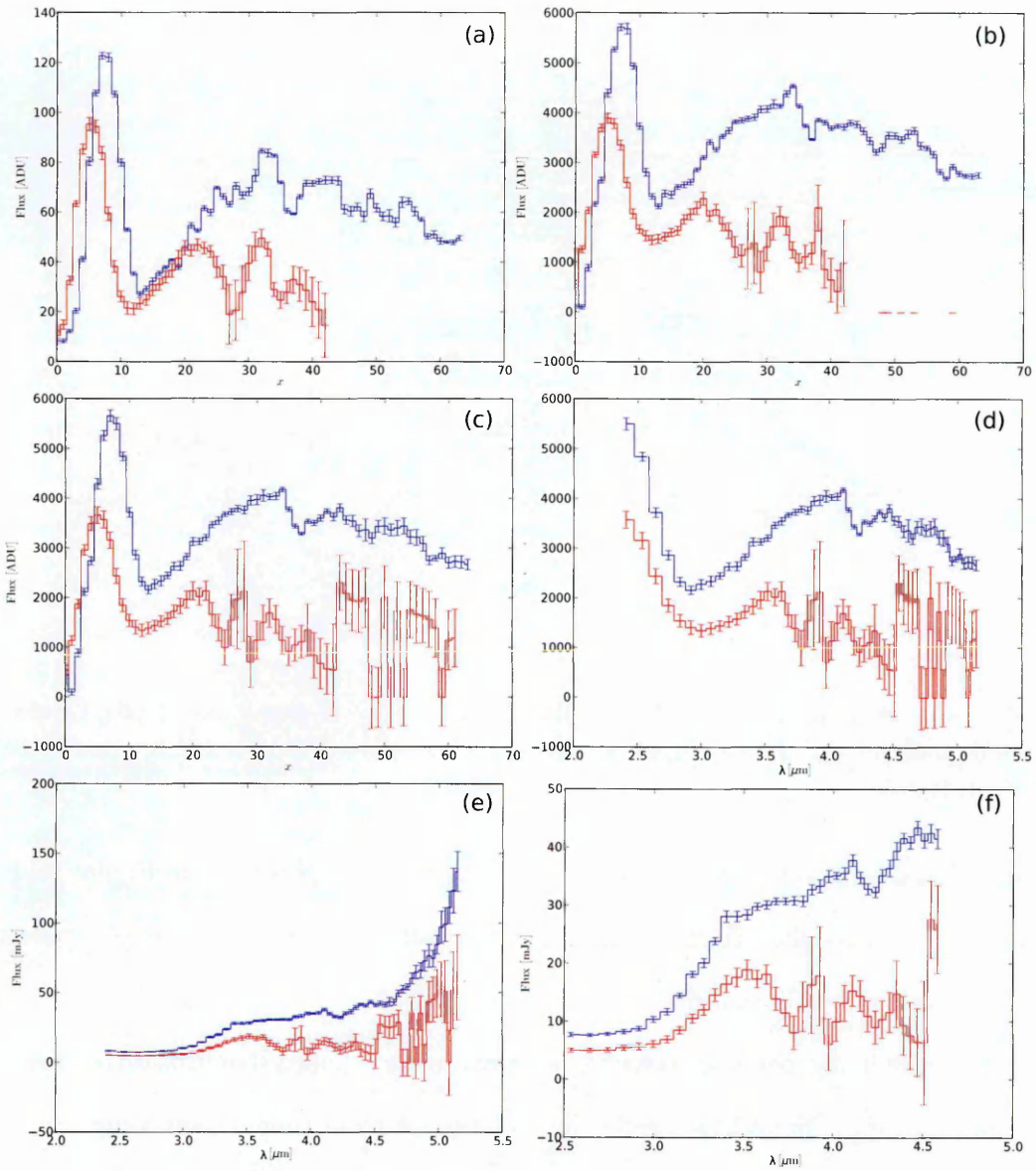

Figure 5.11: The spectrum of the source SSTc2d J054430.9+090826 in its (blue) CLEAN-extracted and (red) Gaussian-extracted form, at various stages of the reduction process. Spectrum (a) shows the spectra immediately after the outlier-filtering step. Spectrum (b) is after the time-merging phase. Spectrum (c) is after the pointing-merging phase. Spectrum (d) is after the wavelength calibration phase. Spectrum (e) after the response calibration phase. Spectrum (f) is the final version, ready for analysis. The spectra presented preceding the time-merging phase are those of the short exposure version, and the spectra presented preceding the pointing-merging phase are from subpointing 1.

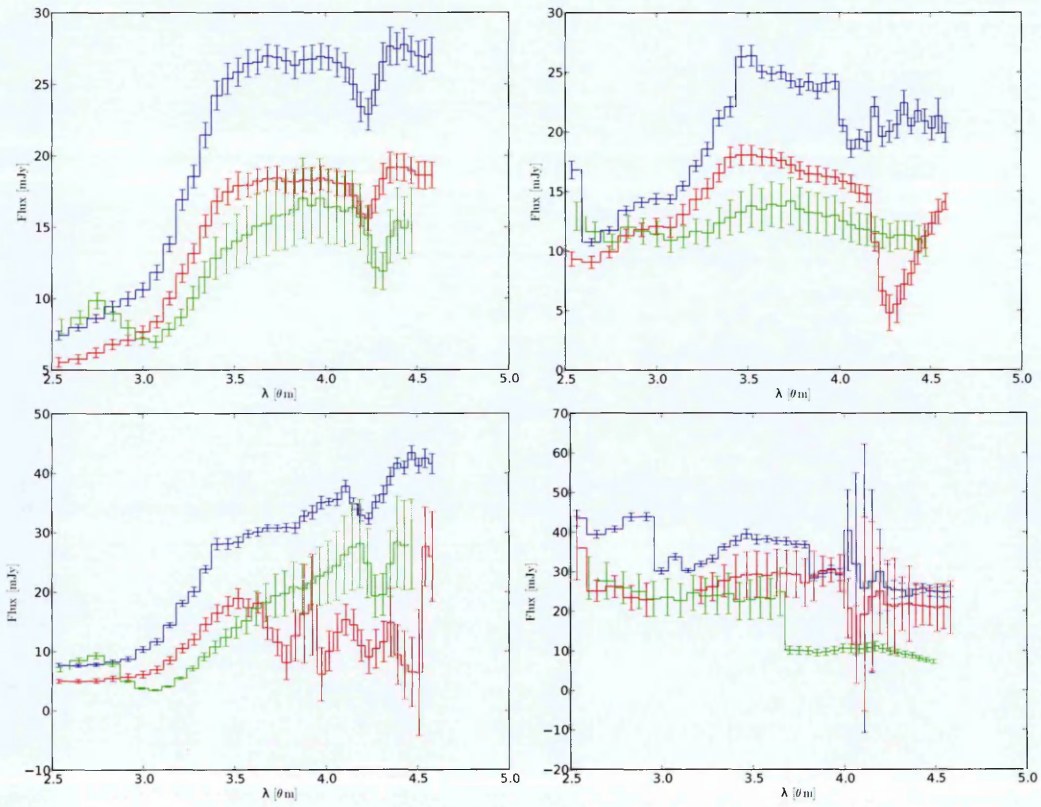

Figure 5.12: A comparison between the (blue) CLEAN-extracted, (red) Gauss-extracted, and (green) JAXA-pipeline extracted spectra towards a small number of sources in B35A.

both its CLEAN-extracted and Gaussian-extracted forms is presented in Figure 5.11. As is seen from this, the offset on the x axis between the two versions is eliminated with the wavelength calibration.

At this point it also becomes possible to compare the reduced spectra with the spectra produced by the official JAXA reduction pipeline. A collection of such comparisons is presented in Figure 5.12. The JAXA pipeline is in some cases capable of producing spectra of similar quality to the CLEAN-extracted spectra, but it can do so towards only very few lines of sight and in many situations just returns obviously incorrect data. However, in a future versions of ARF2 it may be beneficial to reverse-engineer parts of (undocumented parts of) the JAXA spectroscopy pipeline in order to improve the calibration quality of the CLEANed spectra.

5.3.5 Creation of the ice maps

With the extracted, reduced and calibrated spectra at the ready, I am finally able to create the ice maps from the data. This process can be split into two major steps: the conversion of the flux units in the spectra to optical depth units, and the determination of ice column densities.

Before I do any of this, however, I must first choose what ice components I am interested in. I know from other observations that the major expected features in this frequency range arise mainly from CO, CO_2 and H_2O, from wavelengths of 4.67, 4.27, and 3.0 μm, respectively (e.g. Gibb et al., 2004). A visual examination of the reduced spectra shows signs of the O-H stretching feature (which is responsible mainly for water, though see Chapter 3) in several cases. The features associated with CO and CO_2 are intermittently visible, but very rare. The lack of these features is suspected to be a result of the very poor S/N ratio and outright missing data at the relevant frequencies. Regardless, these two molecules lack a sufficient number of detections for the creation of any kind of meaningful map, due to lack of data points. For this reason I stick to creating a map of water ice in the observed pointings.

In calculating the optical depth the primary objective is to fit continuum baseline around the 3-micron O-H stretching feature, visible in many of the extracted spectra. The continuum was calculated as a 2nd order polynomial fit to the data, fitted to the wavelength ranges 2.5-2.7, 3.5-4.3, and 4.47-4.55 μm. These ranges were selected so as to make the baseline fit avoid any of the ice and other features noticed in the data. A second order polynomial fit was chosen as the continuum instead of a third order one because a third order fit was found to behave more erratically with the relatively small number of occasionally very noisy datapoints available in the fitting range. The weakness of the second order polynomial fit is that it sometimes does not describe the continuum very well especially at long wavelengths, but after testing it was still used because it describes the continuum adequately at 3 microns, where the H_2O ice feature of interest to this study is found. The continuum baseline allowed the calculation of

the optical depth spectra, by applying

$$\tau = \ln(I_{\text{cont}}) - \ln(I_{\text{obs}}), \tag{5.10}$$

where I_{cont} is the fitted continuum flux of the source, while I_{obs} is its observed flux. At the end of this I had successfully converted the flux spectra to optical depth spectra. At the end of this step, a visual inspection was performed on the resulting spectra, and cases with an irrecovably bad baseline fit were dropped from the data set, to avoid false detections.

To calculate the column density of water ice, a laboratory water ice spectrum from Noble et al. (2013) was fitted to the optical depth spectra using OMNIFIT. From the fit results N(H2O,solid) was calculated in the manner previously described in Section 1.4.3 of Chapter 1. In these calculations the non-CDE corrected A for water ice column density calculated from the 3-micron O-H stretch is $2.0 \cdot 10^{-16}\,\text{cm molecule}^{-1}$ (Gerakines et al., 1995).

Figure 5.13 highlights four of the most imporant stages of a single extracted spectrum on its journey to a water ice column density estimate. Application of the column density calculations to the fitted water ice spectra bring me to the results of this chapter: the ice maps.

5.4 Results

5.4.1 Water ice maps

The feature which was most detectable in the final spectra was the O-H stretching mode at 3 microns, which is most often attributed to H_2O ice. Using this feature, it was possible to estimate the column density of water ice towards 207 lines of sight, consisting 131 non-detections and 76 detections. The criterion for choosing between a detection and non-detection lied in the 2σ noise threshold. Any estimate of column density based on data with an absorption feature rising above the 2σ noise level was

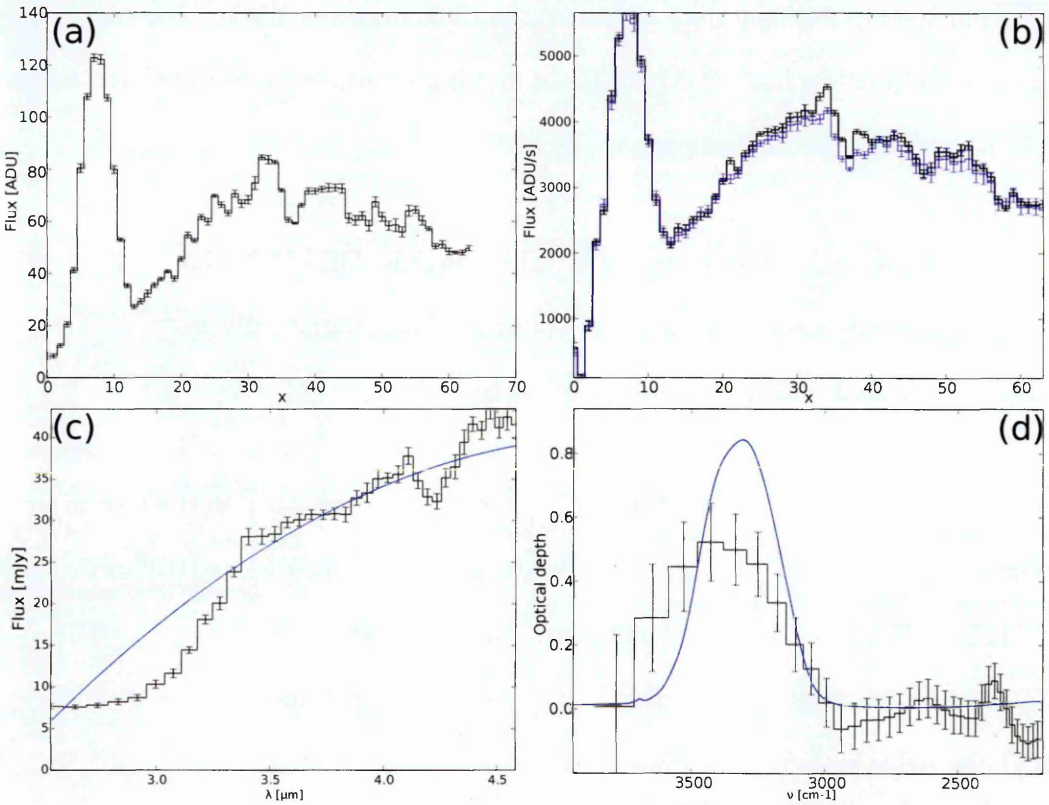

Figure 5.13: The spectrum of a single source (SSTc2d J054430.9+090826, from B35A) in various stages of reduction. Spectrum (a) shows the raw spectrum (the short exposure version, from subpointing 1), immediately following extraction. Spectrum (b) shows the spectrum after it has been merged with the second subpointing. Spectrum (c) is the final reduced spectrum, fully calibrated and ready for analysis. This spectrum also shows with a solid blue line a second order polynomial fit, which is used in calculating the optical depth spectrum. Spectrum (d) shows the laboratory water ice spectrum fit results (as a solid blue line) to the O-H stretch of the optical depth spectrum of the source.

considered a good detection. Any feature staying below this threshold was classified as a non-detection, and an upper limit was calculated instead. The column densities towards all lines of sight are presented in Tables 5.2 to 5.13. When such information was available from the c2d catalogue, these tables also indicate whether the sources being observed are classified as background sources or YSOs. There is a total of 145 background stars in the final data set, and only 12 sources are YSOs. The remaining 50 sources could not be classified because of missing information. These observations contain no sources classified as galaxies by c2d.

Table 5.2: Ice mapping results towards DC274.2-00.4. Sources named "Unknown" could not be automatically associated with a c2d catalogue source.

Source name	Type	α_{J2000} [deg.]	δ_{J2000} [deg.]	$N(H_2O, \text{solid})$ [$10^{18}\,cm^{-2}$]
SSTc2d J092824.7-513432	Unknown	142.103	-051.576	≤ 0.76
SSTc2d J092828.7-513615	Star	142.119	-051.604	≤ 2.13
SSTc2d J092859.3-513403	Star	142.247	-051.567	≤ 0.56
Unknown-1	Unknown	142.338	-051.584	1.40 ± 0.43
Unknown-2	Unknown	142.120	-051.642	≤ 0.28
Unknown-3	Unknown	142.078	-051.594	≤ 0.58
Unknown-4	Unknown	142.150	-051.655	1.09 ± 0.31
Unknown-5	Unknown	142.254	-051.675	0.28 ± 0.13
Unknown-6	Unknown	142.117	-051.615	1.05 ± 0.49
Unknown-7	Unknown	142.305	-051.555	≤ 4.45

Table 5.3: Ice mapping results towards DC275.9+01.9. Sources named "Unknown" could not be automatically associated with a c2d catalogue source.

Source name	Type	α_{J2000} [deg.]	δ_{J2000} [deg.]	$N(H_2O, solid)$ $[10^{18} cm^{-2}]$
SSTc2d J094636.0-510326	Star	146.650	-051.057	≤ 0.81
SSTc2d J094653.0-510628	Star	146.721	-051.108	≤ 0.44
SSTc2d J094657.3-510728	Star	146.739	-051.124	≤ 0.57
Unknown-8	Unknown	146.579	-051.108	≤ 0.72
Unknown-9	Unknown	146.737	-051.131	≤ 6.50
Unknown-10	Unknown	146.661	-051.146	0.41 ± 0.21

Table 5.4: Ice mapping results towards DC291.0-03.5.

Source name	Type	α_{J2000} [deg.]	δ_{J2000} [deg.]	$N(H_2O, solid)$ $[10^{18} cm^{-2}]$
SSTc2d J105857.2-634311	Star	164.738	-063.720	0.51 ± 0.22
SSTc2d J105905.0-634206	Star	164.771	-063.702	0.49 ± 0.21
SSTc2d J105906.8-634245	Star	164.778	-063.713	7.21 ± 3.41
SSTc2d J105918.8-634144	Star	164.828	-063.696	≤ 1.36
SSTc2d J105922.3-634417	Star	164.843	-063.738	≤ 0.68
SSTc2d J105923.8-634045	Star	164.849	-063.679	0.69 ± 0.17
SSTc2d J105928.3-634118	Star	164.868	-063.688	≤ 1.60
SSTc2d J105929.3-634419	Star	164.872	-063.739	≤ 0.89
SSTc2d J105932.5-634737	Star	164.885	-063.793	0.77 ± 0.21
SSTc2d J105934.9-634438	Star	164.895	-063.744	≤ 0.79

Continued on next page

Table 5.4 – continued from previous page

Source name	Type	α_{J2000} [deg.]	δ_{J2000} [deg.]	$N(H_2O, solid)$ [10^{18} cm^{-2}]
SSTc2d J105936.0-634744	Star	164.900	-063.796	≤ 1.26
SSTc2d J105936.1-634813	Star	164.900	-063.804	≤ 0.48
SSTc2d J105937.9-634639	Star	164.908	-063.778	≤ 1.62
SSTc2d J105938.5-634306	Star	164.911	-063.718	≤ 0.30
SSTc2d J105942.0-634918	Star	164.925	-063.822	1.21 ± 0.47
SSTc2d J105948.9-634749	Star	164.954	-063.797	≤ 0.87
SSTc2d J105950.1-634914	Star	164.959	-063.820	0.42 ± 0.19
SSTc2d J105951.3-633840	Star	164.964	-063.645	1.83 ± 0.50
SSTc2d J105952.5-634229	Star	164.969	-063.708	0.72 ± 0.20
SSTc2d J105955.2-634418	Star	164.980	-063.738	≤ 0.87
SSTc2d J105956.0-634459	Star	164.983	-063.750	≤ 1.87
SSTc2d J105959.6-634628	Star	164.998	-063.774	0.24 ± 0.13
SSTc2d J110000.1-634117	Star	165.000	-063.688	≤ 0.91
SSTc2d J110000.7-634511	Star	165.003	-063.753	0.62 ± 0.28
SSTc2d J110001.1-633741	Star	165.005	-063.628	0.88 ± 0.22
SSTc2d J110007.5-634023	Star	165.031	-063.673	0.43 ± 0.24
SSTc2d J110010.8-634736	Star	165.045	-063.793	≤ 0.73
SSTc2d J110011.7-634404	Star	165.049	-063.734	≤ 0.72
SSTc2d J110012.2-634724	Star	165.051	-063.790	≤ 0.60
SSTc2d J110012.7-634558	Star	165.053	-063.766	≤ 1.27
SSTc2d J110018.9-634546	Star	165.079	-063.763	≤ 0.92
SSTc2d J110020.4-634528	Star	165.085	-063.758	≤ 0.61
SSTc2d J110023.0-634447	Star	165.096	-063.746	1.43 ± 0.37
SSTc2d J110025.8-634138	Star	165.108	-063.694	≤ 0.37
SSTc2d J110039.6-634310	Star	165.165	-063.720	≤ 0.29

Continued on next page

Table 5.4 – continued from previous page

Source name	Type	α_{J2000} [deg.]	δ_{J2000} [deg.]	$N(H_2O, solid)$ [10^{18} cm^{-2}]
SSTc2d J110041.3-634416	Unknown	165.172	-063.738	≤ 0.88
SSTc2d J110048.9-634428	Star	165.204	-063.741	≤ 0.60

Table 5.5: Ice mapping results towards DC300.7-01.0.

Source name	Type	α_{J2000} [deg.]	δ_{J2000} [deg.]	$N(H_2O, solid)$ [10^{18} cm^{-2}]
SSTc2d J123046.9-634458	Unknown	187.695	-063.750	≤ 0.49
SSTc2d J123055.4-634241	Star	187.731	-063.711	≤ 0.37
SSTc2d J123058.0-634559	Star	187.742	-063.766	≤ 0.63
SSTc2d J123102.4-634724	Star	187.760	-063.790	1.18 ± 0.52
SSTc2d J123105.9-634320	Star	187.775	-063.722	≤ 0.78
SSTc2d J123106.5-634424	Star	187.777	-063.740	1.30 ± 0.45
SSTc2d J123122.4-634020	Star	187.843	-063.672	≤ 0.76
SSTc2d J123123.4-634640	Star	187.847	-063.778	≤ 0.72
SSTc2d J123129.6-634050	YSO	187.873	-063.680	≤ 1.34
SSTc2d J123129.6-634706	Star	187.873	-063.785	≤ 1.21
SSTc2d J123129.9-634235	Star	187.875	-063.710	0.59 ± 0.24
SSTc2d J123131.9-634935	Star	187.883	-063.826	≤ 0.54
SSTc2d J123140.5-633940	Star	187.919	-063.661	≤ 0.50
SSTc2d J123141.5-634510	Star	187.923	-063.753	1.29 ± 0.64
SSTc2d J123142.6-634619	Star	187.928	-063.772	1.24 ± 0.51
SSTc2d J123144.6-634900	Star	187.936	-063.817	≤ 0.32
SSTc2d J123147.4-634142	Star	187.947	-063.695	≤ 0.46

Continued on next page

Table 5.5 – continued from previous page

Source name	Type	α_{J2000} [deg.]	δ_{J2000} [deg.]	$N(H_2O, solid)$ $[10^{18}\,cm^{-2}]$
SSTc2d J123157.6-634217	Star	187.990	-063.705	≤ 0.54
SSTc2d J123159.4-634334	Star	187.997	-063.726	≤ 0.43

Table 5.6: Ice mapping results towards DC346.0+07.8.

Source name	Type	α_{J2000} [deg.]	δ_{J2000} [deg.]	$N(H_2O, solid)$ $[10^{18}\,cm^{-2}]$
SSTc2d J163633.7-353853	Unknown	249.141	-035.648	0.89 ± 0.12
SSTc2d J163636.4-354057	Star	249.152	-035.682	≤ 0.37
SSTc2d J163636.8-353743	Unknown	249.153	-035.628	≤ 1.25
SSTc2d J163639.5-354025	Star	249.165	-035.674	0.88 ± 0.23
SSTc2d J163639.8-353746	Unknown	249.166	-035.629	≤ 0.91
SSTc2d J163641.7-353541	Unknown	249.174	-035.595	0.55 ± 0.22
SSTc2d J163643.0-354055	Star	249.179	-035.682	≤ 0.78
SSTc2d J163643.6-353815	Star	249.182	-035.638	≤ 1.29
SSTc2d J163647.9-353403	Star	249.200	-035.567	≤ 1.41
SSTc2d J163650.2-353539	Star	249.209	-035.594	≤ 0.65
SSTc2d J163650.4-353314	Star	249.210	-035.554	0.45 ± 0.13
SSTc2d J163652.6-353744	Star	249.219	-035.629	1.44 ± 0.31
SSTc2d J163654.4-353614	Star	249.227	-035.604	≤ 0.90
SSTc2d J163655.1-353413	Star	249.230	-035.570	0.80 ± 0.17
SSTc2d J163701.7-353732	Star	249.257	-035.626	≤ 0.48
SSTc2d J163709.3-353947	Unknown	249.289	-035.663	≤ 0.50
SSTc2d J163711.5-354009	Unknown	249.298	-035.669	≤ 0.88

Continued on next page

Table 5.6 – continued from previous page

Source name	Type	α_{J2000} [deg.]	δ_{J2000} [deg.]	$N(H_2O, solid)$ [10^{18} cm^{-2}]
SSTc2d J163713.2-353825	Unknown	249.305	-035.640	≤ 1.11

Table 5.7: Ice mapping results towards B35A. Sources named "Unknown" could not be automatically associated with a c2d catalogue source.

Source name	Type	α_{J2000} [deg.]	δ_{J2000} [deg.]	$N(H_2O, solid)$ [10^{18} cm^{-2}]
SSTc2d J054417.2+091439	Star	086.072	+009.244	≤ 0.53
SSTc2d J054419.2+091235	Star	086.080	+009.210	0.38 ± 0.18
SSTc2d J054420.2+090557	Star	086.084	+009.099	≤ 20.13
SSTc2d J054422.8+091415	Star	086.095	+009.237	0.26 ± 0.13
SSTc2d J054422.9+091035	YSO	086.095	+009.176	≤ 0.30
SSTc2d J054426.9+091042	Star	086.112	+009.178	≤ 0.95
SSTc2d J054430.0+090857	YSO	086.125	+009.149	2.96 ± 1.41
SSTc2d J054430.6+091306	Star	086.127	+009.218	0.63 ± 0.13
SSTc2d J054430.9+090826	YSO	086.129	+009.141	1.12 ± 0.33
SSTc2d J054431.3+091203	Star	086.130	+009.201	≤ 12.72
SSTc2d J054433.5+091138	Star	086.139	+009.194	0.76 ± 0.38
SSTc2d J054436.7+091322	Star	086.153	+009.223	0.72 ± 0.30
SSTc2d J054438.4+090842	YSO	086.160	+009.145	0.99 ± 0.29
SSTc2d J054443.8+091133	Star	086.182	+009.192	0.72 ± 0.27
SSTc2d J054443.8+090819	Star	086.182	+009.139	0.32 ± 0.16
SSTc2d J054446.6+091122	YSO	086.194	+009.189	≤ 0.46

Continued on next page

Table 5.7 – continued from previous page

Source name	Type	α_{J2000} [deg.]	δ_{J2000} [deg.]	$N(H_2O, solid)$ $[10^{18}\,cm^{-2}]$
SSTc2d J054449.0+091307	Star	086.204	+009.219	≤ 0.47
SSTc2d J054452.0+091030	Star	086.217	+009.175	≤ 0.44
SSTc2d J054452.8+091305	YSO	086.220	+009.218	0.74 ± 0.42
Unknown-11	Unknown	086.157	+009.182	≤ 25.95

Table 5.8: Ice mapping results towards L1165.

Source name	Type	α_{J2000} [deg.]	δ_{J2000} [deg.]	$N(H_2O, solid)$ $[10^{18}\,cm^{-2}]$
SSTc2d J220548.7+590542	Star	331.453	+059.095	1.07 ± 0.39
SSTc2d J220606.6+590514	Star	331.528	+059.087	≤ 0.56
SSTc2d J220621.2+590352	Star	331.588	+059.064	0.98 ± 0.44
SSTc2d J220621.4+590730	Star	331.589	+059.125	≤ 0.70
SSTc2d J220629.6+590301	Star	331.623	+059.050	≤ 0.37
SSTc2d J220629.9+590517	Star	331.625	+059.088	0.83 ± 0.21
SSTc2d J220631.5+590827	Star	331.631	+059.141	≤ 1.56
SSTc2d J220632.0+590936	Star	331.633	+059.160	≤ 0.87
SSTc2d J220634.4+590558	Star	331.643	+059.100	≤ 0.58
SSTc2d J220637.7+590452	Star	331.657	+059.081	1.14 ± 0.21
SSTc2d J220641.0+590147	YSO	331.671	+059.030	≤ 1.19
SSTc2d J220641.8+590600	Star	331.674	+059.100	1.06 ± 0.44
SSTc2d J220642.4+590527	Star	331.677	+059.091	1.21 ± 0.46
SSTc2d J220643.4+590238	Star	331.681	+059.044	≤ 0.44
SSTc2d J220649.8+591040	Star	331.707	+059.178	≤ 0.93

Continued on next page

Table 5.8 – continued from previous page

Source name	Type	α_{J2000} [deg.]	δ_{J2000} [deg.]	$N(H_2O, solid)$ $[10^{18}\,cm^{-2}]$
SSTc2d J220652.0+590201	Star	331.717	+059.034	5.42 ± 1.95
SSTc2d J220703.9+590900	Star	331.766	+059.150	≤ 1.10
SSTc2d J220729.7+590612	Star	331.874	+059.103	≤ 0.59

Table 5.9: Ice mapping results towards DC269.4+03.0.

Source name	Type	α_{J2000} [deg.]	δ_{J2000} [deg.]	$N(H_2O, solid)$ $[10^{18}\,cm^{-2}]$
SSTc2d J092213.1-454722	Star	140.554	-045.789	2.00 ± 0.96
SSTc2d J092220.1-454926	Star	140.584	-045.824	0.38 ± 0.19
SSTc2d J092231.7-454358	Star	140.632	-045.733	≤ 0.73
SSTc2d J092233.0-455158	Star	140.638	-045.866	≤ 0.53
SSTc2d J092245.6-454825	Star	140.690	-045.807	≤ 0.40
SSTc2d J092253.5-454628	Unknown	140.723	-045.775	≤ 1.76

Table 5.10: Ice mapping results towards BHR59. Sources named "Unknown" could not be automatically associated with a c2d catalogue source.

Source name	Type	α_{J2000} [deg.]	δ_{J2000} [deg.]	$N(H_2O, solid)$ $[10^{18}\,cm^{-2}]$
SSTc2d J110655.1-620435	Star	166.730	-062.076	≤ 0.22

Continued on next page

Table 5.10 – continued from previous page

Source name	Type	α_{J2000} [deg.]	δ_{J2000} [deg.]	$N(H_2O, solid)$ $[10^{18}\,cm^{-2}]$
SSTc2d J110704.9-620401	Star	166.770	-062.067	≤ 1.65
SSTc2d J110713.0-620350	YSO	166.804	-062.064	0.68 ± 0.27
SSTc2d J110727.6-620748	Star	166.865	-062.130	≤ 0.56
Unknown-12	Unknown	166.891	-062.065	≤ 0.37
Unknown-13	Unknown	166.813	-062.022	≤ 1.39
Unknown-14	Unknown	166.934	-062.114	≤ 0.59

Table 5.11: Ice mapping results towards Mu8.

Source name	Type	α_{J2000} [deg.]	δ_{J2000} [deg.]	$N(H_2O, solid)$ $[10^{18}\,cm^{-2}]$
SSTc2d J122950.9-710242	Star	187.462	-071.045	≤ 0.67
SSTc2d J123008.8-710459	Star	187.537	-071.083	≤ 0.23
SSTc2d J123012.1-710456	Star	187.550	-071.082	≤ 2.01
SSTc2d J123020.4-710430	Star	187.585	-071.075	0.54 ± 0.29
SSTc2d J123023.9-710443	Star	187.599	-071.079	≤ 0.87
SSTc2d J123024.6-710554	Star	187.602	-071.098	0.80 ± 0.32
SSTc2d J123030.9-710324	Star	187.629	-071.057	0.81 ± 0.14
SSTc2d J123044.2-710235	Star	187.684	-071.043	0.78 ± 0.16
SSTc2d J123049.6-710419	Star	187.707	-071.072	≤ 0.38
SSTc2d J123115.3-710442	Star	187.814	-071.078	0.68 ± 0.19
SSTc2d J123121.3-710059	Star	187.839	-071.017	≤ 0.91
SSTc2d J123142.1-710355	Star	187.925	-071.065	0.77 ± 0.17
SSTc2d J123159.8-710219	Unknown	187.999	-071.039	0.44 ± 0.12

Table 5.12: Ice mapping results towards CB188. Sources named "Unknown" could not be automatically associated with a c2d catalogue source.

Source name	Type	α_{J2000} [deg.]	δ_{J2000} [deg.]	$N(H_2O, solid)$ [10^{18} cm^{-2}]
SSTc2d J192002.1+113611	Star	290.009	+011.603	≤ 0.56
SSTc2d J192004.2+113237	Unknown	290.017	+011.544	2.65 ± 1.27
SSTc2d J192004.6+113126	Star	290.019	+011.524	≤ 0.25
SSTc2d J192010.5+113529	Star	290.044	+011.592	0.48 ± 0.34
SSTc2d J192012.5+113748	YSO	290.052	+011.630	1.14 ± 0.13
SSTc2d J192013.9+113718	Star	290.058	+011.622	≤ 0.44
SSTc2d J192014.9+113540	YSO	290.062	+011.595	1.38 ± 0.39
SSTc2d J192016.2+113629	Star	290.068	+011.608	1.56 ± 0.17
SSTc2d J192020.1+113206	Star	290.084	+011.535	≤ 0.33
SSTc2d J192026.7+113822	Unknown	290.111	+011.639	0.53 ± 0.22
SSTc2d J192028.1+113860	Star	290.117	+011.650	≤ 0.51
SSTc2d J192028.7+113616	Unknown	290.120	+011.604	0.60 ± 0.08
SSTc2d J192029.2+113616	Unknown	290.122	+011.604	0.49 ± 0.15
SSTc2d J192030.8+113351	Star	290.128	+011.564	≤ 0.58
Unknown-15	Unknown	290.133	+011.650	0.80 ± 0.26
Unknown-16	Unknown	290.115	+011.669	≤ 0.51
Unknown-17	Unknown	289.990	+011.638	0.53 ± 0.14
Unknown-18	Unknown	289.988	+011.637	0.46 ± 0.18
Unknown-19	Unknown	290.131	+011.649	0.70 ± 0.30
Unknown-20	Unknown	289.983	+011.621	0.40 ± 0.16
Unknown-21	Unknown	289.981	+011.620	≤ 0.26

Continued on next page

Table 5.12 – continued from previous page

Source name	Type	α_{J2000} [deg.]	δ_{J2000} [deg.]	$N(H_2O, solid)$ $[10^{18} cm^{-2}]$
Unknown-22	Unknown	290.138	+011.595	0.49 ± 0.24
Unknown-23	Unknown	290.117	+011.670	≤ 0.44
Unknown-24	Unknown	290.102	+011.666	≤ 0.55

Table 5.13: Ice mapping results towards DC300.2-03.5. Sources named "Unknown" could not be automatically associated with a c2d catalogue source.

Source name	Type	α_{J2000} [deg.]	δ_{J2000} [deg.]	$N(H_2O, solid)$ $[10^{18} cm^{-2}]$
SSTc2d J122353.2-661346	Unknown	185.971	-066.229	≤ 1.89
SSTc2d J122354.2-661160	Star	185.976	-066.200	≤ 1.08
SSTc2d J122358.6-661110	Star	185.994	-066.186	≤ 0.53
SSTc2d J122401.4-661224	Star	186.006	-066.207	0.55 ± 0.22
SSTc2d J122405.5-661220	Star	186.023	-066.206	≤ 1.68
SSTc2d J122415.2-661011	Star	186.063	-066.170	≤ 0.46
SSTc2d J122426.3-661347	Star	186.110	-066.230	≤ 0.46
SSTc2d J122434.5-661243	Star	186.144	-066.212	≤ 3.16
SSTc2d J122445.1-661200	Star	186.188	-066.200	0.57 ± 0.18
SSTc2d J122453.6-661050	Star	186.224	-066.181	≤ 0.31
Unknown-25	Unknown	186.253	-066.196	≤ 0.65
Unknown-26	Unknown	186.306	-066.208	≤ 0.42
Unknown-27	Unknown	185.983	-066.158	≤ 1.93
Unknown-28	Unknown	186.220	-066.228	0.23 ± 0.11

Continued on next page

Table 5.13 – continued from previous page

Source name	Type	α_{J2000} [deg.]	δ_{J2000} [deg.]	$N(H_2O, \text{solid})$ $[10^{18}\,cm^{-2}]$
Unknown-29	Unknown	186.257	-066.224	≤ 1.43
Unknown-30	Unknown	186.084	-066.275	≤ 1.55
Unknown-31	Unknown	186.220	-066.227	≤ 0.26
Unknown-32	Unknown	185.949	-066.150	≤ 0.44
Unknown-33	Unknown	186.241	-066.162	≤ 0.99

Getting a good idea on the meaning behind this cornucopia of column densities is difficult with the help of only a collection of tabulated values, and thus alternate ways of looking at them are required.

One way is to produce maps of the ice column density in each core. The method of presenting the maps was chosen to be in the form of bubble plots, i.e. scatter plots of the field of view where the size of the symbol represents the calculated column density and its location represents the originating line of sight. This is an effective visualization method in a case such as mine, with sparsely and unevenly sampled values spread out over several separate fields of view. An overview of all the ice maps created in such a way is presented in Figures 5.14 and 5.15.

Figures 5.16 to 5.21 offer a more detailed view towards each core, with additional information about uncertainties and lines of sight towards which there were non-detections. To help understand the shape of the cloud, these bubble plots are also overlaid on top of supplementary data from either Spitzer or Herschel. Several of the cores had either Herschel/SPIRE Photometer Short Wavelength (PSW; 250 μm, traces mainly cold dust) or Spitzer/IRAC 8 μm (traces mostly polyaromatic hydrocarbons or PAHs) maps available for public use and these were used when possible, with Herschel maps prioritized over SPITZER maps. In cases where neither Herschel nor

Spitzer maps fully covering the $10' \times 10'$ window were available, AKARI N3 data was used as the background image. The choice of background image is detailed in the captions of the maps.

From the tabulated values and ice maps I see that N(H_2O, solid) tends to usually stay at values close to $\sim 10^{18}\,cm^{-2}$, with the lowest detections being slightly below $\sim 5 \times 10^{17}\,cm^{-2}$ and the highest column densities occasionally rising up to $\sim 7 \times 10^{18}\,cm^{-2}$. The spatial variation in the ice column density within each field of view is usually small, but a few exceptions can be noticed towards e.g. DC291.0-03.5 and B35A, where the column density exhibits a sharp increase towards individual lines of sight, sometimes less than an arc minute away from a much lower estimate.

5.4.2 The presence of CO_2 ice

The 4.3 μm CO_2 ice absorption feature was detected towards a small number of objects in the ice final spectra. An example of the feature in my spectra is shown in Figure 5.22. Though easy enough to identify when present, features such as this are identifiable in less than a dozen of the reduced spectra, and thus were not analysed for the purposes of mapping. The presence of a CO_2 ice feature also seems to be accompanied by a H_2O ice detection.

5.5 Discussion

The primary purpose of this study was to map the prevalence of H_2O ice towards as many lines of sight as can be extracted from the AKARI NP data. A large number of lines of sight yielded such estimates, and thus the logical next step is to compare them with other H_2O ice estimates in the literature, and to also study any possible (non-)correlations between the ice column densities and anything else that is publicly available towards the examined line of sights. Before any of these can be discussed, though, the quality of both the spectra and the ice fits done on them is a necessary topic to address.

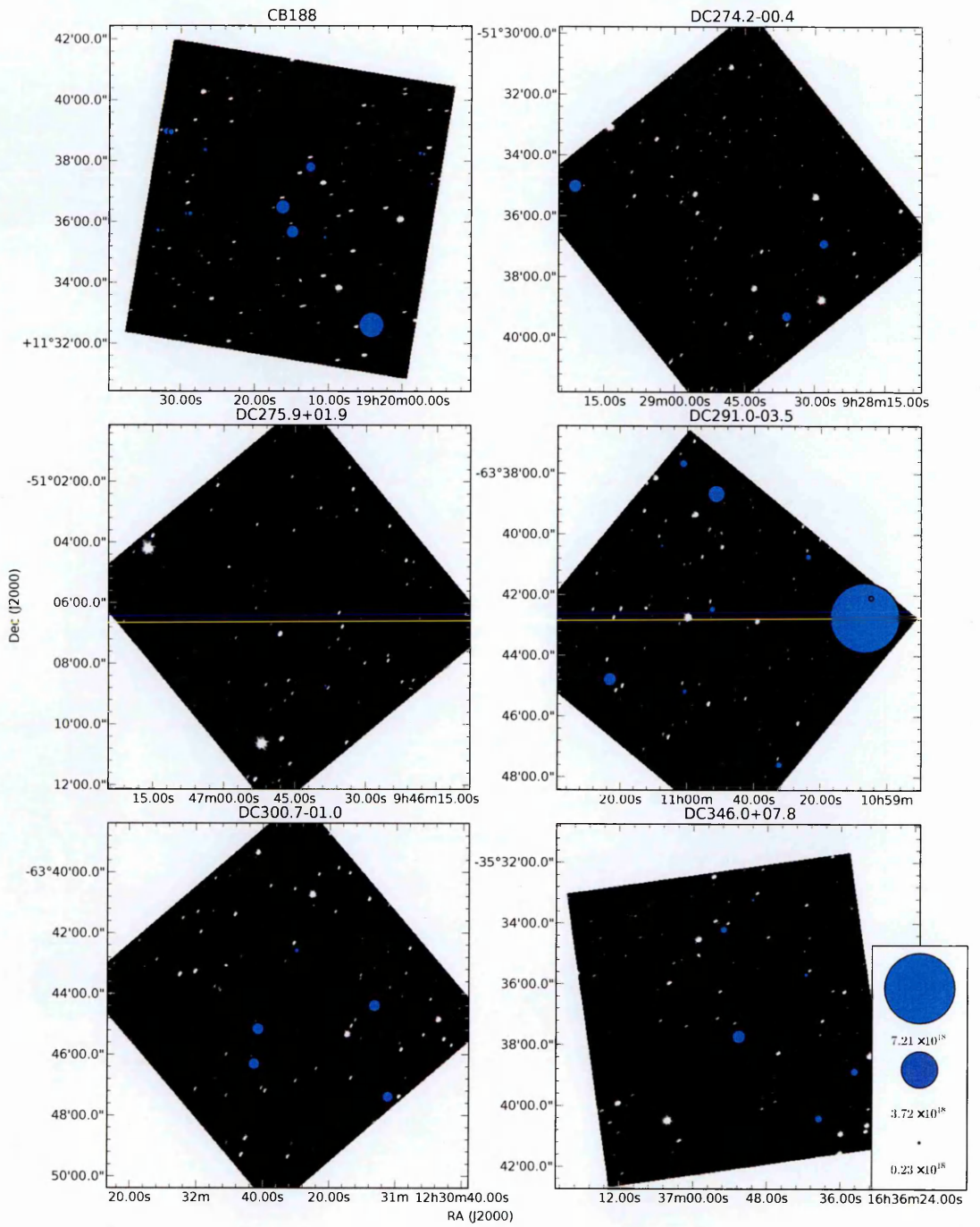

Figure 5.14: An overview of the H_2O ice mapping results towards 6 of the 12 cores studied in this chapter, expressed as bubble plots. The name of the core is indicated in the title on top of its respective map. The size of the bubble (legend on the bottom left corner applies to each of these maps) is proportional to the H_2O ice column density on the line of sight towards its centre. Only detections are plotted in these maps. The background images are the AKARI N3 frames towards their respective cores.

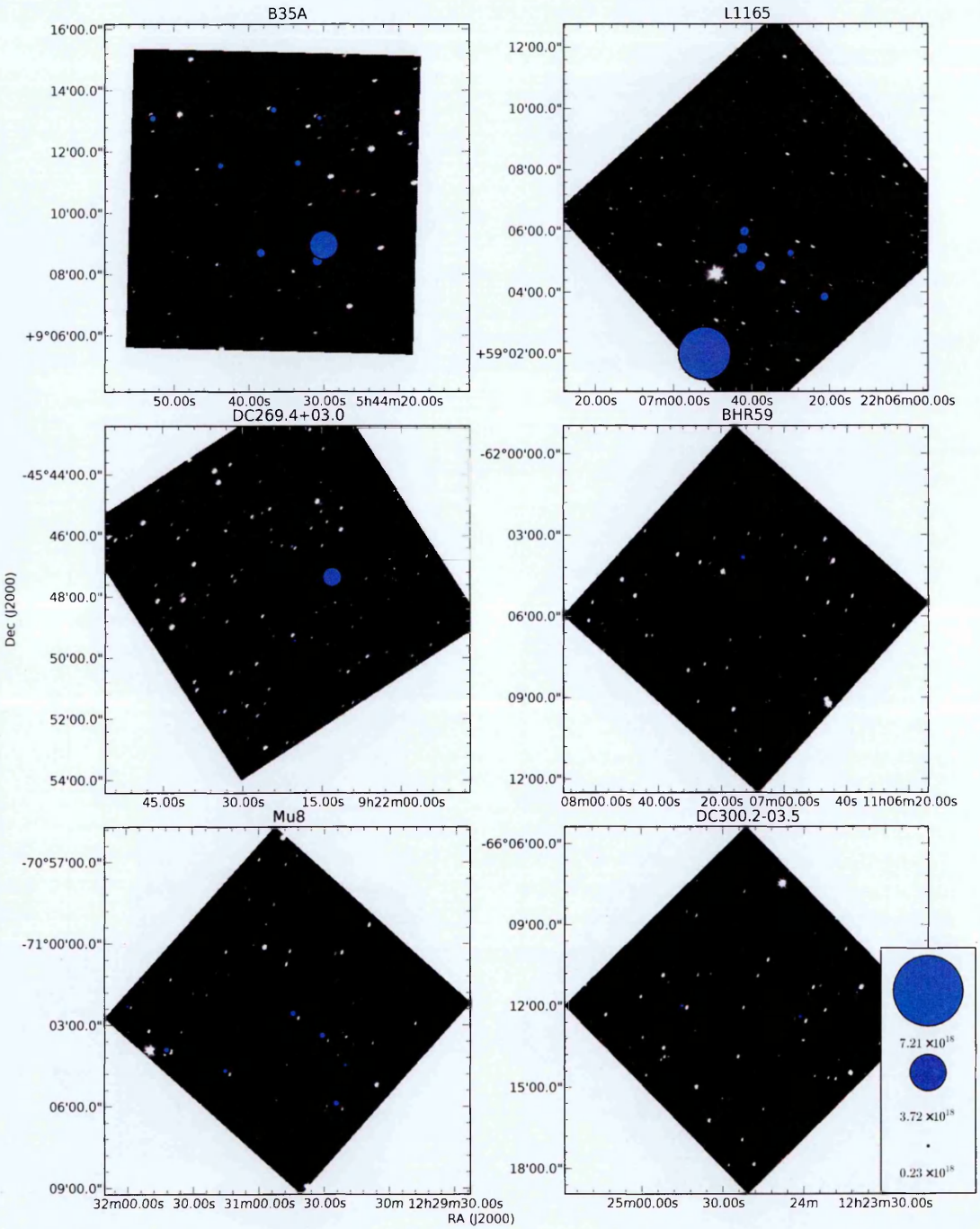

Figure 5.15: An overview of the H_2O ice mapping results towards 6 of the 12 cores studied in this chapter, expressed as bubble plots. The name of the core is indicated in the title on top of its respective map. The size of the bubble (legend on the bottom left corner applies to each of these maps) is proportional to the H_2O ice column density on the line of sight towards its centre. Only detections are plotted in these maps. The background images are the AKARI N3 frames towards their respective cores.

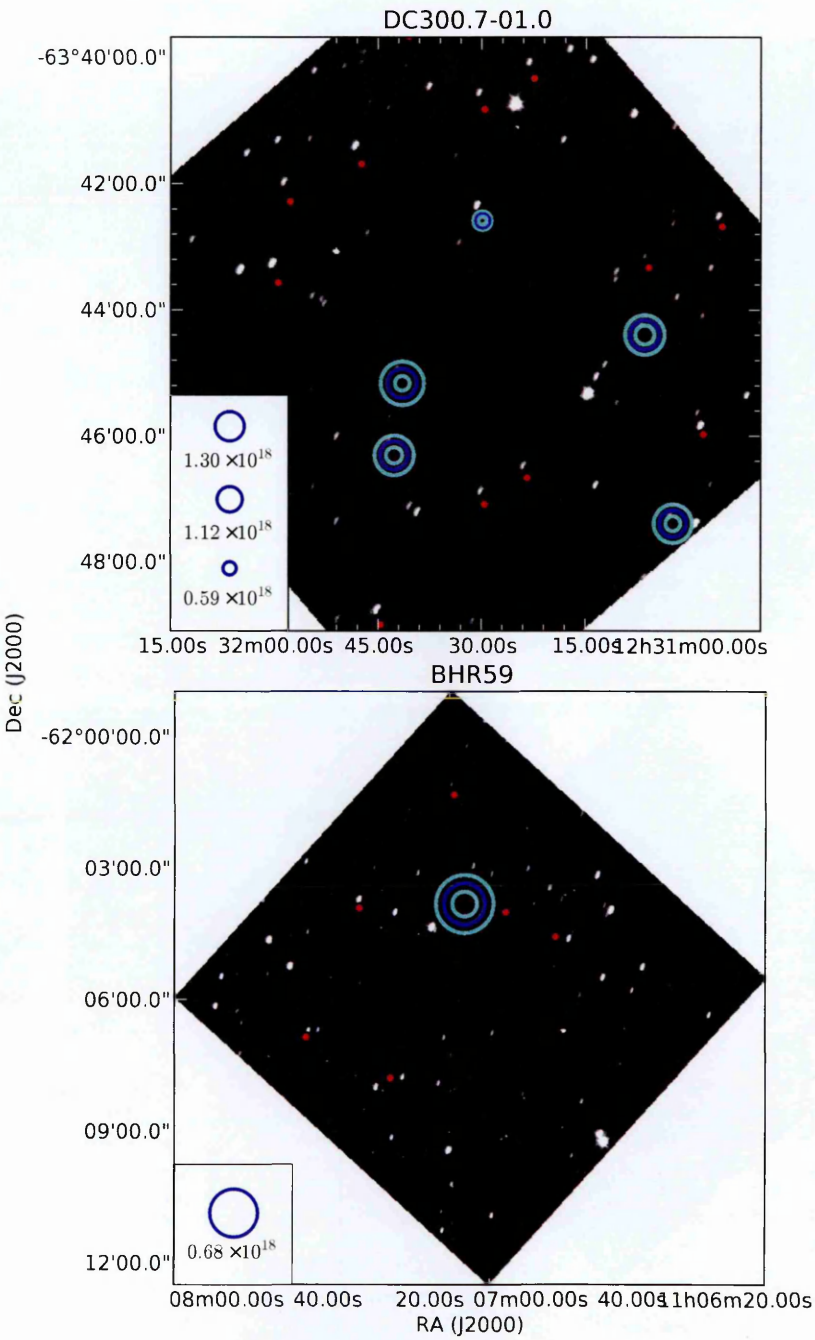

Figure 5.16: Bubble plots representing the distribution of H_2O ice towards (upper figure) DC300.7-01.0 and (lower figure) BHR59. The size of the circles represent the column densities detected towards their center, as indicated by the figures' respective legends. The blue circles represent the measured amount, with the concentric cyan circles representing its uncertainty. The red circles represent lines of sight classified as non-detections, towards which only upper limits could be estimated. The background image is an AKARI N3 frame towards the core.

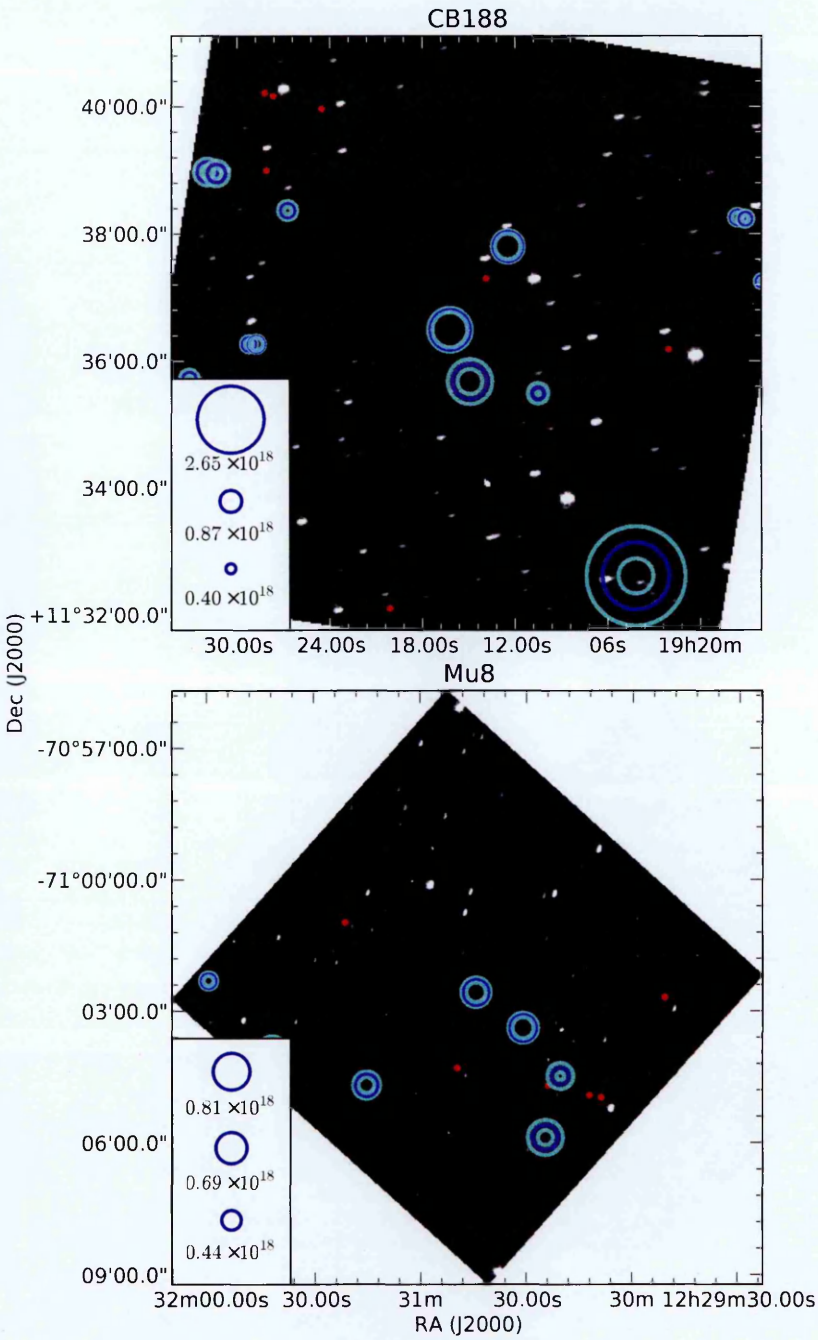

Figure 5.17: Bubble plots representing the distribution of H_2O ice towards (upper figure) CB 188 and (lower figure) Mu 8. The size of the circles represent the column densities detected towards their center, as indicated by the figures' respective legends. The blue circles represent the measured amount, with the concentric cyan circles representing its uncertainty. The red circles represent lines of sight classified as non-detections, towards which only upper limits could be estimated. The background image is an AKARI N3 frame towards the core.

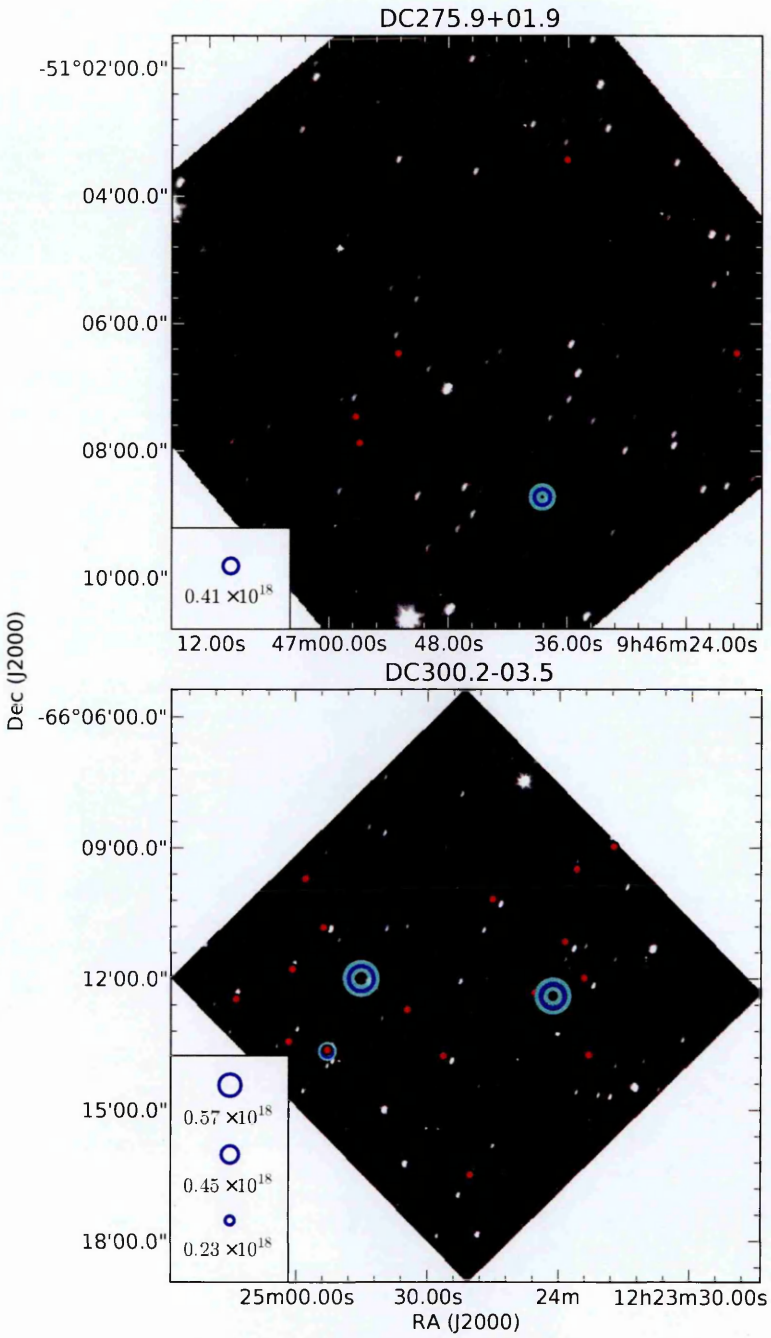

Figure 5.18: Bubble plots representing the distribution of H_2O ice towards (upper figure) DC275.9+01.9 and (lower figure) DC300.2+03.5. The size of the circles represent the column densities detected towards their center, as indicated by the figures' respective legends. The blue circles represent the measured amount, with the concentric cyan circles representing its uncertainty. The red circles represent lines of sight classified as non-detections, towards which only upper limits could be estimated. The background image is an AKARI N3 frame towards the core.

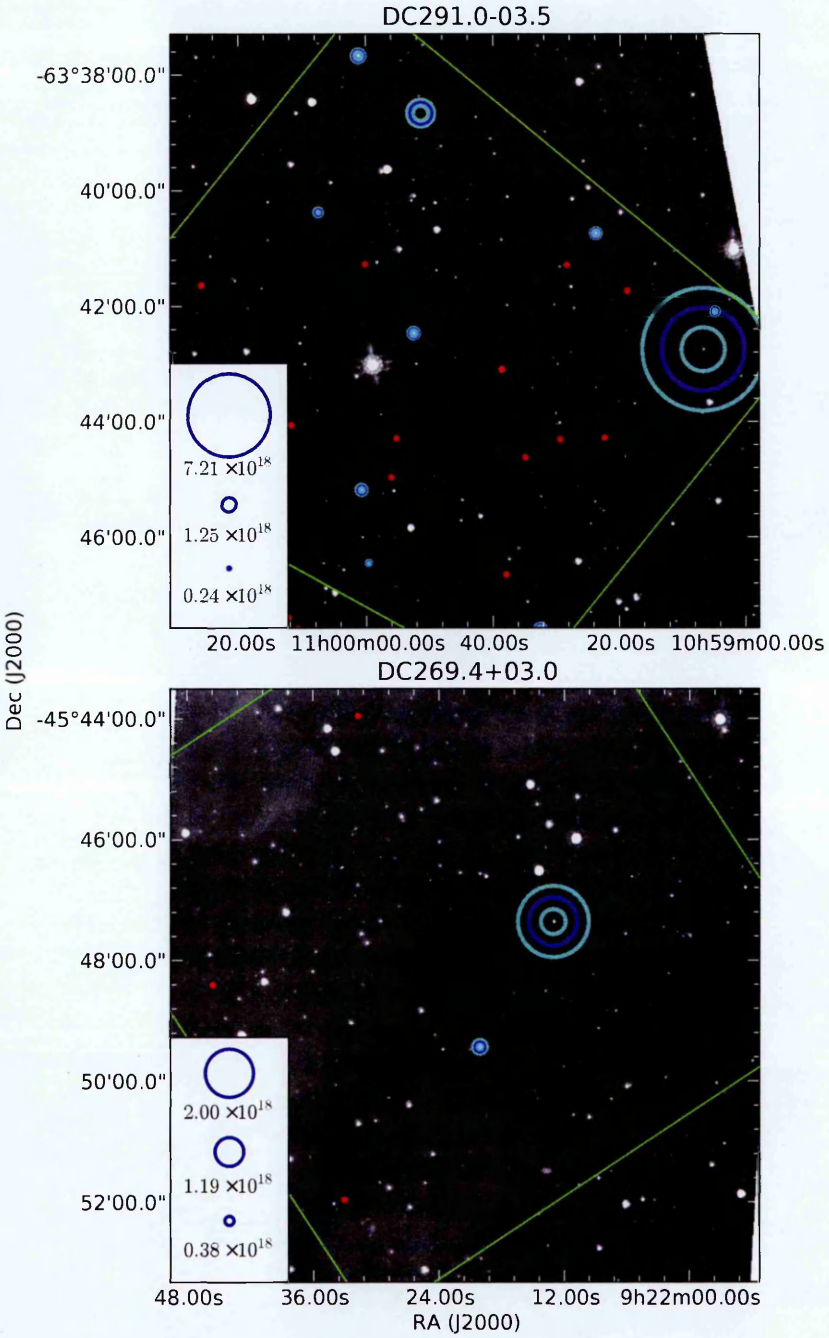

Figure 5.19: Bubble plots representing the distribution of H_2O ice towards (upper figure) DC291.0-03.5 and (lower figure) DC269.4+03.0. The size of the circles represent the column densities detected towards their center, as indicated by the figures' respective legends. The blue circles represent the measured amount, with the concentric cyan circles representing its uncertainty. The red circles represent lines of sight classified as non-detections, towards which only upper limits could be estimated. The background image is a Spitzer/IRAC 8 μm image towards the core.

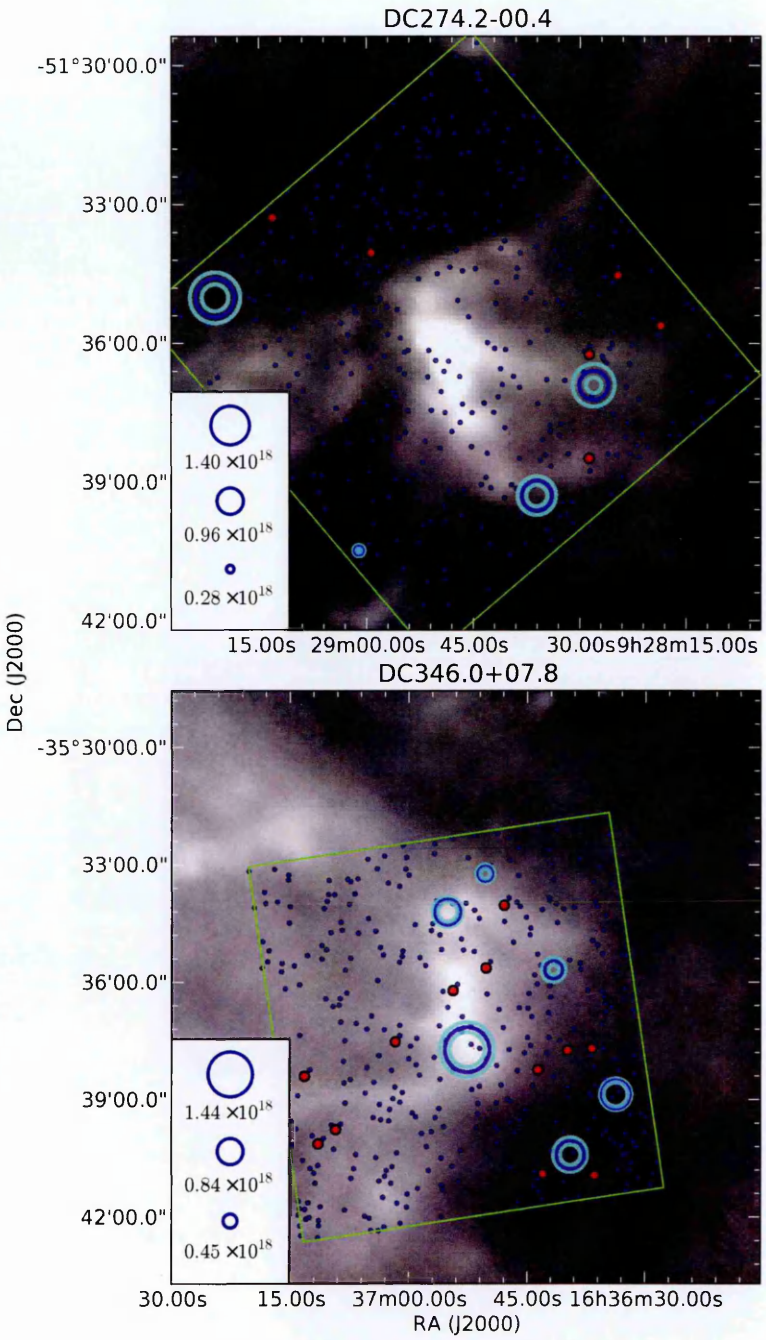

Figure 5.20: Bubble plots representing the distribution of H_2O ice towards (upper figure) DC274.2-00.4 and (lower figure) DC346.0+07.8. The size of the circles represent the column densities detected towards their center, as indicated by the figures' respective legends. The blue circles represent the measured amount, with the concentric cyan circles representing its uncertainty. The red circles represent lines of sight towards classified as non-detections, towards which only upper limits could be estimated. The blue dots indicate lines of sight towards which spectrum extraction was attempted by ARF2. The background image is a Herschel/SPIRE 250 μm map towards the core.

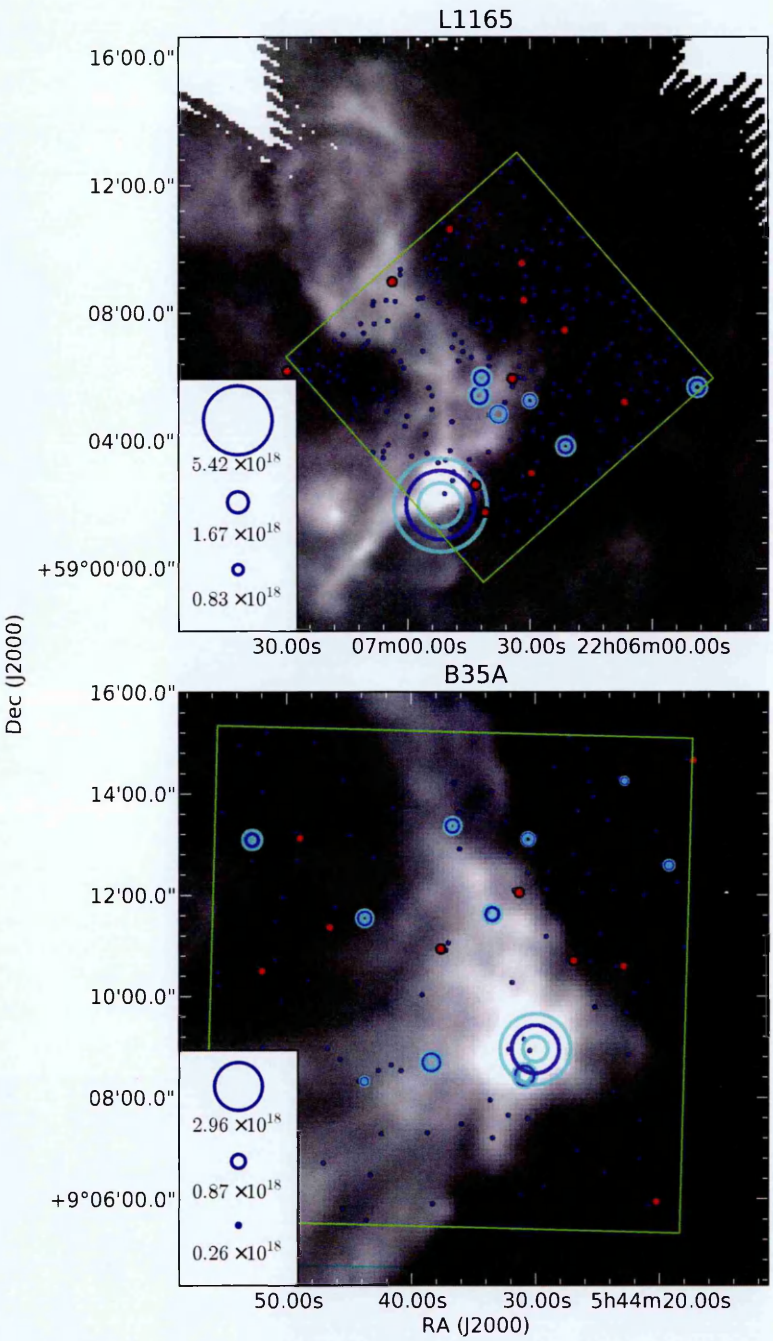

Figure 5.21: Bubble plots representing the distribution of H_2O ice towards (upper figure) L1165 and (lower figure) B35A. The size of the circles represent the column densities detected towards their center, as indicated by the figures' respective legends. The blue circles represent the measured amount, with the concentric cyan circles representing its uncertainty. The red circles represent lines of sight classified as non-detections, towards which only upper limits could be estimated. The blue dots indicate lines of sight towards which spectrum extraction was attempted by ARF2. The background image is a Herschel/SPIRE 250 μm map towards the core.

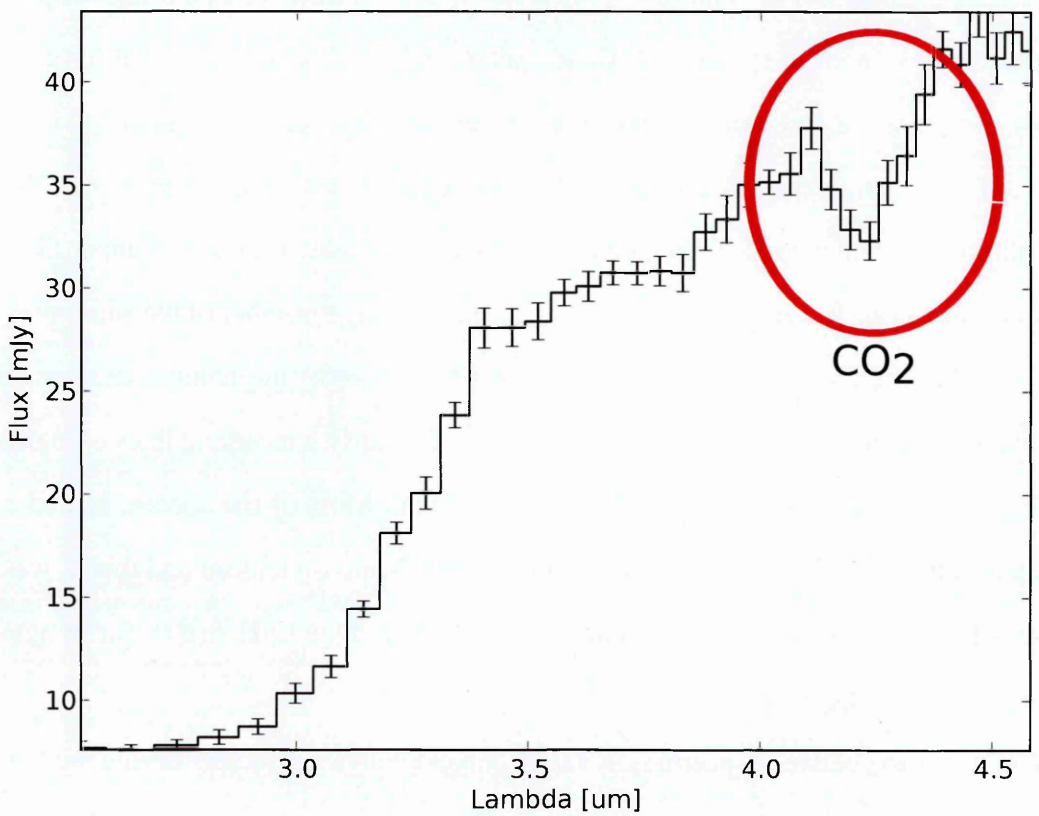

Figure 5.22: An example of a CO_2 ice 4.3 μm absorption feature detected towards one of the lines of sights (SSTc2d J054430.9+090826) towards the core B35A. The feature in question is highlighted with a red ellipse.

5.5.1 The quality of the data

The spectroscopy mode for AKARI was originally intended to be applied for situations with only one or very few well-separated sources per observation. Some of the pointings I have analysed contain hundreds of simultaneous sources, pushing the capabilities of the spectroscopy mode on AKARI to its limits or beyond. This is reflected in the high rate of attrition in the number of spectra left after each reduction step, as the number dwindles from 8280 raw spectra, through 4436 time- and pointing-merged spectra to 1353 finalized spectra. Of these spectra only 207 remained useful for estimating the presence and column density of water, split between 12 distinct fields of view. Of the column density estimates 76 cases register as having a higher than 2σ uncertainty, with any signals falling below this being classified as either an upper limit or a non-detection. It is important to emphasize that the large number of the final spectra not yielding column density estimates is *not* indicative of the column density of H_2O ice being low enough to be undetectable towards nearly a thousand lines of sight, but that it rather indicates missing data towards them. Most of the spectra lacked a sufficient number of data points in the vicinity of the 3-micron feature and thus it was not possible to fit an adequate continuum baseline around the O-H stretch for optical depth estimates to be possible.

The confusion between spectra is by far the largest individual factor causing the low number of final water ice detections. It causes several spectra to be outright dropped from the data set, and for even larger numbers of spectra to be masked to the point of uselessness for producing a good enough continuum baseline fit in order to produce optical depth spectra. The attrition caused by the confusion filtering is especially bad in highly crowded fields such as CB 188 and DC300.7-01.0, meaning that "more is less" when it comes to analysing AKARI spectroscopic observations in the 10×10 arc minute field of view. Despite the efforts of the automatic confusion detection algorithm, some cases of confused spectra remain. These could be visually identified by an anomalous peak appearing in a spectrum, showing a similar shape to what the

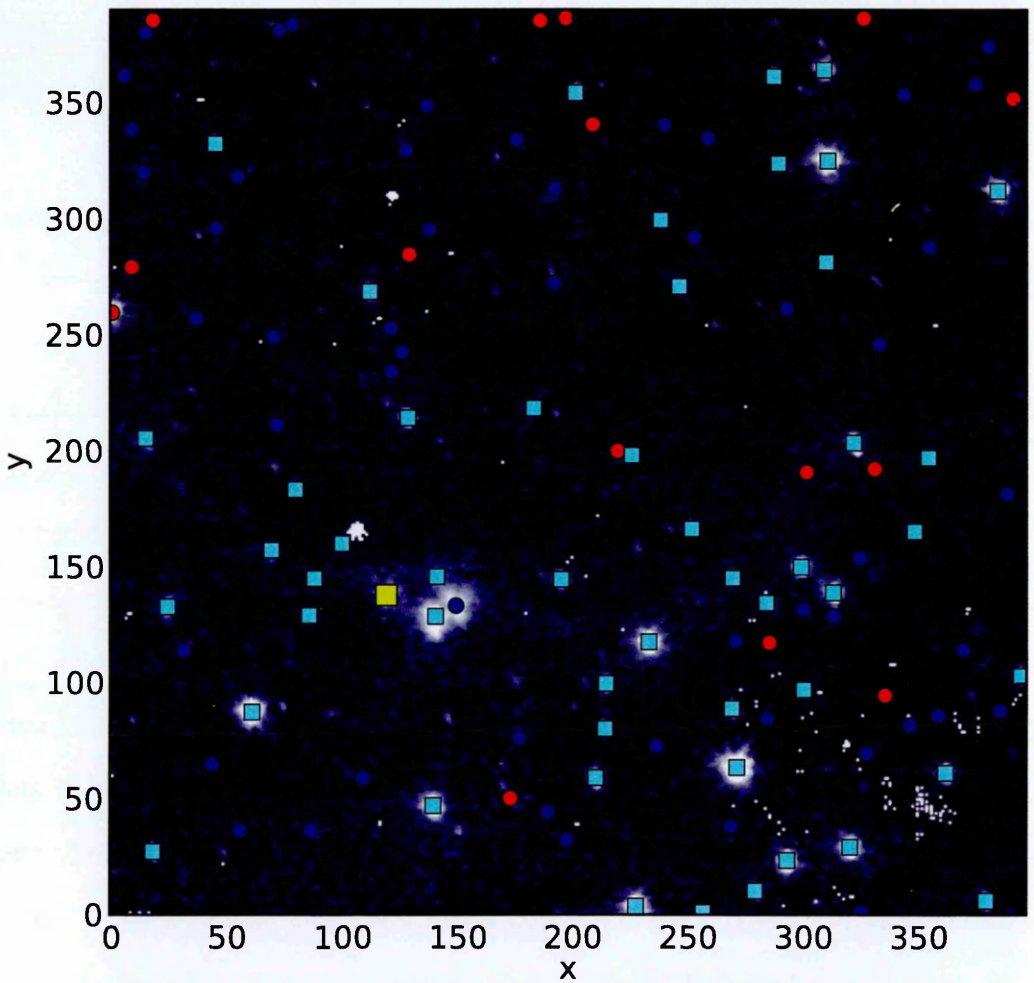

Figure 5.23: A map (towards B35A; pointing 4120021) visualizing the effect of the 'attrition' that the reduction process has on the number of analysed sources. The sources marked with red circles are targets which were ignored by the extraction process, most likely becaue of either confusion or a weak signal. The blue circles are sources which were extracted successfully from the NP frame, but which were dropped during the several reduction steps leading to the final reduced spectra, marked with cyan squares. This map also shows with a yellow square the source SSTc2d J192014.9+113540, which is featured in many other figures and in the discussion as a benchmarking case.

2.4 μm peak shows in the part of the spectrum where it is expected to appear. These spurious confused (but not identified as such) parts of the spectra are usually the result of ARF2 not having detected a weak source in its source identification phase. The lack of detection means that ARF2 could not create an extraction path for the interfering source, and could thus not account for its confusing other sources appropriately. Cases with obvious interference from such sources were manually removed from the final data set –when noticed– before proceeding with calculating ice column densities.

In cases where bad confusion was detected, the most common result of the masking out of confused parts meant that either a large part of the red or the blue end of the spectrum would get masked. This usually meant that the spectrum would have insufficient data points left in it for an adequate baseline estimate, and is the most significant deciding factor in why a large part of the finalized spectra could not be used for column density estimates. Even the spectra from which column densities could be estimated were highly sensitive to the exact method used for the continuum baseline fits, and suffer from (see next section) an up to factor of 3 uncertainty as a result.

As evidenced by the inconsistent short and long exposure time spectra, the non-linearity correction parameters provided as part of the official AKARI pipeline and adapted to ARF2 fail at high enough fluxes. This meant that only the short-exposure version (where the observed counts did not reach high enough numbers for non-linearity to be an issue) of the data could be used in most cases, and that the S/N ratio at the part of the spectrum where the O-H stretch feature is usually observed is weaker than it could be if the non-linearity correction could be performed adequately. Defining the non-linearity parameters to make the long exposure useful at higher fluxes would need an examination of the calibration data of standard sources, which is beyond the scope of this study.

The PSF used in the CLEAN algorithm had to be re-defined for each individual pointing, suggesting that there is an unaccounted-for effect changing it between observations. Distortion effects could be one reason for this discrepancy, and performing the spectrum extraction on a fully de-warped image might be a solution. This, however,

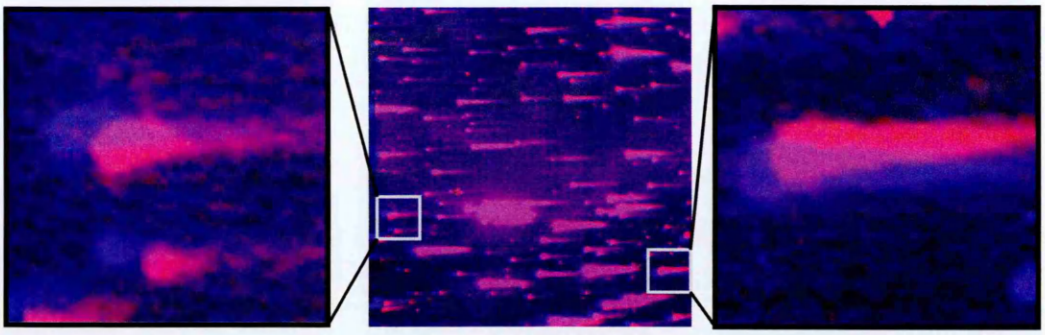

Figure 5.24: An example of the effects of distortion correction attempts on one of the NP frames, specifically pointing 4120021-001 (B35A). The blue-shaded colours show the non-corrected frame, while the red-shaded colours show the corrected frame. The middle image shows the full 10×10 arc minute field of view, and the left and right images show zoomed in parts of it showing how spectra on the distortion-corrected image divert and even slightly tilt in different directions on opposite sides of the field of view. The middle of the field of view being mostly purple with no separate blue or red regions indicates that the middle is mostly unaffected by the distortion correction.

brings with it additional complications as de-warping the NP frames warps the extraction paths, meaning that they can no longer be defined as consistent straight lines. This is evidenced by Figure 5.24, which shows how the extraction path changes in different parts of the de-warped image. Another way to improve the PSF accuracy is to find appropriate calibration data from the AKARI archives, and build a model based on this data. Such an examination is, again, beyond the immediate scope of this study. As it stands, I content myself with defining the uncertainty caused by the imperfect PSF based on the CLEAN residuals, as explained in Section 5.3.3.

Based on the benchmarking done against the Gaussian extraction method, however, it is found that the CLEAN extraction algorithm works adequately by comparison, and should thus be considered a valid way of deconvolving spectra in cases such as the AKARI NP fields. Improving the quality of the final data is thus contingent upon improving the quality of the calibrations. With this in mind I feel content in comparing the data against other similar studies and supplementary data of relevance.

5.5.2 Comparison with other studies of water ice

Water ice has been detected by a multitude of studies (e.g. Aikawa et al., 2012a; Boogert et al., 2011; Chiar et al., 1994; Eiroa and Hodapp, 1989; Leger et al., 1979; Merrill, Russell, and Soifer, 1976; Murakawa, Tamura, and Nagata, 2000; Noble et al., 2013; Öberg et al., 2011a; Oliveira et al., 2009; Pontoppidan, van Dishoeck, and Dartois, 2004; Shimonishi et al., 2008, 2010, 2013; Tanaka et al., 1990; Whittet et al., 1988; Yamagishi et al., 2011, 2013) through its 3-micron feature towards lines of sight ranging from YSOs, background stars and even extragalactic sources.

Many of the previous studies report the abundance of water ice only in terms of the peak optical depth of its corresponding 3-micron feature. The range of variation in peak optical depth consists of most lines of sight having $\tau(3\,\mu\mathrm{m}) \lesssim 0.2$, with a small number of sources exceeding $\tau(3\,\mu\mathrm{m}) \approx 1.5$. A similar trend is noticed in my study: most lines of sight where the 3-micron feature is detectable show its peak optical depth at ~0.5, with a small number of lines of sight having the peak go as high as ~2.0.

The various methods for calculating the column density of ISM ices were discussed in Chapter 1 Section 1.4.3. The method employed for calculating $N(\mathrm{H_2O}, \mathrm{solid})$ in this chapter is a simplified version of the one which was used for estimating ice column densities in Chapter 3. In this chapter I fitted a CDE-corrected pure $\mathrm{H_2O}$ ice laboratory spectrum to the observed blue wing of the 3-micron feature, and calculated $N(\mathrm{H_2O}, \mathrm{solid})$ from the fitting result.

Estimates of $N(\mathrm{H_2O}, \mathrm{solid})$ in the literature vary between $\sim 0.5 \times 10^{18}\,\mathrm{cm^{-2}}$ on the low end and a few$\times 10^{18}\,\mathrm{cm^{-2}}$ on the high end. A similar range of variation was detected in my results, with the lowest water ice column density estimate being $\sim 0.2 \times 10^{18}\,\mathrm{cm^{-2}}$ and the highest estimate being $\sim 7.2 \times 10^{18}\,\mathrm{cm^{-2}}$.

An especially interesting set of data to compare mine with is from the study presented in Noble et al. (2013), which used AKARI NG spectroscopy to calculate a small number of water ice column densities towards many of the same cores which were looked at in my study. In principle my study looked towards all the same sources as No-

ble, but the significant attrition of lines of sight during spectrum reduction means that in the end only a small number of matching sources could be found between my study and that of Noble; two sources towards B35A and one towards L 1165. The two sources in B35A are SSTc2d J054430.9+090826 and SSTc2d J054430.0+090857 which correspond to sources 4 and 3 respectively in Noble. The calculated water ice column density estimate in the first source disagrees by about a factor of 3 ($1.2 \times 10^{18}\,\mathrm{cm}^{-2}$ for me, $3.1 \times 10^{18}\,\mathrm{cm}^{-2}$ for Noble) between mine and Noble's study and the second source is estimated to have about a 10% lower column density ($3.0 \times 10^{18}\,\mathrm{cm}^{-2}$ for me, $3.3 \times 10^{18}\,\mathrm{cm}^{-2}$ for Noble) than what Noble estimates. The source in L 1165 is identified as SSTc2d J220641.8+590600 in my study and marked as source 29 in Noble. The estimates for this source differ between me and Noble by about 80%, with my estimate being $1.1 \times 10^{18}\,\mathrm{cm}^{-2}$, and Noble's estimate being $1.8 \times 10^{18}\,\mathrm{cm}^{-2}$. The close proximity of another source (source 28 in Noble) to this source means that this may be a potential case of confusion, however, and that I am reporting the water ice column density for that source instead. Noble et al reports $N(\mathrm{H_2O}, \mathrm{solid})$ to be $\sim 2.1 \times 10^{18}$ in source 28. This estimate thus differs even more from my estimate than the one for source 29. These differences stand as testament of how much uncertainty is introduced to my column density calculations from especially the high degree of uncertainty in the calibration.

5.5.3 Correlation with other measurables

The c2d catalogue provides both sub-millimetre photometry and visual extinction estimates against which my ice column density estimates (towards the lines of sight associated with c2d catalogue sources) can be correlated. Additionally, the Galactic Dust Reddening and Extinction service (DUST) of IPAC[2] was queried to access low spatial resolution data (~a few arc minutes) on $E(B-V)$ reddening, 100 micron intensity and dust temperature towards the lines of sight I measured in my study.

[2]Schlegel, Finkbeiner, and Davis (1998); `http://irsa.ipac.caltech.edu/applications/DUST/`

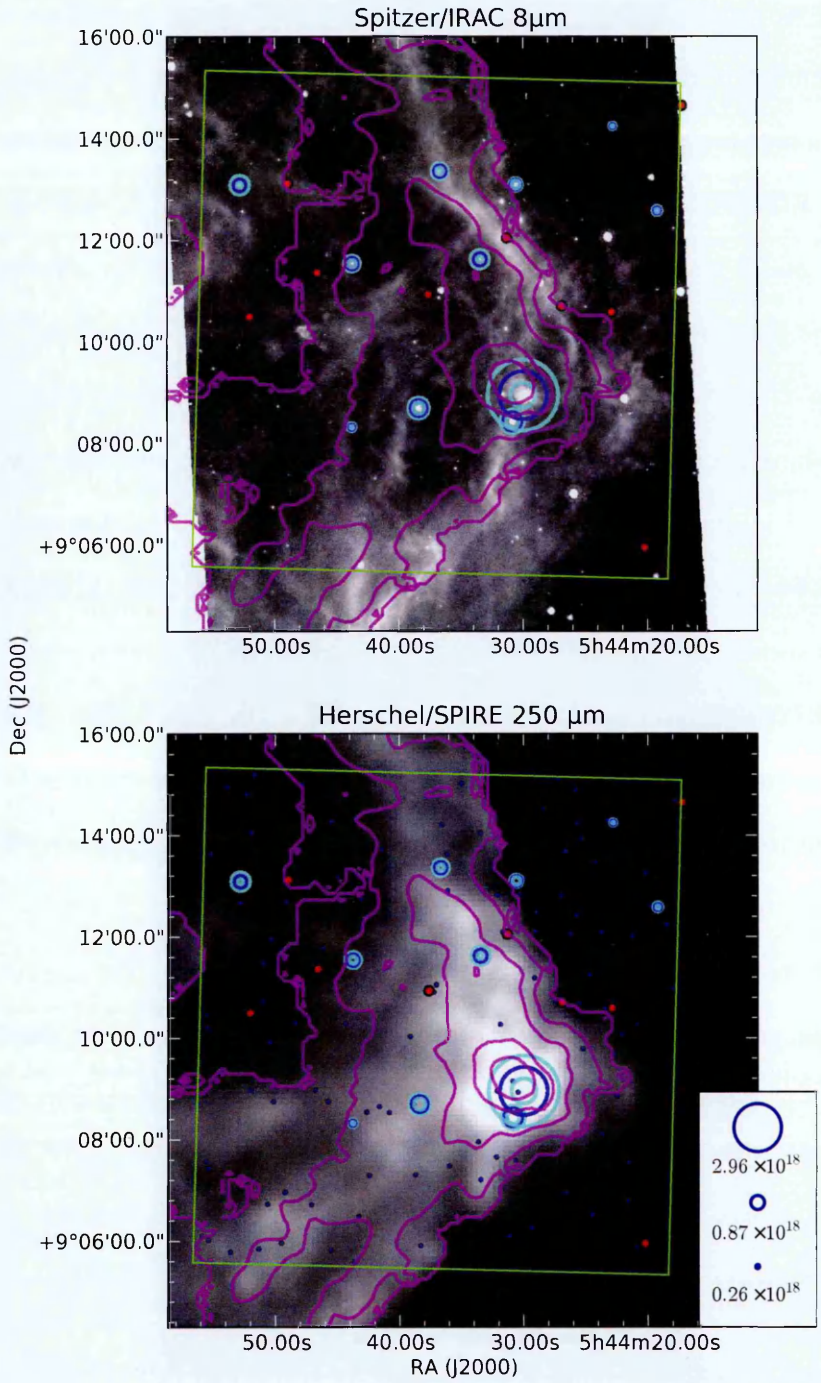

Figure 5.25: Two versions of the ice map towards B35A, with background images from different sources and a CO gas-phase column density contour. The top figure uses a SPITZER/IRAC 8-micron continuum map (traces polyaromatic hydrocarbons i.e. PAHs) and the bottom figure uses a Herschel/SPIRE 250-micron continuum map (commonly used to trace cold dust) as its background image. The ice abundances and the approximate field of view of the AKARI frame are shown in the same way as in Figures 5.16-5.21. Additionally the column density of gas-phase ^{12}CO calculated via its $3-2$ transition (A. Craigon, private communication) is represented via contours. The five increasing contour levels represent the isolines of ^{12}CO column densities of 0.0, $1.32 \cdot 10^{17}$, $2.65 \cdot 10^{17}$, $3.97 \cdot 10^{17}$, and $5.29 \cdot 10^{17}$ cm^{-2}, respectively.

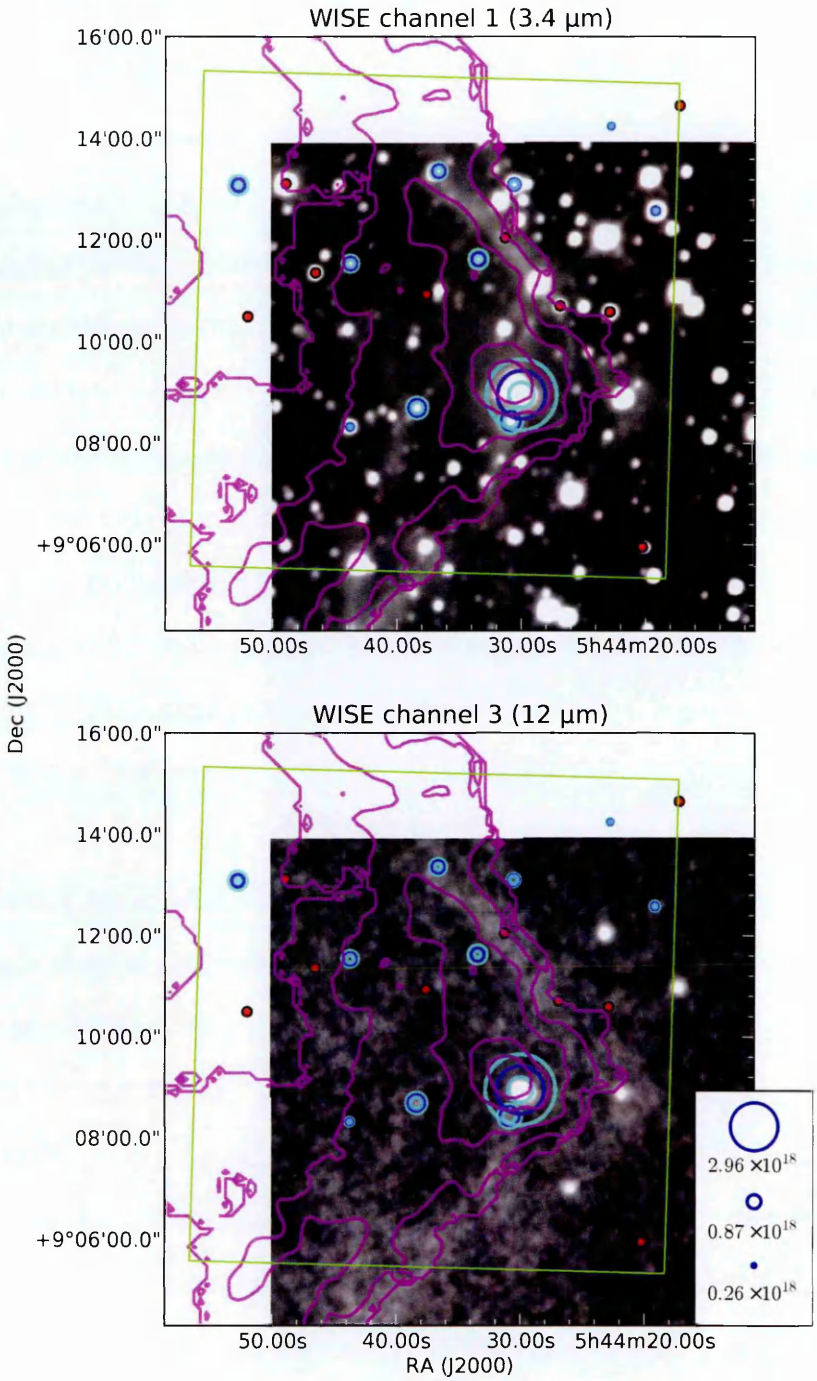

Figure 5.26: Two versions of the ice map towards B35A, with background images from different sources and a CO gas-phase column density contour. The top figure uses a WISE 3.4-micron continuum map (traces PAHs) and the bottom figure uses a WISE 12-micron continuum map (traces warm dust, and YSO envelopes and discs) as its background image. The ice abundances and the approximate field of view of the AKARI frame are shown in the same way as in Figures 5.16-5.17. Additionally the column density of gas-phase ^{12}CO calculated via its $3-2$ transition (A. Craigon, private communication) is represented via contours. The five increasing contour levels represent the isolines of ^{12}CO column densities of 0.0, $1.32 \cdot 10^{17}$, $2.65 \cdot 10^{17}$, $3.97 \cdot 10^{17}$, and $5.29 \cdot 10^{17}$ cm^{-2}, respectively.

The c2d catalogue contains standard J, H, and K- band photometry in addition photometry acquired using SPITZER/IRAC in 3.6, 4.5, 5.8, and 8.0 microns. The catalogue also contains A_V extinction values calculated in the manner described in the c2d data delivery document[3]. The extinction values are of greatest interest to me here, because several studies (e.g. Eiroa and Hodapp, 1989; Murakawa, Tamura, and Nagata, 2000; Noble et al., 2013; Whittet et al., 1988) have found a positive correlation between A_V and either $N(H_2O, \text{solid})$ and/or $\tau(3\,\mu m)$. Therefore my data was also correlated against the A_V, towards sources which had been cross-matched with c2d. Finally, a small number (see Figures 5.20 and 5.21) of the observed cores have publicly available Herschel SPIRE photometric data towards them. The highest spatial resolution data is from the 250-micron PSW band, which usually traces cold dust emission. These maps can be used to acquire 250 micron intensities towards select lines of sight.

The first pair to be correlated was $N(H_2O, \text{solid})$ from my ice mapping against A_V from the c2d data. This correlation plot is presented in Figure 5.27. An alternately scaled version of the same plot is shown in Figure 5.28, where the y axis has been scaled logarithmically in order to highlight some interesting variation in the low $N(H_2O, \text{solid})$ regime. These plots also show the correlations from several other sources (Bergin et al., 2005; Broekhuizen, Kumar, and Abbatt, 2004; Chiar et al., 2011; Murakawa, Tamura, and Nagata, 2000; Noble et al., 2013; Shuping et al., 2000; Whittet et al., 1988, 2007). Some of the sources in the literature only had the optical depth of the 3-micron feature listed instead of the water ice column density. For such cases the 3-micron optical depth was converted to water ice column density using (Murakawa, Tamura, and Nagata, 2000)

$$N(H_2O, \text{solid}) = \tau(3\,\mu m)\frac{\Delta f}{A}, \tag{5.11}$$

where τ is the optical depth, $\Delta f = 360\,\text{cm}^{-1}$ is the usual FWHM, and $A = 2 \cdot 10^{-16}\,\text{cm}$ is the band strength of the water ice feature. Among the first things to notice in either

[3] http://irsa.ipac.caltech.edu/data/SPITZER/c2d/doc/c2d_del_document.pdf

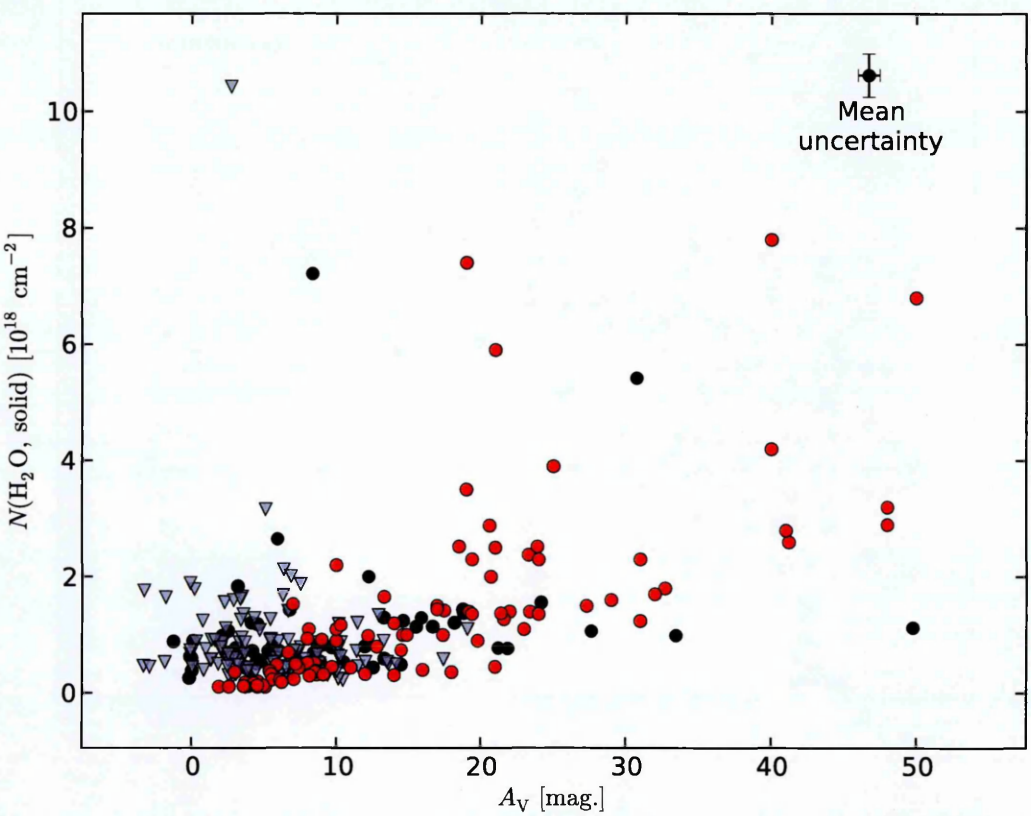

Figure 5.27: The water ice column densities (from my ice maps; y-axis) plotted as (good detections) dark gray circles and (upper limits) light gray triangles against the visual extinction (from c2d; x-axis) towards lines of sight where data from both sources was available. The cross at the top right of the figure shows the mean uncertainty on both axes for my data. Also plotted in this figure as red circles is several data points gathered from several sources (Bergin et al., 2005; Broekhuizen, Kumar, and Abbatt, 2004; Chiar et al., 2011; Murakawa, Tamura, and Nagata, 2000; Noble et al., 2013; Shuping et al., 2000; Whittet et al., 1988, 2007) in the existing literature.

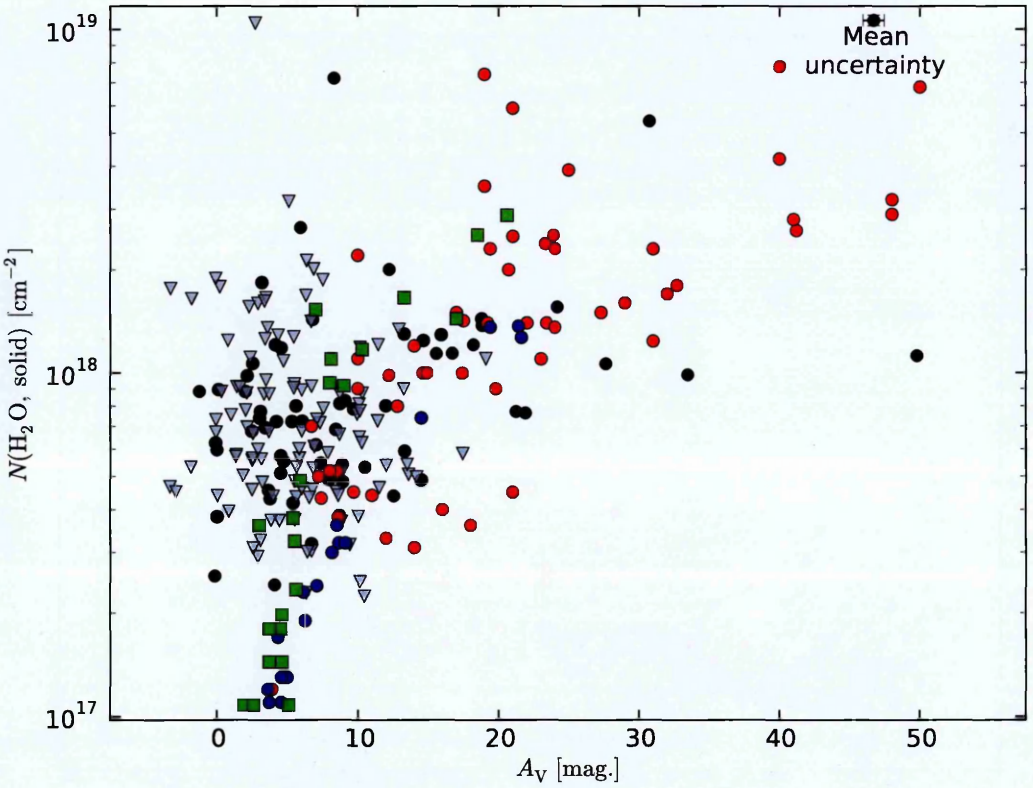

Figure 5.28: The logarithm of the water ice column densities (from my ice maps; y-axis) plotted as (good detections) dark gray circles and (upper limits) light gray triangles against the visual extinction (from c2d; x-axis) towards lines of sight where data from both sources was available. The cross at the top right of the figure shows the mean uncertainty on both axes for my data. Also plotted in this figure are several data points gathered from several sources (Bergin et al., 2005; Broekhuizen, Kumar, and Abbatt, 2004; Chiar et al., 2011; Murakawa, Tamura, and Nagata, 2000; Noble et al., 2013; Shuping et al., 2000; Whittet et al., 1988, 2007) in the existing literature. These are plotted as green squares for Whittet et al. (1988), blue circles for Murakawa, Tamura, and Nagata (2000), and red circles for everything else.

of these figures is that the A_V distribution in my data dips below zero for a number of data points. Such (impossible) extinction values serve as testament on the uncertainty of the extinction estimates available from the c2d catalogue. The c2d data delivery document[4] comments that offsets of 1-2 magnitudes are expected in the A_V, because of the used SED fitting process and the systematic uncertainties in the intrinsic colours of the observed stars. In order to see if the c2d data A_V values could be improved upon, an alternate path of estimating A_V was explored. This alternate method makes use of the E(B-V) colour excess values acquired from IPAC. Visual extinction values can be calculated from colour excess values using the formula (Weingartner and Draine, 2001)

$$A_V = R_V E(B-V), \tag{5.12}$$

where R_V is the ratio of visual extinction to reddening. To be consistent with c2d data, I used the same ratio –$R_V = 5.5$– as they did for their extinction calculations. An alternate version of Figure 5.27 with A_V values calculated from the IPAC data is presented in Figure 5.29. From this figure I can see that the IPAC data is heavily binned along the x-axis, owing to the very low spatial resolution (several arc minutes; compared to the very narrow "pencil beams" effectively used in ice mapping) of the colour excess data available. Thus the c2d A_V values will continue being used, despite the inherent uncertainty in them.

Generally speaking, the distribution of my data agrees with the distribution reported in other pieces of literature. There is a disagreement, however, at low extinction values, especially when the distribution at this range is highlighted in the logarithmic plot shown in Figure 5.28. Particularly the data from Whittet et al. (1988) and Murakawa, Tamura, and Nagata (2000) show a steep decline in H_2O ice column density at around $A_V \approx 2...5$, while my data occupies a wide distribution of A_V and $N(H_2O, \text{solid})$ in the same general A_V range.

When comparing my data against data from other sources, it is however good

[4]Available from `http://irsa.ipac.caltech.edu/data/SPITZER/c2d/doc/c2d_del_document.pdf`

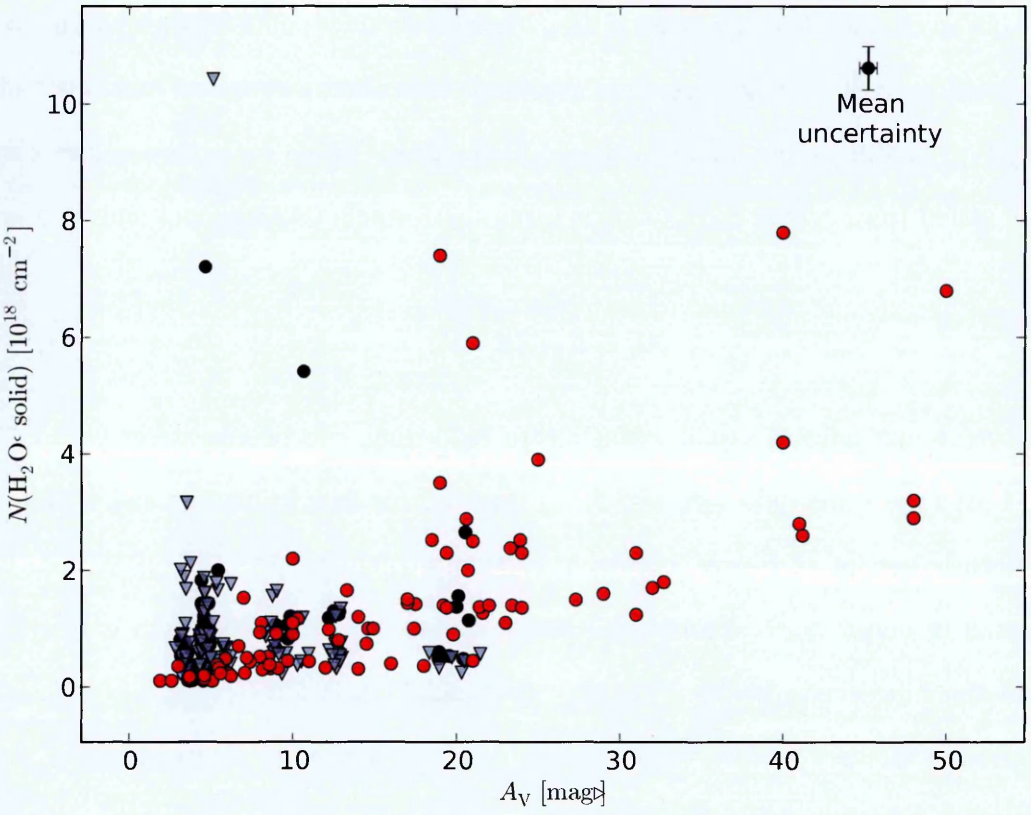

Figure 5.29: The water ice column densities (from my ice maps; y-axis) plotted as (good detections) dark gray circles and (upper limits) light gray triangles against the visual extinction (calculated based on E(B-V) values acquired from IPAC/DUST with $R_V = 5.5$; x-axis) towards lines of sight where data from both sources was available. The cross at the top right of the figure shows the mean uncertainty on both axes for my data. Also plotted in this figure as red circles are several data points gathered from several sources (Bergin et al., 2005; Broekhuizen, Kumar, and Abbatt, 2004; Chiar et al., 2011; Murakawa, Tamura, and Nagata, 2000; Noble et al., 2013; Shuping et al., 2000; Whittet et al., 1988, 2007) in the existing literature.

to keep in mind that (as shown in Figure 5.28) most of the low A_V correlation data in the literature is from Whittet et al. (1988) and Murakawa, Tamura, and Nagata (2000). These data sets consist of observations exclusively towards the Taurus Molecular Cloud (TMC), which has been found (Öberg et al., 2011a) to have an unusual distribution of ices compared to other molecular clouds. This difference between the Taurus data compared to other ice data can also be noticed when comparing correlation coefficients calculated for the $A_V/N(H_2O, \text{solid})$ pairs. The correlation coefficient R is very high for the Taurus sources, with $R \approx 0.94$ for Whittet et al. (1988) and $R \approx 0.97$ for Murakawa, Tamura, and Nagata (2000). By contrast, if the same correlation coefficient (A_V versus $N(H_2O, \text{solid})$) is calculated for the combined non-Taurus data in the literature (from Bergin et al., 2005; Broekhuizen, Kumar, and Abbatt, 2004; Chiar et al., 2011; Noble et al., 2013; Shuping et al., 2000; Whittet et al., 2007), I get a diminutive value of $R \approx 0.08$. If the Taurus data is combined with all the literature data I get $R \approx 0.66$. My data alone has $R \approx 0.25$, and if combined with the literature data points I get $R \approx 0.58$.

The non-Taurus data from the literature seems to have a similar (non-)correlation that my data does, while the individual cloud of Taurus correlates very well in the two sets of data published on it. What if this correlation is cloud dependent? To study this, I correlated the detections in each of my studied molecular clouds individually in cases where a cloud had at least four (because correlating with fewer makes little sense with the uncertainties in my data) such detections. Of the clouds I studied 7 had enough data points to make this possible, and these correlations are presented in Figures 5.30 and 5.31. Three of the clouds –B35A, DC 346.0+07.8, and L1165– show a comparatively strong correlation when studied in this way. The sources used for these correlations are mostly background sources, but also contain a few YSOs. The remaining 4 clouds with poor correlation either contain a very flat distribution of points, where $N(H_2O, \text{solid})$ does not seem to vary noticeably with A_V and/or contain individual outliers with considerably high $N(H_2O, \text{solid})$ detections compared to other lines of sight in the same set. If the outliers were to be ignored in the data containing

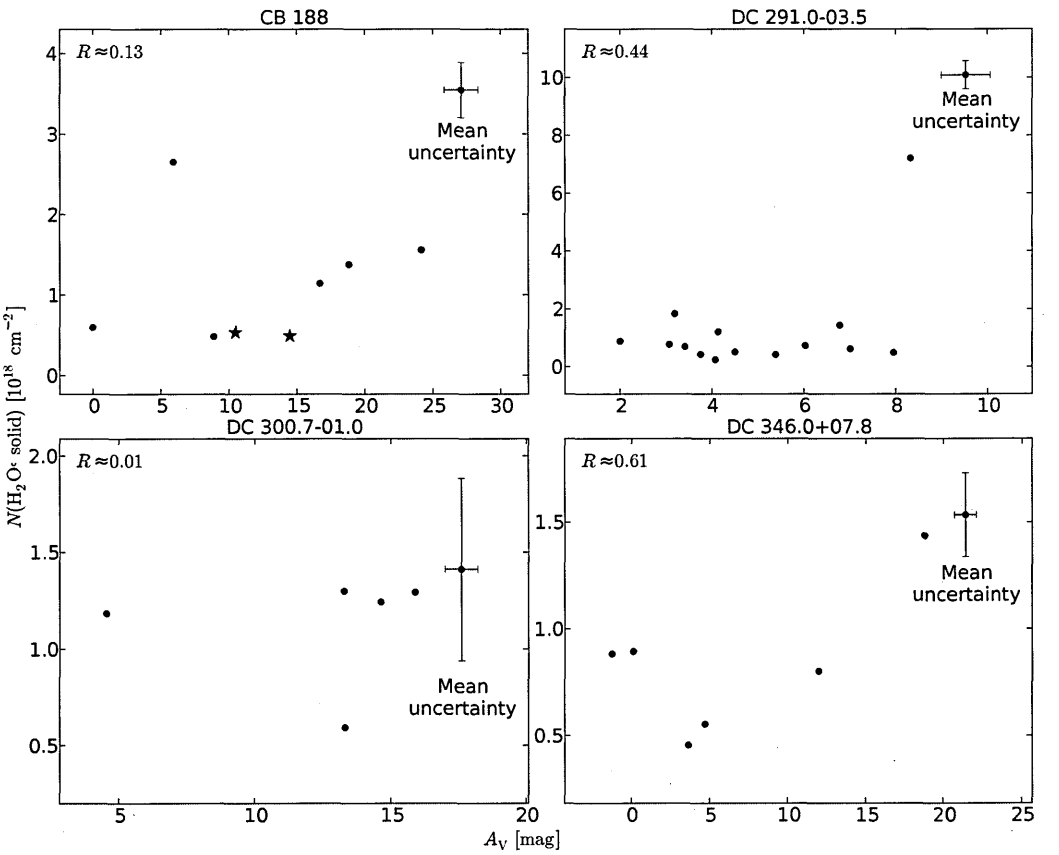

Figure 5.30: A correlation of A_V (x-axis; from c2d) against $N(H_2O, \text{solid})$ (y-axis) on a per-cloud basis towards 4 of the 7 clouds (the other 3 are shown in Figure 5.31) towards which more than 3 non-upper limit detections existed. The name of each cloud is indicated at the top of each plot, in addition to the correlation coefficient R for the plotted points and the mean uncertainties being shown in the left and right corners of the plots, respectively. Background stars are indicated by circle-shaped markers, and YSOs are indicated by star-shaped markers.

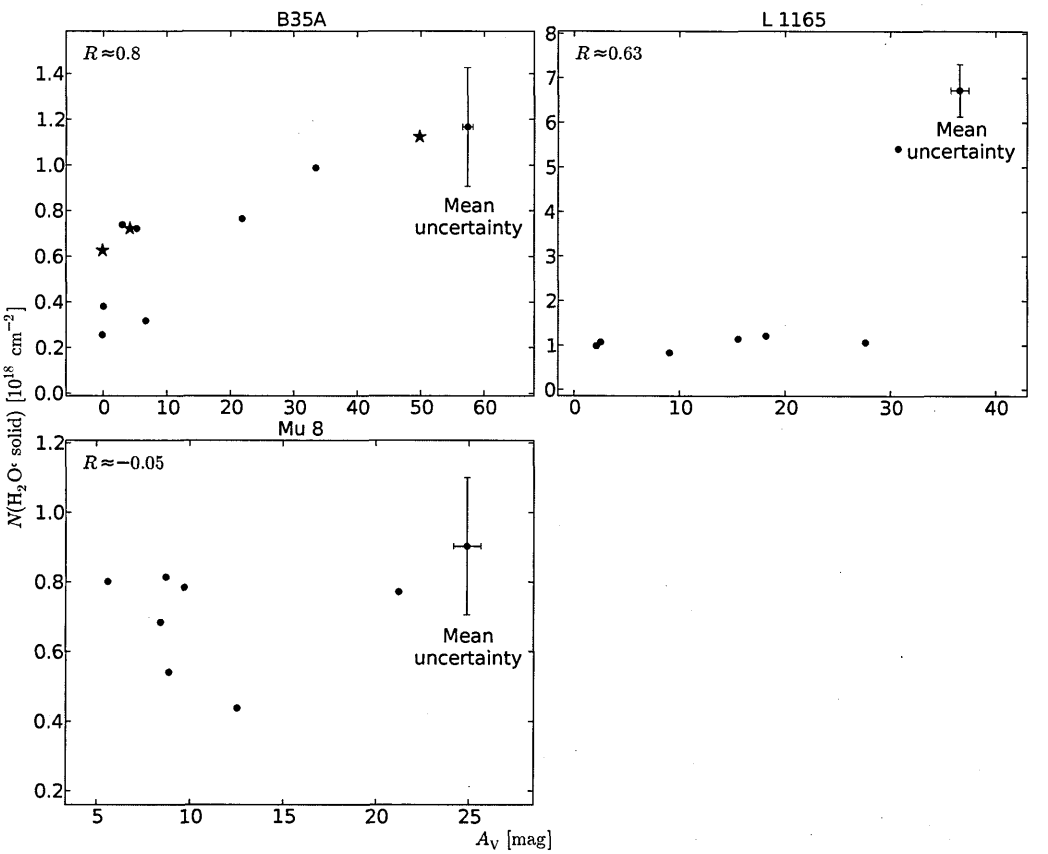

Figure 5.31: A correlation of A_V (x-axis; from c2d) against $N(H_2O, \text{solid})$ (y-axis) on a per-cloud basis towards 3 of the 7 clouds (the other 4 are shown in Figure 5.30) towards which more than 3 non-upper limit detections existed. The name of each cloud is indicated at the top of each plot, in addition to the correlation coefficient R for the plotted points and the mean uncertainties being shown in the left and right corners of the plots, respectively. Background stars are indicated by circle-shaped markers, and YSOs are indicated by star-shaped markers.

them, the result would be a more or less flat (within the y-axis error bars) distribution. While the small number of data points per cloud leaves room for doubt, all of this seems to imply that the correlation between extinction and water ice column density varies from cloud to cloud.

Another potentially interesting correlation pairing is possible: the far infra-red dust optical depth is (e.g. Schlegel, Finkbeiner, and Davis, 1998; Suutarinen et al., 2013) to be closely related to A_V. Given a map of observed far-IR intensity at wavelength λ and another map of dust temperatures T_{dust}, the FIR optical depth τ_λ can be calculated from the approximation

$$\tau_\lambda \approx \frac{I_\lambda}{B_\lambda(T_{\mathrm{dust}})}, \tag{5.13}$$

where $B_\lambda(T_{\mathrm{dust}})$ is Planck's law for black-body emission at wavelength λ given temperature T_{dust}. This equation applies when the dust can be assumed to be optically thin; a common assumption in the literature which I will also make use of.

The two sets of data from which I could calculate τ were the 100-micron maps from the IPAC/DUST data, and the Herschel/SPIRE PSW maps which were available towards a few of the cores considered in this study. The Herschel maps available from the Herschel Science Archive come in two forms: a map calibrated for point-sources and another calibrated for extended sources. The dust temperatures necessary for calculating black-body emission were taken from the (very low spatial resolution, with an approximately degree-sized effective beam) IPAC/DUST data. The correlation plots created for $\tau_{100\mu\mathrm{m}}$ and $\tau_{250\mu\mathrm{m}}$ are presented in Figures 5.32 and 5.33, respectively. The effect on the correlation coefficient arising from the usage of low-resolution (IPAC/-DUST) versus high-resolution (c2d or Herschel) data is seen in these two correlation plots as well, much like they were seen in the A_V correlation plots. The 100-micron correlation was created using low-resolution data and suffers from the same type of binning as the extinction correlation plot (Figure 5.29) created from IPAC colour excesses.

The 250-micron correlation was calculated based on significantly higher-resolution

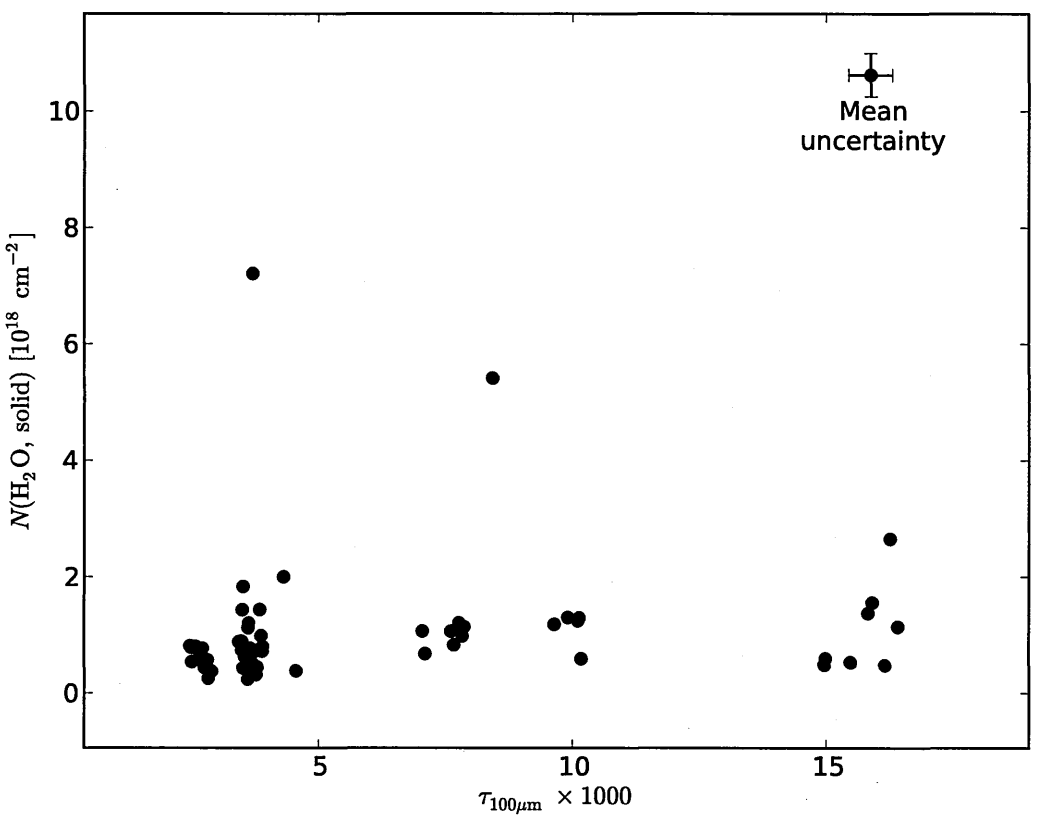

Figure 5.32: The water ice column densities (from my ice maps; y-axis) plotted as gray circles against the 100-micron optical depth (calculated from 100-micron intensities and dust temperatures acquired from IPAC/DUST; x-axis) towards lines of sight where data from both sources was available. The value presented on the top left of the figure is the correlation coefficient for the data, and the cross at the top right shows the mean uncertainty on both axes.

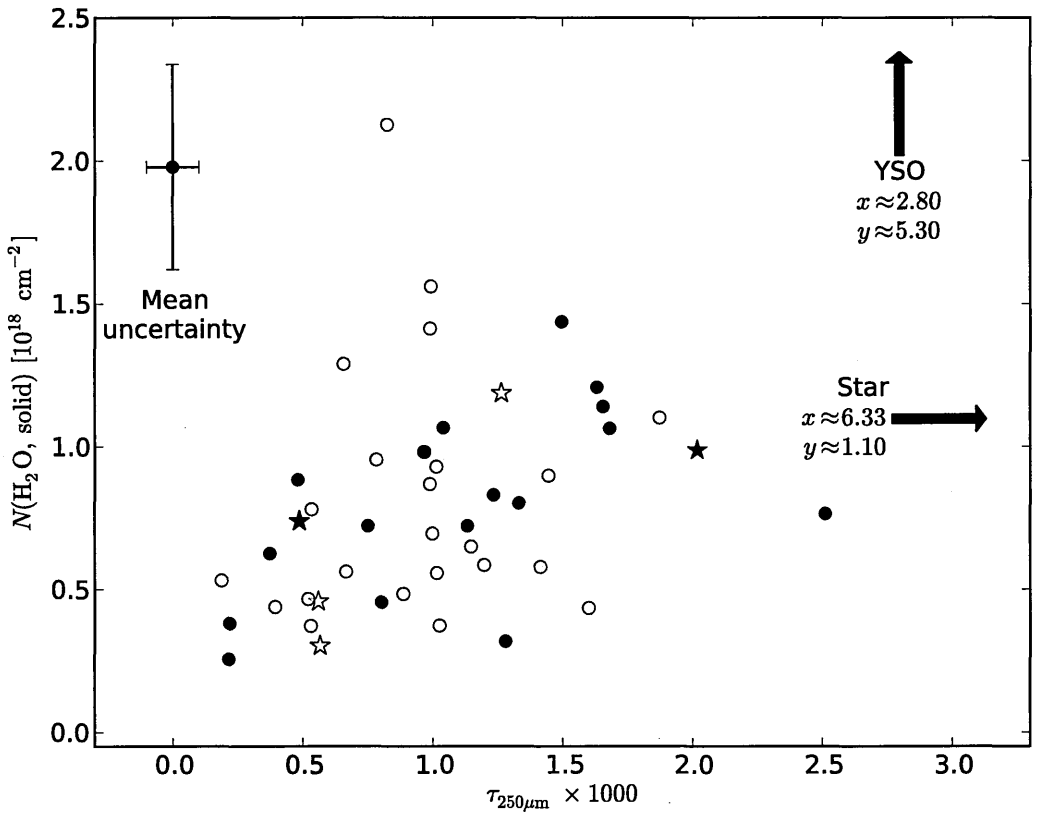

Figure 5.33: The water ice column densities (from my ice maps; y-axis) plotted against the 250-micron optical depth (calculated from 250-micron intensities acquired from Herschel/SPIRE PSW and dust temperatures acquired from IPAC/DUST; x-axis) towards lines of sight where data from both sources was available. Dark gray symbols indicate proper detections, while light gray ones represent upper limits. The circles represent background stars and the star symbols represent YSOs. Two sources falling beyond the axis limits are indicated by the arrows, with an annotation of their approximate plot coordinates. The error bars on the top left corner indicate the mean x and y uncertainties of the plotted data.

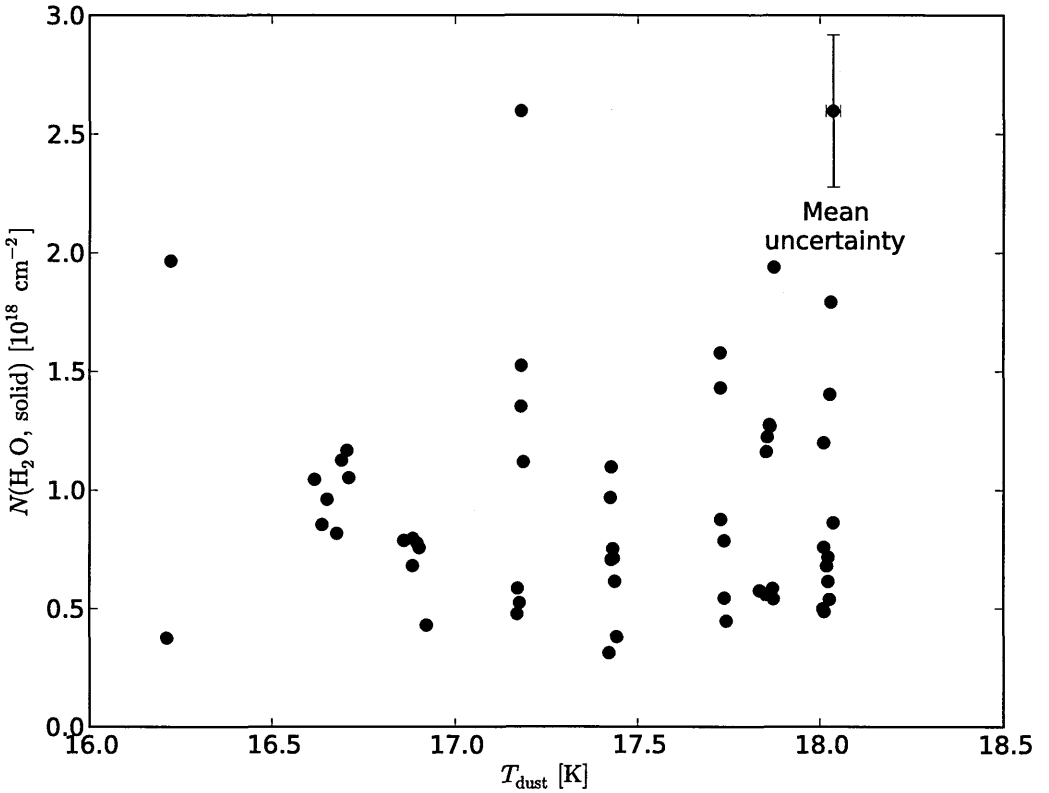

Figure 5.34: The correlation of The water ice column densities (from my ice maps; y-axis) plotted against dust temperature (from IPAC/DUST; x-axis). The mean uncertainty on both axes is shown in the top right corner.

Herschel maps, and its correlation coefficient is $R \approx 0.35$. While the optical depth also depends on dust temperature, the very low spatial resolution dust temperature data I am using effectively smooths out any short-scale variations in dust temperature. This is best illustrated with a correlation plot of water ice column density against the dust temperature I am using. As is seen from Figure 5.34, no discernible pattern is to be found in the small temperature range ocupied by my datapoints.

As a final point of interest, the 250-micron optical depth correlation plot can be split between three separate cores where a sufficient number of datapoints exists for correlation estimates to make sense. The three cores which could be looked at individually were L 1165, B35A, and DC 346.0+07.8. Containing the same number of datapoints as they did when correlating against A_V in this way, their correlation coefficients are moderately high: 0.89, 0.72, and 0.61, respectively. This further reinforces the idea that water ice column density correlations may vary from cloud to cloud.

All these correlations come with the caveat that water ice column density has in the past mostly been correlated against extinction towards young stellar objects, while my sources are mostly background stars. It is entirely possible that a different type of correlation is to be expected in my case, compared to the correlations seen in YSO-dominated data.

5.6 Concluding remarks

In this chapter the most recent results of the AKARI ice mapping project are presented, the number of water ice column density estimates in the literature are increased by 76 detections and 131 upper limits. Most of these estimates are towards lines of sight not previously observed, and they cover a total of 12 molecular clouds, covering a patch of the sky approximately $10' \times 10'$ in each. Furthermore, these observations are mostly toward background stars instead of the much more commonly studied young stellar objects.

Based on comparison with other studies done with more high-precision observing methods, the column density estimates in this chapter suffer from a high degree ($\sim 50\%$) of uncertainty. This uncertainty is largely caused by incomplete calibration data, most notably the lack of an adequate point spread function for the AKARI NP observations, and the apparent inaccuracy of the NP flux response function at high wavelengths. These two factors together lead to a high degree of uncertainty in the continuum fit performed on the data.

Despite the uncertainties in the results, they are still precise enough to be correlated with supplementary data to a moderate degree of confidence. The presence of an extinction threshold remains ambiguous based on my data, but I find that the correlation between water ice column density and both visual extinction and (at least) 250-micron optical depth may vary from cloud to cloud.

Chapter 6

Conclusions and further work

How is ice distributed in star forming regions?

How is ice affected by star formation processes?

These are the two questions asked at the beginning of this thesis and these are the two questions which have been answered. Water ice is truly ubiquitous in the ISM, and can be found in a wide range of physical environments. Methanol ice is far more common that previously believed, its formation happening in a water-ice-rich environment and its nearly complete destruction happening in the violent outflow environment of young stellar objects.

The work presented in this thesis has looked at the life cycle of ice in the interstellar medium, with a special emphasis on water and methanol. The results shed new light on the formation and destruction processes of ice layers in the ISM. Additionally the first ever set of large scale ice mapping data is presented, and two software utilities (ARF2 and OMNIFIT) written in PYTHON are showcased. This chapter will summarise all of this, followed by a discussion on the future applicability and interesting research avenues pointed at by the results this thesis.

6.1 New discoveries

The discoveries made in the research of this thesis can be summarised as follows:

(i) Thanks to the research done in Chapter 3, our understanding of CH_3OH ice is enhanced.

- Based on observations of the 3-micron ice feature, CH_3OH ice is detected on most lines of sight ranging from low mass YSOs to background stars. The relative abundance of CH_3OH against H_2O ice ranges from a few to $\sim 40\%$, even on lines of sight where it had not previously been observed.
- CH_3OH ice occurs predominantly in CO-rich ice environments (as opposed to a H_2O-rich ice), which is consistent with observed 3-micron ice absorption features and an earlier hypothesis of Cuppen et al. (2011).

(ii) In Chapter 4 we gained greater understanding of the formation and destruction of water and methanol in young stellar objects.

- In the outflows of low-mass young stellar objects, where the stellar wind of the YSO impacts with its envelope, the post-shock gas shows evidence of gas-phase H_2O formation reactions. This happens in a region of the outflow associated by velocity with secondary CJ- and C- type shocks, and entrained envelope material. The gas-phase formation mechanism enhances the abundance (relative to CO) of H_2O in these regions by roughly a factor of 2.
- In these same shocked regions, there is evidence of CH_3OH destruction during the sputtering of methanol ice from dust grains. Up to $\sim 90-99\%$ of CH_3OH is destroyed in this way. The extent of this destruction may be even greater than what was concluded in Chapter 4, which assumes methanol ice abundance estimates pre-dating the study done in Chapter 3.

6.2 New ice maps

The AKARI ice mapping programme discussed in Chapter 5 has –using a novel spectrum extraction and analysis technique– produced new H_2O ice maps towards a total of 12 star-forming regions, with each region covering an approximately $10' \times 10'$ patch of the sky. This data consists of 76 H_2O ice detections and 131 upper limits. When added to the existing number of H_2O ice estimates in the literature, this new data almost doubles the number of lines of sight towards which the abundance H_2O ice is estimated. Most (145) of my lines of sight are towards background stars, a source category towards which H_2O ice abundances have been very rarely estimated as most of the literature H_2O ice estimates are towards YSOs. Comparing my ice abundance estimates to supplementary archival data, I found $N(\mathrm{H_2O\,ice})$ to possibly correlate with dust opacity at 250 microns. I also found signs suggesting that the correlation between the water ice column density $N(\mathrm{H_2O\,ice})$ and both visual extinction A_V and dust opacity $\kappa_{250\mu m}$ may vary from cloud to cloud.

6.3 New utilities

To facilitate the research done in this thesis, two major pieces of software were created: ARF2 and OMNIFIT. Documented in Appendix A and exploited in Chapters 3 and 5, these two utilities have been created with future applicability in mind. ARF2 is intended as a general-purpose reduction and analysis tool for AKARI slitless spectroscopic data, utilising a variation of the CLEAN (Högbom, 1974) algorithm to deconvolve partially overlapping spectra from a dispersed field of view. OMNIFIT is intended to make the fitting methodology between laboratory and observational ice spectra described in Chapter 3 simple to reproduce with any arbitrary wavelength range of spectroscopic observations, assuming it is provided with the necessary laboratory data to fit against.

Both utilities are in the process of being prepared for public open source release.

6.4 Further work

Already mentioned in passing in their respective chapters, the research done in this thesis hints at interesting future avenues of study. These avenues can be categorized between the observational, theoretical and experimental.

6.4.1 Observational

The results of my research of water and methanol gas-phase abundances in YSOs presented in Chapter 4 depend on a number of assumptions associated with the physical conditions and kinematics of the outflow material. Specifically, the number density of molecular hydrogen –$N(H_2)$– and the kinetic temperature –T_{kin}– of the gas could play a significant role, if they were found to vary spatially within the observed line of sight. Furthermore, the location from which H_2O emission originates is assumed based on our current understanding of the kinematics of how YSO outflows link to the velocity profile of the emission.

Given a detector of suitably high spatial and spectral resolution and access to the appropriate frequency ranges, direct high-resolution observations of of the YSO system would potentially help constrain both the physical conditions around the outflow and the precise origin of the H_2O emission. The latter is difficult to achieve with any existing or planned sub-mm observatories, as the appropriate H_2O emission line is attenuated by absorption in the Earth's atmosphere and thus observations with a sufficient spatial resolution (∼milliarcsecond-scale) would require a space-borne sub-mm interferometer. Evaluating the physical conditions in the YSO outflow may be plausible with telescopes such as ALMA (Atacama Large Millimeter Array) or PdBI/-NOEMA (Plateau de Bure Interferometer/NOrthern Extended Millimeter Array); both of which are submm range interferometer arrays. Further in the future, the Square Kilometer Array (SKA) is a radio frequency interferometer which is set to begin construction in 2018. It is scheduled to become active in 2 phases between 2020 and 2030. ALMA, PdBI, and SKA are all capable of imaging at the spatial scales required

to examine the outflow structure of YSOs. Examining the physical conditions is thus a matter of locating a suitably positioned nearby young stellar object, and deciding upon appropriate tracers of kinetic temperature and H_2 density. Kinetic temperature is commonly (e.g. Juvela et al., 2012; Kirsanova et al., 2014; Walmsley and Ungerechts, 1983) traced with low-J gas-phase NH_3 emission which is detectable at radio frequencies. It may be useful in this role at probing the kinetic temperature of YSO systems as well. The density of molecular hydrogen is much more difficult to probe without making several assumptions about the geometry of the system and both the excitation conditions (which we are trying to learn more about!) applying to a potential tracer molecule and the way it traces $n(H_2)$. A likely better route for estimating $n(H_2)$ variations would be magnetohydrodynamic models of YSO systems.

When it comes to ices, the James Webb Space Telescope (JWST) is set to bring with it numerous discoveries. The MIRI and NIRSPEC instruments of the JWST bring with them the potential to observe both the near-IR and mid-IR ice features of any line of sight concurrently, and also to create spectroscopic data cubes (such as the ones used to create the Spitzer ice map of Sonnentrucker et al. 2008) of the entire field of view. This would allow for the abundances of CO, H_2O, CH_3OH and more ices to be determined from even more features (such as the 9-micron feature tracing e.g. silicates and CH_3OH) than the two features used in Chapter 3. Usage of multiple features may help remove some of the degeneracies of the fitting, and help further understand the distribution of ices in the ISM. In anticipation of JWST, however, it is ice maps such as the ones presented in Chapter 5 which help us decide which regions should be observed first.

6.4.2 Theoretical

An alternate (or more likely supplementary) approach to constraining the physical conditions of YSO outflows comes from simulations. A magnetohydrodynamics simulation of the shocked region consistent with observations would help further constrain

the H_2 density and kinetic temperature of the gas contained therein.

Further development of the software created for this thesis also counts as an avenue of future theoretical study. Most importantly determining a good point spread function (PSF) to use in the spectrum extraction process in Chapter 5 would play a critical role in improving the quality of the extracted near-IR spectra and thus both improve the reliability of the ice mapping data and most likely also add more H_2O ice detections to each field of view. There is also further untapped AKARI data left to analyse, most notably the mid-IR data, which covers the wavelength range between 5.4 and 12.9 μm. The most significant additional complication of this data arises from the complex background emission which is present in the mid-IR waveband. Also, there exists near-IR spectroscopy from Phase 3 (the post-helium phase) of AKARI, towards the same star-forming regions as were looked at in Chapter 5. This data –if the significant noise in it can be handled properly- can potentially be used to increase the S/N ratio of the existing observations, and possibly add some extra data points to most observed star–forming regions.

In Chapter 3 the nature of the so far unexplained "red wing" of the 3-micron ice absorption feature was also studied to some extent. It is under this feature where most of the additional CH_3OH ice detected in Chapter 3 can be "hidden". As is discussed in the chapter, most of the absorption in the red wing is ignored by previously used ice abundance estimation methods. This ignored residual in the red wing takes the shape of a gaussian (or possibly a lopsided gaussian adapted from Lan and Jorgenson 2001) distribution. The nature of the red wing remains a mystery, but may be associated with either light scattering effects and/or the products of energetically processed ices. If light scattering effects are the reason for the shape of the red wing, an avenue of future study would be to replace the CDE model (used in Chapter 3 for modifying the shape of laboratory spectra) with a more sophisticated model taking into account light scattering and polarization effects on coated dust grains.

6.4.3 Experimental

The destruction of CH_3OH in YSO outflows would be verifiable by constructing a laboratory experiment which emulates the interaction between CH_3OH ice and neutral species (most notably hydrogen) in a controlled setting. This would help either confirm or refute the conclusion regarding CH_3OH at the end of Chapter 4. The second likely effects for reproducing the red wing discussed in Chapter 3 is the energetic processing of ices. Energetic processing of methanol has been previously found (Palumbo, Castorina, and Strazzulla, 1999) to change the shape of the red wing towards what is observed in the ISM, and thus further experimentation in this direction may be the key to understanding the origin and shape of the red wing in astronomical spectra.

6.5 Closing words

Many of the new discoveries in science arise from places where multiple fields meet, and this thesis is no exception. The results presented in the preceding chapters have been made possible through the cooperation of most notably astronomy, physics and chemistry, with the data enabling the analysis having acquired through observations, laboratory experiments and computer models. Methods originating from computer science and statistics have been used to perform the analysis.

As discussed in this chapter, the journey ahead is also one where cooperation between multiple fields is required. The ice observations acquired from the JWST –which tell us where the ice is– would be worthless without the struggles of laboratory astrochemists in helping us put the observations in the right context, and computer models are then required to build the larger chemical picture around this single snapshot on an astronomical timescale. This picture can then be extrapolated into both the past and future through computational astrochemical models and magnetohydrodynamical simulations, which will give us information about where the gas and ice came from and what lies in store for it in the future. It is this cooperation and collaboration which allows us to understand the process of star formation, and possibly even life itself.

And with that in mind, we continue mapping the frozen void.

Appendix A

Software documentation

A large part of modern astronomy –regardless of sub-field– involves programming in its many forms. Specialized software and scripts are often created as part of every-day research but they are rarely produced in a way that they can be efficiently re-used for follow-up research based on the original work they were created for. One of the reasons why such software and scripts never see public release is their lack of documentation; an extra effort which is necessary to make the program useful for those who did not create it. The purpose of this appendix is to document the two major pieces of software created during the research done for this thesis: ARF2 and OMNIFIT. ARF2 is intended to work as a general-purpose AKARI slitless spectroscopy extraction and reduction tool (used in Chapter 5), and OMNIFIT is an ice spectroscopy fitting library for applying the fitting methodology presented in Chapter 3 to an arbitrary set of spectroscopic observations. Both of these pieces of software (written in PYTHON) have been designed to be useful in not only reproducing the results of their respective chapters but also to help anyone wishing to do so conduct follow-up studies (such as those suggested in Chapter 6) of the research in those chapters. The documentation in this chapter is intended to provide a starting point for such endeavours.

A.1 AKARI Reduction Facility 2

A.1.1 Introduction

The AKARI Reduction Facility 2 (ARF2) is an evolution of the first AKARI Reduction Facility (ARF1; Noble, 2011), with an emphasis on being able to reducing and analysing the 10×10.0 arcmin field of view AKARI prism spectroscopy data in the near-infrared. ARF2 has been designed to be capable of the following:

- Parse the directory trees used in storing raw AKARI data, and locate the interesting files (dark frames, frames taken using a specific filter etc.) in it.
- Perform basic reduction steps (dark subtraction, outlier subtraction, flat-fielding, stacking etc.) on the raw data in order to produce a set of reduced prism (NP), grism (NG) and imaging (N3) frames for each pointing and sub-pointing.
- Locate the sources detected in the N3 frame and extract their pixel coordinates.
- Parse catalogue data towards the observed fields of view, and acquire pixel coordinates of the catalogue sources in the reduced frames.
- Cross-match the extracted N3 sources with the catalogue sources, and create a distortion map for converting pixel coordinate information between the N3 frames and catalogue data.
- Estimate the pixel coordinates of the sources in the NP frames.
- Cross-match the NP pixel coordinates with the N3 pixel coordinates, and create a distortion map between the two.
- Locate "extraction paths" for the spectra of each cross-matched source in the NP frames and evaluate where two extraction paths overlap to a sufficient degree to count as confused.
- Extract spectra from the NP frames along the non-confused parts of the extraction paths.

- Perform the necessary reduction steps (wavelength and sensitivity calibration, continuum baseline fitting) to the extracted raw spectra to make them useful for evaluation the column density of H_2O ice in them.
- Evaluate N(H_2O,solid) from the extracted spectra.
- Create maps of H_2O ice towards the observed fields of view, based on the N(H_2O) data.

The reasoning, algorithms and subtleties behind these steps were further elaborated upon in Chapter 5, while this section focuses on the practicalities of operating ARF2 and how the intermediate data generated during the steps on the way to producing ice maps are stored, organized and accessed. While the scripts were created with the primary purpose of reducing and analysing the data from the IMAPE ice mapping survey, ARF2 itself and its scripts are generic enough that the software can be with little trouble modified to suit the reduction and analysis any AKARI near-IR NP filter spectroscopy. With a little extra trouble ARF2 would also be suitable for reducing and analysing other AKARI filters, including the NG and mid-IR spectroscopy filters and even the noisy "phase 3" data taken close to the end of the AKARI mission.

A.1.2 System requirements

ARF2 has been designed to run under PYTHON 2.7 and has been tested to work under at least Debian-like Linux distributions. A number of additional python libraries are required for ARF2 to operate. Firstly, OMNIFIT(see Section A.2) is required and thus naturally all its requirements (Section A.2.2) are also needed. The MYSQL functionality of ARF2 is handled by the MYSQL-PYTHON library, available at `http://mysql-python.sourceforge.net/`. The handling of FITS files and world coordinate system (WCS) transformations is handled through ASTROPY (Astropy Collaboration et al., 2013, tested to work with version 0.3.x).

Additionally, the third party point-source extraction program SEXTRACTOR (Bertin and Arnouts, 1996) is required by ARF2 in its extraction of astrometric and photo-

metric information from the N3 frames. ARF2 makes use of the PYSEXTRACTOR[1] PYTHON wrapper for interfacing with SEXTRACTOR.

A.1.3 Basic usage

ARF2 is called from the command line with the python interpreter by using the command:

```
python arf2.py <startup options>
```

where *<startup options>* are the strings for optional startup options, described below. Running ARF2 without any options launches ARF2 in fully interactive mode, after reading and parsing the settings from arf2.cfg.

When calling ARF2 from the command line, a number of options are available, which will change how ARF2 behaves. The first option is "silent mode", which is toggled on by starting ARF2 with the option "-s" or "–silent". This suppresses most printed output from ARF2. The second possible option is "-i *<path>*" or "–includedir *<path>*" which allows the user to override the default ARF2 program path (*./include/*) with a custom path as indicated by *<path>*. ARF2 will look for the commands used by both interactive and non-interactive mode in the new include directory. The third option, "-c *<path>*" or "–config *<path>*" allows the user to override the default configuration file (*./arf2.cfg*) with a path to another file as described by *<path>*. Finally, "-r *<path>*" or "–script *<path>*" will prevent ARF2 from launching in interactive mode and cause it to instead run the set of commands described in the file found at *<path>*.

A.1.3.1 Interactive mode vs. non-interactive mode

When running ARF2 in interactive mode, i.e. without the "–script" parameter, the user is presented with an interactive mode command prompt. This mode allows the user to manually enter commands to ARF2. Interactive mode accepts a few built-in commands and any number of commands it has located in the "include directory"

[1] https://gitorious.org/pysextractor

as defined by the "–include" parameter. The built-in commands "quit" and "exit" both cause ARF2 to exit back into the command prompt, and "list" will display the available commands, including those found in the include directory.

The commands found in the include directory can be called in interactive mode by inputting the (case sensitive) name of their respective files without the "*.py*" extension, e.g. "*extract_CLEAN.py*" can be run by inputting "*extract_CLEAN*" into the prompt. These commands often allow for custom parameters passed to them, when using a specific syntax. The function of the custom parameters can range from e.g. choosing a specific pointing to be used or for overriding the usage of previously generated iterated data and re-starting the iterations from scratch. To pass custom parameters to a command, the user must input the pipe symbol "|" immediately after the command, followed by a set of variable names and values contained within curly brackets in the style of a PYTHON dictionary. For example, to call extract_CLEAN with custom parameters, one should write the calling command in the form

```
extract_CLEAN|{'pointing':'4120021-001','k_limit':3.5}
```

This will cause extract_CLEAN to adopt '4120021-001' and 3.5 as the values for the variables pointing and k_limit. Only certain variables can be set in this way, as defined in the command (see next subsection), and all such variables have a default value which will be used in the case of no custom parameters being passed. For instance, extract_CLEAN has the default values of 'ALL' and 2.0 for the variables pointing and k_limit. In addition, in the above example a third parameter named x_limit will retain its default value of -7 due to no custom parameter by that name being passed to the command. If an unidentified parameter is defined when calling the command, an exception (error) will be raised by ARF2.

A.1.3.2 Writing your own commands

The command files callable through both interactive or non-interactive modes are normal PYTHON scripts, with a few extra options and considerations that the user should

keep in mind.

The first consideration is that the script should contain two lines for the purposes of parsing input parameters, as explained above. These two lines follow the style

```
defaultPars = {'par1name':par1value,'par2name':par2value}
cmdPars = verify_arfpars(cmdPars,defaultPars)
```

The first line defines both the list of acceptable input parameters and their default values in the form of a PYTHON dictionary, with the keys forming the names of the parameters. The second line compares the input parameters with the default parameters, and stores the combination of input parameters and default parameters (when no relevant input parameter was given) into a new dictionary pointed at by the variable cmdPars.

Second, the user has by default access to all the libraries imported by ARF2 during startup. These libraries are:

- matplotlib.pyplot (for plotting; imported as plt)
- numpy (handling of numerical arrays; np)
- astropy.wcs (world coordinate system transformations; wcs)
- astropy.io.fits (FITS file handling; fits)
- os (operating system interface)
- sys (access to objects related to the PYTHON interpreter)
- shutil (advanced shell commands)
- copy (variable copying)
- re (regular expression parsing)
- httplib (accessing the world wide web)
- MySQLdb (interfacing the MYSQL database;db)

Third, there are a number of functions and variables in ARF2 that will likely be of use. What follows is a listing of these.

arfmessage (function)

Description

Used to print out messages in a fashion that respects the –silent flag.

Input

msg = string to be printed

yell = if set to true, ignores the –silent flag *Default:False*

Output

None

progressbar (function)

Description

Produces a general ASCII progress bar, which can be used for tracking the progress of large computations.

Input

current = number representing e.g. the number of steps taken so far in the current computation

target = target value to which the variable "current" will be compared

Output

None

db_cursor (class instance)

Description

a MySQLdb cursor instance, which can be used for interfacing with the ARF2 MYSQL database.

There exist also a number of variables pointing to directory paths which are relevant for the operation of ARF2. These are described below.

A.1.3.3 The configuration file

The configuration file of ARF2 –located by default at *./arf2.cfg* relative to the ARF2 root directory– contains a number of default settings used by several of the commands utilised with ARF2. The configuration file is formatted in a way to be readable with the CONFIGPARSER library built into PYTHON, and is split into several sections.

The first section, **General**, contains parameters relevant to the general operations of ARF2. The parameters are:

silent (boolean) – Another way of setting whether ARF2 runs in silent or non-silent mode.

omnifit_path (string) – The absolute to the directory in which the OMNIFIT library is located.

The second section, **SQL**, contains information which is used for logging to and accessing the MYSQL database which is used by ARF2 for keeping track of its data. The parameters are:

sql_host (string) – Host name or address of the MYSQL server. If the server is located on the machine running ARF2, this can be either localhost or 127.0.0.1.

schema_name (string) – Name of the MYSQL database/schema containing the tables used by ARF2.

sql_user (string) – Username with which to log in to the MYSQL database. This user should have full read and write access to the database/schema being operated on.

sql_password (string) – The password of the logging into the MYSQL database.

The third section, **File system**, contains parameters relating to the locations of various directories used by ARF2 in its operations. The parameters are:

root_datadir (string) – The root directory used for storing ARF2 data. Most of the other directories are defined relative to this directory.

tempdir (string) – A directory in which various temporary files will be stored in by ARF2. This directory will be automatically emptied at the beginning of each new ARF2 session.

raw_datadir (string) – The directory which contains the raw AKARI data.

calibdir (string) – The directory which contains the various calibration data used especially during the reduction phases of ARF2.

reduced_dir (string) – The directory which will be used for storing the reduced data.

graph_dir (string) – The directory which will contain the variety of figures generated during the operations of ARF2.

sextractor_dir (string) – The directory which will contain the files generated by SExtractor, including the "check" images and raw extracted lists.

The fourth section, **Field of view**, contains parameters used in cropping sub-frames from the full AKARI frames. The parameters are:

bigfov_xmin (integer) – The minimum pixel x coordinate which will be used for extracting the "big" $10' \times 10'$ field of view from the full AKARI frame.

bigfov_xmax (integer) – As *bigfov_xmin*, but specifies the maximum x coordinate.

bigfov_ymin (integer) – As *bigfov_xmin*, but on the y axis.

bigfov_ymax (integer) – As *bigfov_xmax*, but on the y axis.

smallfov_xmin (integer) – As *bigfov_xmin*, but for specifying the "small" $1' \times 1'$ field of view.

smallfov_xmax (integer) – As *smallfov_xmin*, but specifies the maximum x coordinate.

smallfov_ymin (integer) – As *smallfov_xmin*, but on the y axis.

smallfov_ymax (integer) – As *smallfov_xmax*, but on the y axis.

A.1.4 Database description

ARF2 uses a MYSQL database to manage and organize the large amounts of files and data it creates during its various reduction and analysis stages. The purpose of this section is to give a description of all the tables and their columns, as used by ARF2. The purpose of each table is described individually, as are the purposes and types of the data they can contain.

A.1.4.1 raw_info

Description

Stores various kinds of information about AKARI observations, as accessible from the raw data files.

Columns

pointing_id (int 11) – Unique numerical identifier of the pointing, as generated by MYSQL

pointing (varchar 11) – The full name of the pointing, expressed in the numerical format xxxxxxx-yyy

mainpointing (int 11) – The identifier of the "main" part of the pointing, i.e. the xxxxxxx part.

subpointing (int 11) – The identifier of the "sub" part of the pointing, i.e. the yyy part.

proposal (varchar 5) – The abbreviated name of the observing proposal

object (varchar 45) – The name of the object being observed

observer (varchar 45) – Name of the PI of the observing proposal

comment (text) – Additional comments on the entry, if applicable

A.1.4.2 raw_files

Description

Stores information about the raw FITS files

Columns

file_id (int 11) – Unique numerical identifier of the file, as generated by MySQL

pointing_id (int 11) – The numerical identifier of the pointing the file is relevant to

file_name (varchar 45) – Name of the FITS file

file_path (varchar 256) – Full path to the file

filter_name (varchar 8) – Name of the AKARI filter (e.g. N3, NP, NG etc.) used in the observation responsible for the file

filter_type (varchar 45) – Type of filter used (image, grism or prism)

comment (text) – Additional comments on the entry, if applicable

A.1.4.3 akari_external

Description

Like raw_info, except for the entire AKARI archive, and with download information.

Columns

external_id (int 11) – Unique numerical identifier of the pointing, as generated by MYSQL

internal_id (int 11) – pointing_id of the entry in raw_info, if the entry exists there as well

pointing (varchar 11) – The full name of the pointing, expressed in the numerical format xxxxxxx-yyy

mainpointing (int 11) – The identifier of the "main" part of the pointing, i.e. the xxxxxxx part.

subpointing (int 11) – The identifier of the "sub" part of the pointing, i.e. the yyy part.

proposal (varchar 5) – The abbreviated name of the observing proposal

instrument (varchar 3) – The AKARI instrument (IRC or FIS) used in the observing

aot (varchar 5) – Observing mode used in the observation

obstime (datetime) – The date of observation

A.1.4.4 reduced_pointing_files

Description

Contains information about the reduced AKARI files.

Columns

file_id (int 11) – Unique numerical identifier of the file, as generated by MYSQL

pointing_id (int 11) – Identifier of the AKARI pointing of the observation

exposure (varchar 8) – Indicates whether the reduction was performed on the short or long exposure observation or a combination of both

field (varchar 8) – Indicates whether this is the file for "big" or "small" field of view frame

filter_name (varchar 8) – Name of the AKARI filter

file_name (varchar 45) – Name of the FITS file

file_path (varchar 256) – Full path to the file

comment (varchar 45) – Additional comments on the entry, if applicable

A.1.4.5 extracted_catalogue

Description

Contains information about sources extracted with SExtractor

Columns

object_id (int 11) – Unique numerical identifier of the extracted source, as generated by MySQL

pointing_id (int 11) – Numerical identifier of the pointing (in raw_info) from which the source was extracted

x (double) – Pixel x coordinate of the source

y (double) – Pixel y coordinate of the source

mag (double) – Photometric magnitude of the source. Note that this has not been calibrated to conform with any common scale

delta_mag (double) – Uncertainty of the photometric magnitude

exposure (varchar 8) – Indicates whether the extraction was performed on the short or long exposure observation

field (varchar 8) – Indicates whether the "big" or "small" field of view of the frame was used in the extraction

comment (varchar 45) – Additional comments on the entry, if applicable

A.1.4.6 c2d_catalogue

Description

Contains information from the C2D catalogue (Evans et al., 2003) towards the AKARI fields of view.

Columns

object_id (int 11) – Unique numerical identifier of the source, as generated by MySQL

ra (double) – The J2000 right ascension of the source

de (double) – The J2000 declination of the source

pointing (varchar 45) – The AKARI pointing towards which this source is found

c2d_id (varchar 45) – C2D catalogue identifier for the source

c2d_name (varchar 45) – Name of the source in the C2D catalogue

type (varchar 45) – Type of source, as categorized in the C2D catalogue

AV (double) – A_V of the source, in magnitudes

delta_AV (double) – Uncertainty of the A_V

J (double) – J-band flux of the source in mJy

delta_J (double) – Uncertainty of the J-band flux

H (double) – H-band fluxof the source in mJy

delta_H (double) – Uncertainty of the H-band flux

K (double) – K-band fluxof the source in mJy

delta_K (double) – Uncertainty of the K-band flux

I1 (double) – IRAC1 flux of the source in mJy

delta_I1 (double) – Uncertainty of the IRAC1 flux

I2 (double) – IRAC2 flux of the source in mJy

delta_I2 (double) – Uncertainty of the IRAC2 flux

I3 (double) – IRAC3 flux of the source in mJy

delta_I3 (double) – Uncertainty of the IRAC3 flux

I4 (double) – IRAC4 flux of the source in mJy

delta_I4 (double) – Uncertainty of the IRAC4 flux

M1 (double) – MIPS1 flux of the source in mJy

delta_M1 (double) – Uncertainty of the MIPS1 flux

comment (varchar 45) – Additional comments on the entry, if applicable

A.1.4.7 frame_shift_info

Description

Contains information about the relative pixel shifts between the N3, NP frames and the C2D catalogue.

Columns

shift_id (int 11) – Unique numerical identifier of the shift, as generated by MYSQL

pointing_id (int 11) – The identifier of the AKARI pointing towards which this shift is performed.

obsX (double) – x axis coordinate of the source in the extracted N3 catalogue

obsY (double) – y axis coordinate of the source in the extracted N3 catalogue

prismX (double) – x axis coordinate of the source in the NP frame

prismY (double) – y axis coordinate of the source in the NP frame

catX (double) – x axis coordinate of the source in the N3 frame, according to astrometry from the C2D catalogue

catY (double) – y axis coordinate of the source in the N3 frame, according to astrometry from the C2D catalogue

A.1.4.8 N3_object_association

Description

Contains information about associating sources between the extracted N3 catalogue and the C2D catalogue

Columns

assoc_id (int 11) – Unique numerical identifier of the association, as generated by MYSQL

pointing_id (int 11) – Identifier of the AKARI pointing towards which the association takes place

obs_id (int 11) – Identifier of the source in the extracted N3 catalogue

cat_id (int 11) – Identifier of the source in the C2D catalogue

comment (varchar 45) – Additional comments on the entry, if applicable

A.1.4.9 NP_object_association

Description

Contains information about associating sources between the extracted N3 catalogue and their estimated NP frame positions

Columns

assoc_id (int 11) – Unique numerical identifier of the association, as generated by MYSQL

pointing_id (int 11) – Identifier of the AKARI pointing towards which the association takes place

obs_id (int 11) – Identifier of the source in the extracted N3 catalogue

object_x (double) – Estimated x axis coordinate of the source in the NP frame

object_y (double) – Estimated y axis coordinate of the source in the NP frame

comment (varchar 45) – Additional comments on the entry, if applicable

A.1.4.10 raw_spectra

Description

Contains information about the raw extracted spectra.

Columns

spectrum_id (int 11) – Unique numerical identifier of the spectrum, as generated by MYSQL

pointing_id (int 11) – Identifier of the AKARI pointing towards which the spectrum was extracted

assoc_id (int 11) – Identifier of the NP association of the spectrum

field (varchar 8) – Indicates whether the "big" or "small" field of view of the frame was used in the extraction

object_x (double) – x axis coordinate of the source in the frame

object_y (double) – y axis coordinate of the source in the frame

filter_type (varchar 45) – Name of the AKARI filter using which the frame was taken

method (varchar 45) – The name of the extraction method that was used

file_path (varchar 256) – Full path to the CSV file

comment (varchar 45) – Additional comments on the entry, if applicable

A.1.4.11 reduced_spectra

Description

Contains information about the extracted spectra in various stages of reduction.

Columns

spectrum_id (int 11) – Unique numerical identifier of the spectrum, as generated by MYSQL

raw_id (int 11) – Identifier of the raw spectrum

reduced_state (varchar 45) – The last reduction step performed on the spectrum

file_path (varchar 256) – Full path to the CSV file

comment (varchar 45) – Additional comments on the entry, if applicable

A.1.4.12 od_spectra

Description

Contains information about the optical depth spectra generated after baseline fitting

Columns

spectrum_id (int 11) – Unique numerical identifier of the spectrum, as generated by MYSQL

c2d_id (int 11) – Identifier of the C2D catalogue source associated with the spectrum

fit_badness (int 11) – Numerical indicator of the fit badness. This is 0 by default, and will be incremented by 1 each time a "bad fit" condition is fulfilled, i.e. a bigger number indicates a worse fit. In the current version of ARF2 the only bad fit condition of this type is if any of the fitting windows lack data points.

mainpointing (varchar 11) – The identifier of the "main" part of the pointing

primary_pointing_id (int 11) – Identifier of the 001-subpointing in raw_info

object_x (double) – x axis coordinate of the source in the frame

object_y (double) – y axis coordinate of the source in the frame

comment (varchar 45) – Additional comments on the entry, if applicable

A.1.4.13 column_densities

Description

Contains information about the (ice) column densities derived from the optical depth spectra.

Columns

coldens_id (int 11) – Unique numerical identifier of the column density entry, as generated by MYSQL

origin_spectrum_id (int 11) – Identifier of the optical depth spectrum from which the column density was derived

molecule (varchar 45) – Name of the molecule of which the column density was calculated

column_density (double) – The column density, in units of cm^{-1}

uncertainty (double) – Uncertainty of the column density

is_upper_limit (tinyint 1) – If 1, the column density is an upper limit

comment (varchar 45) – Additional comments on the entry, if applicable

A.1.5 Description of default ARF2 commands

What follows is a description of the commands used by ARF2 to perform the tasks it was designed to do. Each entry describes what the command is intended to do, what its input parameters and data are, which MYSQL tables it accesses and what it is expected to produce in the end.

A.1.5.1 parse_rawdata

Purpose

Crawls through raw_datadir to find the raw AKARI data and populates the database with information found therein.

Input parameters

None

Input data

A collection of decompressed raw AKARI data in raw_datadir

Database access

raw_info (write)

raw_files (write)

calibration_files (write)

Output

Populates the database with information about raw N3, NP and NG frames, and their dark frames.

A.1.5.2 find_default_calibrators

Purpose

Finds the default "2007Feb"[2] calibrator files in calibdir and adds them to the database.

Input parameters

None

Input data

The default calibration data files, located at CALIBDIR.2007Feb under <calibdir>.

Database access

calibration_files (write)

Output

Populates the calibration_files table with information on the default calibrator files.

A.1.5.3 create_master_darks

Purpose

Combines all the observed dark frames for a master dark frame for long and short exposures separately.

Input parameters

proposal (string) = Limits creation of master dark frames to AKARI proposals only of this name (default:'IMAPE')

Input data

[2]While the name "2007Feb" implies calibrator files originating from February 2007, this name is merely a directory name employed by the official JAXA AKARI pipeline to store all the calibration data. The actual data contained in this directory is much more recent, where updated calibration information is available.

The observed dark frames from each pointing being processed.

Database access

raw_info (read)

calibration_files (read+write)

Output

Creates master dark frames for each pointing in <calibdir>/master/

A.1.5.4 exclude_darks

Purpose

Used to remove bad dark frames from the database through the use of manual inspection

Input parameters

set (string) = Limits inspection to dark frames belonging only to a specific set. If 'ALL' is selected, all sets are inspected. (default:'ALL')

Input data

Dark frames belonging to selected set.

Database access

calibration_files (read+write)

Output

Removes dark frames from calibration_files based on user selection.

A.1.5.5 create_master_pixel_mask

Purpose

Combines the outlier mask from the default calibrator data with outliers found in the master dark frames of each pointings, to create a master pixel mask for each pointing.

Input parameters

clip (float) = The threshold multiplier fed to the sigma-clipping routine which finds outliers in the dark frames (default:5.0)

iters (integer) = Number of iterations performed by the sigma-clipping routine (default:3)

proposal (string) = Limits creation of master pixel masks to AKARI proposals only of this name (default:'IMAPE')

Input data

The pixel mask from the "2007Feb" calibration dataset, and the master dark frames of each pointing belonging to the given proposal.

Database access

calibration_files (read+write)

Output

Creates outlier masks for each pointing in <calibdir>/master/

A.1.5.6 find_external_akari_data

Purpose

Clones a part of the full AKARI database found on the JAXA servers into the local database.

Input parameters

verify_url (boolean) = If set to true, verifies that the raw observational data actually exists and is accessible on the JAXA servers, before adding an entry on it to the local database. This is a very slow process. (default:False)

Input data

Plaintext dumps[3] of the contents of the MYSQL databases located on the JAXA servers, in the form of the files AKARI_PROGRAM.1.txt, AKARI_PKGINFO.1.txt, and AKARI_OBSLOG.1.txt located under <root_datadir>/misc/

Database access

akari_external (write)

Output

Populates akari_external with information about the entire AKARI archive.

A.1.5.7 reduce_N3_frames

Purpose

Performs full reduction on the raw N3 frames.

Input parameters

proposal (string) = Limits creation of master dark frames to AKARI proposals only of this name. (default:'IMAPE')

flat (string) = Type of flat field frame to use in the reduction. (default: '2007Feb')

Input data

[3]Downloadable from `http://darts.isas.jaxa.jp/ir/akari/pointing.tables.html`

The raw N3 frames for all the pointings, and their corresponding calibration files.

Database access

calibration_files (read)

raw_info (read)

raw_files (read)

reduced_pointing_files (write)

Output

6 reduced N3 frames per pointing. The reduced frames are of the small and large fields of view, with separate files for the short, long and combined exposures.

A.1.5.8 reduce_NP_frames

Purpose

Performs full reduction on the raw NP frames.

Input parameters

proposal (string) = Limits creation of master dark frames to AKARI proposals only of this name (default:'IMAPE')

flat (string) = Type of flat field frame to use in the reduction. (default: '2007Feb')

Input data

The raw NP frames for all the pointings, and their corresponding calibration files.

Database access

calibration_files (read)

raw_info (read)

raw_files (read)

reduced_pointing_files (write)

Output

6 reduced NP frames per pointing. The reduced frames are of the small and large fields of view, with separate files for the short, long and combined exposures.

A.1.5.9 reduce_NG_frames

Purpose

Performs full reduction on the raw NG frames.

Input parameters

proposal (string) = Limits creation of master dark frames to AKARI proposals only of this name (default:'IMAPE')

flat (string) = Type of flat field frame to use in the reduction. (default: '2007Feb')

Input data

The raw NG frames for all the pointings, and their corresponding calibration files.

Database access

calibration_files (read)

raw_info (read)

raw_files (read)

reduced_pointing_files (write)

Output

6 reduced NG frames per pointing. The reduced frames are of the small and large fields of view, with separate files for the short, long and combined exposures.

A.1.5.10 extract_N3_sources

Purpose

Uses SExtractor to extract the source locations from all the big FoV N3 frames. Requires manual input for filtering of false positives.

Input parameters

pointing (string) = Name of the pointing to be processed. If set to 'ALL', all pointings will be processed. (default:'ALL')

threshold (float) = Sets the 'detect_thresh' parameter of SExtractor (default:3.0)

filter (string) = 3 parameters separated by commas, which set the SExtractor PARAMETERS 'filter', 'filter_name', and 'filter_thresh' respectively. (default:'N,default.conv,')

Input data

sex.conf.template and sex.param from <sextractor_dir>, and the reduced N3 frame(s) being processed.

Database access

reduced_pointing_files (read)

raw_info (read)

extracted_catalogue (write)

Output

Populates extracted_catalogue with pixel coordinates and (uncalibrated) photometric magnitudes of the extracted sources

A.1.5.11 find_c2d_data

Purpose

Populates the MYSQL database with data from the C2D files.

Input parameters

pointing (string) = Name of the pointing to be processed. If set to 'ALL', all pointings will be processed. (default:'ALL')

Input data

The C2D data files located at <root_datadir>/C2D_CAT/

Database access

c2d_catalogue (write)

Output

Populates c2d_catalogue with the data contained in the C2D catalogue files

A.1.5.12 jitter_correction

Purpose

Manually correct for large-scale jitter/warping by locating a shared source in the C2D catalogue and the N3 and NP frames.

Input parameters

pointing (string) = Name of the pointing to be processed. If set to 'ALL', all pointings will be processed. (default:'ALL')

Input data

The N3 and NP frames of the relevant pointing(s) and the C2D data associated with it/them.

Database access

raw_info (read)

reduced_pointing_files (read)

extracted_catalogue(read)

c2d_catalogue (read)

frame_shift_info (write)

Output

Populates frame_shift_info with the manually located associations.

A.1.5.13 distortion_correction

Purpose

Perform iterative construction of a "distortion matrix" between the extracted N3 sources and the C2D data by association.

Input parameters

pointing (string) = Name of the pointing to be processed. If set to 'ALL', all pointings will be processed. (default:'ALL')

"warp_info" (string) = Path to the file containing information about the distortion matrix. If file does not exist, it will be created after the first iteration. (default:'<calibdir>/warp_info.npz')

preview (boolean) = If set to true, the latest iteration of the distortion vectors will be shown between each iteration. (default:True)

re-associate (boolean) = If set to true, an existing warp_info file will be ignored and the iteration will start from scratch. (default:False)

Input data

The source locations from both c2d_catalogue and extracted_catalogue, and their respective N3 frames to act as a visual aid. If the warp_info file already exists, it will be used as the starting point of the iterations.

Database access

raw_info (read)

reduced_pointing_files (read)

extracted_catalogue(read)

c2d_catalogue (read)

frame_shift_info (read)

Output

The file pointed to by warp_info will be created/updated to contain distortion information between the C2D and N3 catalogues.

A.1.5.14 distortion_correction_NP

Purpose

Perform iterative construction of a "distortion matrix" between the extracted N3 sources and estimate of source locations in the NP data by association.

Input parameters

pointing (string) = Name of the pointing to be processed. If set to 'ALL', all pointings will be processed. (default:'ALL')

"warp_info" (string) = Path to the file containing information about the distortion matrix. If file does not exist, it will be created after the first iteration. (default:'<calibdir>/warp_info.npz')

re-associate (boolean) = If set to true, an existing warp_info file will be ignored and the iteration will start from scratch. (default:False)

Input data

The source locations from both extracted_catalogue, and their respective N3 frames to act as a visual aid. The NP frame for estimating source locations in it. If the warp_info file already exists, it will be used as the starting point of the iterations.

Database access

raw_info (read)

reduced_pointing_files (read)

extracted_catalogue(read)

c2d_catalogue (read)

frame_shift_info (read)

Output

The file pointed to by warp_info will be created/updated to contain distortion information between the N3 catalogue and estimates of NP source locations.

A.1.5.15 N3_source_association

Purpose

Uses the previously created distortion information between the extracted N3 sources and the C2D data to associate the sources in their respective catalogues.

Input parameters

pointing (string) = Name of the pointing to be processed. If set to 'ALL', all pointings will be processed. (default:'ALL')

"warp_info" (string) = Path to the file containing information about the distortion matrix. (default:'<calibdir>/warp_info.npz')

re-associate (boolean) = If set to true, any pre-existing source associations will be ignored, and instead be re-estimated using the distortion calculations. (default:False)

Input data

The source locations from both c2d_catalogue and extracted_catalogue, and their respective N3 frames to act as a visual aid. The file pointed to by warp_info contains the information about the distortion.

Database access

raw_info (read)

reduced_pointing_files (read)

extracted_catalogue(read)

c2d_catalogue (read)

frame_shift_info (read)

N3_object_association (write)

Output

N3_object_association will be populated with information on associations between the two catalogues.

A.1.5.16 NP_source_association

Purpose

Uses the previously created distortion information between the extracted N3 sources and estimates of NP source locations to create associations between the two sets.

Input parameters

pointing (string) = Name of the pointing to be processed. If set to 'ALL', all pointings will be processed. (default:'ALL')

"warp_info" (string) = Path to the file containing information about the distortion matrix. (default:'<calibdir>/warp_info_NP.npz')

re-associate (boolean) = If set to true, any pre-existing source associations will be ignored, and instead be re-estimated using the distortion calculations. (default:False)

Input data

The source locations from both c2d_catalogue and extracted_catalogue, and their respective N3 frames to act as a visual aid. The file pointed to by warp_info contains the information about the distortion.

Database access

raw_info (read)

reduced_pointing_files (read)

extracted_catalogue(read)

frame_shift_info (read)

NP_object_association (write)

Output

NP_object_association will be populated with information on associations between the N3 and NP sources.

A.1.5.17 visualize_distortion

Purpose

Produces a visualization of the distortion between the C2D and N3 data.

Input parameters

"warp_info" (string) = Path to the file containing information about the distortion matrix. (default:'<calibdir>/warp_info.npz')

gridstep (integer) = Grid size in pixels used to generate the vector field representing the distortion. Smaller number creates a finer field with more vectors. (default:15)

Input data

The file pointed to by warp_info contains the information about the distortion.

Database access

frame_shift_info (read)

Output

Plots and shows a savable figure representing the distortion.

A.1.5.18 visualize_distortion_NP

Purpose

Produces a visualization of the distortion between the N3 and NP data.

Input parameters

"warp_info" (string) = Path to the file containing information about the distortion matrix. (default:'<calibdir>/warp_info_NP.npz')

gridstep (integer) = Grid size in pixels used to generate the vector field representing the distortion. Smaller number creates a finer field with more vectors. (default:15)

Input data

The file pointed to by warp_info contains the information about the distortion.

Database access

frame_shift_info (read)

Output

Plots and shows a savable figure representing the distortion.

A.1.5.19 extract_manual

Purpose

Manual spectrum extraction of selected sources from the NP frames. Extracts only one spectrum at a time, using the Gaussian fit method.

Input parameters

pointing (string) = Name of the pointing to be processed. If set to 'ALL', all pointings will be processed. (default:'ALL')

k_limit (float) = K flux limit of the C2D data. Sources with flux lower than this will not be extracted. (default:2.0)

x_limit (float) = Magnitude limit of source extracted N3 data. Sources with magnitude higher than this will not be extracted. (default:-7.0)

Input data

The NP frames to be used in the extraction.

Database access

frame_shift_info (read)

raw_info (read)

reduced_pointing_files (read)

NP_object_association (read)

N3_object_association (read)

extracted_catalogue (read)

c2d_catalogue (read)

raw_spectra (write)

Output

raw_spectra will be populated with data about extracted spectra, and the extracted spectra will be placed in CSV files under subdirectories in <reduced_dir>.

A.1.5.20 extract_CLEAN

Purpose

Automatic extraction of all spectra from the NP frames. Extraction is performed using a 1-dimensional variant of the CLEAN (Högbom, 1974) algorithm.

Input parameters

pointing (string) = Name of the pointing to be processed. If set to 'ALL', all pointings will be processed. (default:'ALL')

k_limit (float) = K flux limit of the C2D data. Sources with flux lower than this will not be extracted. (default:2.0)

x_limit (float) = Magnitude limit of source extracted N3 data. Sources with magnitude higher than this will not be extracted. Note that these are (by default) uncalibrated magnitudes and not representative of true N3 magnitudes of the sources. (default:-7.0)

Input data

The NP frames to be used in the extraction.

Database access

frame_shift_info (read)

raw_info (read)

reduced_pointing_files (read)

NP_object_association (read)

N3_object_association (read)

extracted_catalogue (read)

c2d_catalogue (read)

raw_spectra (write)

Output

raw_spectra will be populated with data about extracted spectra, and the extracted spectra will be placed in CSV files under subdirectories in <reduced_dir>.

A.1.5.21 plot_raw_spectra

Purpose

Creates plots of the raw extracted spectra.

Input parameters

pointing (string) = Name of the pointing to be plotted. If set to 'ALL', all pointings will be plotted. (default:'ALL')

method (string) = Only spectra extracted with this method will be plotted. (default:'CLEAN')

Input data

The raw extracted spectra.

Database access

raw_info (read)

raw_spectra (read)

Output

Plots of the raw spectra will created in <graph_dir>.

A.1.5.22 filter_spectra_outliers

Purpose

Removes outliers from the extracted spectra.

Input parameters

pointing (string) = Name of the pointing to be processed. If set to 'ALL', all pointings will be processed. (default:'ALL')

method (string) = Only spectra extracted with this method will be processed. (default:'CLEAN')

plot (boolean) = If set to true, plots of the outlier-filtered spectra will be created in <graph_dir> (default:True)

Input data

The raw extracted spectra.

Database access

raw_info (read)

raw_spectra (read)

reduced_spectra (write)

Output

reduced_spectra will be populated with data about outlier-filtered spectra, and the reduced spectra will be placed in CSV files under subdirectories in <reduced_dir>.

A.1.5.23 merge_spectra_time

Purpose

Merges the long and short exposure spectra together.

Input parameters

pointing (string) = Name of the pointing to be processed. If set to 'ALL', all pointings will be processed. (default:'ALL')

method (string) = Only spectra extracted with this method will be processed. (default:'CLEAN')

plot (boolean) = If set to true, plots of the time-merged spectra will be created in <graph_dir> (default:True)

Input data

The outlier-filtered spectra.

Database access

raw_info (read)

raw_spectra (read)

reduced_spectra (read+write)

Output

reduced_spectra will be populated with data about time-merged spectra, and the reduced spectra will be placed in CSV files under subdirectories in <reduced_dir>.

A.1.5.24 filter_confused_spectra

Purpose

Detects and filters out confused parts of the time-merged spectra.

Input parameters

pointing (string) = Name of the pointing to be processed. If set to 'ALL', all pointings will be processed. (default:'ALL')

plot (boolean) = If set to true, plots of the confusion-filtered spectra will be created in <graph_dir> (default:True)

Input data

The time-merged spectra.

Database access

raw_info (read)

raw_spectra (read)

reduced_pointing_files (read)

reduced_spectra (read+write)

Output

reduced_spectra will be populated with data about confusion-filtered spectra, and the reduced spectra will be placed in CSV files under subdirectories in <reduced_dir>.

A.1.5.25 merge_spectra_pointings

Purpose

Merges the spectra of each sub-pointing within an AKARI pointing together.

Input parameters

pointing (string) = Name of the pointing to be processed. If set to 'ALL', all pointings will be processed. (default:'ALL')

plot (boolean) = If set to true, plots of the pointing-merged spectra will be created in <graph_dir> (default:True)

Input data

The confusion-filtered spectra.

Database access

raw_info (read)

raw_spectra (read)

N3_object_association (read)

NP_object_association (read)

extracted_catalogue (read)

raw_spectra (read)

reduced_spectra (read+write)

Output

reduced_spectra will be populated with data about pointing-merged spectra, and the reduced spectra will be placed in CSV files under subdirectories in <reduced_dir>.

A.1.5.26 manual_wavelength_calibration

Purpose

Used for manually determining the optimal parameters used in the spectral wavelength calibration step. See Chapter 5 Section 5.3.4 for more information about the manual wavelength calibration.

Input parameters

file_path (string) = Path to the pointing-merged spectrum which will be used as the template against which to perform the calibration. Needs to be manually set. (default:None)

lam_peak (float) = Wavelength in microns at which the local peak in uncalibrated intensity is expected to happen (default:2.4)

poly_a (float) = Multiplier for the second-order term of the calibration polynomial (default:4.82)

poly_b (float) = Multiplier for the first-order term of the calibration polynomial (default:17.33)

poly_c (float) = Multiplier for the zeroth-order term of the calibration polynomial (default:221.59)

Input data

A single pointing-merged spectrum, and the NP response function found in the "2007Feb" calibration set.

Database access

None

Output

None, but interactively shows the shape of the response function against the manually wavelength-calibrated spectrum, and shows which parameters were used to produce the produced calibration.

A.1.5.27 wavelength_calibration

Purpose

Performs wavelength calibration on the pointing-merged spectra.

Input parameters

plot (boolean) = If set to true, plots of the wavelength-calibrated spectra will be created in <graph_dir> (default:True)

drop-notglobalmax (boolean) = If set to true, spectra where the peak at the local peak close to ~ 2.4 μm is not the global maximum of the spectrum will cause the spectrum to be flagged as bad data. (default:True)

drop-fewpoints (boolean) = If set to true, spectra where the final number of datapoints is less than 4 will cause the spectrum to be flagged as bad data. (default:True)

Input data

The pointing-merged spectra.

Database access

reduced_spectra (read+write)

Output

reduced_spectra will be populated with data about wavelength-calibrated spectra, and the reduced spectra will be placed in CSV files under subdirectories in <reduced_dir>.

A.1.5.28 response_calibration

Purpose

Performs response calibration on the wavelength-calibrated spectra.

Input parameters

plot (boolean) = If set to true, plots of the wavelength-calibrated spectra will be created in <graph_dir> (default:True)

Input data

The wavelength-calibrated spectra.

Database access

reduced_spectra (read+write)

Output

reduced_spectra will be populated with data about response-calibrated spectra, and the reduced spectra will be placed in CSV files under subdirectories in <reduced_dir>.

A.1.5.29 finalize_spectra

Purpose

Creates final reduced versions of the spectra by cropping the response-calibrated spectra.

Input parameters

plot (boolean) = If set to true, plots of the finalized spectra will be created in <graph_dir> (default:True)

Input data

The response-calibrated spectra.

Database access

reduced_spectra (read+write)

Output

reduced_spectra will be populated with data about the finalized reduced spectra, and the reduced spectra will be placed in CSV files under subdirectories in <reduced_dir>.

A.1.5.30 create_od_spectra

Purpose

Creates optical depth spectra from the finalized reduced spectra, by fitting a 2^{nd} order polynomial baseline to them. This fit is designed to produce an adequate 3-micron O-H stretch feature.

Input parameters

plot (boolean) = If set to true, plots of the optical depth spectra will be created in <graph_dir> (default:True)

pointing (string) = Name of the pointing to be processed. If set to 'ALL', all pointings will be processed. (default:'ALL')

Input data

The optical depth spectra.

Database access

raw_info (read)

reduced_spectra (read)

raw_spectra (read)

extracted_catalogue (read)

N3_object_association (read)

NP_object_association (read)

od_spectra (write)

Output

od_spectra will be populated with data about the optical depth spectra, and the spectra will be placed in CSV files under subdirectories in <reduced_dir>.

A.1.5.31 calculate_NH2O

Purpose

Calculates $N(H_2O, \text{solid})$ from the fetures detected in the optical depth spectra.

Input parameters

plot (boolean) = If set to true, plots of the fit results will be created in <graph_dir> (default:True)

Input data

The optical depth spectra.

Database access

od_spectra (read)

column_densities (read)

Output

column_densities will be populated with data about $N(H_2O, solid)$.

A.1.5.32 map_NH2O

Purpose

Creates bubble plot maps of $N(H_2O, solid)$.

Input parameters

None

Input data

$N(H_2O, solid)$ from column_densities.

Database access

reduced_pointing_files (read)

od_spectra (read)

column_densities (read)

Output

Bubble plot maps of $N(H_2O, solid)$ will be created under <graph_dir>.

A.1.5.33 map_NH2O_spline

Purpose

Creates split-interpolated maps of $N(H_2O, solid)$.

Input parameters

None

Input data

$N(H_2O, solid)$ from column_densities.

Database access

reduced_pointing_files (read)

od_spectra (read)

column_densities (read)

Output

Spline-interpolated maps of $N(H_2O, solid)$ will be created under <graph_dir>.

A.1.5.34 plot_NH2O_vs_AV

Purpose

Creates a plot of $N(H_2O, solid)$ versus A_V.

Input parameters

None

Input data

$N(H_2O, solid)$ from column_densities and A_V from c2d_catalogue

Database access

c2d_catalogue (read)

od_spectra (read)

column_densities (read)

Output

A plot of $N(H_2O, solid)$ versus A_V is created under <graph_dir>.

A.1.5.35 plot_NH2O_vs_EBV

Purpose

Creates plots of $N(H_2O$, solid) versus $E(B-V)$, 100 μm dust emission and T_{dust}.

Input parameters

None

Input data

$N(H_2O$, solid) from column_densities and $E(B-V)$, $I(100\ \mu m)$ and T_{dust} fetched from IPAC[4].

Database access

c2d_catalogue (read)

od_spectra (read)

column_densities (read)

Output

Plots of $N(H_2O$, solid) versus $E(B-V)$, 100 μm dust emission and T_{dust} are created under <graph_dir>.

A.2 The Omnifit ice spectroscopy fitting utility

A.2.1 Introduction

OMNIFIT was originally created to be an easy to use and modify implementation of the multi-component ice fitting method presented in Noble et al. (2013). The basic features offered by the utility are as follows:

[4] http://irsa.ipac.caltech.edu/cgi-bin/DUST/nph-dust

- Is capable of importing and handling empirical (observational or laboratory) spectra in a single unified data structure.
- Match the resolution of two spectra through interpolation.
- Perform a least-squares fit of an arbitrary number of other spectra to a (usually observational, but does not have to be) target empirical spectrum.
- The fitted spectra can be either empirical spectra, or be defined through a mathematical function.
- The possible fit parameters for an empirical spectrum is a multiplier and a shift (although the shift is not used for the analysis done in this thesis).
- The fit parameters for non-empirical spectrum depend on the nature of the mathematical function used to define it.
- The fit can either be performed on the full spectral range available in the data, or be restricted to use only specific sub-spectral windows in its optimizations in cases where e.g. a part of the spectrum is known to be invalid.
- Any fit parameter can be allowed to vary freely or constrained within a set range.
- Estimate with a (non-reduced) χ^2 value the quality of the fit in either the full fitting range or only within specific fitting windows.
- The fit results can either be plotted into a MATPLOTLIB axis entity, or exported to a set of human and machine- readable files for analysis with other utilities.

While the utility was originally constructed to work with AKARI as the target spectrum for the fits, it has been made generic enough that it should be capable of handling any spectroscopic data with little difficulties. Indeed, in Chapter 3 I showed that it is capable of handling data from the VLT/ISAAC instrument as well. Furthermore, though the utility was designed with ice absorption spectroscopy in mind, it should be capable of handling any type of 1-dimensional spectroscopic data where a fit of either empirical data or mathematical functions is desirable.

A.2.2 System requirements

The program has been written using PYTHON 2.7 and tested to work under both Debian-like and Fedora-like Linux distributions. Omnifit makes use of a few external libraries without which it will not function. The non-linear least-squares fitting package LMFIT[5] is used for the constrained fits. Scientific python[6] (SCIPY; also required by LMFIT) is used for handling the various numerical arrays used by OMNIFIT, and MATPLOTLIB[7] is used for the plotting functions.

A.2.3 Example session

What follows is the code listing of a short session in which two sets of data, one observational (optical depth versus wavelength; I assume the continuum fit has already been performed and that flux has been turned to optical depth) and one laboratory (optical constants versus frequency) are loaded into omnifit, followed by fitting the laboratory data along with a single gaussian to the observational data. The fit results are plotted and exported to files.

```
1  from omnifit import *
2  import numpy as np
3  import matplotlib.pyplot as plt
4  obs_wl,obs_od = np.loadtxt('./obsdata.dat',dtype=float,usecols=(0,1))
5  lab_wn,lab_n,lab_k = np.loadtxt('./labdata.dat',dtype=float,usecols=(0,1,2))
6  obs_spec = spectrum(wl2wn(obs_wl),obs_od,specname='Observed data',xUnit='Wave number'
       ,yUnit='Optical depth')
7  lab_spec = labSpectrum(lab_wn,lab_n,lab_k,specname='Laboratory data')
8  interp_lab = lab_spec.interpolate(obs_spec)
9  fitter_example = fitter(obs_spec.x,obs_spec.y,modelname='Example fit')
10 lab_par = Parameters()
11 #                (Name,     Value,  Vary,  Min,     Max,     Expr)
12 lab_par.add_many(('mul',    0.5,    True,  0.0,     None,    None))
13 fitter_example.add_lab(interp_lab,lab_par,funcname='Example lab function')
14 theory_par=Parameters()
15 #                  (Name,    Value, Vary, Min,       Max,       Expr)
16 theory_par.add_many(('peak', 2.5,   True, 0.0,       None,      None),
```

[5] http://lmfit.github.io/lmfit-py/
[6] http://numpy.org/
[7] http://matplotlib.org/

```
17                      ('pos',    3000., True, 3000.-200., 3000.+200., None),
18                      ('fwhm',   50.0,  True, 0.0,        None,       None),
19                     )
20 fitter_example.add_theory('gaussian',theory_par,funcname='Example_gaussian')
21 fitter_example.perform_fit()
22 fitter_example.fitresults_tofile('example_fitres')
23 fig = plt.figure()
24 ax  = fig.add_subplot(111)
25 fitter_example.plot_fitresults(ax)
26 plt.savefig('example_fitres.pdf')
27 plt.close(fig)
```

In this, line 1-3 imports OMNIFIT, NUMPY and MATPLOTLIB. Strictly speaking, importing NUMPY and MATPLOTLIB is not necessary because OMNIFIT already imports them, but this way we prevent any ambiguity when calling either package in this example session. Lines 4 and 5 involve reading the observational and laboratory datas into their respective arrays. On the observational data file, columns 1 and 2 contain the wavelength and optical depth, respectively. For the laboratory data file columns 1-3 contain the frequency (in cm^{-1}), and n and k values respectively. Line 6 initializes the observational spectrum in the spectrum class, while line 7 calculates a CDE-corrected spectrum of the laboratory data. Line 8 creates a version of the laboratory spectrum which is interpolated to match the spectral resolution of the observation spectrum. Line 9 initializes the fitter class with the x (wavenumber) and y (optical depth) data of the observational spectrum. Lines 10-13 add the interpolated laboratory spectrum to the collection of fittable functions with an initial guess of the multiplier at 0.5. Lines 14-20 add a Gaussian to the function collection, with initial guesses of 2.5, 3000.0, and 50.0 for the peak, centroid position and full width half-maximum of the function, and with a constraint on the centroid position which permits it to deviate only up to $200\,cm^{-1}$ from the initial guess. Line 21 performs the actual fit, and line 22 saves the fit results to two files starting with "example_fitres". The files created are "example_fitres.xml" which contains various information (such as the best-fit parameters) and "example_fitres.csv" which contains the x,y information of the target data and the best-fitted data each separated to their own columns. Finally, lines 23-27 plot and save the fit results to the file

"example_fitres.pdf".

A.2.4 Command reference

OMNIFIT can be broadly speaking separated into two classes (the spectrum and fitter) and a small number of supporting functions. The operation of both classes and the supporting functions are detailed in this section.

A.2.4.1 Supporting functions

wl2wn

Description

Converts input from frequency (in μm) to wave number (in cm^{-1}).

Input

iWavelength = input wavelength

Output

wavelength converted to frequency

wn2wl

Description

Converts input from frequency (in cm^{-1}) to wavelength (in μm).

Input

iWavenumber = input frequency

Output

frequency converted to wavelength

cde_correct

Description

Turn given optical constants into CDE-corrected optical depths.

Input

wn = input frequency in cm^{-1}

n = real part of the complex refractive index

k = imaginary part of the complex refractive index

Output

the list [cabs_vol,cscat_vol], where

cabs_vol = average absorption cross section

cscat_vol = average scattering cross section

A.2.4.2 Class: spectrum

spectrum (class)

Description

The generic class for describing a 1-dimensional spectrum.

Constructor function input

iX = x axis data (usually wavelength or frequency, but can be other)

iY = y axis data (usually flux or optical depth)

specname = Name of the spectrum. *Default:'Unknown spectrum'*

xUnit = name of the units used on the x axis. *Default:'Unknown'*

yUnit = name of the units used on the y axis. *Default:'Unknown'*

nonData = variable names which contain no array data. It should not be necessary to set this manually. *Default:[]*

sort (function of *spectrum*)

Description

Automatically sort all the array data in the spectrum to go in increasing order of x. Automatically called after initializing the class.

Input

None.

Output

None.

dropbad (function of *spectrum*)

Description

Iterate through all the array data in the spectrum, and automatically drop elements containing non-finite data. Automatically called after initializing the class.

Input

None.

Output

None.

plot (function of *spectrum*)

Description

Plot the x,y data contained in the spectrum. Plotting defaults to x and y values defined during initialization, but variable choice can be overridden with optional parameters.

Input

iAx = MATPLOTLIB axis instance on which the plot should be drawn.

plotstyle = a string which MATPLOTLIB can interpret into a colour-linestyle combination. *Default:'k-'*

drawstyle = name of plotting style with which MATPLOTLIB should draw the plot. *Default:'steps-mid'*

x = if set, name of variable which should be plotted on the x axis. *Default:None*

y = if set, name of variable which should be plotted on the y axis. *Default:None*

Output

None.

subspectrum (function of *spectrum*)

Description

Create a new, cropped version of the spectrum.

Input

minX = Inclusive minimum x axis value on which to crop the spectrum.

maxX = Inclusive maximum x axis value on which to crop the spectrum.

Output

A new cropped spectrum instance

interpolate (function of *spectrum*)

Description

Create a new spectrum which is this spectrum interpolated to match the spectral resolution of a target spectrum.

Input

targSpectrum = spectrum instance with desired spectral resolution.

Output

A new interpolated spectrum instance with resolution matching that of targSpectrum

yat (function of *spectrum*)

Description

Get value of y at a specific value of x in the spectrum.

Input

x = value of x which is of interest

Output

value of y at x (interpolate when necessary)

convolve (function of *spectrum*)

Description

Perform a convolution to the y data in the the spectrum with a given point spread function (PSF)

Input

psf = Point spread function with which to convolve the spectrum

Output

None

gconvolve (function of *spectrum*)

Description

Perform a convolution to the y data in the the spectrum using a PSF which is a Gaussian with a designated full width half-maximum

Input

fwhm = Desired full width half-maximum of the Gaussian PSF in units of the x axis

Output

None

gpsf (function of *spectrum*)

Description

Generate a Gaussian PSF for the gaussian convolution function.

Input

fwhm = Desired full width half-maximum of the Gaussian PSF

Output

Point spread function which is usable by the convolution function

smooth (function of *spectrum*)

Description

Smooth the data with a specified smoothing window. Available options are: flat (moving average), hanning, hamming, bartlett, blackman. Function adapted from the guide posted by Kyle Brandt at `http://bit.ly/1pjj1v3`.

Input

window_len = Size of the smoothing window. *Default:11*

window = Type of smoothing window to be used. *Default:'hanning'*

Output

None

baseline (function of *spectrum*)

Description

Fit and subtract a specified polynomial baseline from the spectrum. Can also write fitted baseline to a file or, if said file already exists and its use is not overridden by the input parameters, use the fit parameters in that file to perform a baseline subtraction from the data without performing a new fit. The baselining also defines the noise in the spectrum data and stores it in the class instance.

Input

degree = Degree of polynomial to be fitted *Default:1*

windows = One or more windows within (or outside of, depending on exclusivity flag) which to perform the polynomial fit. *Default: [[0.0,1.0e6]]*

exclusive = If set to True, given windows are ignored by the baseline fit instead of used for performing it. *Default: False*

useFile = Path to file which will either (if it does not yet exist) be written to contain the fitted baseline. If the file already exists and a new baseline is not forced, the baseline designated by the file will be used in the baseline subtraction instead of a newly fitted polynomial. *Default:None*

overWrite = If set to True and a file already exists in the path designated by useFile, the data contained in the file will be ignored and overwritten with a newly fitted baseline. *Default:False*

Output

None

shift (function of *spectrum*)

Description

Shifts the data along the x axis by a set amount.

Input

amount = The amount (can be positive or negative) by which to shift the x axis values, in units of the x axis.

Output

None

max (function of *spectrum*)

Description

Returns either the global maximum of the spectrum y axis, or a local maximum within a specified range.

Input

checkrange = If set, the maximum is calculated within the specified window [minX,maxX] instead of the full spectral range. *Default:None*

Output

Global or local maximum, depending on whether checkrange is set or not.

min (function of *spectrum*)

Description

Returns either the global minimum of the spectrum y axis, or a local minimum within a specified range.

Input

checkrange = If set, the minimum is calculated within the specified window [minX,maxX] instead of the full spectral range. *Default:None*

Output

Global or local minimum, depending on whether checkrange is set or not.

info (function of *spectrum*)

Description

Prints out a summary of the spectrum.

Input

None

Output

None, but prints out assorted information about the spectrum.

absorptionSpectrum (child class of *spectrum*)

Description

A spectrum child class with additional internal variables which contain optical depth- specific information.

Constructor function input

iWn = x axis data in wavenumbers

iOd = y axis data in optical depth

specname = Name of the spectrum. *Default:'Unknown absorption spectrum'*

nonData = variable names which contain no array data. It should not be necessary to set this manually. *Default:[]*

plotod (function of *absorptionSpectrum*)

Description

Plots an optical depth spectrum.

Input

iAx = MATPLOTLIB axis instance on which the plot should be drawn.

in_wl = If True, plot x axis in units of wavelength instead of wave numbers. *Default:False*

Any parameters which would normally be accepted by spectrum.plot

Output

None

labSpectrum (child class of *absorptionSpectrum*)

Description

An absorptionSpectrum child class which is capable of performing CDE-correction on given laboratory data containing the complex refractive index of the material.

Constructor function input

iWn = x axis data in wavenumbers

iN = the real part of the complex optical refractive index

iK = the imaginary part of the complex optical refractive index

specname = Name of the spectrum. *Default:'Unknown CDE-corrected laboratory spectrum'*

plotnk (function of *labSpectrum*)

Description

Plots the real and imaginary parts of the complex optical refractive index as a function of wave number.

Input

xrange = if set, x axis range in which to plot the refractive indices. *Default:None*

Output

None

A.2.4.3 Class: fitter

fitter (class)

Description

The class which handles the fitting of the different spectra together, and the plotting and exporting of the fit results.

Constructor function input

iX = x axis data of the target function to which other functions are to be fitted.

iY = y axis data of the target function to which other functions are to be fitted.

dY = 1-σ uncertainty of the y axis data of the target function. Will be used in weighted calculation of the residuals. If not defined, all data points have equal weight.

modelname = name of the fitted model. *Default:'Unknown model'*

psf = point spread function of the target data, if known. *Default:None*

fitrange = list of x axis ranges to which the fitting is to be done. If not defined, the full x axis range will be used. *Default:None*

color = colour of the target function in the plotted fit results. *Default:'blue'*

customfunctions = whether to allow the fitting of un-tested analytical functions. Currently tested functions are a Gaussian and a CDE-corrected Lorentzian (see Chapter 3. *Support for other functions is still experimental. Default:False*

add_lab (function of *fitter*)

Description

Adds given "laboratory" data (though it can be any type of empirical data) to the total collection of functions to be fitted.

Input

iSpectrum = the spectrum instance which will be added

iParams = first guess of the fitting parameters, defined by an *lmfit* Parameters instance. Desired parameter is 'mul'.

funcname = name of the function to be fitted. If not set, uses name of spectrum as defined in the spectrum instance. *Default:None*

color = colour of the spectrum which will be plotted in the fit results. *Default:'red'*

Output

None

add_theory (function of *fitter*)

Description

Adds given analytical function to the collection of functions to be fitted to the target data.

Input

iShape = name of the function to be called. Unless customfunctions is activated in the fitter instance, only 'gaussian' and 'Lorentzian' are valid choices.

iParams = first guess of fitting parameters, defined by an *lmfit* Parameters instance. Desired parameters vary depending on iShape.

funcname = name of the function to be fitted. *Default:'Unknown function'*

color = colour of the spectrum which will be plotted in the fit results. *Default:'red'*

Output

None

perform_fit (function of *fitter*)

Description

Perform a least-squares fit of all previously given functions to the target function, and store the results in the fitter instance. Raises an exception if the fitting fails.

Input

None

Output

None

fit_residual (function of *fitter*)

Description

Calculate the residual of the fittable functions against the target function, given specific set of fitting parameters. This function is mostly used internally by the class, and should rarely be called manually.

Input

iPar = Input fitting parameters, as generated by extract_pars

custrange = Override parameter for the fitting range. If not set, fitting range defined during class instance initialization is used. *Default:None*

Output

The residual function

chisq (function of *fitter*)

Description

χ^2 value of the fit results, either in the full fitting range defined during initialization, of in a custom range defined during function call.

Input

custrange = Override parameter for the fitting range used for calculating χ^2. If not set, fitting range defined during class instance initialization is used. *Default:None*

Output

The χ^2 value of the fit results.

plot_fitresults (function of *fitter*)

Description

Plots the fit results to a given MATPLOTLIB axis instance.

Input

iAx = The MATPLOTLIB axis instance to which the fit results will be plotted.

autorange = toggles whether or not the x-axis of the axis instance will be automatically scaled to match the data range of the fitted functions. *Default: True*

drawstyle = name of the plotting style with which MATPLOTLIB should draw the plot. *Default:'steps-mid'*

legend = toggles whether or not a legend detailing which line represents which fitted component is generated in the axis. *Default:True*

Output

None, but axis instance pointed to by iAx will be modified to contain the plot.

fitresults_tofile (function of *fitter*)

Description

Export fit results to two output files. First file is filename.xml, which contains information about both the best-fit parameters and of function names etc. Second file is filename.csv, which contains x and y data of the fitted models, as would be visualized in a plotted fit result. First column of csv is the x value, which is shared by all models. Second column is y value of data that was being fitted to. Third column is total sum of fitted models. Fourth to Nth columns are the individual models, in the order described in filename.xml.

Input

filename = path with name (without suffix) of the file with which the two files "filename.xml" and "filename.csv" will be created.

Output

None, but the designated files will be created.

lowsigma (function of *fitter*)

Description

Returns dictionary indicating whether the total fit result or any of the individual fitted components fall below a noise threshold defined as a multiplier of the noise level.

Input

sigma = Multplier of the noise below which the fit result(s) must fall to be considered weak. *Default:1.0*

Output

Dictionary containing a boolean value for each of the fitted function and their total sum. If the peak of any of the functions or their sum fall below the noise level multiplied by the input parameter, their respective return value is set to True.

fit_results (function of *fitter*)

Description

Returns the fit results as a dictionary containing a separate entry for each fitted function.

Input

None

Output

A dictionary containing an entry for the fit results (including uncertainty of fit) of each function, under entries designated by the function names.

fit_result (function of *fitter*)

Description

Returns the fit result of a specific fitted function, as indicated by the input value. This is usually only used internally by the fitter instance; it is simpler to request fit results from the fitter by using the function fit_results.

Input

indFunc = The index of the fitted function, as defined by the internal function storage system. Usually 0 returns the first function to be added to the pool of fittable functions, 1 returns the second and so on.

Output

The fit results, including uncertainties, for the requested function.

parse_function (function of *fitter*)

Description

Parse the internally stored function type/function parameter combination in a way for it to be useful to the LMFIT minimization algorithms. This function is intended to be used internally by the fitter class, and it should not usually be necessary to call it manually.

Input

iPar = the Parameters instance corresponding to the function described in iFunc

iFunc = a dictionary information about the function being parsed. Usually generated internally by the fitter class during addition of a new

fittable function.

Output

The output of the function defined by iFunc when called with the parameters defined by iPar.

extract_pars (function of *fitter*)

Description

Extract the paramers from the internal function list so they can be manipulated by the residual minimization routines of the fitter class. Used internally by the fitter class and rarely necessary to call manually.

Input

None

Output

an LMFIT Parameters instance containing all the parameters needed for performing a fit of all the input functions into the target data

func_ident (function of *fitter*)

Description

Returns a string capable of uniquely identifying a specific function. Used internally by the fitter class and rarely necessary to call manually.

Input

indFunc = the index of the function as it is contained by the internal function list in the fitter class instance

Output

a string which acts as a unique identifier for the function pointed to by indFunc

A.3 Concluding remarks

Both ARF2 and OMNIFIT have been created in a way to allow them to be potentially useful in any future research involving the reduction of AKARI slitless spectroscopy and analysis of ice absorption features. This documentation applies to ARF2 and OMNIFIT in the forms they have taken at the conclusion of this thesis, but ongoing development is planned for both pieces of software and they are intended to be eventually released as open source. Consequently the documentation presented in this chapter is also liable to undergo changes and will likely no longer apply to future versions. Updated versions of this documentation –split into separate documents for ARF2 and OMNIFIT– will be provided with its respective software. Future inquiries about the state of the software and its documentation can be sent to `aleksi.suutarinen@iki.fi`.

Bibliography

Adams, W. S. (1941). In: *Astrophysical Journal* 93, p. 11.

Aikawa, Y. (2013). In: *Chemical reviews* 113, pp. 8961–80.

Aikawa, Y. et al. (2012a). In: *Astronomy and Astrophysics* 538, A57, A57.

Aikawa, Y., V. Wakelam, F. Hersant, R. T. Garrod, and E. Herbst (2012b). In: *Astrophysical Journal* 760, p. 40.

Al-Halabi, A., H. J. Fraser, G. J. Kroes, and E. F. van Dishoeck (2004). In: *Astronomy and Astrophysics* 422, pp. 777–791.

Allamandola, L. J., S. A. Sandford, A. G. G. M. Tielens, and T. M. Herbst (1992). In: *Astrophysical Journal* 399, p. 134.

ASTRO-F User Support Team (2005). *ASTRO-F Observer's Manual*. URL: `http://www.ir.isas.jaxa.jp/ASTRO-F/Observation/ObsMan/afobsman30.pdf`.

Astropy Collaboration et al. (2013). In: *Astronomy and Astrophysics* 558, A33, A33.

Bachiller, R., S. Liechti, C. M. Walmsley, and F. Colomer (1995). In: *Astronomy and Astrophysics* 295, p. L51.

Balog, R. et al. (2009). In: *Journal of the American Chemical Society* 131, pp. 8744–8745.

Barsony, M., M. E. Ressler, and K. A. Marsh (2005). In: *Astrophysical Journal* 630, pp. 381–399.

Beckford, A. F., P. W. Lucas, A. C. Chrysostomou, and T. M. Gledhill (2008). In: *Monthly Notices of the RAS* 384, pp. 907–929.

Belloche, A., R. T. Garrod, H. SP. Müller, and K. M. Menten (2014). In: *Science* 345, pp. 1584–1587.

Bergin, E. A. and W. D. Langer (1997). In: *Astrophysical Journal* 486, pp. 316–328.

Bergin, E. A., W. D. Langer, and P. F. Goldsmith (1995). In: *Astrophysical Journal* 441, pp. 222–243.

Bergin, E. A., D. A. Neufeld, and G. J. Melnick (1998). In: *Astrophysical Journal* 499, p. 777.

— (1999). In: *Astrophysical Journal* 510, p. L145.

Bergin, E. A. and R. L. Snell (2002). In: *Astrophysical Journal, Letters* 581, pp. L105–L108.

Bergin, E. A., G. J. Melnick, P. A. Gerakines, D. A. Neufeld, and D. C. B. Whittet (2005). In: *Astrophysical Journal* 627, pp. L33–L36.

Bertin, E. and S. Arnouts (1996). In: *Astronomy and Astrophysics, Supplement* 117, pp. 393–404.

Bisschop, S. E., H. J. Fraser, K. I. Öberg, E. F. van Dishoeck, and S. Schlemmer (2006). In: *Astronomy and Astrophysics* 449, pp. 1297–1309.

Bjerkeli, P. et al. (2012). In: *Astronomy and Astrophysics* 546, A29.

Blanksby, S. J. and G. B. Ellison (2003). In: *Accounts of Chemical Research* 36, p. 25.

Bohren, C. F. and D. R. Huffman (1983). *Absorption and Scattering of Light by Small Particles*. Wiley-VCH Verlag GmbH, pp. 499–519.
Boogert, A. C. A., M. R. Hogerheijde, and G. A. Blake (2002). In: *Astrophysical Journal* 568, pp. 761–770.
Boogert, A. C. A. et al. (2008). In: *Astrophysical Journal* 678, p. 985.
Boogert, A. C. A. et al. (2011). In: *Astrophysical Journal* 729, p. 92.
Boogert, A. C. A. et al. (2013). In: *Astrophysical Journal* 777, p. 73.
Born, M. and R. Oppenheimer (1927). In: *Annalen der Physik* 389, pp. 457–484.
Bottinelli, S. et al. (2010). In: *Astrophysical Journal* 718, p. 1100.
Broekhuizen, K., P. P. Kumar, and J. P. D. Abbatt (2004). In: *Geophysics Research Letters* 31, p. 1107.
Brooke, T. Y., K. Sellgren, and T. R. Geballe (1999). In: *Astrophysical Journal* 517, p. 883.
Brown, W. A. and A. S. Bolina (2007). In: *Monthly Notices of the RAS* 374, p. 1006.
Burke, D. J. and W. A. Brown (2010). In: *Physical Chemistry Chemical Physics* 12, p. 5947.
— (2015). In: *Monthly Notices of the RAS* 448, pp. 1807–1815.
Cabrit, S. and C. Bertout (1986). In: *Astrophysical Journal* 307, p. 313.
— (1990). In: *Astrophysical Journal* 348, p. 530.
Capps, R. W., F. C. Gillett, and R. F. Knacke (1978). In: *Astrophysical Journal* 226, pp. 863–868.
Caselli, P., C. M. Walmsley, M. Tafalla, L. Dore, and P. C. Myers (1999). In: *Astrophysical Journal, Letters* 523, pp. L165–L169.
Caselli, P. et al. (2012). In: *Astrophysical Journal* 759, p. L37.
Cazaux, S. and A. G. G. M. Tielens (2004). In: *Astrophysical Journal* 604, p. 222.
Charnley, S. B. (1999). In: *NATO ASIC Proc. 523: Formation and Evolution of Solids in Space*, p. 131.
Chiar, J. E., A. J. Adamson, and D. C. B. Whittet (1996). In: *Astrophysical Journal* 472, p. 665.
Chiar, J. E., A. J. Adamson, T. H. Kerr, and D. C. B. Whittet (1994). In: *Astrophysical Journal* 426, pp. 240–248.
Chiar, J. E. et al. (2011). In: *Astrophysical Journal* 731, p. 9.
Codella, C. et al. (2010). In: *Astronomy and Astrophysics* 518, p. L112.
Collings, M. P., J. W. Dever, H. J. Fraser, and M. R. S. McCoustra (2003b). In: *Astrophysics and Space Science* 285, pp. 633–659.
Collings, M. P., J. W. Dever, H. J. Fraser, M. R. S. McCoustra, and D. A. Williams (2003a). In: *Astrophysical Journal* 583, pp. 1058–1062.
Collings, M. P. et al. (2004). In: *Monthly Notices of the RAS* 354, pp. 1133–1140.
Connelley, M. S., B. Reipurth, and A. T. Tokunaga (2008). In: *Astronomical Journal* 135, pp. 2496–2525.
Crutcher, R. M., B. Wandelt, C. Heiles, E. Falgarone, and T. H. Troland (2010). In: *Astrophysical Journal* 725, pp. 466–479.
Cuppen, H. M. and E. Herbst (2007). In: *Astrophysical Journal* 668, pp. 294–309.
Cuppen, H. M., E. F. van Dishoeck, E. Herbst, and A. G. G. M. Tielens (2009). In: *Astronomy and Astrophysics* 508, pp. 275–287.
Cuppen, H. M., E. M. Penteado, K. Isokoski, N. van der Marel, and H. Linnartz (2011). In: *Monthly Notices of the RAS* 417, p. 2809.

Cutri, R. M. et al (2003). In: *VizieR Online Data Catalog* 2246, p. 0.
Daniel, F., M.-L. Dubernet, and A. Grosjean (2011). In: *Astronomy and Astrophysics* 536, A76.
Dartois, E. et al. (1999). In: *Astronomy and Astrophysics* 342, p. L32.
Dartois, E., L. d'Hendecourt, W. Thi, K. M. Pontoppidan, and E. F. van Dishoeck (2002). In: *Astronomy and Astrophysics* 394, pp. 1057–1068.
Dartois, E. et al. (2003). In: *Galactic Star Formation Across the Stellar Mass Spectrum.* Ed. by J. M. De Buizer and N. S. van der Bliek. Vol. 287. Astronomical Society of the Pacific Conference Series, pp. 187–192.
de Graauw, T. et al. (2010). In: *Astronomy and Astrophysics* 518, p. L6.
de Jong, T., A. Dalgarno, and S.-I. Chu (1975). In: *Astrophysical Journal* 199, pp. 69–78.
de Marcellus, P. et al. (2015). In: *Proceedings of the National Academy of Sciences*, p. 201418602.
D'Hendecourt, L. B. and L. J. Allamandola (1986). In: *Astronomy and Astrophysics, Supplement* 64, pp. 453–467.
Dionatos, O. et al. (2013). In: *Astronomy and Astrophysics* 558, A88.
Draine, B. T. and C. F. McKee (1993). In: *Annual Review of Astron and Astrophys* 31, pp. 373–432.
Draine, B. T., W. G. Roberge, and A. Dalgarno (1983). In: *Astrophysical Journal* 264, p. 485.
Drozdovskaya, M. N., C. Walsh, R. Visser, D. Harsono, and E. F. van Dishoeck (2014). In: *Monthly Notices of the RAS* 445, pp. 913–929.
Duley, W. W. (1974). In: *Astrophysics and Space Science* 26, pp. 199–205.
Dulieu, F. et al. (2010). In: *Astronomy and Astrophysics* 512, A30.
Dulieu, F. et al. (2013). In: *Scientific reports* 3, p. 1338.
Ehrenfreund, P., A. C. A. Boogert, P. A. Gerakines, A. G. G. M. Tielens, and E. F. van Dishoeck (1997). In: *Astronomy and Astrophysics* 328, pp. 649–669.
Einstein, A. (1905). In: *Annalen der Physik* 322, pp. 132–148.
Eiroa, C. and K.-W. Hodapp (1989). In: *Astronomy and Astrophysics* 210, pp. 345–350.
Emprechtinger, M. et al. (2013). In: *Astrophysical Journal* 765, p. 61.
Evans II, N. J. et al. (2003). In: 115, pp. 965–980.
Fayolle, E. C., K. I. Öberg, H. M. Cuppen, R. Visser, and H. Linnartz (2011a). In: *Astronomy and Astrophysics* 529, A74.
Fayolle, E. C. et al. (2011b). In: *Astrophysical Journal, Letters* 739, p. L36.
Fayolle, E. C. et al. (2013). In: *Astronomy and Astrophysics* 556, A122.
Fedoseev, G., H. M. Cuppen, S. Ioppolo, T. Lamberts, and H. Linnartz (2015). In: *Monthly Notices of the RAS* 448, pp. 1288–1297.
Ferrière, K. M. (2001). In: *Rev. Mod. Phys.* 73, pp. 1031–1066.
Flower, D. R. and G. Pineau des Forêts (2010). In: *Monthly Notices of the RAS* 406, p. 1745.
Flower, D. R., J. Le Bourlot, G. Pineau des Forêts, and S. Cabrit (2003). In: *Monthly Notices of the RAS* 341, p. 70.
Fraser, H. J., M. R. S. McCoustra, and D. A. Williams (2002). In: *Astronomy & Geophysics* 43, pp. 2.10–2.18.

Fraser, H. J. and E. F. van Dishoeck (2004). In: *Advances in Space Research* 33, pp. 14–22.
Fraser, H. J., M. P. Collings, M. R. S. McCoustra, and D. A. Williams (2001). In: *Monthly Notices of the RAS* 327, p. 1165.
Fraser, H. J., M. P. Collings, J. W. Dever, and M. R. S. McCoustra (2004). In: *Monthly Notices of the RAS* 353, pp. 59–68.
Fuchs, G. W. et al. (2009). In: *Astronomy and Astrophysics* 505, pp. 629–639.
Garrod, R., I. Hee Park, P. Caselli, and E. Herbst (2006). In: *Faraday Discussions* 133, p. 51.
Garrod, R. T. (2013). In: *Astrophysical Journal* 765, p. 60.
Garrod, R. T. and E. Herbst (2006). In: *Astronomy and Astrophysics* 457, pp. 927–936.
Garrod, R. T., V. Wakelam, and E. Herbst (2007). In: *Astronomy and Astrophysics* 467, pp. 1103–1115.
Garrod, R. T., S. L. W. Weaver, and E. Herbst (2008). In: *Astrophysical Journal* 682, pp. 283–302.
Gavilan, L., J. L. Lemaire, and G. Vidali (2012). In: *Monthly Notices of the RAS* 424, pp. 2961–2970.
Geballe, T. R. (1986). In: *Astronomy and Astrophysics* 162, pp. 248–252.
Geppert, W. D. and M. Larsson (2008). In: *Molecular Physics* 106, pp. 2199–2226.
Geppert, W. D. et al. (2006). In: *Faraday Discussions* 133, p. 177.
Gerakines, P. A., W. A. Schutte, J. M. Greenberg, and E. F. van Dishoeck (1995). In: *Astronomy and Astrophysics* 296, pp. 810–818.
Gibb, E. L., D. C. B. Whittet, A. C. A. Boogert, and A. G. G. M. Tielens (2004). In: *Astrophysical Journal, Supplement* 151, p. 35.
Gillett, F. C. and W. J. Forrest (1973). In: *Astrophysical Journal* 179, pp. 483–491.
Glassgold, A. E., R. Meijerink, and J. R. Najita (2009). In: *Astrophysical Journal* 701, p. 142.
Goldsmith, P. F. and W. D. Langer (1999). In: *Astrophysical Journal* 517, pp. 209–225.
Green, J. D. et al. (2013). In: *Astrophysical Journal* 770, p. 123.
Grim, R. J. A., F. Baas, J. M. Greenberg, T. R. Geballe, and W. Schutte (1991). In: *Astronomy and Astrophysics* 243, pp. 473–477.
Haas, M. et al. (2008). In: *Astronomy and Astrophysics* 488, pp. 987–996.
Hagen, W., L. J. Allamandola, and J. M. Greenberg (1979). In: *Astrophysics and Space Science* 65, pp. 215–240.
— (1980). In: *Astronomy and Astrophysics* 86, pp. L3–L6.
Hagen, W., A. G. G. M. Tielens, and J. M. Greenberg (1981). In: *Chemical Physics* 56, pp. 367–379.
Hartquist, T. W. and D. A. Williams (1998). *The molecular astrophysics of stars and galaxies.* 4th ed. Oxford University Press.
Heisenberg, W. (1927). In: *Zeitschrift fur Physik* 43, pp. 172–198.
Herbst, E. and H. M. Cuppen (2006). In: *Proceedings of the National Academy of Science* 103, pp. 12257–12262.
Herczeg, G. J. et al. (2012). In: *Astronomy and Astrophysics* 540, A84.
Herpin, F. et al. (2012). In: *Astronomy and Astrophysics* 542, A76.
Hiraoka, K. et al. (2002). In: *Astrophysical Journal* 577, pp. 265–270.
Hocuk, S., S. Cazaux, and M. Spaans (2014). In: *Monthly Notices of the RAS* 438, pp. L56–L60.

Högbom, J. A. (1974). In: *Astronomy and Astrophysics, Supplement* 15, p. 417.
Hollas, J. M. (1992). *Modern Spectroscopy*. 2nd ed. John Wiley & Sons.
Hollenbach, D. and C. F. McKee (1989). In: *Astrophysical Journal* 342, p. 306.
Hornekær, L., A. Baurichter, V. V. Petrunin, D. Field, and A. C. Luntz (2003). In: *Science* 302, pp. 1943–1946.
Hudgins, D. M., S. A. Sandford, L. J. Allamandola, and A. G. G. M. Tielens (1993). In: *Astrophysical Journal, Supplement* 86, pp. 713–870.
Hudson, R. L. and M. H. Moore (1999). In: *Icarus* 140, pp. 451–461.
Imanishi, M. and P. R. Maloney (2003). In: *Astrophysical Journal* 588, p. 165.
Ioppolo, S., H. M. Cuppen, C. Romanzin, E. F. van Dishoeck, and H. Linnartz (2008). In: *Astrophysical Journal* 686, p. 1474.
Ioppolo, S., Y. van Boheemen, H. M. Cuppen, E. F. van Dishoeck, and H. Linnartz (2011). In: *Monthly Notices of the RAS* 413, pp. 2281–2287.
Ioppolo, S. et al. (2014). In: *Physical Chemistry Chemical Physics* 16, pp. 8270–8282.
Johnson, R. E. (1990). *Energetic charged-particle interactions with atmospheres and surfaces*. Vol. 19. Springer.
— (1998). "Sputtering and desorption from icy surfaces". In: *Solar System Ices*. Springer, pp. 303–334.
Juvela, M., J. Harju, N. Ysard, and T. Lunttila (2012). In: *Astronomy and Astrophysics* 538, A133.
Karska, A. et al. (2013). In: *Astronomy and Astrophysics* 552, A141.
Kirsanova, M. S., D. S. Wiebe, A. M. Sobolev, C. Henkel, and A. P. Tsivilev (2014). In: *Monthly Notices of the RAS* 437, pp. 1593–1608.
Kitta, K. and W. Kraetschmer (1983). In: *Astronomy and Astrophysics* 122, pp. 105–110.
Klotz, A. et al. (2008). In: *Astronomy and Astrophysics* 488, pp. 559–564.
Kristensen, L. E. et al. (2010a). In: *Astronomy and Astrophysics* 516, A57.
Kristensen, L. E. et al. (2010b). In: *Astronomy and Astrophysics* 521, p. L30.
Kristensen, L. E. et al. (2011). In: *Astronomy and Astrophysics* 531, p. L1.
Kristensen, L. E. et al. (2012). In: *Astronomy and Astrophysics* 542, A8.
Kristensen, L. E. et al. (2013). In: *Astronomy and Astrophysics* 557, A23.
Lacy, J. H., R. Knacke, T. R. Geballe, and A. T. Tokunaga (1994). In: *Astrophysical Journal* 428, p. L69.
Lamberts, T., H. M. Cuppen, S. Ioppolo, and H. Linnartz (2013). In: *Physical Chemistry Chemical Physics* 15, p. 8287.
Lan, K. and J. W. Jorgenson (2001). In: *Journal of Chromatography A* 915, pp. 1–13.
Langer, W. (1976). In: *Astrophysical Journal* 206, pp. 699–712.
Lee, H.-H., R. P. A. Bettens, and E. Herbst (1996). In: *Astronomy and Astrophysics, Supplement* 119, p. 111.
Leger, A. et al. (1979). In: *Astronomy and Astrophysics* 79, pp. 256–259.
Lesaffre, P., J.-P. Chièze, S. Cabrit, and G Pineau des Forêts (2004). In: *Astronomy and Astrophysics* 427, pp. 157–167.
Lesaffre, P. et al. (2013). In: *Astronomy and Astrophysics* 550, A106.
Leurini, S. et al. (2004). In: *Astronomy and Astrophysics* 422, pp. 573–585.
Lorente, R. et al. (2007). *AKARI IRC Data User Manual*. URL: `http://www.ir.isas.jaxa.jp/ASTRO-F/Observation/IDUM/IRC_IDUM_1.3.pdf`.
Manoj, P. et al. (2013). In: *Astrophysical Journal* 763, p. 83.

Maret, S. et al. (2005). In: *Astronomy and Astrophysics* 442, p. 527.
Mastrapa, R. M., S. A. Sandford, T. L. Roush, D. P. Cruikshank, and C. M. Dalle Ore (2009). In: *Astrophysical Journal* 701, pp. 1347–1356.
Mathis, J. S., W. Rumpl, and K. H. Nordsieck (1977). In: *Astrophysical Journal* 217, pp. 425–433.
McKee, C. F. and D. J. Hollenbach (1980). In: *Astronomy and Astrophysics Reviews* 18, p. 219.
Merrill, K. M., R. W. Russell, and B. T. Soifer (1976). In: *Astrophysical Journal* 207, pp. 763–769.
Moorwood, A. et al. (1998). In: *The Messenger* 94, pp. 7–9.
Mottram, J. C. et al. (2013). In: *Astronomy and Astrophysics* 558, A126.
Mottram, J. C. et al. (2014). In: *Astronomy and Astrophysics* 572, A21.
Müller, H. S. P., S. Thorwirth, D. A. Roth, and G. Winnewisser (2001). In: *Astronomy and Astrophysics* 370, p. L49.
Müller, H. S.P., F. Schlöder, J. Stutzki, and G. Winnewisser (2005). In: *Journal of Molecular Structure* 742, p. 215.
Murakawa, K., M. Tamura, and T. Nagata (2000). In: *Astrophysical Journal, Supplement* 128, pp. 603–613.
Nakanishi, K. (1962). *Infrared absorption spectroscopy, practical.* Holden-Day.
Neufeld, D. A. and A. Dalgarno (1989). In: *Astrophysical Journal* 340, p. 869.
Nisini, B. et al. (2010). In: *Astronomy and Astrophysics* 518, p. L120.
Nisini, B. et al. (2013). In: *Astronomy and Astrophysics* 549, A16.
Noble, J. A (2011). PhD thesis. University of Strathclyde.
Noble, J. A., F. Dulieu, E. Congiu, and H. J. Fraser (2012). "The formation of carbon dioxide in molecular cores by a non-energetic route". In: *EAS Publications Series.* Vol. 58. EAS Publications Series, pp. 353–356.
Noble, J. A., H. J. Fraser, Y. Aikawa, K. M. Pontoppidan, and I. Sakon (2013). In: *Astrophysical Journal* 775, p. 85.
Öberg, K. I., S. Bottinelli, and E. F. van Dishoeck (2009). In: *Astronomy and Astrophysics* 494, pp. L13–L16.
Öberg, K. I., T. Lauck, and D. Graninger (2014). In: *Astrophysical Journal* 788, p. 68.
Öberg, K. I., E. F. van Dishoeck, and H. Linnartz (2009). In: *Astronomy and Astrophysics* 496, pp. 281–293.
Öberg, K. I. et al. (2008). In: *Astrophysical Journal* 678, pp. 1032–1041.
Öberg, K. I., H. Linnartz, R. Visser, and E. F. van Dishoeck (2009). In: *Astrophysical Journal* 693, pp. 1209–1218.
Öberg, K. I., S. Bottinelli, J. K. Jørgensen, and E. F. van Dishoeck (2010a). In: *Astrophysical Journal* 716, pp. 825–834.
Öberg, K. I., E. F. van Dishoeck, H. Linnartz, and S. Andersson (2010b). In: *Astrophysical Journal* 718, pp. 832–840.
Öberg, K. I. et al. (2011b). In: *Proceedings of the International Astronomical Union* 7, pp. 65–78.
Öberg, K. I. et al. (2011a). In: *Astrophysical Journal* 740, p. 109.
Ohyama, Y. et al. (2007). In: *Publications of the Astronomical Society of Japan* 59, S411–S422.
Oliveira, J. M. et al. (2009). In: *Astrophysical Journal* 707, pp. 1269–1295.

Palumbo, M. E., A. C. Castorina, and G. Strazzulla (1999). In: *Astronomy and Astrophysics* 342, pp. 551–562.
Palumbo, M. E. et al. (2008). In: *Journal of Physics Conference Series* 101.1, p. 012002.
Pearce, M. P. et al. (2012). In: *Physical Chemistry Chemical Physics* 14, p. 3444.
Pei, C. C., Q. Q. Gou, and Q. Zeng (1988). In: *Astronomy and Astrophysics, Supplement* 76, pp. 35–52.
Petuchowski, S. J., E. Dwek, J. E. Allen Jr., and J. A. Nuth III (1989). In: *Astrophysical Journal* 342, pp. 406–415.
Pickett, H. M. et al. (1998). In: *J. Quant. Spectrosc. & Rad. Transfer* 60, p. 883.
Pilbratt, G. L. et al. (2010). In: *Astronomy and Astrophysics* 518, p. L1.
Pilbratt, Göran L. (2008). *Herschel Mission Overview and Key Programmes*. URL: `http://herschel.esac.esa.int/Publ/2008/SPIE2008_Herschel_paper.pdf`.
Plekan, O., A. Cassidy, R. Balog, N. C. Jones, and D. Field (2011). In: *Physical Chemistry Chemical Physics* 13, pp. 21035–21044.
Pontoppidan, K. M. (2006). In: *Astronomy and Astrophysics* 453, pp. L47–L50.
Pontoppidan, K. M., E. F. van Dishoeck, and E. Dartois (2004). In: *Astronomy and Astrophysics* 426, p. 925.
Pontoppidan, K. M., E. Dartois, E. F. van Dishoeck, W.-F. Thi, and L. D'Hendecourt (2003b). In: *Astronomy and Astrophysics* 404, p. L17.
Pontoppidan, K. M. et al. (2003a). In: *Astronomy and Astrophysics* 408, p. 981.
Pontoppidan, K. M. et al. (2005). In: *Astrophysical Journal* 622, pp. 463–481.
Pontoppidan, K. M. et al. (2008). In: *Astrophysical Journal* 678, pp. 1005–1031.
Pottage, J. T., D. R. Flower, and S. L. Davis (2001). In: *Journal of Physics B Atomic Molecular Physics* 34, pp. 3313–3330.
Powell, M. J. D. (1964). In: *The Computer Journal* 7, pp. 155–162.
Rabli, D. and D. R. Flower (2010). In: *Monthly Notices of the RAS* 406, p. 95.
Roelfsema, P. R. et al. (2011). In: *Astronomy and Astrophysics* 537, A17.
Rybicki, G. B. and A. P. Lightman (1985). *Radiative processes in astrophysics*. Wiley-VCH.
Rydbeck, O. E. H., J. Elldér, and W. M. Irvine (1973). In: *Nature* 246, pp. 466–468.
Sander, S. P. et al. (2011). In: *JPL Publication* 10, p. 6.
Sandford, S. A., L. J. Allamandola, A. G. G. M. Tielens, and G. J. Valero (1988). In: *Astrophysical Journal* 329, pp. 498–510.
Santangelo, G. et al. (2012). In: *Astronomy and Astrophysics* 538, A45.
Santangelo, G. et al. (2013). In: *Astronomy and Astrophysics* 557, A22.
Schlegel, D. J., D. P. Finkbeiner, and M. Davis (1998). In: *Astrophysical Journal* 500, pp. 525–553.
Schmalzl, M. et al. (2014). In: *Astronomy and Astrophysics* 572, A81.
Schöier, F. L., F. F. S. van der Tak, E. F. van Dishoeck, and J. H. Black (2005). In: *Astronomy and Astrophysics* 432, p. 369.
Shematovich, V. I. (2012). In: *Solar System Research* 46, pp. 391–407.
Shimonishi, T. et al. (2008). In: *Astrophysical Journal, Letters* 686, pp. L99–L102.
— (2010). In: *Astronomy and Astrophysics* 514, A12, A12.
— (2013). In: *Astronomical Journal* 145, p. 32.
Shuping, R. Y., T. P. Snow, J. E. Chiar, and T. Kerr (2000). In: *Astrophysical Journal* 529, pp. 932–935.

Smith, M. D., T. Khanzadyan, and C. J. Davis (2003). In: *Monthly Notices of the RAS* 339, p. 524.
Smith, R. G., K. Sellgren, and A. T. Tokunaga (1989). In: *Astrophysical Journal* 344, pp. 413–426.
Snell, R. L. et al. (2000). In: *Astrophysical Journal* 539, p. L93.
Soifer, B. T. et al. (1979). In: *Astrophysical Journal* 232, p. L53.
Sonnentrucker, P. et al. (2008). In: *Astrophysical Journal* 672, pp. 361–370.
Spoon, H. W. W., J. V. Keane, A. G. G. M. Tielens, D. Lutz, and A. F. M. Moorwood (2001). In: *Astronomy and Astrophysics* 365, pp. L353–L356.
Spoon, H. W. W. et al. (2002). In: *Astronomy and Astrophysics* 385, pp. 1022–1041.
Spoon, H. W. W. et al. (2004). In: *Astrophysical Journal, Supplement* 154, pp. 184–187.
Sutton, E. C. and E. Herbst (1988). In: *Astrophysical Journal* 333, pp. 359–365.
Suutarinen, A. N. et al. (2013). In: *Astronomy and Astrophysics* 555, A140.
Suutarinen, A. N., L. E. Kristensen, J. C. Mottram, H. J. Fraser, and E. F. van Dishoeck (2014). In: *Monthly Notices of the RAS* 440, pp. 1844–1855.
Tafalla, M., J. Santiago-Garcia, A. Hacar, and R. Bachiller (2010). In: *Astronomy and Astrophysics* 522, A91.
Tafalla, M. et al. (2013). In: *Astronomy and Astrophysics* 551, A116.
Takahashi, S. et al. (2008). In: *Astrophysical Journal* 688, pp. 344–361.
Tanaka, M., S. Sato, T. Nagata, and T. Yamamoto (1990). In: *Astrophysical Journal* 352, pp. 724–730.
Thi, W.-F. et al. (2006). In: *Astronomy and Astrophysics* 449, pp. 251–265.
Tielens, A. G. G. M. (2005). *The Physics and Chemistry of the Interstellar Medium.* Cambridge University Press.
Tielens, A. G. G. M. and W. Hagen (1982). In: *Astronomy and Astrophysics* 114, p. 245.
Tielens, A. G. G. M., A. T. Tokunaga, T. R. Geballe, and F. Baas (1991). In: *Astrophysical Journal* 381, p. 181.
Tsumura, K. et al. (2013). In: *Publications of the ASJ* 65, p. 119.
Turner, B. E. (1998). In: *Astrophysical Journal* 501, p. 731.
van der Tak, F. F. S., E. F. van Dishoeck, and P. Caselli (2000). In: *Astronomy and Astrophysics* 361, p. 327.
van der Tak, F. F. S., J. H. Black, F. L. Schoier, D. J. Jansen, and E. F. van Dishoeck (2007). In: *Astronomy and Astrophysics* 468, p. 627.
van Dishoeck, E. F. (2014). In: *Faraday Discussions* 168 (0), pp. 9–47.
van Dishoeck, E. F. and G. A. Blake (1998). In: *Annual Review of Astron and Astrophys* 36, pp. 317–368.
van Dishoeck, E. F. et al. (2011). In: *Publications of the ASP* 123, p. 138.
van Kempen, T. A., C. McCoey, S. Tisi, D. Johnstone, and M. Fich (2014). In: *Astronomy and Astrophysics* 569, A53.
Van Loo, S., I. Ashmore, P. Caselli, S. A. E. G. Falle, and T. W. Hartquist (2013). In: *Monthly Notices of the RAS* 428, pp. 381–388.
van Loon, J. T. et al. (2005). In: *Monthly Notices of the RAS* 364, pp. L71–L75.
Vasta, M. et al. (2012). In: *Astronomy and Astrophysics* 537, A98.
Verdugo, E. et al. (2007). *AKARI FIS Data User Manual.* URL: `http://www.ir.isas.jaxa.jp/ASTRO-F/Observation/IDUM/FIS_IDUM_1.3.pdf`.
Visser, R. (2009). PhD Thesis. Leiden Observatory, Leiden University.

Visser, R., E. F. van Dishoeck, S. D. Doty, and C. P. Dullemond (2009). In: *Astronomy and Astrophysics* 495, p. 881.

Viti, S., M. P. Collings, J. W. Dever, M. R. S. McCoustra, and D. A. Williams (2004). In: *Monthly Notices of the RAS* 354, pp. 1141–1145.

Viti, S. et al. (2011). In: *Astrophysical Journal* 740, p. L3.

von Fraunhofer, J. (1814). In: *Denkschriften der Königlichen Akademie der Wissenschaften zu München* 5, p. 193.

Wada, A., N. Mochizuki, and K. Hiraoka (2006). In: *Astrophysical Journal* 644, pp. 300–306.

Walmsley, C. M. and H. Ungerechts (1983). In: *Astronomy and Astrophysics* 122, pp. 164–170.

Ward-Thompson, D. and A. P. Whitworth (2011). *An Introduction to Star Formation.* 1st ed. Cambridge University Press.

Watanabe, N. and A. Kouchi (2002). In: *Astrophysical Journal, Letters* 571, pp. L173–L176.

— (2008). In: *Progress in Surface Science* 83, pp. 439 –489.

Watanabe, N., A. Nagaoka, T. Shiraki, and A. Kouchi (2004). In: *Astrophysical Journal* 616, pp. 638–642.

Weingartner, J. C. and B. T. Draine (2001). In: *Astrophysical Journal* 548, pp. 296–309.

Whittet, D. C. B., M. F. Bode, D. W. T. Baines, A. J. Longmore, and A. Evans (1983). In: *Nature* 303, pp. 218–221.

Whittet, D. C. B. et al. (1988). In: *Monthly Notices of the RAS* 233, pp. 321–336.

Whittet, D. C. B. et al. (2007). In: *Astrophysical Journal* 655, pp. 332–341.

Willacy, K. and D. A. Williams (1993). In: *Monthly Notices of the RAS* 260, pp. 635–642.

Williams, David A and Eric Herbst (2002). In: *Surface Science* 500, pp. 823–837.

Wollaston, W. H. (1802). In: *Philosophical Transactions of the Royal Society of London* 92, pp. 365–380.

Woon, D. E. (2002). In: *International Journal of Quantum Chemistry* 88, p. 226.

Yamagishi, M. et al. (2011). In: *Astrophysical Journal, Letters* 731, p. L20.

Yamagishi, M. et al. (2012). In: *Publications of the Korean Astronomical Society* 27, pp. 249–252.

Yamagishi, M. et al. (2013). In: *Astrophysical Journal, Letters* 773, p. L37.

Yang, B., P. C. Stancil, N. Balakrishnan, and R. C. Forrey (2010). In: *Astrophysical Journal* 718, p. 1062.

Yıldız, U. A. et al. (2013). In: *Astronomy and Astrophysics* 556, p. 48.